Heterogeneous catalysis in microreactors : study of the performance of various supports

Xiaotong Zhan

▶ **To cite this version:**

Xiaotong Zhan. Heterogeneous catalysis in microreactors : study of the performance of various supports. Chemical and Process Engineering. Ecole Centrale Marseille, 2018. English. NNT : 2018ECDM0007 . tel-02071335

HAL Id: tel-02071335

https://theses.hal.science/tel-02071335

Submitted on 18 Mar 2019

HAL is a multi-disciplinary open access archive for the deposit and dissemination of scientific research documents, whether they are published or not. The documents may come from teaching and research institutions in France or abroad, or from public or private research centers.

L'archive ouverte pluridisciplinaire **HAL**, est destinée au dépôt et à la diffusion de documents scientifiques de niveau recherche, publiés ou non, émanant des établissements d'enseignement et de recherche français ou étrangers, des laboratoires publics ou privés.

ÉCOLE CENTRALE DE MARSEILLE

École Doctorale – Sciences de l'environnement ED 251

Laboratoire de Mécanique, Modélisation et Procédés Propre (UMR7340)

THÈSE DE DOCTORAT

pour obtenir le grade de

DOCTEUR de l'ÉCOLE CENTRALE de MARSEILLE

Discipline : Génie des procédés

Heterogeneous catalysis in microreactors: study of the performance of various supports

Par

ZHAN Xiaotong

Directrice de thèse : Pr. DUPRAT Françoise
Co-directeur de thèse : Dr. HÉRAULT Damien

Soutenue le 19 Octobre 2018

Jury

Dr. DUFAUD-NICCOLAI Véronique	Université Claude Bernard Lyon 1	Rapporteur
Pr. COMMENGE Jean-Marc	Université de Lorraine	Rapporteur
Pr. GUICHARDON Pierrette	École Centrale de Marseille	Examinateur
Dr. FAVRE-REGUILLON Alain	Conservatoire National des Arts et Métiers	Examinateur
Pr. FOTIADU Frédéric	École Centrale de Marseille	Membre invité
Pr. DUPRAT Françoise	École Centrale de Marseille	Directrice de thèse
Dr. HÉRAULT Damien	École Centrale de Marseille	Co-Directeur de thèse

Acknowledgements

First of all, I would like to express my deepest gratitude towards my PhD supervisor Pr. Françoise DUPRAT for her enthusiastic and strong support to my PhD achievement, and Dr. Damien HÉRAULT for his kindness and his precise assistance all along this work. Although this thesis is interdisciplinary and its complexity is beyond expectation, thanks to Françoise and Damien, the emerged problems are well handled. They gave me great help not only in academic filed but also in general life. It is a really great privilege for me to work with them and I have realized how valuable these experiences in the three years will be during my entire life.

I am also grateful to the committee members: Dr. DUFAUD-NICCOLAI Véronique, Pr. COMMENGE Jean-Marc, Pr. GUICHARDON Pierrette and Dr. FAVRE-REGUILLON Alain, for providing their time in the examination and evaluation of my thesis.

I would like to thank persons who have contributed to my PhD works: M. PUJOL Didier for technical support, M. TREUVEY Arnaud for the help with UV analysis, Dr. CHEVALLIER-MICHAUD Sabine for the help with LC-MS measurements, Dr. NUEL Didier for the help with GC analysis, Dr. NICOLETTI Cendrine for teaching me the ultramicrotomy technology, Dr. CABIE Martiane for the help with TEM analysis and Dr. DOMINICI Chrisitian for the help with SEM analysis. I also thank the internship students TAGO Makoto, HORIOT Guillaume, GONÇALVES NETO João and LATTES Sophie for their contributions in the synthesis of monolith.

I would like to thank all my colleagues of Chiroscience group of ISM2 and TED group of M2P2. The interdisciplinary working atmosphere greatly helped my researches. I warmly thank Dr. Estelle GODART and HENNEBELLE Marc for their delicious cakes, Dr. Innocenzo DE RIGGI for the delicious croissants, and Augustin for the organization of football score contest and barbecue.

I want to express my heartfelt gratitude to my parents and other family members. I cannot finish my PhD without their love, selfless support and encouragement.

I would like to thank all my friends, especially friends in Marseille, for their kindness help in my daily life. I also thank the association of Chinese students in Marseille, for providing the warmth of home and enriching my social experience.

Last but not least, I sincerely thank the China Scholarship Council (CSC) for the doctoral scholarship.

`

List of abbreviations

Chemical groups and molecules

APTS	(3-Aminopropyl)-triethoxysilane
ASM	Aminopropyl silica monoliths
CPL	ε-Caprolactam
DPTS	3-(2,4-Dinitrophenylamino)-propyltriethoxysilane
FA	Formic acid
MCM	Mobil Composition of Matter
MMA	Methylmethacrylate
MPTS	(3-Mercaptopropyl)- trimethoxysilane
MSM	Mercaptopropyl silica monoliths
NSM	Native silica monoliths
PAD	4,4'-Azodiphenol
PAP	*p*-aminophenol
PAXD	4,4'-Azoxydiphenol
PBQI	*p*-Benzoquinone imine
Pd	Palladium
PDMS	Polydimethylsiloxane
PEO	Polyethylene oxide
Ph	Phenyl
PHB	4,4'-Azodiphenol
PHx	*p*-Hydroxylaminophenol
PNP	*p*-Nitrophenol
PNS	*p*-Nitrosophenol
PPh_3	Triphenylphosphine
PP-PE	Polypropylene-polyethylene
PTFE	Polytetrafluoroethylene
SBA	Stanta barbara amorphous
TEOS	Tetraethylorthosilane
THF	Tetrahydrofuran
TTAB	Tetradecyltrimethylammonium bromide

Instruments and analyses

BET	Brunauer–Emmett–Teller
C.D.	Condensation degree
CED	Cumulative energy demand
CMR	Chip microreactor
CP-MAS	Cross polarization magic angle spinning
EDS	Energy-dispersive X-ray spectroscopy

`

HPLC	High performance liquid chromatography
LCA	Life cycle assessment
LFR	Low-flow reactor
MR	Microreactor
MS	Mass spectroscopy
NMR	Nuclear magnetic resonance
PDA	Photo-diode array
SEM	Scanning electron microscopy
TEM	Transmission electron microscope
UV	Ultraviolet

Parameters

A_c	cm^2	Cross-sectional area of tube
C_e	mmol/L	Solution concentration
C_{FA}	mmol/L	Concentration of formic acid
C_{FA}^0	mmol/L	Initial concentration of formic acid
C_i	mmol/L	Molar concentration of component i in the liquid phase within the reactor
$C_i°$	mmol/L	Feeding concentration of component i in the liquid phase within the reactor
C_{PAP}^f	mmol/L	Concentrations of PAP at the exit of reactor
C_{PNP}	mmol/L	Concentration of *p*-nitrophenol
C_{PNP}^0	mmol/L	Initial concentration of *p*-nitrophenol
C_{PNP}^f	mmol/L	Concentrations of PNP at the exit of reactor
$D_{cat,\ PB}$	mm	Catalyst average diameter in packed-bed microreactor
D_{ML}	mm	Internal diameter of monolithic microreactor
D_{PB}	mm	Internal diameter of packed-bed microreactor
E	J	Activation energy
E_{app}	J	Apparent activation energy
ES-		Negative electrospray ionisation in mass spectrometry
ES+		Positive electrospray ionisation in mass spectrometry
k	$(mol/L)^{1-n}/min$	Reaction rate constant
K	-	Adsorption equilibrium constant
K_D	m^2	Darcy permeability
L_{ML}	mm	Length of monolithic microreactor
L_{PB}	mm	Length of packed-bed microreactor
m		Stechiometric ratio ($m = C_{FA}^0/3\ C_{PNP}^0$)
m/z		Mass to charge ratio
$m_{cat,ML}$	mg	Catalyst mass
$m_{cat,PB}$	mg	Catalyst mass in packed-bed microreactor
$m_{pd,\ PB}$	mg	Palladium mass in packed-bed microreactor
$m_{pd,ML}$	mg	Palladium mass
n	mol	Mole of substance
N_A	mol^{-1}	Avogadro's number

`

n_{Pd}	mmol	Moles of palladium in the reactor
Q	mL/min	Flow rate in microreactor
q_I	mmol/g	Molar concentration of I component adsorbed on the catalyst surface
q_T	mmol/g	Total concentration of catalyst sites
r	mol/L/min	Reaction rate of PNP per unit of catalyst volume
R_1		Total aqueous phase volume/dodecane volume
R_2		Mass of TTAB/mass of total aqueous phase
R_3		Mass of TEOS/mass of total aqueous phase
R_4		n(TEOS)/n(organosilane)
RF		Response factor
s	mmol/g	Concentration of free catalyst sites
s_c	cm^2	Adsorption cross section of the adsorbing species
S_s	m^2/g	Specific surface areas of solids
T	°C	Temperature of reaction
t_{batch}	min	Time of reaction in batch reactor
TOF	h^{-1}	Turnover frequency
TON		Turnover number
V	mL	Volume of solution
V_a	cm^3/g	Adsorbed gas quantity per unit of solid
V_{batch}	mL	Total volume of the reactant
V_{CAT}	mL	Total volume of catalyst
V_{LIQ}	mL	Volume of the reaction mixture in batch reactor
V_m	cm^3/g	Monolayer adsorbed gas quantity per unit of solid
V_{ML}	mL	Volume of tube of monolithic microreactor
V_{PB}	mL	Volume of tube of packed-bed microreactor
X		Conversion of p-nitrophenol
X_{SR}		Shrinkage ratio
Δp	kPa	Pressure drop
η	mPa·s	Viscosity of liquid
ε		Void fraction in the catalyst bed = $V_{LIQ}/(V_{LIQ}+V_{CAT})$

Others

RTD	Residence time distribution
API	Active pharmaceutical ingredients
cGMP	Current good manufacturing practices
equiv.	Equivalent
FU	Functional unit
HIPE	High internal phase emulsions
ID	Internal diameter
PDE	Partial differential equation

`

Table of contents

Introduction

Nowadays, the fine chemical and pharmaceutical industry must satisfy the demand of the increasing market requirements, meanwhile, respond specific needs of customer and social, such as environmental friendly production and energy savings. The microreactor technology, which has been proposed and investigated for two decades, which has a great potential for improving the current production mode: 50% of reactions in the fine chemical/pharmaceutical industry could benefit from a continuous process based mainly on microreactor technology.[1]

The role of catalysis in industry is irreplaceable. Over 90% of all industrial chemicals are produced in a catalytic process.[2] Compared with homogeneous catalysis, heterogeneous catalyst, particularly solid catalyst, are widely used in industrial production because it can be separated in the process and recycled. Moreover, it can be implemented in fixed-bed reactor to improve the production efficiency.[3] Hence, the combination of heterogeneous catalysis and continuous-flow microreactors has drawn attention recently.

Among different microreactors with heterogeneous catalysts, packed-bed microreactor is the most mentioned and investigated, because of its easy fabrication and high catalyst loading.[4] It is commonly composed by a micro-channel randomly filled with powders or small pellets catalyst. The applications of microreactors with powder catalysts are largely limited in industry because the pressure drop could be significant and the possible catalyst aging could lead to the risk of clogging of microchannels. The monolithic microreactor is a rather new field and is currently in very rapid expansion in laboratory researches, due to its intrinsic advantages such as high porosity and large specific surface of catalyst support.[5] However, the lack of effective preparation method of monolithic catalyst in industrial-grade reactor immensely limits its development. Thus, the key issue of this thesis resides in mastering the synthesis of monolithic microreactors, understanding the nature properties and differences between packed-bed and monolithic microreactor, and evaluating their industrial potentials.

Hence, the general objective of this study is to prepare the microreactors with mechanically stable monolithic catalyst. To prove the concept, the immobilization of a hybrid inorganic-organic monolithic will be realized in stainless-steel tube. Therefore, its performance will be compared to a packed-bed microreactor by a convenient model reaction.

This investigation is interdisciplinary: the chemical engineering contributes to the kinetic analysis and modelisation of the reaction tested in the

---

[1] Roberge, D. M.; Ducry, L.; Bieler, N.; Cretton, P.; Zimmermann, B., *Chemical Engineering & Technology* **2005,** *28* (3), 318-323.

[2] Armor, J. N., *Catalysis Today* **2011,** *163* (1), 3-9.

[3] (a) Descorme, C.; Gallezot, P.; Geantet, C.; George, C., *ChemCatChem* **2012,** *4* (12), 1897-1906. (b) Frost, C. G.; Mutton, L., *Green Chemistry* **2010,** *12* (10), 1687-1703. (c) Sheldon, R. A.; Downing, R. S., *Applied Catalysis A: General* **1999,** *189* (2), 163-183.

[4] Tanimu, A.; Jaenicke, S.; Alhooshani, K., *Chemical Engineering Journal* **2017,** *327*, 792-821.

[5] Rossetti, I., *Catalysis Today* **2017**, *308,* 20-31.

microreactor, and the chemistry serves in the monolithic catalyst preparation and characterization. For this reason, the project has been supervised by two researchers, respectively of chemical engineering and chemistry, who can well handle the emerged problems from their respective fields. This work takes also into account the parallel studies of internship students who have been involved in the synthesis of monolith notably.

This thesis is divided in five chapters, and the organization is as follows:

The first one **"Bibliographic study"** gives an overview of the background knowledge of microreactors, emphasizing industrial applications and classification of reactions that take advantage of microreactor technology. The combination of heterogeneous catalysts with microreactors is discussed. Afterwards, the investigations on the reduction of *p*-nitrophenol in neutral, alkaline and acidic conditions are presented. The transfer hydrogenation of *p*-nitrophenol with formic acid is chosen as the model reaction of this thesis, because it seems a simple, clean and safe reaction, the reactive and product have important applications in chemical industry.

The second chapter **"Study of *p*-nitrophenol hydrogenation as model reaction in a packed-bed microreactor"** presents the investigations of model reaction catalyzed with a commercial Pd@alumina powder. First of all, the set-up is developed, as well as an analytical method precise enough to get quantitative information about the concentrations of *p*-nitrophenol and *p*-aminophenol, because published analytical methods didn't work in our experimental conditions. Then, the commercial catalyst is tested, and the effect of reaction parameters on conversion such as temperature, flow rate, initial concentration of reactants and time on flow are observed, with a special attention to the beginning of each run (dynamic study) and to their steady-state.

The third chapter **"Modelisation of the reaction in packed-bed microreactor with heterogeneous catalyst"** describes the modeling investigations based on the experimental observations in chapter 2. The ideal plug flow model is adopted to describe the packed-bed microreactor. The modelisation under transient conditions is firstly established for the rationalization of experimental observations, and then the model under stationary conditions is investigated to determine the reaction rate expression.

The fourth chapter **"Preparation and characterization of monolithic microreactor"** is dedicated to the preparation and characterization of the silica-based monolith with incorporated palladium nanoparticles. General research status about the preparation method of monolithic catalyst is firstly introduced, with the highlight of silica-based monolith. Then, series of silica-based monoliths have been prepared in cylinder PP-PE polymer tubes (syringe), for optimizing the preparation conditions of the stable, well-formed, hierarchically porous and functionalized silica monoliths. Thereafter, the functionalized silica monolith is prepared in a stainless-steel reactor tube with the optimized preparation conditions, and the palladium nanoparticles are immobilized by continuous flow method. A series of characterization methods are investigated to evaluate the monolith properties and confirm the effectiveness of preparation method.

The last chapter **"Study of *p*-nitrophenol hydrogenation as model reaction in the monolithic microreactor and comparison with packed-bed microreactor"** includes the catalytic test of monolithic catalyst with model reaction and the comparison of its properties with that of the commercial powder catalyst in packed-bed microreactor. The first experimental section presents the influence of reaction parameters such as temperature, flow rate and initial concentration of reactants on the conversion of *p*-nitrophenol in monolithic microreactor. Then the kinetic model of the reaction under stationary conditions is established, and the dynamic study of the reaction is presented. Finally, the performances of monolithic microreactor and packed-bed microreactor are compared, including their catalytic performances, the differences in dynamic study and kinetic model, and their pressure drop and permeability comparison.

Chapter 1 - Bibliographic study

This chapter concerns the background knowledge about heterogeneous catalyst in microreactor. At first, general introduction of microreactors and different types of microreactors with heterogeneous catalyst are presented; secondly, the model reaction chosen for catalytic tests: transfer hydrogenation of *p*-nitrophenol with formic acid is introduced, including the methods of the reduction and the mechanism of the reaction.

1.1 Microreactor with heterogeneous catalyst

1.1.1 Overview of microreactor

Over the past two decades, microfluidic technology has been advanced as means of process intensification[6]. Microreactor (MR) is currently burgeoning and is an interdisciplinary field that combines science and engineering[7]. The chemical industry[8], biotechnology[9], pharmaceutical industry[10] and energy[11] are just some of the fields where this new concept in production, analysis and research could find applications[12].

A "microreactor" is a miniaturized reaction system with dimensions in the millimeter and submillimeter range, that is operated under flow conditions. Other names that are rarely used are nano-, mili- and mini-reactors.[7(b)] Most of the currently used microstructured devices take advantage of microfluidics and nanofluidics, which ensure high efficiency as well as repeatability of chemical processes[13], due to high heat and mass transfer properties. More precisely, their thermal Peclet numbers[14] are below 1,000 under operation and their Reynolds numbers are below 250, corresponding to laminar flow conditions.[7(a)]

The history of microfluidic devices dates back to 1940s when a millimeter scale electrophoretic separator has been studied by Philpot[15]. Then, in 1979, Terry[16] realized a miniaturized gas chromatography apparatus on a silicon wafer, including fluid propulsion within microchannels of

---

[6] Pohar, A.; Plazl, I., *Chemical and Biochemical Engineering Quarterly* **2009,** *23* (4), 537-544.

[7] (a) Elvira, K. S.; Casadevall i Solvas, X.; Wootton, R. C.; deMello, A. J., *Nature Chemistry* **2013,** *5* (11), 905-15. (b) Šalić, A.; Tušek, A.; Zelić, B., *Journal of Applied Biomedicine* **2012,** *10* (3), 137-153.

[8] (a) Hessel, V.; Löb, P.; Löwe, H., *Studies in Surface Science and Catalysis*, Eds. Elsevier: 2006; pp 35-46. (b) Kralisch, D.; Kreisel, G., *Chemical Engineering Science* **2007,** *62* (4), 1094-1100. (c) Al-Rifai, N.; Cao, E.; Dua, V.; Gavriilidis, A., *Current Opinion in Chemical Engineering* **2013,** *2* (3), 338-345.

[9] (a) Tu, S. T.; Yu, X.; Luan, W.; Löwe, H., *Chemical Engineering Journal* **2010,** *163* (3), 165-179. (b) Cho, W.; Maeng, J. H.; Ahn, Y.; Hwang, S. Y., *Eletrophoresis* **2013,** *34* (17), 2531-2537. (c) Lien, K. Y.; Lin, W. Y.; Lee Y. F.; Wang, C. H.; Lei, H. Y.; Lee, G. B., *Journal of Microelectromechanical Systems* **2008,** *17* (2), 288-301.

[10] (a) Nagaki, A.; Imai, K.; Kim, H.; Yoshida, J.-i., *RSC Advances* **2011,** *1* (5), 758-760. (b) Yoshida, J.-i.; Kim, H.; Nagaki, A., *ChemSusChem* **2011,** *4* (3), 331-340.

[11] Kolb, G., *Chemical Engineering and Processing: Process Intensification* **2013,** *65*, 1-44.

[12] Yao, X.; Zhang, Y.; Du, L.; Liu, J.; Yao, J., *Renewable and Sustainable Energy Reviews* **2015,** *47*, 519-539.

[13] Urban, P. L.; Goodall, D. M.; Bruce, N. C., *Biotechnology Advances* **2006,** *24* (1), 42-57.

[14] Peclet number: a dimensionless number representing the ratio of heat transport by convection to heat transport by conduction, i.e. UpC_P/λ, U:flow velocity, ρ:density, C_P:specific heat capacity, λ:thermal conductivity

[15] Philpot, J. S. L., *Transactions of the Faraday Society* **1940,** *35*, 38-46.

[16] Terry, S. C.; Jerman, J. H.; Angell, J. B., *IEEE Transactions on Electron Devices* **1979,** *26* (12), 1880-1886.

sub-millimeter cross section. The fabrication of the first high performance liquid chromatography (HPLC) device (a 5 x 5 mm chip containing an open-tubular column of 6 µm x 2µm x 15 cm) using Si-Pyrex technology published by Manz[17] greatly boosts the development of microfluidic technology. The first micro-valves[18] and micro-pumps[19] based on silicon micro-machining have been studied and presented in the end of 1980s. Then in the 1990s, Manz[20], Mathies[21] and others have studied the microfluidic systems in the field of chip-based separations. Following these pioneer works, new microfluidic components were developed for fluid transport, fluid metering, fluid mixing, valving, or concentration and separation of molecules within miniaturized quantities of fluids[22]. Meanwhile, the research fields of continuous flow microreactors have been also well exploited in catalysis[23], nanoparticle synthesis[24], sensing[25], electrochemistry[26], polymerization[27] among a lot of applications.

Microreactors are often compared with batch reactors. The characterization of the performances of reactors includes the conversion (for simple reaction), the yield (or selectivity) and the productivity. The ideal reactor models show that the performance equations, which reflect the effect of the operating conditions, are the same in a batch reactor and in a perfect plug flow reactor, which well represent microreactor. That is to say a reaction should follow identical reaction sequences, conversion rate and yield in an “ideal” microreactor and in an “ideal” batch reactor.

The implementation in real reactors brings out differences. Compared with conventional batch reactors, microreactors exhibit numerous advantages that have been discussed extensively.[6-9]

- Advantages of a flow-reaction: (1) in a batch reactor, the reactants are initially charged, and left to react for a certain period, then the final reaction mixture is discharged. So, under continuous operation, the productivity can be improved, by eliminating the steps related to loading and discharge; (2) the continuous operation can be automated more easily.

- Advantages related to the small dimensions of microreactors: (1) the reagent consumption is low, and changes in operating conditions are fast and easy to do, so microreactors are attractive during the process development phase; (2) the amount of reaction product is reduced, which is interesting in the case of synthesis of hazardous intermediate compounds.

---

[17] A.Manz; Y.Miyahara; J.Miura; Y.Watanabe; H.Miyagi; K.Sato, *Sensors and Actuators B: Chemical* **1990,** *1* (1-6), 249-255.

[18] Shoji, S.; Esashi, M.; Matsuo, T., *Sensors and Actuators* **1988,** *14* (2), 101-107.

[19] (a) Lintel, H. T. G. V.; Vandepol, F. C. M.; Bouwstra, S., *Sensor and Actuators* **1988,** *15* (2), 153-167. (b) V.Gass; Schoot, B. H. v. d.; S.Jeanneret; Rooij, N. F. d., *Sensors and Actuators A: Physical* **1994,** *43* (1-3), 335-338.

[20] Manz, A.; Graber, N.; Widmer, H. M., *Sensors and Actuators B: Chemical* **1990,** *1* (1), 244-248.

[21] Woolley, A. T.; Mathies, R. A., *Proceedings of the National Academy of Sciences* **1994,** *91* (24), 11348-11352.

[22] Haeberle, S.; Zengerle, R., *Lab on a Chip* **2007,** *7* (9), 1094-110.

[23] (a) Kobayashi, J.; Mori, Y.; Okamoto, K.; Akiyama, R.; Ueno, M.; Kitamori, T.; Kobayashi, S., *Science* **2004,** *304* (5675), 1305-1308. (b) Kobayashi, S., *Chemistry – An Asian Journal* **2016,** *11* (4), 425-436. (c) Rebrov, E. V.; Berenguer-Murcia, A.; Skelton, H. E.; Johnson, B. F. G.; Wheatley, A. E. H.; Schouten, J. C., *Lab on a Chip* **2009,** *9* (4), 503-506.

[24] Maki, T.; Kitada, J. I.; Mae, K., *Chemical Engineering & Technology* **2013,** *36* (6), 1027-1032.

[25] Wirnsberger, G.; Scott, B. J.; Stucky, G. D., *Chemical Communications* **2001,** *0* (1), 119-120.

[26] Watts, K.; Baker, A.; Wirth, T., *Journal of Flow Chemistry* **2014,** *4* (1), 2-11.

[27] Seo, M.; Nie, Z.; Xu, S.; Mok, M.; Lewis, P. C.; Graham, R.; Kumacheva, E., *Langmuir* **2005,** *21* (25), 11614-11622.

- Advantages related to the geometry of microreactors, that offers great control of the reaction conditions such as concentrations and temperatures: (1) the control of temperature is obtained with the high surface area-to-volume ratio of microreactor, in the range of 10000 to 50000 m^{-1} in microreactor while it is usually less than 100 m^{-1} in traditional reactors[28]. This allows to use the full potential of temperature during highly exothermic reactions and avoids hot-spots formation[29]. According to their efficient heat transfer and small volume, the reactions involving reactive, toxic or explosive intermediates can be carried out in safety in microreactors[6]; (2) the control of concentrations in microreactors is achieved by an efficient micro-mixing and a short radial diffusion time, leading to a narrow residence time distribution (RTD) which give them a behavior close to the ideal plug flow model[28]. This behavior allows usage of minimal amounts of reagent to precisely control the reaction and provide high selectivity towards the desired product.[7(b)] The quality of mixing is especially important in the case of fast biphasic reactions or fast competitive reactions.

1.1.2 Application of microreactors and industrial examples

Although most of microreactors applications have been studied in academia, industry has also taken an inquisitive interest in this new technology. As proposed by Roberge, 50% of the reaction in pharmaceutical and fine chemical industry would benefit from a continuous process, and microreactor technology could be preferred reaction device in 44% of these reactions[1]. The question remaining is whether these microreactor devices are able to meet the expectations for industrial use raised in the academic environment. In the last fifteen years, a lot of companies, especially some microreactor builders such as BASF, Lonza, Corning, IMM, have studied microstructured devices as tools for process intensification, and they conclude that, not all chemical reactions can profit from microreactors. Hence, in the following part, the different types of reactions that take advantage in microreactors and some examples of industrial interest are presented.

1.1.2.1 Contribution of microreactors to different types of reactions

Among the great number of reactions carried out in microreactors in the lab or in the chemical industry[30], three main types of reactions emerge clearly.

1.1.2.1.1 Fast and exothermic reactions

The batch reactors have many obvious advantages because they are easy to be handled, and also it is easy to visualize how a reaction proceeds, when a reagent or a catalyst is added into a flask or when heat is added to initiate a reaction. However, chemists usually slow-down organic

---

[28] Kiwi-Minsker, L.; Renken, A., *Catalysis Today* **2005,** *110* (1-2), 2-14.
[29] Kolb, G.; Hessel, V., *Chemical Engineering Journal* **2004,** *98* (1), 1-38.
[30] (a) Kristal, J.; Stavarek, P.; Vajglova, Z.; Vondrackova, M.; Pavlorkova, J.; Jiricny, V., *Research on Chemical Intermediates* **2015,** *41* (12), 9357-9371. (b) McQuade, D. T.; Seeberger, P. H., *Journal of Organic Chemistry* **2013,** *78* (13), 6384-6389. (c) Wiles, C.; Watts, P., *Green Chemistry* **2014,** *16* (1), 55-62.

synthesis because it is very difficult or practically impossible to conduct some extremely fast or/and exothermic reactions in a flask due to the lack of control of the side reactions. The three following examples show how microreactors technology could contribute to the development of fast organic synthesis.

a- More than ten years ago a concept called "flash chemistry" was presented by Yoshida[31]. It is defined as a field of chemical synthesis where extremely fast reactions are conducted in a highly controlled manner to produce desired compounds with high selectivity. Among a number of studies conducted by Yoshida group on the potential of microreactors, an impressive example concerning the control of the fast organolithiums isomerization is presented here[32]. A chip microreactor (CMR), characterized by a submillisecond range reaction time even at cryogenic temperature has been designed. It allowed the formation of the desired product **2** from **1** with a 86% yield, without isomeric byproducts **3** (as shown in Figure 1) at a total flow rate of 4.5 mL/min corresponding to a residence time of 0.33 ms. The competitive very rapid anionic Fries rearrangement has been avoided, and a high chemoselectivity was observed. For a comparison, the reaction conducted in a conventional flask generated only the isomer **3**. The rapid continuous flow nature of the CMR delivered a throughput of 5.3 g/hour, which show a great potential for scalable industrial chemical synthesis.

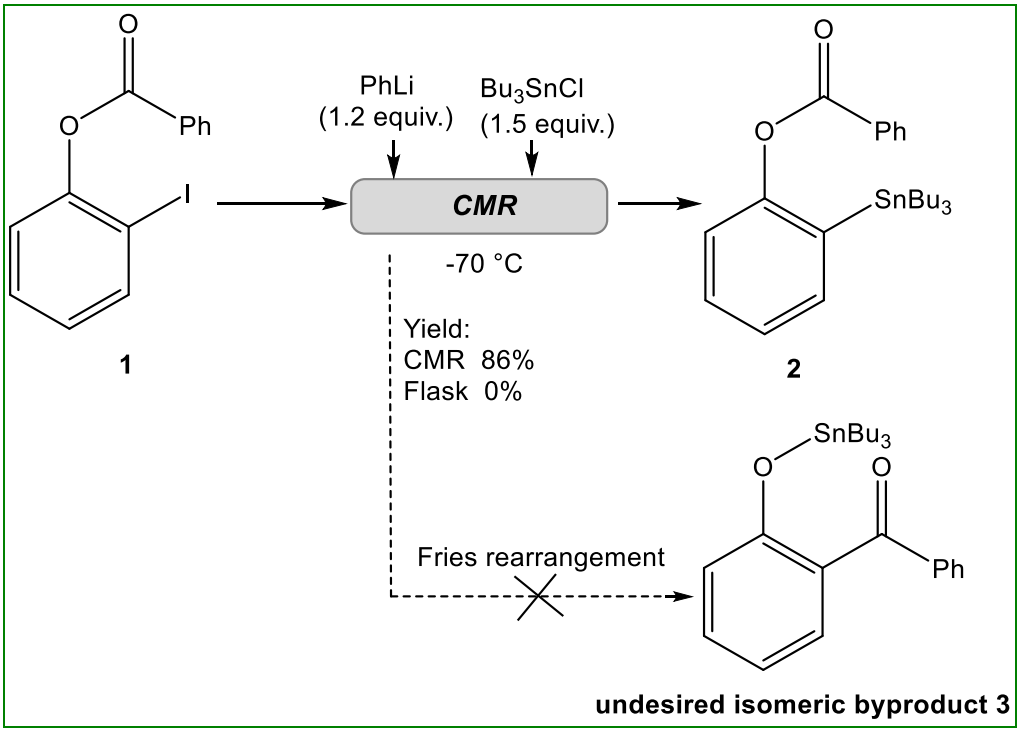

Figure 1 Reaction of unrearranged intermediates **1** to desired product **2** in CMR

[31] (a) Yoshida, J. I.; Takahashi, Y.; Nagaki, A., *Chemical Communications* **2013,** *49* (85), 9896-904. (b) Yoshida, J. I., *Chemical Communications* **2005,** *0* (36), 4509-4516.

[32] Kim, H.; Min, K. I.; Inoue, K.; Im, D. J.; Kim, D. P.; Yoshida, J. I., *Science* **2016,** *352* (6286), 691-694.

b- Wolf investigated the quite exothermic selective oxidation of primary alcohols to the aldehyde with oxygen using silver as the catalyst (Figure 2(A))[33]. The microreactor developed for this reaction is a cube of 1 cm edge length and having 200 crossed channels for the reactants and for the coolant (Figure 2(B)). Because of the efficient heat transfer, the reaction temperature could be controlled accurately, avoiding hot spots. Compared to traditional reactor consisting of thick catalyst layer placed on a gas-permeable plate, the reactor volume has been greatly reduced so that the residence time is largely decreased, and the selectivity could be increased from 40% and 85% to 96%, moreover, the hot spot has been reduced from 160℃ to 0℃.

A

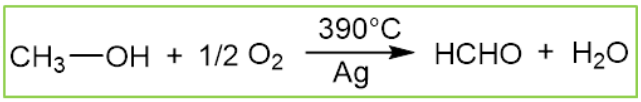

B

Different process	Existing process	In the work of Wolf	
Illustration	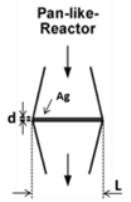	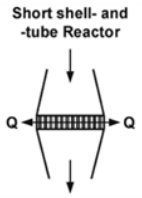	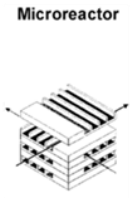
Dimensions	d = 2 cm L = 3 m	d = 10 cm L = 3 m	Cube edge length = 1 cm
Selectivity	40%	85%	96%
Conversion	50%	50%	55%
Hot spot	160℃	60℃	0

Figure 2 Comparison of different reactors in the work of Wolf with the oxidative dehydrogenation

c- The two-step synthesis of *m*-anisaldehyde **5** from *m*-bromoanisole **4** as shown in Figure 3 is highly exothermic. Kralisch and Kreisel have studied this reaction in microreactor at both laboratory scale and industrial scale[8(b)]. At the laboratory scale, the synthesis was conducted at 273K in a Cytos® microreactor with an internal volume of 1.1 mL with 88% yield, 28% higher than the yield obtained in a batch reactor. For the industrial scale, the numbering-up method has been chosen. The Cytos® Pilot System used was composed of 11 microreactors in parallel. The product mass flow of 0.06 kg/h per microreactor was the same on both scales. With same yield of 88%, the microreactor is at 273K while the reaction temperature of batch process should be held under 193K. Various indicators of life cycle assessment (LCA) showed that the application of microreactor could gain significant ecological advantages in comparison to the batch reactor, and the total CED (Cumulative Energy Demand) of microreactor is 500 GJ/FU (functional unit, 1 t m-anisaldehyde) lower than that of batch reactor.

[33] Wörz, O.; Jäckel, K. P.; Richter, T.; Wolf, A., *Chemical Engineering & Technology* **2001,** *24* (2), 138-142.

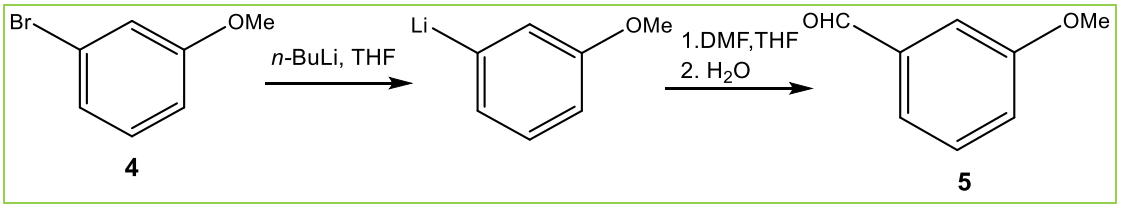

Figure 3 Two-step synthesis of m-anisaldehyde 5 from m-bromoanisole 4

1.1.2.1.2 Hazardous reactions

The highly toxic or explosive nature of reactants or byproducts in some reactions can make it difficult to handle and control in a conventional lab or industrial scale. Indeed, the process involving hydrazine, diazo compounds, azides or cyanides can be problematic in the industrial production. However, the safe usage of these "dangerous materials" is recommended, especially if their applications offer better atom economy and process intensification. The reduction of risk and improvement of reactions have been demonstrated with the use of flow microreactor[34].

a- Hydrazine (N_2H_4) is a well-known powerful bi-functional nucleophile and a readily available reducing agent. However, its utilization on a large scale has been limited because of the high toxicity and the high corrosiveness. The explosive and gaseous hydrazine in the batch reactor also makes the safety issues quite important[35]. For example, hydrazine is used in Wolff-Kishner reaction to reduce ketones and aldehydes to the corresponding alkane. The hydrazone intermediate could lead to formation of heterocycles such as insoles and azine by-products that should be discarded. In batch process, the reaction proceeds in the high temperature boiling solvent, in order to remove the hydrazone from the reactor. The method requires several hours of operation and a large excess of hydrazine. The microreactor could overcome these limitations, because its small volume and the improved mass and heat transfer reduce the risk of thermal runaway and explosions. Jensen[35(a)] has investigated the Wolff-Kishner reductions in a novel silicon carbide microreactor that prevents the hydrazine from boiling out of the reactor. Compared with typical batch conditions, the reaction time has been reduced by two orders of magnitude, and a high yield was obtained without requiring a large amount of hydrazine (Figure 4).

[34] (a) Movsisyan, M.; Delbeke, E. I.; Berton, J. K.; Battilocchio, C.; Ley, S. V.; Stevens, C. V., *Chemical Society Reviews* **2016,** *45* (18), 4892-928. (b) Fanelli, F.; Parisi, G.; Degennaro, L.; Luisi, R., *Beilstein Journal of Organic Chemistry* **2017,** *13*, 520-542. (c) Gutmann, B.; Cantillo, D.; Kappe, C. O., *Angewandte Chemie International Edition* **2015,** *54* (23), 6688-6728.

[35] (a) Newman, S. G.; Gu, L.; Lesniak, C.; Victor, G.; Meschke, F.; Abahmane, L.; Jensen, K. F., *Green Chemistry* **2014,** *16* (1), 176-180. (b) Wojewódka, A.; Bełzowski, J.; Wilk, Z.; Staś, J., *Journal of Hazardous Materials* **2009,** *171* (1), 1175-1177.

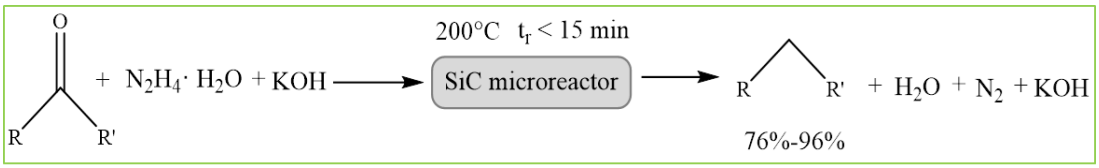

	Batch reactor	Microreactor
Reaction temperature (°C)	210	200
Reaction time (min.)	~500	2 – 15
Hydrazine quantity	2 - 8 equiv.	1.5 equiv.

Figure 4 Comparison of batch and microreactor with the Wolff-Kishner reaction

b- Diazomethane (CH_2N_2) is one of the most versatile and powerful reagents available for the preparation of carbon–carbon and carbon–heteroatom bonds in chemistry[36]. Nevertheless, diazomethane is an extremely volatile, poisonous, carcinogenic and explosive gas. Furthermore, it is extraordinary reactive and high sensitive to light, heat and mechanical shock[34]. The batch preparation of the diazomethane is always performed in specialized glass equipment without ground glass joints to avoid the light and shock. Purification and transportation of the diazomethane generated are also quite complicated[37]. Kim[36] has investigated a dual-channel microreactor containing a highly hydrophobic poly (dimethylsiloxane) (PDMS) membrane that separated a channel for diazomethane generation and channel for synthesis. In the bottom channel, diazald® and KOH generate diazomethane, the PDMS membrane allow the transfer of diazomethane to the top channel while leaving water and other ionic salts behind. In the top channel, the gaseous diazomethane could react with various substrates with excellent yield (> 81%). Although the productivity in lab is only 0.58-2.88 mmol/day, this continuous in-situ generation, separation and reaction of high toxic reagents could be potentially useful for large-scale production.

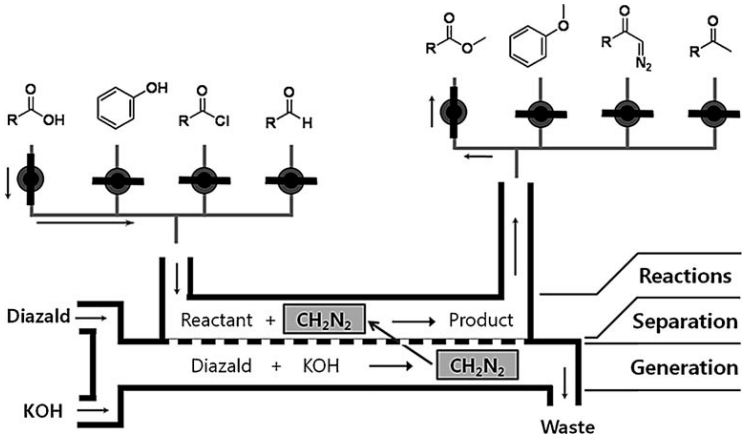

Figure 5 Illustration of the microreactor (60 μL in volume with the 45 μm thick membrane) for in-situ generation, separation, and reactions of diazomethane[36]

[36] Maurya, R. A.; Park, C. P.; Lee, J. H.; Kim, D. P., *Angewandte Chemie International Edition* **2011,** *50* (26), 5952-5955.
[37] Deadman, B. J.; Collins, S. G.; Maguire, A. R., *Chemistry – A European Journal* **2015,** *21* (6), 2298-2308.

1.1.2.1.3 Reactions with unstable intermediates or consecutive products

The reduction and elimination of short-lived intermediate and the consecutive product are always an important issue to deal with not only in laboratory but also in industrial production, in order to improve the productivity and purity of target product and to cut down the manufacturing cost. The continuous flow microreactor systems is an effective solution to this problem, which can greatly reduce the residence time to the order of milliseconds, keeping the flexibility of the addition order of reaction components. Moreover, the connection of different steps in microreactor could be much tighter in some reactions to reduce the undesired side or consecutive products, thereby to increase the purity of final product.

a- During the conversion from aryl and alkyl Grignard reagents to aryl and alkyl boron compounds, a number of elemental reactions give rise to side products which reduce the yield of the target product and generate purification problems. Hessel[38] have investigated the replacement of a batch process by a continuous-flow process composed of a micromixer and a tubular reactor for the phenyl boronic acid **6** production. It results in notable process intensification: the best yield of microreactor investigations was 89%, about 24% more than the industrial batch-wise process. In addition, the energy expenditure was also reduced, due to operation at ambient temperature while the batch process was carried out at cryogenic temperatures. A pilot-scale configuration was achieved with a throughput of about 6kg of phenyl boronic acid per day, equivalent to a production of 20 tons of product per year. Last but not least, as intermediates may precipitate in the course of reaction, the results show that microreactors may adapt to fouling-sensitive reactions.

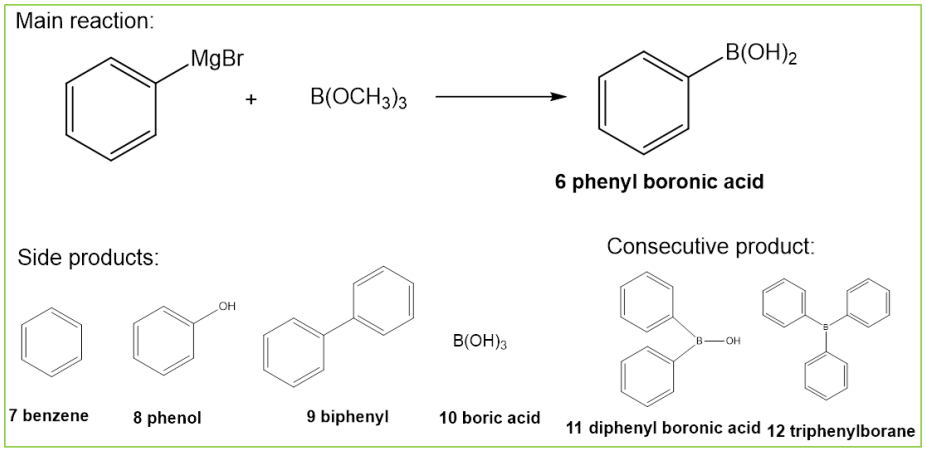

	Laboratory-scale batch reactor	Microreactor
Residence time	22 min	5 - 180 s
Yield of target product 6	70.6%	89%
Total amount of 7-12	10-15%	5-10%

Figure 6 Main reaction of the Phenyl Boronic Acid Process and side/consecutive products (target poduct **6**, side/consecutive products **7-12**) and comparison of microreactor and batch reactor in the Phenyl Boronic Acid **6** Process

[38] Hessel, V.; Hofmann, C.; Löwe, H.; Meudt, A.; Scherer, S.; Schönfeld, F.; Werner, B., *Organic Process Research & Development* **2004,** *8* (3), 511-523.

b- ε-caprolactam(CPL) **16** is a commercially important chemical product, mainly used in the production of nylon 6 fibers and resins. Nevertheless, among the traditional methods of CPL synthesis, the CPL selectivity is usually lower than 90% in industrial process using consecutive continuous stirred tank reactors, on account of the several side products and the inefficient pre-mixing process. Wang[39] has developed a system containing two consecutive microreactors and a stirred vessel to improve the selectivity of the synthesis of CPL. The first microreactor was used to conduct the reaction of cyclohexanecarboxylic acid **13** and oleum **14**, and then the intermediate product named mixed anhydride was obtained with 97% selectivity. The mixed anhydride then reacted quickly with nitroso-sulfuric acid **15** in the second microreactor, and then the reaction was finished in the vessel. The selectivity of CPL can reach 93.9%, much higher than that achieved in a batch reactor they investigated (84.6%).

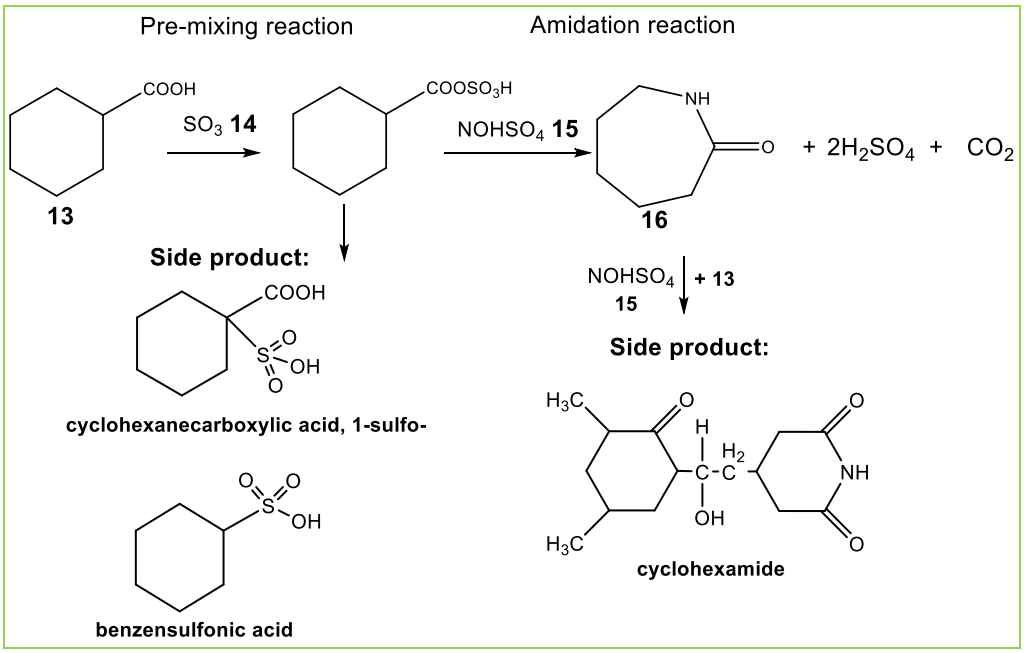

Figure 7 Caprolactam **16** synthesis from cyclohexanecarboxylic acid **13**

1.1.2.2 Examples of industrial production with microreactor

1.1.2.2.1 Scale-up methods

After the demonstration of the performance of microreactor in laboratory, the challenge is how to get benefits of microreactor in chemical industry while increasing the throughput for production. Two approaches to increase the production rate of microreactor are possible Figure 8 : scale-up by increasing the setup size and flow rates or numbering-up by parallelization of units.

[39] Wang, K.; Zhang, J.; Zheng, C.; Dong, C.; Lu, Y.; Luo, G., *AIChE Journal* **2015,** *61* (6), 1959-1967.

Scale-up method can be more easily realized, while taking the risk of losing mass and heat transfer performance. Numbering-up could require hundreds of units to achieve the large-scale production and more complex and expensive control systems, but the desired features of a basic unit could be guaranteed[40].

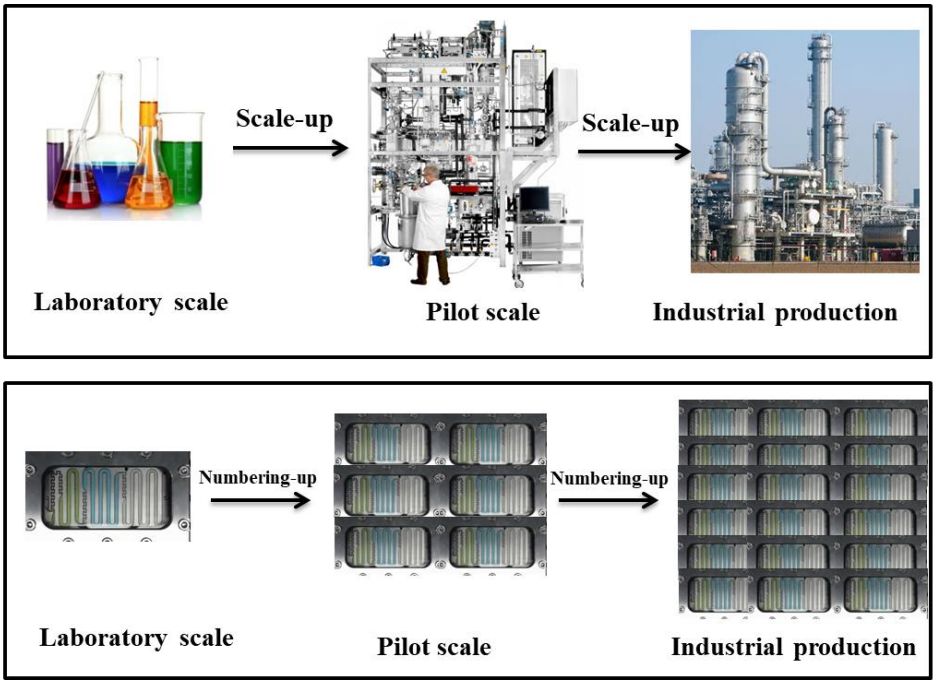

Figure 8 Simplified scheme illustrating scale-up versus numbering-up strategies

Within the context of microreactor scale-up, Corning combines the 2 approaches and offers several reactor volumes, following the same heart design. As shown in Figure 9, the Low-Flow reactor (LFR) has an internal volume of 0.45 mL, and has a throughput of 5t/year. The larger versions of reactor G1, G2, G3 and G4, have larger internal volumes and larger throughputs up to 2000t/year. In addition, Corning proposes the set-up with several parallel plates (Figure 10) to enlarge the productivity.

[40] (a) Kockmann, N.; Gottsponer, M.; Zimmermann, B.; Roberge Dominique , M., *Chemistry-A European Journal* **2008,** *14* (25), 7470-7477. (b) Ehrfeld, W.; Hessel, V.; Löwe, H., *Microreactors: New Technology for Modern Chemistry*, Wiley-VCH Verlag GmbH: 2004; pp 1-14.

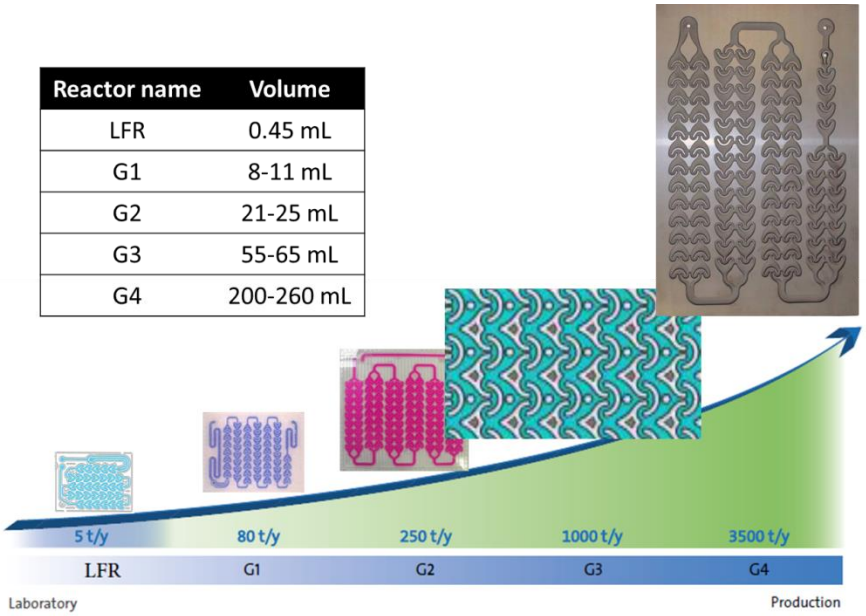

Figure 9 The internal volume and throughput of Corning Advanced-Flow Reactors

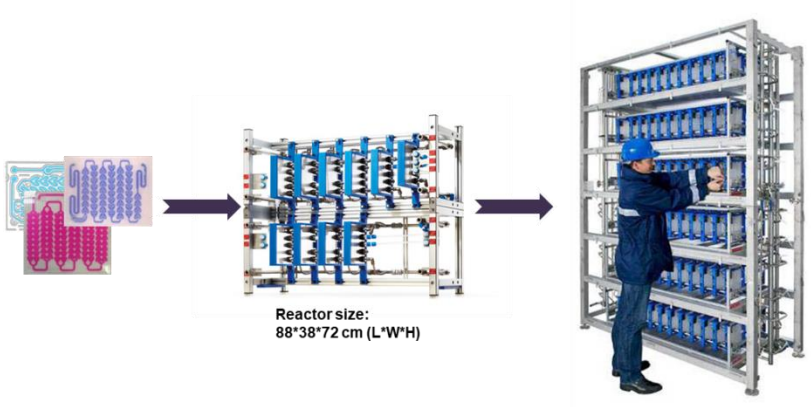

Figure 10 Numbering-up set-up of Corning with several parallel plates

Lonza has also developed single-channel microreactors with different characteristics in terms of temperature control and production capacity, in view of scale-up from lab development to pilot-scale avoiding parallelization. The concept was exemplified with the fast and highly exothermic lithiation reaction (Li–H exchange and coupling, shown in Figure 11 (A))[41]. The first reaction has an adiabatic temperature rise of more than 75°C, and feeds were precooled to the cryogenic reactor temperature. Two types of Lonza microreactors, a Lab-Plate and modular plate A6 or A5, shown in Figure 11 (B), were compared with a classic static mixer. The results are summarized in Figure 11 (C).

[41] Kockmann, N.; Gottsponer, M.; Roberge, D. M., *Chemical Engineering Journal* **2011,** *167* (2-3), 718-726.

A

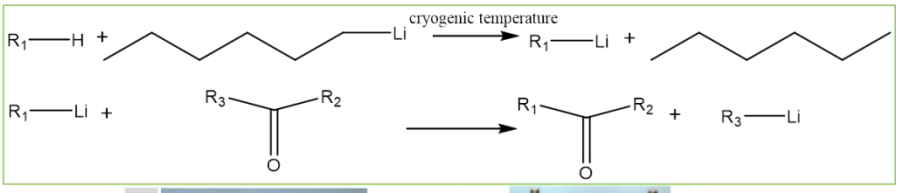

B

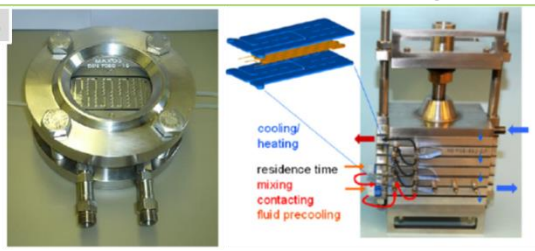

C

Reactor	Internal diameter	Flow rate (g/min)	Outlet temperature (°C)	Pressure loss (bar)	Isolated yield (%)
Static mixer	3/8''	148	41	1.6	84
Lab-Plate MR	0.5 mm	148	15	3.2	88
Lonza MR-A6	0.5 mm	140	-16	8.8	90
Lonza MR-A5	1.0 mm	237	-16	4.5	88

Figure 11 Research of lithiation reaction with Lonza microreactor. (A) Reaction scheme of Li–H exchange and coupling; (B) Different Lonza microreactors (left: Lab-Plate 0.4-3 mL, Right: plate A6 (3-12 mL) or A5 (7-33 mL)); (C) Comparison of different reactors and flow rates for scale-up of the lithiation reaction

The results with the Lab-plate show a loss of temperature control, but not yet reflected in the product yield, while the largest reactor (Lonza MR-A5), could achieve a throughput over 200 g/min by keeping the pressure drop well under control. 700 kg of isolated material were produced in a pilot campaign, showing the long-term robustness of the process and reliability of the installed reactor equipment.[41]

1.1.2.2.2 Applications of microreactors in industrial productions

Industry is not very active in publishing not only because of confidentiality reasons. This may also be caused by the fact that many aspects of this new technology were covered by patents[42]. Scarce publications are probably the tip of the iceberg, and as several of the earlier patents have now expired, known examples of applications of microreactors in industrial productions will increase.

Initiated in 2005 in Germany, the DEMiS projet (Degussa, Uhde, TU Chemnitz, TU Darmstadt, MPI Mulheim) is the first and most often mentioned example for microreactor industrial process up to now [43]. A microstructured reactor has been used for the epoxidation of propylene to propylene oxide with H_2O_2 on a TS-1 zeolite. The production capacity of this process approximates 5-10 t/year.

---

[42] (a) Hessel, V.; Knobloch, C.; Löwe, H., *Recent Patents on Chemical Engineering* **2008,** *1*(1), 1-16. (b) Dencic, I.; Hessel, V.; de Croon, M. H.; Meuldijk, J.; van der Doelen, C. W.; Koch, K., *ChemSusChem* **2012,** *5* (2), 232-45.

[43] Reschetilowski, W., *Microreactors in Preparative Chemistry*, Wiley-VCH Verlag GmbH & Co. KGaA: 2013; pp 1-12.

A nitroglycerin pilot plant with the productivity 10kg/h has been installed at Xi'an site in China and has started up in 2005 with the collaboration from Germany's Institute for microtechnology Mainz (IMM)[44]. Microreactor technology is the key to this production process and the plant is foreseen to operate safely and fully automated [8].

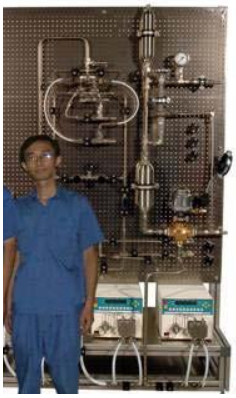

Figure 12 Nitroglycerin microstructured reactor based pilot plant (Xi'an/ China)

An industrial scale plant for the free radical polymerisation of methylmethacrylate (MMA) was designed by Iwasaki and Yoshida. This pilot plant was installed in Japan, at the Idemitsu Company and its capacity of production is 10t/year [8]. Eight micro-reactor blocks are arranged in a parallel manner. Each of these blocks contains three micro-tube reactors of 11.8 mL (500 μm internal diameter, 60 cm length) in series.

Figure 13 Industrial pilot plant (10 t/year) with three micro-reactor blocks for radical polymerisation in Japan [8]

It should be noticed that the performance of this pilot plant was similar to that of a single micro-reactor tube, which demonstrates that external numbering-up of microreactors is able to be successfully applied to industrial production.

[44] Thayer, A. M., *Chemical & Engineering News* **2005,** *83* (22), 43-52.

Another impressive industrial production with microreactor is the process development for pharmaceutical production under cGMP (current Good Manufacturing Practices) conditions, developed by DSM, a manufacturer of fine chemicals and active pharmaceutical ingredients, and Corning Inc.[45]. The goal of this project was to develop a safe and highly selective nitration process using pure nitric acid, and get the desired amount and quality of product at full GMP level. A commercially viable approach to a cGMP nitration reaction was investigated with individual reactor modules, then the numbering-up concept was applied. After nine months, the production process had a capacity of approximately 100 kg/h which corresponds to nearly 800 tons per year.

Figure 14 Production bank with four identical reactors and distribution [45]

1.1.3 Research status of microreactor with heterogeneous catalyst

The role of catalysis in industry is irreplaceable. Over 90% of all industrial chemicals are produced in a catalytic process [2]. Both homogeneous and heterogeneous catalysis find wide application in chemicals production. Compared with homogeneous catalysis, heterogeneous catalysts, especially the solid catalysts, gain more attention in the industrial production because they are easily separated in the process, and they can be implemented in fixed-bed reactor to improve the production efficiency[3]. In addition, they are cheap, easy to get, and have good thermal stability.

However, heterogeneous catalysts are difficult to implement in microreactor. So, this combination has drawn attention only recently. The potential advantages of the microreactor with heterogeneous catalysts have been discussed in some recent reviews [3-5,46]: ultra-low catalyst consumption, more efficient use of resources and generation of less waste, high specific surface areas of catalysis and so on. In the following part, we present different types of microreactors with heterogeneous catalyst and their applications.

---

[45] Braune, S.; Pöchlauer, P.; Reintjens, R.; Steinhofer, S.; Winter, M.; Lobet, O.; Guidat, R.; Woehl, P.; Guermeur, C., *Chemistry Today* **2009,** *27* (1), 26-29.

[46] (a) Yue, J., *Catalysis Today* **2017**. (b) Munirathinam, R.; Huskens, J.; Verboom, W., *Advanced Synthesis & Catalysis* **2015,** *357* (6), 1093-1123.

1.1.3.1 Different types and comparison of microreactors with heterogeneous catalysts

1.1.3.1.1 Methods of immobilization of heterogeneous catalyst in microreactors

Heterogeneous catalytic microreactors can be classified into three main types as shown in Figure 15: (i) packed-bed microreactor, (ii) wall-coated microreactor and (iii) monolithic microreactor.

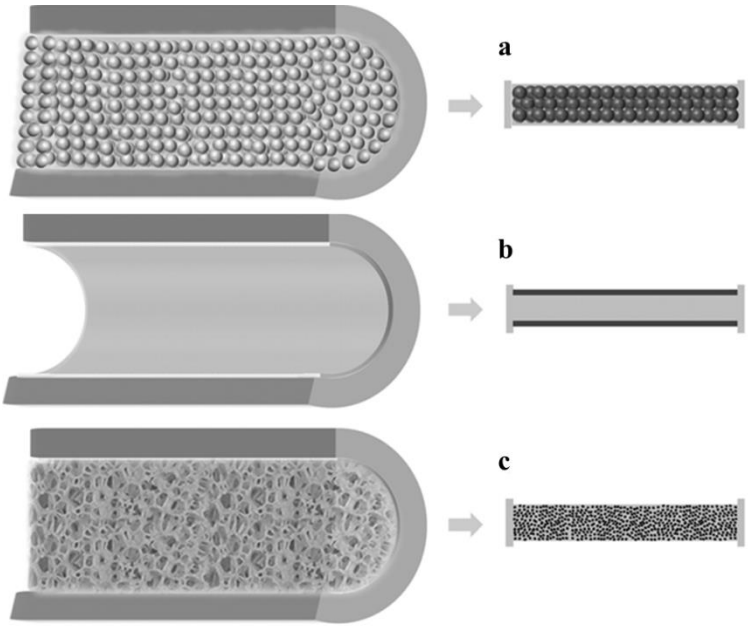

Figure 15 Schematic representation of the cross-section of a microchannel in (a) packed-bed, (b) wall-coated, and (c) monolithic microreactors [46(b)]

Packed-bed microreactor is among the most studied, commonly composed by a micro-channel randomly filled with powders or small pellets catalyst. The support of the catalyst is an insoluble solid, either a polymeric or inorganic particle. The particles are generally smaller than 50μm, less than 1/20 of the bed diameter to avoid the channeling or misdistribution of flow [4]. Catalyst can be loaded into the microchannel either by manual filling, or by applying a pump or vacuum at the reactor outlet. Besides, the packed catalyst should be retained inside the microchannel by sinters at both ends. The possibility to use either commercial or synthesized bulk catalysts greatly expands the application areas [46(a)].

Wall-coated microreactor has inner wall with a uniform and thin layer thickness (usually in the 1–10 μm range) of catalytic coating. Several reviews [5,46-47] have discussed the methods of the immobilization of catalytic wall coatings into capillary- or chip-based microreactors, such as the sol-gel deposition [48], electrophoretic deposition [49] and electroless plating, chemical vapor

[47] Meille, V., *Applied Catalysis A: General* **2006,** *315*, 1-17.
[48] Peneau, V.; Shaw, G.; Freakley, S. J.; Forde, M. M.; Dimitratos, N.; Jenkins, R. L.; Taylor, S. H.; Hutchings, G. J., *Catalysis Science & Technology* **2015,** *5* (8), 3953-3959.
[49] Wunsch, R.; Fichtner, M.; Görke, O.; Haas‐Santo, K.; Schubert, K., *Chemical Engineering & Technology* **2002,** *25* (7), 700-703.

deposition technique[50]. The general steps of the immobilization often involves [46]: i) pre-treatment of the microreactor wall surface; ii) application of a porous coating of the catalyst support; iii) immobilization of the catalyst itself (usually noble metal like Pt, Pd or Au) onto the catalyst support.

Monolithic microreactor is a microreactor in the form of column with monolith inside. Monolith is the solid material polymeric[51] or inorganic[52], structured with interconnected pores that are both macropores (larger than 50nm in diameter) and mesopores (2-50nm) or micropores (less than 2nm)[53]. Different from the mature packed-bed technology, monolithic microreactor is a rather new field, which is currently in very rapid expansion, due to the huge interest and spread in organic flow synthesis[5].

1.1.3.1.2 Characteristic and comparison of different microreactors with heterogeneous catalysts

The relative advantages and disadvantages of heterogeneous catalytic microreactors have been discussed in several publications [4,46,54].

Generally speaking, packed-bed microreactors can be made easily because the catalysts can be directly introduced into the microreactors after suitable size reduction. This approach gives access to a large range of catalytic supports. Advantages of such packed-bed are high catalyst loading and fairly easy characterization and quantification of the catalyst. However, limitations can be the poorly controlled fluid dynamics and the significant pressure drops along the microchannel. In addition, the presence of solid catalyst may limit heat transfer and lead to hot-spot formation.

Unlike packed-bed microreactors, the mass transfer resistance is minimized in wall-coated microreactors to ensure smooth flow of reagents, without leading significant pressure drops or blockage of microchannels. Moreover, the fluid dynamics, the heat and mass transfer properties inside the wall-coated microreactors can be well predicted due to the well-defined flow geometries. Despite of the good flow-through properties, the major disadvantage is the low catalyst loading, owing to the thin layer of catalyst supported on the inner walls.

Monolithic catalysts are designed to have quite high void volume and a large specific surface area, leading to efficient contact of the catalyst, allowing high productivity and selectivity. The drawbacks of monolithic microreactors could be the compromise between the pressure drop and the flow rate, the preparation of the catalyst inside the microreactor channels, leading to difficulty of modelization and the risk of pore clogging or non-uniformity of radial permeability [5].

---

[50] Janicke, M. T.; Kestenbaum, H.; Hagendorf, U.; Schüth, F.; Fichtner, M.; Schubert, K., *Journal of Catalysis* **2000,** *191* (2), 282-293.
[51] Viklund, C.; Svec, F.; Fréchet, J. M. J.; Irgum, K., *Chemistry of Materials* **1996,** *8* (3), 744-750.
[52] Walsh, Z.; Paull, B.; Macka, M., *Analytica Chimica Acta* **2012,** *750*, 28-47.
[53] According to IUPAC definition
[54] (a) Sachse, A.; Galarneau, A.; Coq, B.; Fajula, F., *New Journal of Chemistry* **2011,** *35* (2), 259-264. (b) Kirschning, A.; Solodenko, W.; Mennecke, K., *Chemistry-A European Journal* **2006,** *12* (23), 5972-5990.

1.1.3.2 Applications of microreactors with heterogeneous catalyst

In the recent review by Alhooshani [4], applications of heterogeneous catalytic microreactors have been discussed. We present some examples of applications of microreactors with heterogeneous catalyst with impressive performance in pharmacy.

The pharmaceutical industry is going through a change from batch systems to continuous-flow systems. During each stage of the development of a drug, the quantities of active compound required increase: for the initial tests during discovery, only 5-10 mg is required; for the toxicology and pharmacokinetics studies, 500 mg-2 g are required; finally, kilogram-amounts are required for larger trials. The microreactors with heterogeneous catalyst are easily compatible with the aim of small amounts production. In addition, with the scale-up or numbering-up method, they have great potential in the pharmaceutical production.

Recently, applications of continuous flow processes in pharmaceutical industry such as the preparation of fine chemicals, active pharmaceutical ingredients (API) and finished dosage forms have been gained much attention, especially in academia [55].

a- Recently, the Novartis/MIT partnership demonstrates an excellent example of industry/academic collaboration in a fully automated integrated continuous flow synthesis apparatus[55(e)(f),56]. The instrument is not bigger than a kitchen refrigerator (as shown in Figure 16) and can be easily adapted to produce a variety of target molecules meeting U.S. pharmacopeia standards, for example the Aliskiren (drug for hypertension) with a productivity of 41g/h.

[55] (a) Baumann, M.; Baxendale, I. R., *Beilstein Journal of Organic Chemistry* **2015,** *11*, 1194-219. (b) Porta, R.; Benaglia, M.; Puglisi, A., *Organic Process Research & Development* **2015,** *20* (1), 2-25. (c) Battilocchio, C.; Deadman, B. J.; Nikbin, N.; Kitching, M. O.; Baxendale, I. R.; Ley, S. V., *Chemistry* **2013,** *19* (24), 7917-7930. (d) Malet-Sanz, L.; Susanne, F., *Journal of Medicinal Chemistry* **2012,** *55* (9), 4062-4098. (e) Mascia, S.; Heider, P. L.; Zhang, H.; Lakerveld, R.; Benyahia, B.; Barton, P. I.; Braatz, R. D.; Cooney, C. L.; Evans, J. M.; Jamison, T. F.; Jensen, K. F.; Myerson, A. S.; Trout, B. L., *Angewandte Chemie International Edition* **2013,** *52* (47), 12359-12363. (f) Adamo, A.; Beingessner, R. L.; Behnam, M.; Chen, J.; Jamison, T. F.; Jensen, K. F.; Monbaliu, J.-C. M.; Myerson, A. S.; Revalor, E. M.; Snead, D. R.; Stelzer, T.; Weeranoppanant, N.; Wong, S. Y.; Zhang, P., *Science* **2016,** *352* (6281), 61-67. (g) Tsubogo, T.; Oyamada, H.; Kobayashi, S., *Nature* **2015,** *520* (7547), 329-332. (h) Poechlauer, P.; Manley, J.; Broxterman, R.; Gregertsen, B.; Ridemark, M., *Organic Process Research & Development* **2012,** *16* (10), 1586-1590. (i) Cole, K. P.; Johnson, M. D., *Expert Review Clinical Pharmacology* **2018,** *11* (1), 5-13. (j) Hawkins, J. M., *Nature* **2015,** *520*, 302-303.

[56] Heider, P. L.; Born, S. C.; Basak, S.; Benyahia, B.; Lakerveld, R.; Zhang, H.; Hogan, R.; Buchbinder, L.; Wolfe, A.; Mascia, S.; Evans, J. M. B.; Jamison, T. F.; Jensen, K. F., *Organic Process Research & Development* **2014,** *18* (3), 402-409.

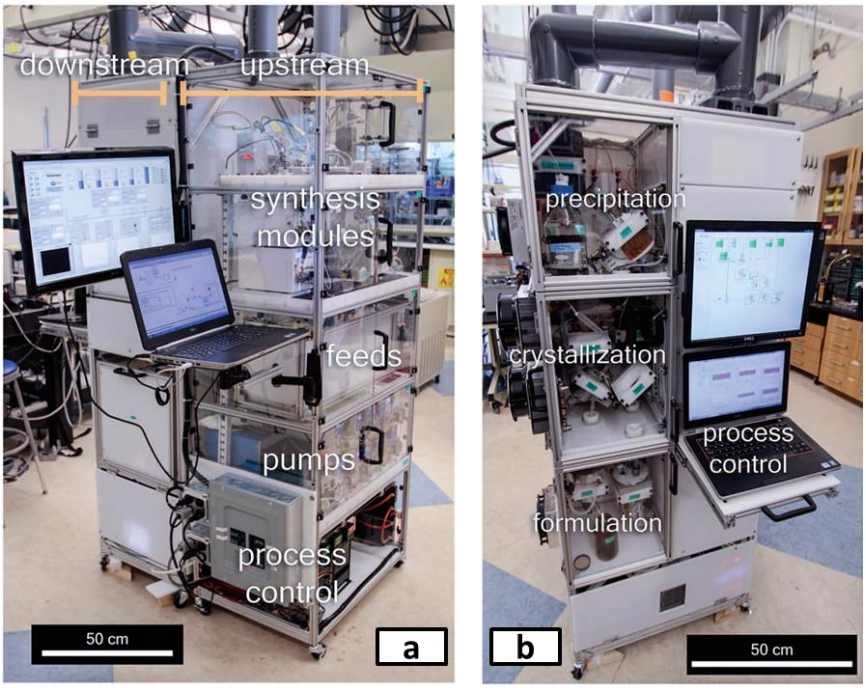

Figure 16 Reconfigurable system for continuous production and formulation of APIs developed by a Novartis/MIT group [55(f)] (a: Labeled photograph of the stack of upstream synthesis modules; b: Labeled photograph of the downstream purification and formulation modules.)

The continuous-flow system contains four types of microreactors, types I and II without catalyst, types III and IV with catalyst, as illustrated in Figure 17. In type I, all the reagents are passed through the reactor, and the exiting mixture contains target products with the unreacted reagents or by-products and a further separation step is necessary. In type II, one of the reagents, saying B, is supported and confined into the reactor. If an excess amount of supported B is used, the exiting reaction mixture will contain the target product only. However, the reactor must be changed frequently due to the consumption of B. In type III, a homogeneous catalyst is employed; similar to type I, the further separation step is necessary. In type IV, the heterogeneous catalyst is immobilized into the reactor, so the catalyst can be reused easily. According to authors, this type of reactor is regarded as the most convenient for continuous-flow synthesis because the catalytic methodologies are nowadays imperative for the development of sustainable and efficient processes[55(b)(g)].

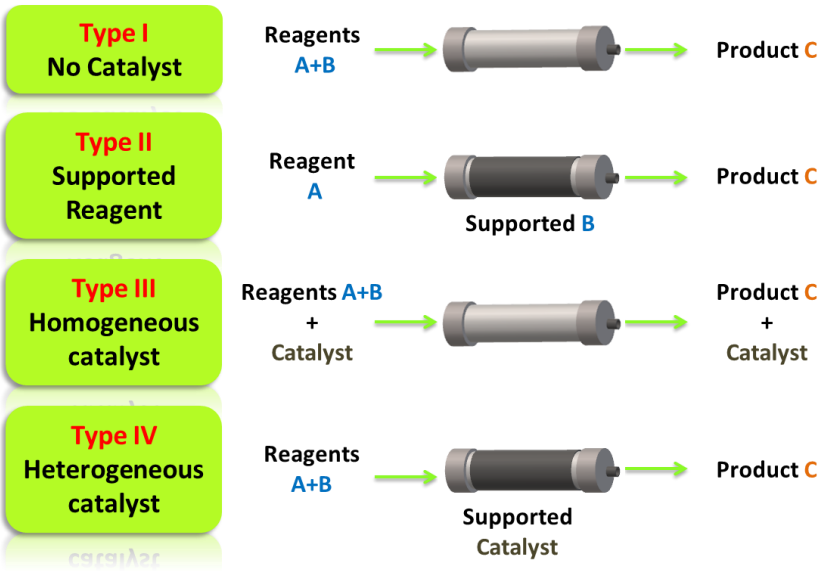

Figure 17 Four types of continuous-flow microreactors

b- An impressive, complete and chiroselective synthesis of an API, (*R*)-Rolipram **18**, using heterogeneous catalytic continuous-flow system has been described by Kobayashi [55(g)(j)]. The starting materials and related reagents have been passed through a sequence of chiral and achiral solid catalysts as shown in Figure 18. Moreover, the (*S*)-Rolipram **19** was obtained simply by replacing the chiral heterogeneous catalyst in reactor II with the opposite enantiomer catalyst. The yield is 50% from commercially available aldehyde **17**, the productivity is 1g per 24 h and the enantiomeric excess is 96% for both of the products **18** and **19**.

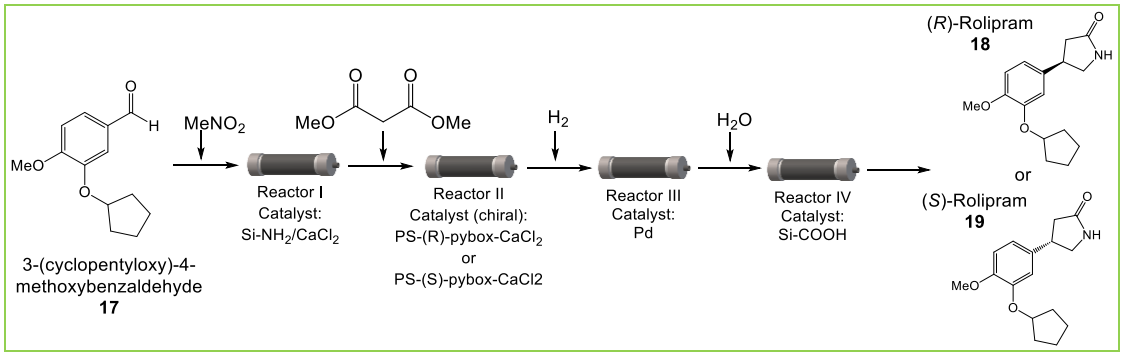

Figure 18 Flow synthesis of the anti-inflammatory drug (*R*)-Rolipram and (*S*)-Rolipram with four reactors (D: 5-10mm, L: 50-300 mm) packed with solid catalysts

1.1.4 Conclusion

The overview of microreactors and their advantages related to continuous operation, small dimension and geometry have been introduced. Microreactors have been applied in different types of reactions, in order to control the reaction rate, reduce the release the highly toxic products and reduce the side-products. Compared to related traditional batch processes, the

heat and mass transfer, mixing efficiency, residence time control, process safety, production costs and environmental conservation of continuous manufacturing with microreactors are much improved. The combination of heterogeneous catalysts with microreactors has been discussed, and three different methods of immobilization of heterogeneous catalyst in microreactors have been summarized: (i) packed-bed microreactor, (ii) wall-coated microreactor and (iii) monolithic microreactor.

1.2 Reduction of *p*-nitrophenol as model reaction

In order to test and compare the performance of heterogeneous catalytic microreactors with various supports, a model reaction should be selected, which should be simple, safe, easy to handle and to analyze.

In this thesis, we have focused on the transfer hydrogenation of *p*-nitrophenol (PNP) with formic acid (FA) on palladium catalyst. This reaction starts only in presence of catalysts in a low temperature range[57] and satisfies all the above conditions. In addition, it has a particular environmental interest:

- All the reagents (PNP and FA) and product *p*-aminophenol (PAP) are commercial, so the study of the reaction is convenient;
- The PNP is among the most common nitrophenolic compounds that widely used in chemical industry. It is listed as the priority pollutant by the United States Environmental Protection Agency due to its water solubility, chemical stability and toxicity to human health [58]. Compared to the current methods of pollutant treatment such as biological treatment [59], catalytic reduction method of PNP is more efficient and more sustainable, because it converts PNP to more environmental friendly products [58(a)].
- The PAP is an important intermediate in fine and pharmacy industry for the synthesis of several important analgesic and antipyretic drugs, such as paracetamol, acetanilide, phenacetin [60]. Besides, PAP can be also applied in the field of dyes, anticorrosive lubricants and pharmaceuticals[57(b),60-61];

---

[57] (a)Rambabu, D.; Pradeep, C. P.; Pooja, P.; Dhir, A., *New Journal of Chemistry* **2015,** *39* (10), 8130-8135. (b) Javaid, R.; Kawasaki, S.; Suzuki, A.; Suzuki, T. M., *Beilstein Journal of Organic Chemistry* **2013,** *9*, 1156-1163.

[58] (a) Jadbabaei, N.; Slobodjian, R. J.; Shuai, D.; Zhang, H., *Applied Catalysis A: General* **2017,** *543*, 209-217. (b) Chauhan, A.; Pandey, G.; Sharma, N. K.; Paul, D.; Pandey, J.; Jain, R. K., *Environmental Science & Technology* **2010,** *44* (9), 3435-3441. (c) Letzel, S.; Göen, T.; Bader, M.; Angerer, J.; Kraus, T., *Occupational and Environmental Medicine* **2003,** *60* (7), 483-488.

[59] Yi, S.; Zhuang, W. Q.; Wu, B.; Tay, S. T. L.; Tay, J. H., *Environmental Science & Technology* **2006,** *40* (7), 2396-2401.

[60] (a) Jiang, Z.; Xie, J.; Jiang, D.; Jing, J.; Qin, H., *CrystEngComm* **2012,** *14* (14), 4601-4611. (b) Rana, S.; Parida, K. M., *Catalysis Science & Technology* **2012,** *2* (5), 979-986. (c) Lu, Y.; Mei, Y.; Ballauff, M.; Drechsler, M., *The Journal of Physical Chemistry B* **2006,** *110* (9), 3930-3937. (d) Jiang, Z.; Xie, J.; Jiang, D.; Wei, X.; Chen, M., *CrystEngComm* **2013,** *15* (3), 560-569.

[61] Saha, S.; Pal, A.; Kundu, S.; Basu, S.; Pal, T., *Langmuir* **2010,** *26* (4), 2885-2893.

- The transfer hydrogenation provides an attractive option for the reduction of nitrophenol. This method avoids the use of dihydrogen gas under high temperature and high pressure, therefore is beneficial to reduce the energy consumption, and reduce the additional cost of transport and storage of dihydrogen gas[62];
- Among the available hydrogen donors [63], FA is a safe, cheap and plentiful hydrogen source with high stability and low toxicity, and could be derived from biomass [62(c),64]. By biological or chemical method, the only byproduct of dehydrogenation reaction of FA, CO_2, could be regenerated to FA in large quantities [64], completing the sustainable cycles for the potential use of FA as hydrogen source;
- In the nanoparticle state, palladium is a distinct material with a strong affinity to hydrogen owing to both its catalytic and hydrogen absorbing properties, which makes it a good catalyst for various hydrogenation reactions[65]. Pd nanoparticles have an excellent activity [62(c)] in the catalytic hydrogenation reactions and in the decomposition of FA[57(2),62(c),66].

1.2.1 Reduction of *p*-nitrophenol in heterogeneous conditions

1.2.1.1 Methods of reduction

In current researches, the catalytic reduction of PNP is mainly carried out with reducing agents in neutral, alkaline and acidic conditions, such as dihydrogen (H_2), sodium borohydride ($NaBH_4$), and FA. In this part, several studies of different hydrogenation methods in heterogeneous conditions with Pd, Ni etc. are introduced.

1.2.1.1.1 Reduction in neutral condition

In neutral condition, the direct catalytic hydrogenation of PNP is mainly done by dihydrogen. The only byproduct is H_2O and usual catalysts are noble metals.

---

[62] (a) Prasad, K.; Jiang, X.; Slade Joel , S.; Clemens, J.; Repič, O.; Blacklock Thomas , J., *Advanced Synthesis & Catalysis* **2005,** *347* (14), 1769-1773. (b) Wienhofer, G.; Sorribes, I.; Boddien, A.; Westerhaus, F.; Junge, K.; Junge, H.; Llusar, R.; Beller, M., *Journal of the American Chemical Society* **2011,** *133* (32), 12875-9. (c) Li, X. H.; Cai, Y. Y.; Gong, L. H.; Fu, W.; Wang, K. X.; Bao, H. L.; Wei, X.; Chen, J. S., *Chemistry* **2014,** *20* (50), 16732-7.

[63] (a) He, L.; Wang, L. C.; Sun, H.; Ni, J.; Cao, Y.; He, H. Y.; Fan, K. N., *Angewandte Chemie International Edition* **2009,** *48* (50), 9538-41. (b) Lou, X.-B.; He, L.; Qian, Y.; Liu, Y.-M.; Cao, Y.; Fan, K.-N., *Advanced Synthesis & Catalysis* **2011,** *353* (2-3), 281-286.

[64] (a) Tuteja, J.; Nishimura, S.; Ebitani, K., *RSC Advances* **2014,** *4* (72), 38241. (b) Boddien, A.; Gartner, F.; Federsel, C.; Sponholz, P.; Mellmann, D.; Jackstell, R.; Junge, H.; Beller, M., *Angewandte Chemie International Edition* **2011,** *50* (28), 6411-4. (c) Hull, J. F.; Himeda, Y.; Wang, W. H.; Hashiguchi, B.; Periana, R.; Szalda, D. J.; Muckerman, J. T.; Fujita, E., *Nature Chemistry* **2012,** *4* (5), 383-8. (d) Sekizawa, K.; Maeda, K.; Domen, K.; Koike, K.; Ishitani, O., *Journal of the American Chemical Society* **2013,** *135* (12), 4596-9.

[65] (a) Emin, C.; Remigy, J.-C.; Lahitte, J.-F., *Journal of Membrane Science* **2014,** *455*, 55-63. (b) Adams, B. D.; Chen, A., *Materials Today* **2011,** *14* (6), 282-289.

[66] (a) Du, Y.; Chen, H.; Chen, R.; Xu, N., *Applied Catalysis A: General* **2004,** *277* (1-2), 259-264. (b) Tsutsumi, K.; Uchikawa, F.; Sakai, K.; Tabata, K., *ACS Catalysis* **2016,** *6* (7), 4394-4398.

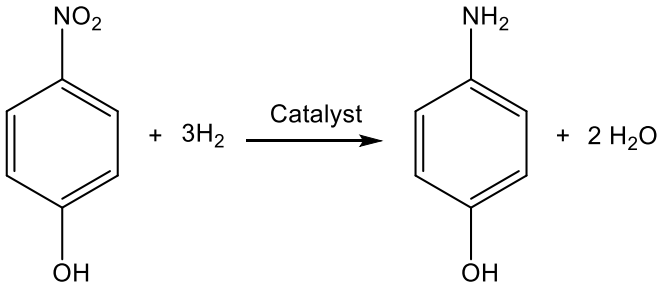

Figure 19 Hydrogenation of PNP with H_2

This reaction has been studied in both continuous and batch reactor. Sá[67] has investigated this reaction in a continuous-flow flooded-bed microreactor (ThalesNano H-Cube Mini®) where the PNP solution and H_2 flow upward through the catalyst bed. The hydrogen gas was generated in situ through electrolysis of water. It was the first time that the novel nano-Cu_2O catalysts grafted on polymeric resins was found active in hydrogenation, without the promotion of a noble metal. Yin[68] has investigated the influence of supports on catalytic activity of Ni catalysts in this reaction, and demonstrated that the catalytic activity increased in the order of Ni@kieselguhr >> Ni@TiO_2 > Ni@Al_2O_3. The surface acidities of these catalysts are critical to their catalytic activity.

Parida [60(b)] has used palladium supported mesoporous silica as catalyst in the flask at room temperature. The influence of catalyst loading and the reaction time on hydrogenation of PNP have been studied and a mechanism of this reaction was proposed as follows: PNP is firstly reduced to *p*-nitrosophenol (PNS) then to *p*-hydroxylaminophenol (PHx), and the intermediate *p*-benzoquinone imine (PBQI) is formed between the reduction of PHx to PAP.

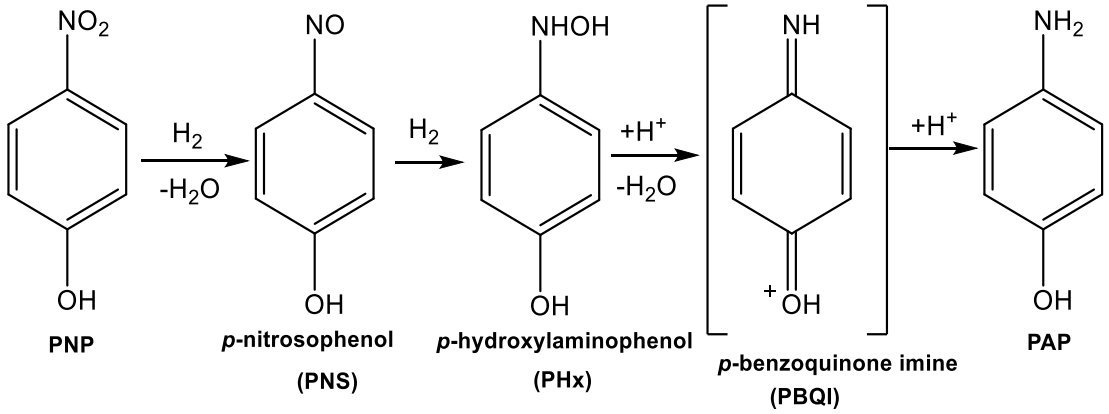

Figure 20 Mechanism of hydrogenation of PNP to PAP with H_2 proposed by Parida [60(b)]

1.2.1.1.2 Reduction in alkaline condition

The reduction of PNP in alkaline condition is mainly investigated with $NaBH_4$, and also with KBH_4 and N_2H_4 as reducing agents, owing to their low prices, efficient reducibility and good solubility in

[67] Paun, C.; Giziński, D.; Zienkiewicz-Machnik, M.; Banaś, D.; Kubala-Kukuś, A.; Sá, J., *Catalysis Communications* **2017,** *92*, 61-64.
[68] Lu, H.; Yin, H.; Liu, Y.; Jiang, T.; Yu, L., *Catalysis Communications* **2008,** *10* (3), 313-316.

water[69]. Moreover, there is no side reaction and the mechanism has been well described. The progress of this reaction can be easily followed by UV-vis. spectroscopy.

The characteristic absorption band of PNP was observed at 317 nm. In alkaline conditions, after adding the $NaBH_4$, the shifted peak at 400 nm corresponding to the *p*-nitrophenolate anion (PNP^-) is observed as show in Figure 21. After the reaction begins, the decrease in absorption of PNP^- was observed on the time scale, meanwhile the formation of a new peak at 300 nm corresponding to PAP. Thus the consumption of PNP and appearance of PAP can be monitored easily.

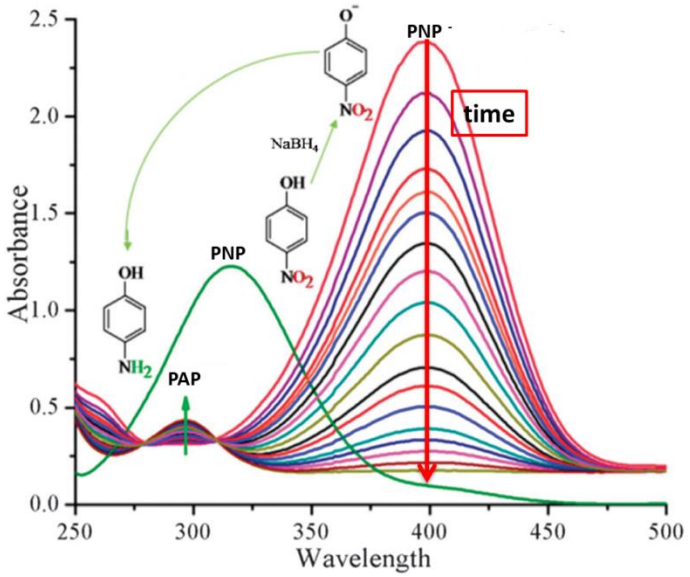

Figure 21 Time dependent evolution of UV-vis. spectra showing the catalytic reduction of *p*-nitrophenol (PNP, pic at 317 nm) to *p*-aminophenol (PAP) by sodium borohydride [57(a)] (Reaction conditions: C_{PNP}^0=1mM, $C_{NaBH_4}^0$=26.4 mM, Pd^0=50μg, time=16 min)

However, a large excess of $NaBH_4$ is usually used for the complete reduction and hydrogen gas bubbles are formed during the process because of the self-hydrolysis of $NaBH_4$ in water [70], which can become a problematic issue for this reaction.

The reduction with $NaBH_4$ has been widely utilized for investigating the new heterogeneous catalyst. Pal[71] has studied this reaction with Ag nanoparticles formed *in situ* and Esumi [72] has utilized this reaction as model reaction to compare the catalytic activity of their dendrimer-Au nanocomposites. Liz-Marzán [73] has summarized the investigations from 2004-2011 of the

[69] (a) Tan, W. L.; Abu Bakar, N. H. H.; Abu Bakar, M., *Catalysis Letters* **2015,** *145* (8), 1626-1633. (b) Bakar, N. H. H. A.; Ridzwan, A.; Tan, W. L.; Bakar, M. A.; Sabri, N. A., *AIP Conference Proceedings* **2017,** *1835* (1), 1-6. (c) Shin, H. J.; Kim, K. K.; Benayad, A.; Yoon, S. M.; Park, H. K.; Jung, I. S.; Jin, M. H.; Jeong, H. K.; Kim, J. M.; Choi, J. Y.; Lee, Y. H., *Advanced Functional Materials* **2009,** *19* (12), 1987-1992. (d) Brown, H. C.; Rao, B. C. S., *Journal of the American Chemical Society* **1956,** *78* (11), 2582-2588.

[70] Liu, A.; Yang, L.; Traulsen, C. H.; Cornelissen, J., *Chemistry Communication* **2017,** *53* (54), 7632-7634.

[71] Pradhan, N.; Pal, A.; Pal, T., *Colloids and Surfaces A: Physicochemical and Engineering Aspects* **2002,** *196* (2), 247-257.

[72] Esumi, K.; Miyamoto, K.; Yoshimura, T., *Journal of Colloid and Interface Science* **2002,** *254* (2), 402-405.

[73] Herves, P.; Perez-Lorenzo, M.; Liz-Marzan, L. M.; Dzubiella, J.; Lu, Y.; Ballauff, M., *Chemical Society Reviews* **2012,** *41* (17), 5577-5587.

reduction of PNP in aqueous solution with $NaBH_4$ utilizing different metal nanoparticles as catalysts such as Pd, Pt, Au, Ag in various supports such as spherical polyelectrolyte brush (SPB), TiO_2, Al_2O_3 and so on that demonstrated that this reaction is extensively adopted in the study of catalyst. He proposed that the Langmuir-Hinshelwood model could well represent the kinetic of this reaction.

This reaction was also studied in microreactors with heterogeneous catalysts [70,74]. Recently Cornelissen [70] has successfully fabricated a wall-coated microreactor by the immobilization of protein cages on the inner surface. The reduction of PNP with $NaBH_4$ has demonstrated the stability of the virus-like particle catalyst and its high efficiency.

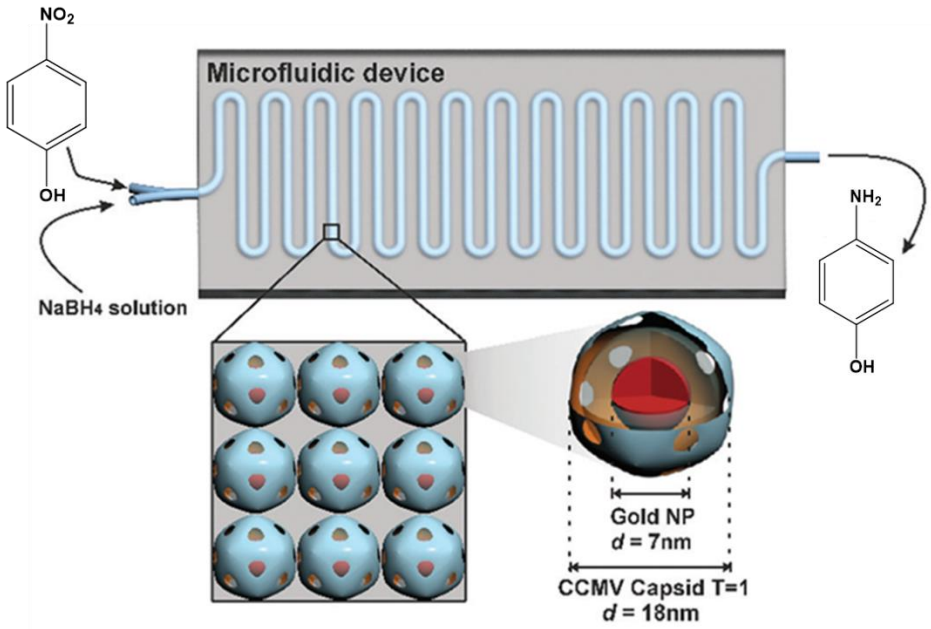

Figure 22 Reduction of PNP with $NaBH_4$ has been used as the model reaction to test a wall-coated microreactor immobilized by catalytic virus-like particles with Au nanoparticles encapsulated inside [70]

Hydrazine (N_2H_4) has also been used as hydrogen donor in the reduction of PNP. Saleh[75] has investigated the nano supported nickel catalyst in this reaction, and described the change in color in this reaction in a sequence of: the yellow color of PNP, the green color which was attributed to intermediate PBQI (see Figure 20), and then the discharge in color of PAP, which demonstrated the presence of an intermediate during this reaction.

[74] Li, J.; Wu, F.; Lin, L.; Guo, Y.; Liu, H.; Zhang, X., *Chemical Engineering Journal* **2018,** *333*, 146-152.
[75] Abd El Maksod, I. H.; Saleh, T. S., *Green Chemistry Letters and Reviews* **2010,** *3* (2), 127-134.

Ballauff has investigated the full kinetic analysis of the catalytic reduction of PNP with sodium borohydride by metallic nanoparticles in some publications[76]. Because of the large excess of BH_4^- (40-300), the reaction follows a pseudo-first order reaction rate with respect to PNP [76(c)]. The mechanism of the reduction of PNP by metallic nanoparticles was proposed as shown in Figure 23: In step A, PNP was first reduced to the PNS which was quickly converted to PHx, which was the only stable intermediate; in step B, PHx could be reduced to the final product PAP. There was an adsorption/desorption equilibrium for all compounds in all steps and all reactions were assumed to take place solely at the surface of the metal nanoparticles (Langmuir-Hinshelwood model). The established full kinetic equations had good agreements with the experimental data. The kinetic constants obtained from this analysis indicated that the step B is the rate-determining step [76(b)]. However, neither PNS nor PHx was detected or isolated during these studies.

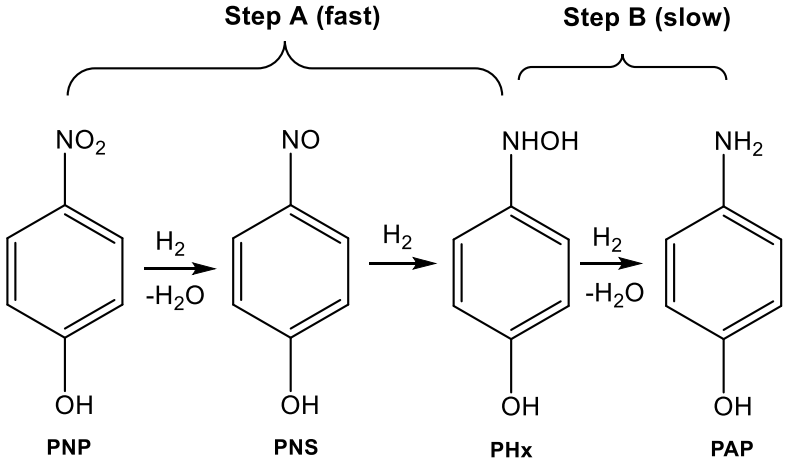

Figure 23 Proposed mechanism of the reduction of PNP with sodium borohydride by metallic nanoparticles by Ballauff [76].

1.2.1.1.3 Reduction in acidic condition

The researches about the reduction of PNP in acidic condition are much fewer than in alkaline condition. The main acidic reducing agent is formic acid [57(b),62(c),66(b)].

Javaid [57(b)] has investigated a wall-coated microreactor and examined the transfer hydrogenation of PNP with aqueous formic acid. Different catalysts such as Pd, porous Pd, Pd-Ag, PdO and porous PdO were coated into the inner surface of a metallic tube (inner volume 196 µL). No side reaction occurred and no hydrogen gas was found during the process. The reaction concentration of PNP is 10mM, and the evolution of CO_2 gas bubbles was observed during the reaction. The porous catalysts showed better catalytic activity than non-porous equivalents, and porous PdO demonstrated the best catalytic activity. The effect of the concentration of FA on the conversion of PNP was studied as shown in Figure 24.

[76] (a) Gu, S.; Lu, Y.; Kaiser, J.; Albrecht, M.; Ballauff, M., *Physical Chemistry Chemical Physics* **2015,** *17* (42), 28137-28143. (b) Gu, S.; Wunder, S.; Lu, Y.; Ballauff, M.; Fenger, R.; Rademann, K.; Jaquet, B.; Zaccone, A., *The Journal of Physical Chemistry C* **2014,** *118* (32), 18618-18625. (c) Gu, S.; Kaiser, J.; Marzun, G.; Ott, A.; Lu, Y.; Ballauff, M.; Zaccone, A.; Barcikowski, S.; Wagener, P., *Catalysis Letters* **2015,** *145* (5), 1105-1112. (d) Wunder, S.; Lu, Y.; Albrecht, M.; Ballauff, M., *ACS Catalysis* **2011,** *1* (8), 908-916.

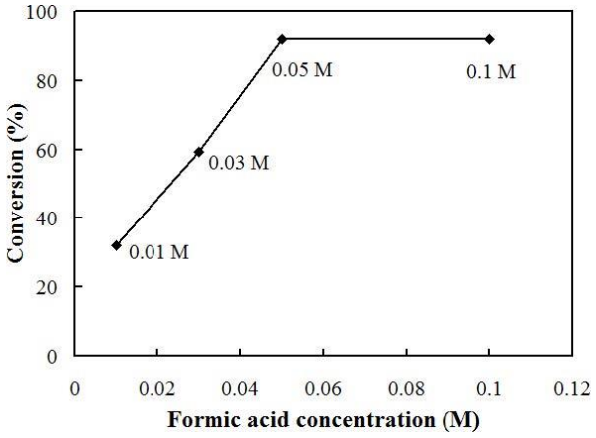

Figure 24 Effect of the concentration of FA on the conversion of PNP (0.01 M). The formic acid concentration varied: 0.01 M, 0.03 M, 0.05 M and 0.1 M. Porous-PdO-coated reactor was used at 30 °C, with a residence time of 14.7 s. [57(b)]

1.2.1.2 Mechanism of reduction in formic acid

The mechanism of the reduction of *p*-nitrophenol in formic acid on Pd catalyst has been rarely studied. Nevertheless, the mechanism of the reduction of aromatic nitro compound such as nitrobenzene to the corresponding aniline has been well discussed[77]. Combining these investigations, the complete mechanism of the reduction of *p*-nitrophenol in formic acid with Pd catalyst has been proposed as shown in Figure 25.

The reduction occurs in several steps along two routes: The first steps are the same as the routes in neutral or alkaline conditions: the PNP is first reduced to the PNS and then further reduced to PHx in two very fast steps [77]. The PNP and PNS are strongly adsorbed on the catalyst surface. Then, in direct route, the product PAP could be formed via a disproportionation pathway: 2 PHx -> PAP+PNS. The PHx reduction is slow because of the cleavage of an O-N bond.

In the condensation route, the 4,4'-Azoxydiphenol (PAXD) is formed by the condensation of the PNS and PHx, then in a series of consecutive steps, the PAXD is reduced to 4,4'-Azodiphenol (PAD) and 4,4'-hydrazobisphenol (PHB), finally the PAP.

[77] (a) Corma, A.; Concepcion, P.; Serna, P., *Angewandte Chemie International Edition* **2007,** *46* (38), 7266-7269. (b) Blaser, H. U., *Science* **2006,** *313* (5785), 312-313.

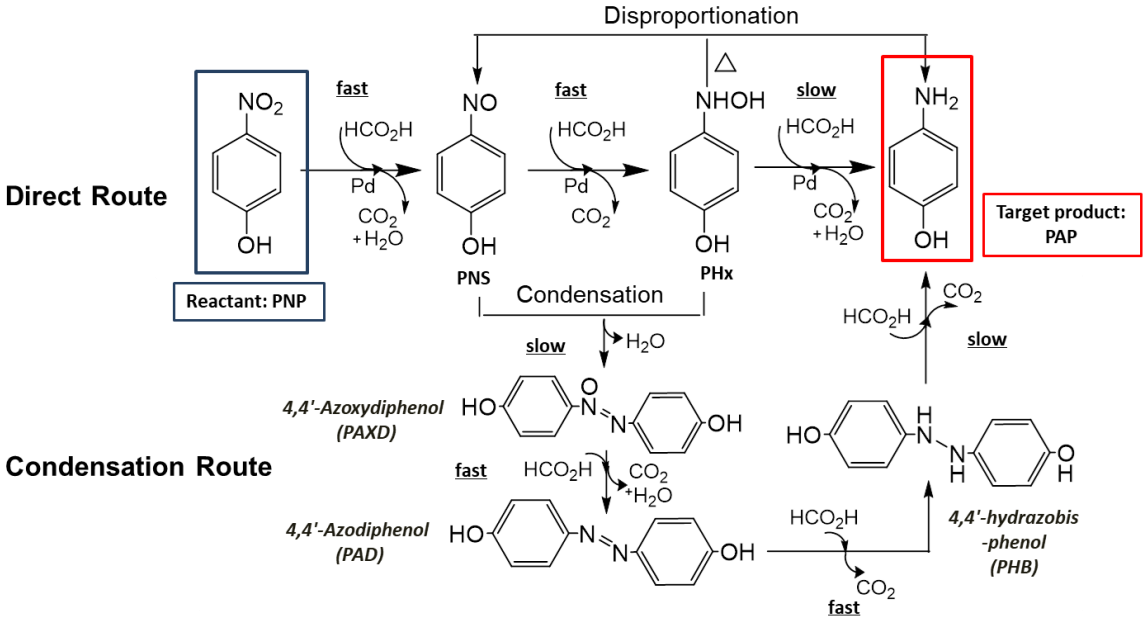

Figure 25 Proposed mechanism of hydrogenation of *p*-nitrophenol with formic acid on Pd (adapted from Blaser [77(b)] for *p*-nitrophenol)

The reaction routes are strongly influenced by the catalyst support and promoters added. For example, a large amount of PHx may accumulate in the direct route [77(b)] if the catalyst is not active enough and/or if the step for the reduction of PHx is slow, but this accumulation of PHx has not been known on the support or not, and has not been proved directly. This accumulation can be reduced through the addition of promoters, especially of vanadium compounds [77-78]. In spite of the lack of direct evidence about this mechanism, the group of Studer [78] has detected the accumulation of the corresponding hydroxylamine in the catalytic hydrogenation of nitroarene (benzenesulfonamide-*N*-cyclohexyl-*N*-methyl-2-nitro) with Pd@C catalyst and acetic acid as reducing agent. They reduced the accumulation by adding vanadium promoters such as $VOSO_4$, V_2O_5 and so on. They also suggested a mechanism which could be called a "catalytic by-pass": the hydroxylamine is not directly hydrogenated to the corresponding aniline but disproportionate rapidly so that the nitroso intermediate could re-enter the catalytic cycle and the amine formation is accelerated. The same principle as the disproportionation of PHx of the direct route is shown in Figure 25.

The group of Cai [79] has investigated the products distribution during the transfer of hydrogenation of nitrobenzene, and detected the formation and decomposition of azoxybezene (Ph-N=NO-Ph) and hydrazobenzene (Ph-NH-NH-Ph), which demonstrated the condensation route.

[78] Baumeister, P.; Blaser, H. U.; Studer, M., *Catalysis Letters* **1997,** *49* (3), 219-222.
[79] Chen, S.; Lu, G.; Cai, C., *New Journal of Chemistry* **2015,** *39* (7), 5360-5365.

Among the majority of the studies of the reduction of PNP, the direct route is mainly concerned. On the basis of the work of Ebitani [64(a)] and Jiao [80], we propose the catalytic cycle corresponding to the direct route of the mechanism in Figure 26.

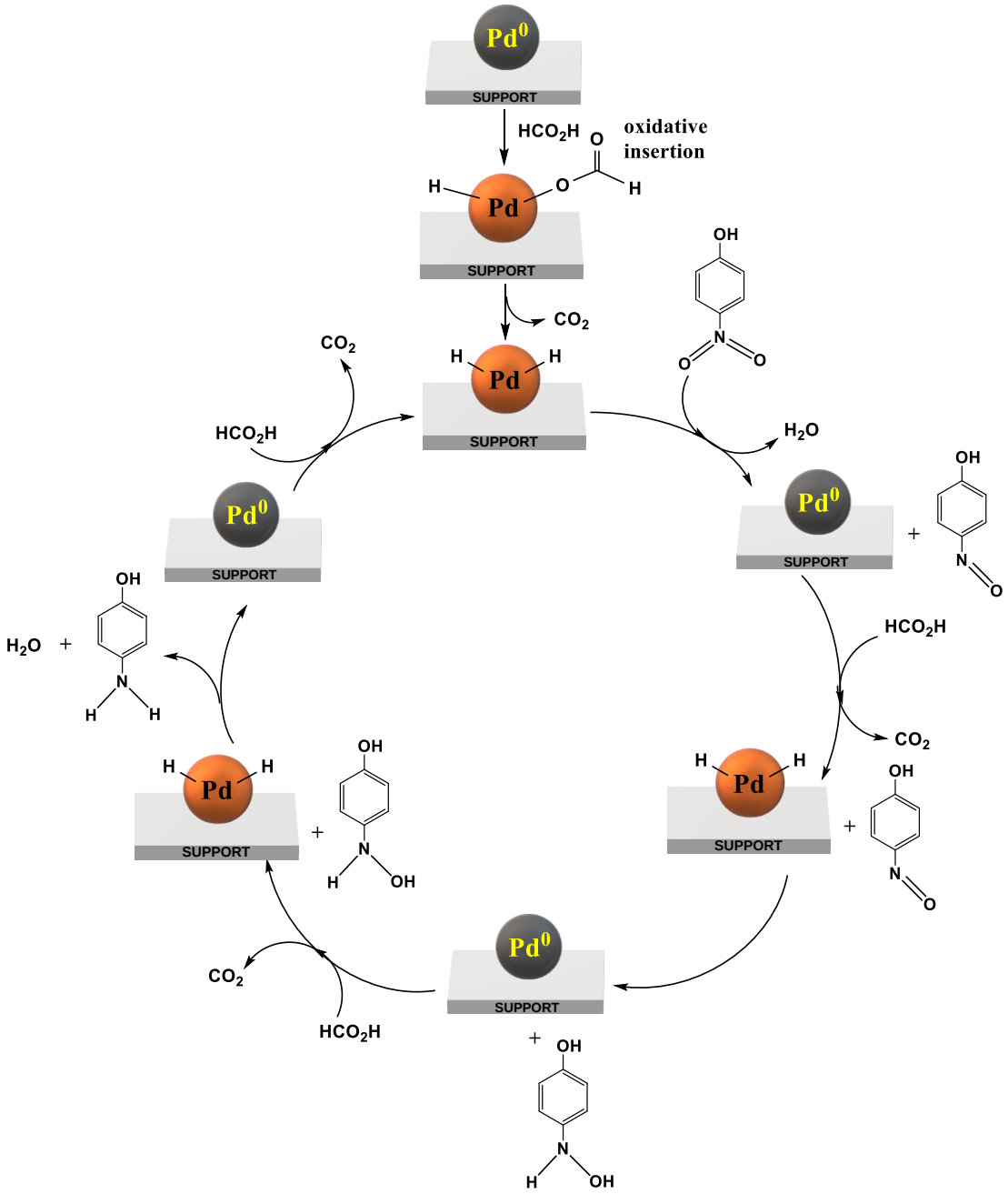

Figure 26 Direct route of the mechanism for transfer hydrogenation of PNP by FA over supported Pd catalyst

[80] Luo, Q.; Wang, T.; Beller, M.; Jiao, H., *Journal of Molecular Catalysis A: Chemical* **2013,** *379*, 169-177.

1.2.2 Methods of analysis

The most commonly used identification and quantitative analysis method of this reaction is the ultraviolet–visible (UV-vis.) spectroscopy, which is usually utilized in the alkaline and acidic conditions[57,60,76,81]. In alkaline conditions, the consumption of PNP and formation of PAP can be monitored easily as discussed in the part of 1.2.1.1.2. However, in acidic conditions, the pH value can impact the UV-vis. spectra of PNP as shown in Figure 27. The peak of PNP varies to lower wavelength when the pH value decreases and the overlap of the spectra of PNP and PAP makes the formation of PAP difficult to be monitored [57(b)].

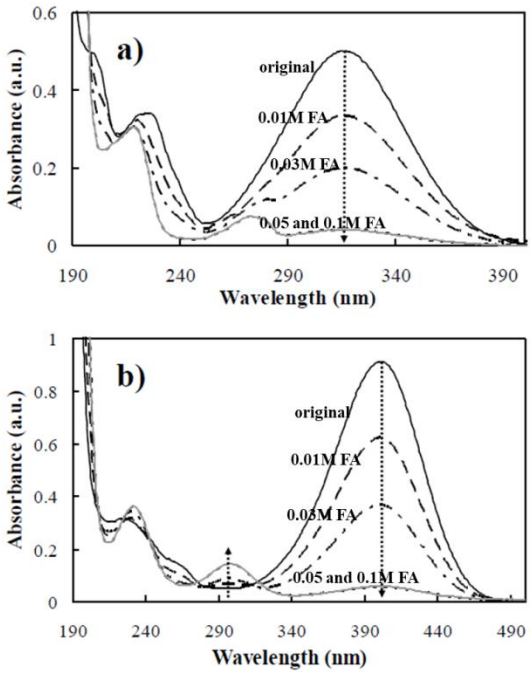

Figure 27 Example of UV–vis. spectra of final product by use of different concentrations of formic acid. Measured pH (a)pH = 2.5 and (b) pH = 5.0. C_{PNP}^0=10 mM, Pd^0=67.3mg, reaction time=14.7 ms.

High performance liquid chromatography (HPLC) is also used to determine the quantity of PNP and PAP in order to calculate the conversion yield of reaction. In both of the investigations of Hart[82] and Hanna[83], a C18 packed column has been utilized in the HPLC system. Hart [82] has adopted a mobile phase consisted of 40% acetonitrile and 60% water, containing 25 mM o-phosphoric acid. The injection volume was 50 μL with a flow rate of 0.5 mL/min and UV detection wavelength of 254 nm. The conditions of Hanna's work [83] are: the mobile phase was a mixture of 50% deionized water, 50% acetonitrile and 1% acetic acid. The flow rate was 1 mL/min and the PNP and PAP were measured at wavelengths of 317 nm and 273 nm, respectively.

---

[81] (a) Venkatesan, P.; Santhanalakshmi, J., *Nanoscience and Nanotechnology* **2012,** *1* (2), 43-47. (b) Sharma, M.; Hazra, S.; Basu, S., *Advanced Powder Technology* **2017,** *28* (11), 3085-3094. (c) Liu, K.; Wang, Y.; Chen, P.; Zhong, W.; Liu, Q.; Li, M.; Wang, Y.; Wang, W.; Lu, Z.; Wang, D., *Applied Catalysis B: Environmental* **2016,** *196*, 223-231.

[82] Honeychurch, K. C.; Hart, J. P., *Electroanalysis* **2007,** *19* (21), 2176-2184.

[83] Bae, S.; Gim, S.; Kim, H.; Hanna, K., *Applied Catalysis B: Environmental* **2016,** *182*, 541-549.

1.2.3 Conclusion

Due to the advantages discussed, the transfer hydrogenation of *p*-nitrophenol with formic acid on palladium catalyst has been chosen as the model reaction. The investigations of the reduction of *p*-nitrophenol in neutral, alkaline and acidic conditions have been introduced and the mechanism of the reduction in formic acid has been discussed. The methods of analysis of the reduction such as UV-vis and HPLC analysis have been summarized.

In the following experimental analysis part, the model reaction will be tested in both packed-bed microreactor and monolithic microreactor mainly analyzed by UV-vis and HPLC methods.

Chapter 2 - Study of *p*-nitrophenol hydrogenation as model reaction in a packed-bed microreactor

In this part, investigations about *p*-nitrophenol (PNP) hydrogenation catalyzed with a commercial Pd@alumina powder are presented. Chapter 2 is devoted to experimental observations and chapter 3 to models, both in transient and stead-state conditions for the establishment of a reaction rate equation. Chapter 2 is divided in 4 sections. A first experimental section presents the set-up and three analysis protocols more and more sophisticated. A second section presents different ways of characterization of reaction: Nuclear Magnetic Resonance (NMR) and Mass Spectroscopy (MS) analysis of the reaction mixture, comparison of batch and flow-reactor experiments and measurements of PNP and PAP adsorption and desorption in the batch reactor. Thirdly, the effect of reaction parameters on conversion such as temperature, flow rate and initial concentration of reactants are summarized. Last but not least, the dynamic studies of the reaction are presented; this part presents the attempts to identify the intermediate products detected in our investigations but never reported in publications.

2.1 Experimental section

2.1.1 Experimental condition

As discussed in 1.2, the model reaction chosen in order to compare the performance of different catalysts is the transfer hydrogenation of *p*-nitrophenol (PNP) by formic acid (FA) with Pd catalyst. The commercial catalyst is powder Pd@alumina catalyst, containing 5% Pd (Strem Chemicals). All reagents are commercial.

The packed-bed microreactor is a stainless-steel tube, with sinters at both ends and that is filled with commercial catalyst powder. The characteristics of microreactor are listed in Table 1.

Table 1 Characteristics of the packed-bed microreactor

Symbol	Parameter	Unit	Dimension
D_{PB}	Internal diameter of packed-bed microreactor	mm	4.47
L_{PB}	Length of packed-bed microreactor	mm	40
V_{PB}	Volume of tube of packed-bed microreactor	mL	0.64
$m_{cat,PB}$	Catalyst mass	mg	639.5
$D_{cat,\ PB}$	Catalyst average diameter	mm	0.07
$m_{pd,\ PB}$	Palladium mass	mg	32

2.1.2 Protocol 1: off-line UV analysis

Three different analytical protocols, more and more sophisticated, were developed for testing the properties of the reaction in packed-bed microreactor. The preliminary experiments have been carried out with off-line UV-visible analysis of samples leaving the reactor.

2.1.2.1 Experimental set-up

The scheme of the experimental set-up is shown in Figure 28. The solutions of PNP and FA are pre-mixed before reaction, as it was preliminary checked that there is no reaction between PNP and FA without catalyst. The aqueous solution containing PNP and FA is degassed and then pumped by a micro flow pump (1µl/min-10ml/min, Thermo Fisher, Model ISO-3100SD) via the reservoir, and the flow rate can be changed by the micro flow pump. The reaction temperature is controlled in a column-oven (High Standard Performances, 39~99℃, Interchim). Samples of the microreactor effluent are collected in flasks and then analyzed by the off-line UV-vis spectroscopy (UVIKON 933, Kontron Instrument).

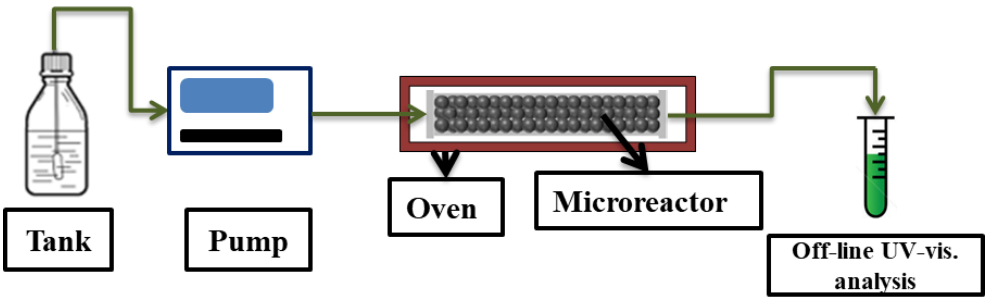

Figure 28 Schematic representation of the experimental set-up of protocol 1 with off-line UV-vis. analysis

2.1.2.2 Off-line UV–vis spectroscopy Calibration

The aim of this part is to find the range of wavelength giving the most precise analysis of the reaction mixture. The method was developed in 3 steps.

(a) The UV–vis absorption spectra of PNP and PAP are shown in Figure 29:

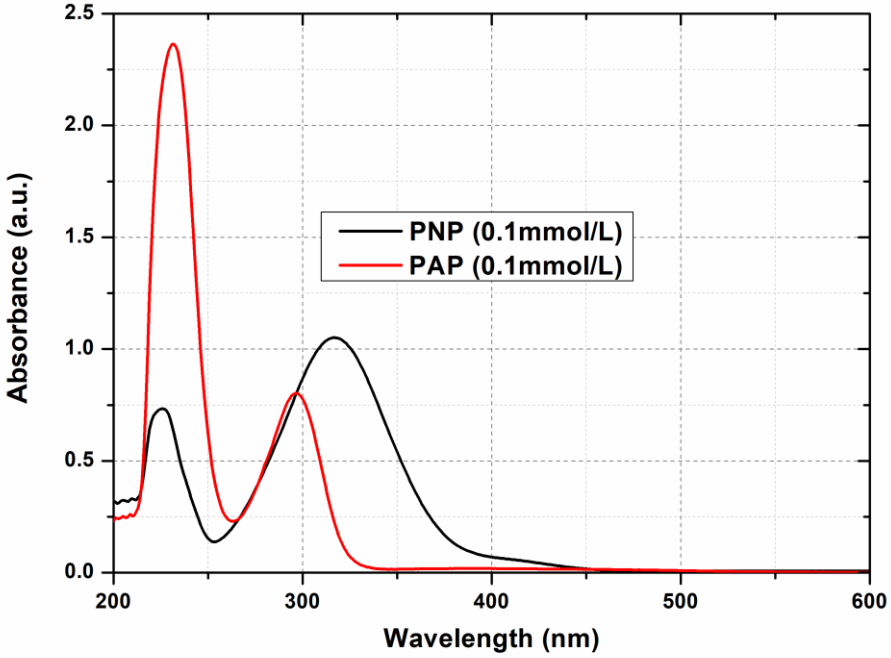

Figure 29 UV–vis absorption spectra of PNP (0.1mmol/L) and PAP (0.1mmol/L)

In the figure above we can see that the spectra of PNP and PAP overlap between 200-330 nm and that only PNP absorbs above 330 nm. So, we can calculate the conversion of PNP in this range. It should be noted that the maximum concentration of PAP or PNP solution that can be measured in off-line UV-vis is about 0.2 mmol/L, so for the further reactions with more concentrated solutions, the product should be diluted before the off-line UV-vis. analysis.

(b) Calibration solutions were prepared in order to define the absorbance range where the response factor is constant. The response factor (RF) of PNP in each wavelength is calculated as follows:

$$\mathrm{RF} = \mathrm{Absorbance}/\mathrm{Concentration\ of\ PNP}$$

If in a certain range of wavelength, the RF of different calibration solutions remains the same, that means the concentration of PNP follows a linear relation with the absorbance without the impact of FA and PAP, so we can choose this range of wavelength as the effective absorption wavelength to calculate the conversion.

The composition of calibration solutions, reported in table 2, corresponds to different degrees of conversion of a mixture containing initially 0.1 mmol/L of PNP. In the first series of experiments, the concentration of FA is always stoichiometric ($C_{FA}^0/C_{PNP}^0 = 3$), and in the second series experiment, C_{FA}^0/C_{PNP}^0 was varied from 1.2 to 18 to eliminate the influence of FA.

Table 2 Summary of conditions of calibration experiments of off-line UV

Assumed C_{PNP}° mmol/L	C_{FA}^{0}/C_{PNP}^{0}	Assumed conversion	Composition of calibration solution		
			C_{PNP} mmol/L	C_{FA} mmol/L	C_{PAP} mmol/L
0.1	3	0	**0.1**	**0.3**	**0**
		0.9	**0.01**	**0.03**	**0.09**
		0.7	**0.03**	**0.09**	**0. 07**
		0.5	**0.05**	**0. 15**	**0.05**
		0.3	**0.07**	**0.21**	**0.03**
		0	**0.01**	**0.03**	**0.09**
	18	0	**0.01**	**0.18**	**0.09**
	1.2	0.5	**0.05**	**0.06**	**0.05**
	3		**0.05**	**0.15**	**0.05**
	2	0.1	**0.09**	**0.18**	**0.01**
	4.67		**0.09**	**0.42**	**0.01**

As a result, the response factor is quite constant in the wavelength range 325-349nm, the standard deviation is 6%. The variation of standard deviation of RF at different wavelength is plot in Annex A-1 Figure A1.

(c) In order to improve the precision of the concentrations measurements, a multilinear regression method was used. We assume that the absorbance (λ) at a given wavelength in the 325-349 nm range can be regarded as a function of concentration of PNP, FA and PAP as:

$$\text{Absorbance}_{\lambda} = \text{a}_{\lambda} \times C_{PNP} + \text{b}_{\lambda} \times C_{FA} + \text{c}_{\lambda} \times C_{PAP}$$

The coefficients a_{λ}, b_{λ} and c_{λ} are calculated from UV spectra of calibration solutions, and then the theoretical absorbance is calculated with the multilinear relation. Coefficients b and c are very low, indicating that the contribution of FA and PAP is not significant. The deviation between measurements and calculations is minimum in the range 330-337 nm. The average deviation over the set of calibration solutions is about 3.4%.

In conclusion, the range of 330-337 nm is chosen to calculate the PNP conversion in the further reaction studies with off-line UV-vis. measurements. The PNP conversion is calculated from the average value over the 330-337 nm range of the absorbance ratio at the exit of the microreactor and in the tank containing the feed mixture. It is notable that the disappearance of PAP cannot be observed nor quantitatively analyzed with UV method.

2.1.3 Protocol 2: on-line UV analysis

Acquisition of a new UV-visible Photo-Diode Array (PDA) detector (MD-4010 Diode-array Detector, Jasco) allows combining the reaction and spectroscopic detection under the same continuous

flow. The software of the detector monitors three dimension spectra (time-wavelength-intensity), and offers the possibility to plot either complete UV-visible spectrum at a given time, or intensity-time profile at a given wavelength, or a 3D-representation.

2.1.3.1 Experimental set-up

The new experimental set-up with integrated on-line PDA detector is shown in Figure 30.

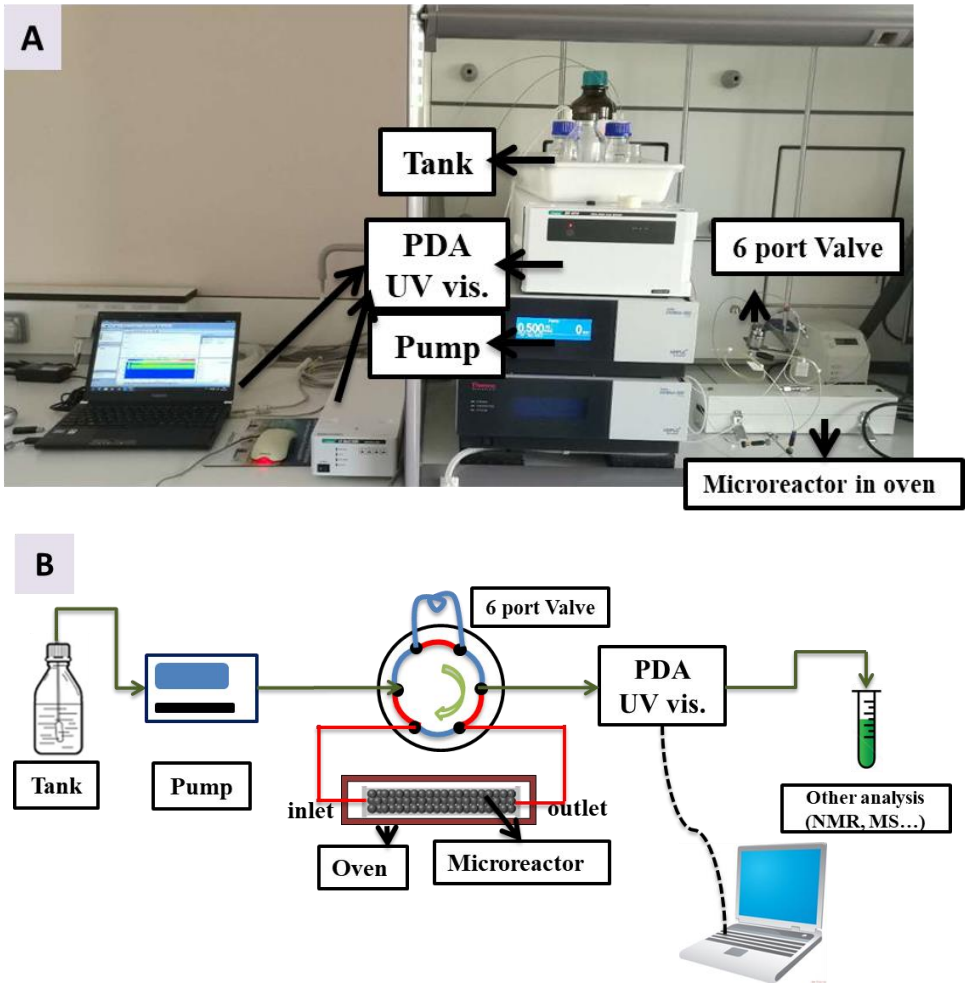

Figure 30 (A) Photo and (B) Schematic representation of the experimental set-up of protocol 2 with on-line UV-vis. detector

The 6 port valve is added in order to analysis both feed and reacted mixture. The valve can be switched to direct the flow toward the bypass (blue), where the feed solution is directly pumped into the PDA detector, or the route of reaction (red) where the solution is pumped through the microreactor and then through the PDA detector. In this way, we can know the variation of the product composition as the function of time. The pump and the oven are the same as in the first set-up.

The reaction protocol includes a 5-10 min sequence for analysis of feed mixture, followed by an 80-120 min sequence for the continuous analysis of the reactor effluent. The sequence ends when steady-state is clearly established. Calibration method used for PNP-conversion calculation is similar as presented for off-line UV vis. calibration. The concentrations of calibration solutions are listed in Annex A-2 Table A1. The calculations on the response factor and regression are in Annex A-2 Figure A2 and Figure A3, respectively. The final range for the calculation of PNP conversion with online UV PDA is 357-367 nm.

A three dimension spectrum (Time-Wavelength-Intensity) obtained by the software of the detector is shown in Figure 31.

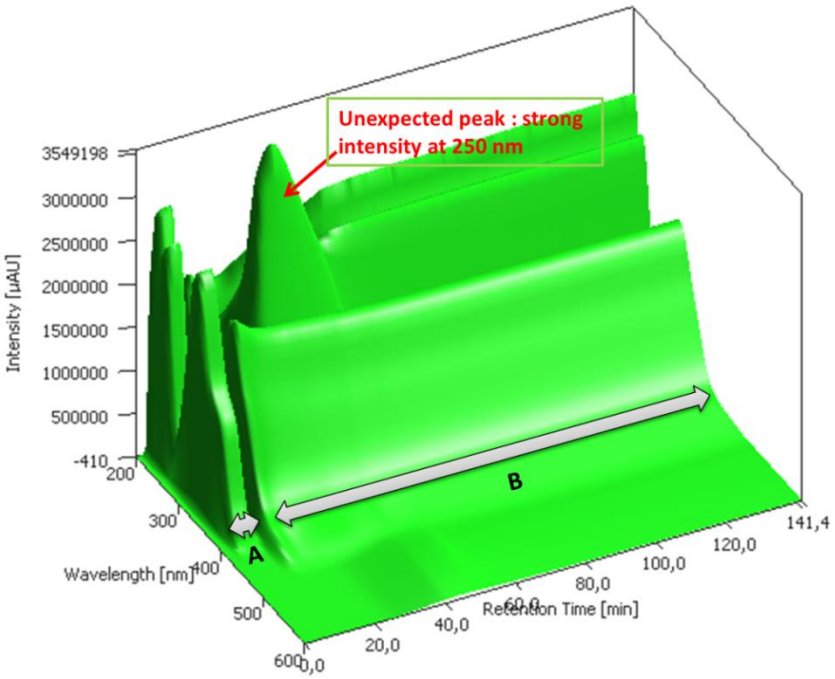

Figure 31 Example of 3D (Time-Wavelength-Intensity) PDA UV-vis. spectrum
A: measurement of the feed concentration; B: measurement of the product concentration
(Condition: C_{PNP}^0= 0.4 mmol/L, C_{FA}^0 = 1.2 mmol/L, T = 40°C, Q = 0.5 mL/min)

It is worth noting that Figure 31 exhibits an unexpected peak with a strong intensity at 250 nm. Further experiments have shown that this peak is not an artefact, but it corresponds to a real component that is neither PNP nor PAP. We name it intermediate I250. Attempts to identify I250 are presented in part 2.4.2. It was also observed that the intensity of I250 depends on the reaction conditions and on the history of the catalyst. Hence, in order to ensure repeatable catalyst conditions, a washing protocol was developed, as discussed in the following part.

2.1.3.2 Washing protocols

In order to assess the effect of catalyst washing on the UV intensity of I250, a series of experiments with different washing temperatures have been carried out. In all these experiments, the condition of reaction remains the same, with flow rate Q = 1mL/min, reaction temperature

$T_{reaction}$ = 30°C, $C_{PNP}{}^{0}$=0.4mmol/L, $C_{FA}{}^{0}$=1.2mmol/L. After each reaction sequence, we wash the microreactor set-up with distilled water during about 2 hours. The washing temperature varies from 30 to 80°C. Figure 32 shows the absorbance profiles of reaction sequence at 250nm realized after washing at different temperatures. Figure 32 indicates: (i) the intensity returns to the level of the feed solution after 2 hours, which means I250 no longer flows out of the microreactor. (ii) After a higher washing temperature, the I250 peak appears later, it is lower and wider. In addition, the surface areas under the peaks are roughly the same whatever the washing temperature (75.4, 77.8, 78.7, 77.1 for 30°C, 50°C, 70°C, 80°C, respectively), indicating that approximately the same quantity of I250 is formed and desorbed at the beginning of the reaction sequence.

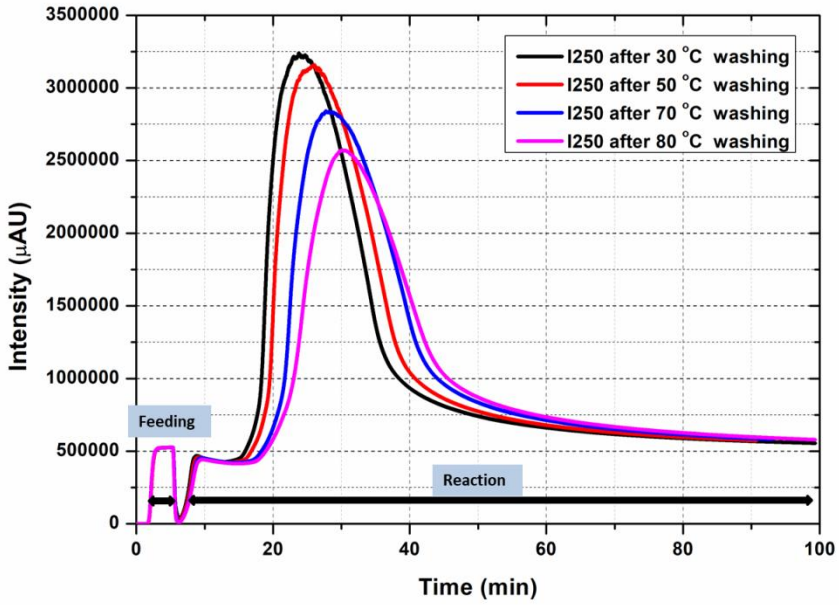

Figure 32 Variation of intensity of I250 of the reaction with time after different washing temperatures measured by PDA UV-vis. at 250 nm wavelength

In order to have a better insight on the washing process, the 250 nm-absorbance was also measured during washing process (Figure 33). At higher temperature, I250 flows out of the reactor faster, and the quantities of I250 washed out, estimated from the surface area under the peak, seems to be higher. It should be noted that the I250 amount washed out is about 10 times lower than the amount desorbed during the reaction sequence.

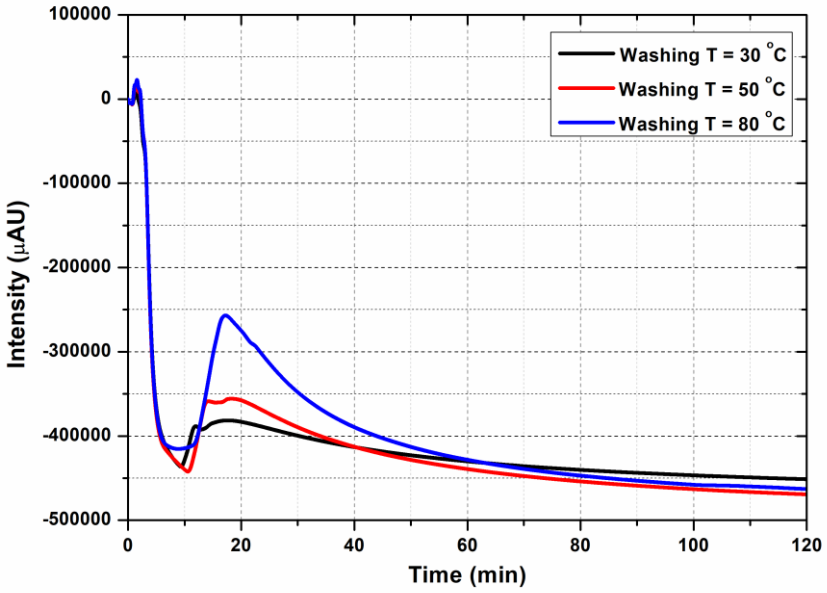

Figure 33 Variation of intensity of I250 with time during the washing process after reactions

These experiments indicate that the amount of I250 produced during reaction sequence is little dependent on the temperature of washing, even if I250 seems to be more strongly retained on the catalyst surface when it has been washed at higher temperature.

It is noteworthy that the I250 disappears if the packed-bed microreactor is left unused for about 1 month after washing, and it reappears after about five reactions-washing sequences I250 returns again. This probably indicates that, small quantity of I250 can be adsorbed and "stored" on the catalyst support. I250 amounts above this "stored I250" could be transformed to PAP or desorbed, but this stored I250 still remains on the support even after reaction and washing, unless the long-time immersion in water.

Finally, the washing protocol was fixed as follows: washing with distilled water, at 40°C and during 60 minutes. This protocol was applied after each reaction sequence.

2.1.3.3 Analysis with off-line HPLC

As neither off-line nor on-line UV vis. can analyze quantitatively the PAP, analysis with off-line HPLC has been investigated to prepare the next protocol.

Two publications (Hart[82] and Hanna[83]) have reported HPLC analysis in studies of PNP hydrogenation. In both cases, chromatography is made on a reverse-phase C18 column, with a mixture of acidified acetonitrile and water as the mobile phase, at flow rate between 0.5 mL/min -1 mL/min.

In our study, we used a C18 reversed phase HPLC column (3.5 µm, 4.6×100mm, XBridge®, WATERS), and a mixture of deionized water and acetonitrile acidified by 0.05% FA as the mobile phase, at a 0.5 mL/min flow rate. As shown in the UV-visible absorption spectra in Figure 29, both PNP and PAP have significant absorption intensity around 225nm and 300nm, here we have chosen 225 nm as the UV detection wavelength. The proportion of acetonitrile and FA was varied in order to optimize the quality of the resolution, results are reported in Table 3.

Table 3 Optimization of proportion of mobile phase and the retention time of PAP and PNP

Proportion		Retention time of PAP (min)	Retention time of PNP (min)
Water (acidified by 0.05 % FA)	**Acetonitrile (acidified by 0.05 % FA)**		
50%	50%	0.76	1.29
60%	40%	0.80	1.80
70%	30%	0.85	3
80%	20%	0.85	4.5
90%	10%	0.88	11.14

It indicates that the retention time of PAP does not change a lot, while the retention time of PNP increases with the increase of the proportion of water. In order to insure the good separation of PNP and PAP meanwhile cut down the analysis time, we adopt the following mobile phase composition: 60% water, 40% acetonitrile, both acidified by 0.05% FA.

The calibration of the method has shown excellent linear correlation between PNP or PAP concentration as a function of the surface area of chromatographic peaks, in the range of concentrations below 0.4 mmol/L, typical of experiments with protocol 2 (see Annex A-3).

2.1.4 Protocol 3: on-line UV analysis coupled with HPLC

The aim of the third protocol is to get a quantitative analysis of both PNP and PAP by HPLC directly at the outlet of the microreactor.

2.1.4.1 Experimental set-up with PDA and HPLC

As discussed before, HPLC is an effective quantitative analysis method of PNP and PAP, but with off-line HPLC we have to collect samples at the outlet of microreactor and then carry out HPLC analysis. The delay between reaction and analysis may lose the opportunity to analyze some unstable intermediates. Hence, the experimental set-up with on-line reactor and HPLC equipment (i.e. injection valve, chromatographic column and PDA detector) has been developed as shown in Figure 34.

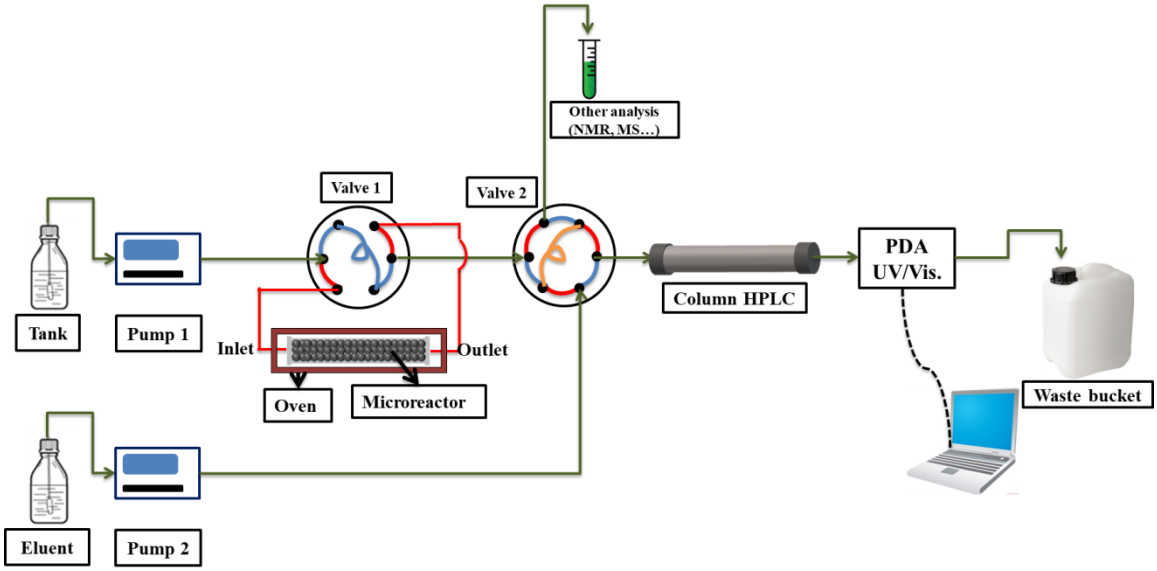

Figure 34 Experimental set-up with PDA and HPLC

The reactants mixture is pumped by Pump 1, and the mobile phase is pumped by Pump 2. Valve 1 directs the reactants mixture either towards the by-pass (blue), or toward the reactor (red), as previously. With Valve 2, in load position (orange), the reaction mixture fills in the injection loop (20µL); in inject position (red), the mixture is injected into the HPLC column and then components are detected in the PDA after separation in the column.

2.1.4.2 Analysis and washing protocols

The full protocol includes the following sequences:

- Analysis of the reactor feed mixture: valve 1 on by-pass, valve 2 in load position, thus the reactant flows in the by-pass and then fills the loop of Valve 2, meanwhile the HPLC column is washed by eluent; Then valve 2 is switched to inject position, for HPLC analysis.
- Reaction sequence: valve 1 on reactor, in order that reaction mixture reacts on the catalyst, and valve 2 in load position. Every 10-20 minutes, the effluent of the reactor is analyzed by manual switch of valve 2 (load/inject).
- After the reaction, the washing process is carried out by distilled water of 40℃ for 1 hour.

2.1.4.3 Calibration and corrections

First calibration curves were obtained with PNP and PAP mixtures in the concentration range 0.04-0.4 mmol/L. As experiments were done with concentrations up to 5 mmol/L, the calibration should be done again. In this new series of calibration solutions indicated in Figure 35, the FA concentration is always 3 times of that of PNP, there is not FA in the PAP solutions. From this figure, we conclude that the PNP and PAP concentrations have a polynomial relation (calculated by OriginPro 8.5 software) with the surface area of chromatographic peaks:

$$C_{PNP} = 1.55 \times 10^{-6} \times S_{PNP}^2 + 0.00253 \times S_{PNP} \ (R^2 = 0.99867) \qquad \textbf{(1)}$$

$$C_{PAP} = 7.68 \times 10^{-6} \times S_{PAP}^2 + 0.00371 \times S_{PAP} (R^2 = 0.9963) \quad \textbf{(2)}$$

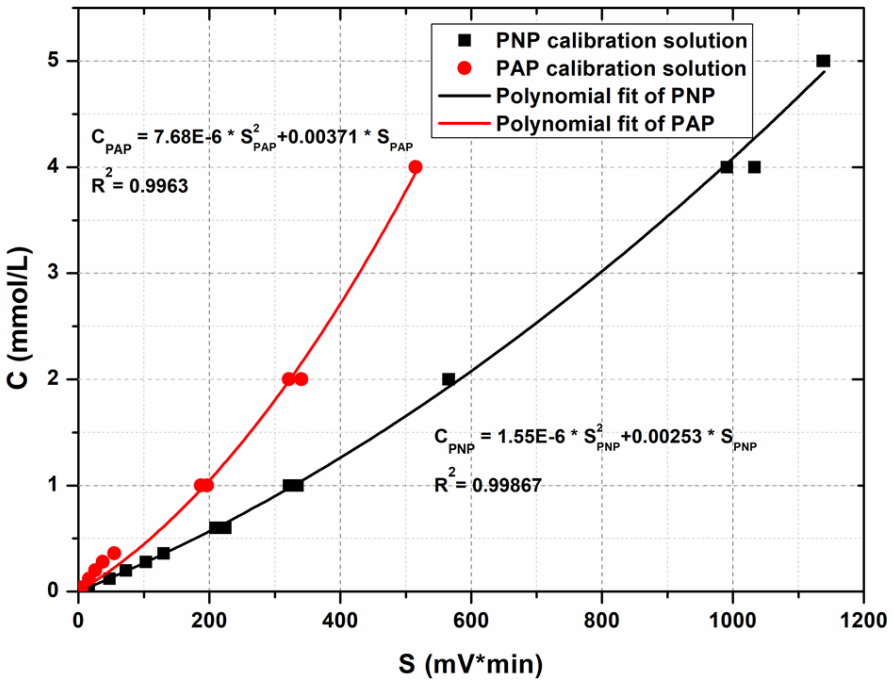

Figure 35 Calibration of PNP and PAP with on-line HPLC: concentration of different calibration solutions and polynomial fit of concentration of PNP and PAP as a function of S (integration of peak)

During the calibration measurements, we observed the effect of pH value on the PAP chromatogram. In order to improve the precision of measurements, the effect of pH, varied either with hydrochloric acid (HCl) or FA, has been investigated (detailed information is in Annex A-4). We noted that HCl and FA have the same effect, and there is a linear relation between PAP surface area and pH : S_{PAP}=9.825×pH+139.29 (R^2=0.93)

As pH is related to logarithm of acid concentration, a direct relation between the surface area of PAP peak (S_{PAP}) and FA concentration of (C_{FA}) was tested for commodity:

$$S_{PAP,FA} = 2.209 \times C_{FA}^2 - 18.98 \times C_{FA} + 202.45 \quad (R^2 = 0.966) \quad \textbf{(3)}$$

Hence, the method of estimating concentrations is:

- Calculation of PNP concentration from calibration equation **(1)**
- Calculation of FA concentration from C_{PNP} material balance: $C_{FA} = C^0_{FA} - 3(C_{PNP}° - C_{PNP})$
- Correction of measured PAP surface area: $S_{PAP,corr} = S_{PAP,mes} \times (\frac{S_{PAP,C_{FA}}}{S_{PAP,0}})$, with $S_{PAP,C_{FA}}$ corresponding to equation **(3)**
- Calculation of PAP concentration C_{PAP} from calibration equation **(2)** with $S_{PAP,corr}$

2.2 Reaction characterization

2.2.1 Identification of products

2.2.1.1 Analysis by nuclear magnetic resonance (NMR)

In order to identify the product of reaction, we utilized D_2O as the solvent of the reaction in microreactor, and then the product of reaction has been analyzed by off-line UV-vis. spectroscopy and ^1H NMR. The conversion measured by off-line UV is 0.938. For comparison, the mixed solution of commercial PNP, FA and PAP (C_{PNP}: C_{FA}: C_{PAP} = 1:3:9) has been prepared and analyzed by ^1H NMR (detailed information of NMR in Annex A-5).

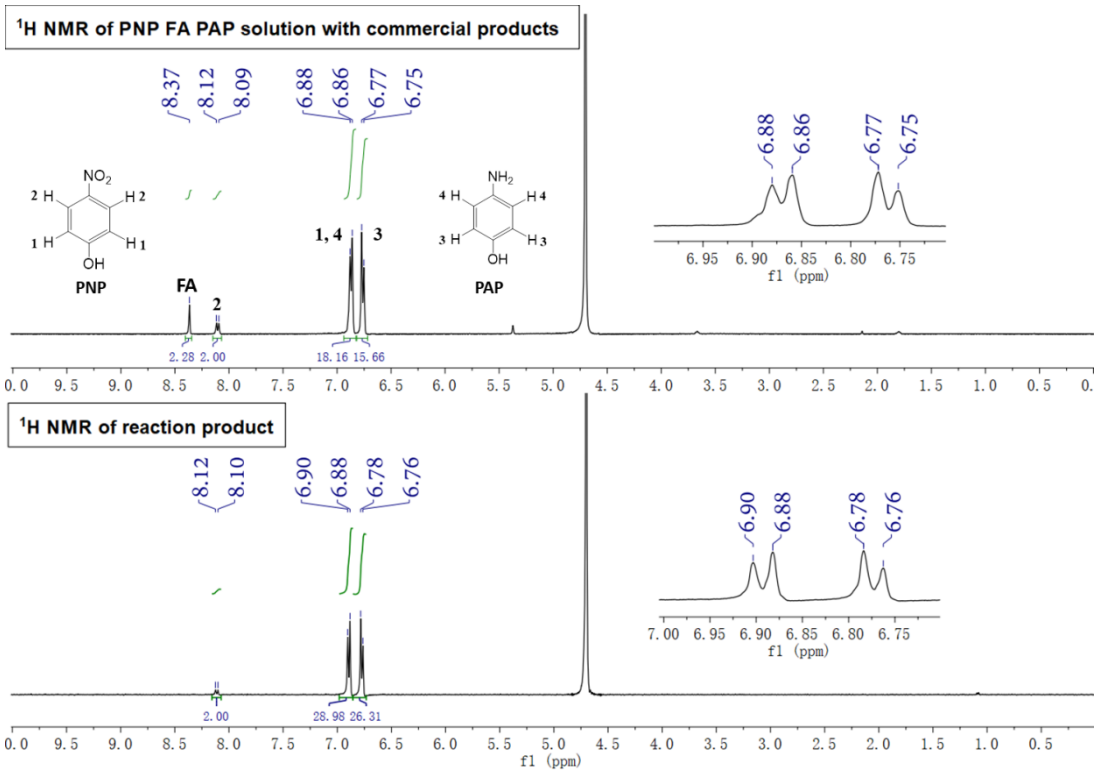

Figure 36 ^1H NMR spectra of PNP, FA and PAP the reference solution (C_{PNP}=1, C_{FA}=3, C_{PAP} =9 mmol/L) and product of reaction (condition: C_{PNP}^0=10 mmol/L, C_{FA}^0=30 mmol/L, T=30°C, Q=1mL/min calculated concentrations : C_{PNP}=0.6, C_{FA}=1.8, C_{PAP} =9.4 mmol/L).

As we can see from Figure 36, only PNP and PAP are visible on the reaction product spectra. The FA has disappeared during the reaction, perhaps because of proton exchange with D_2O. RMN integration confirms exactly the PNP conversion determined by UV.

2.2.1.2 Analysis by mass spectrometry (MS)

The MS analysis (3100 Mass Detector, WATERS) has been utilized to confirm the product of reaction and to identify the intermediate I250. As we can see in Figure 37, analysis with ES- mode of a reaction mixture whose PNP conversion measured by UV is 61% exhibits only the peak at m/z = 109 corresponding to PAP produced and the peak at m/z = 138 corresponding to residual PNP.

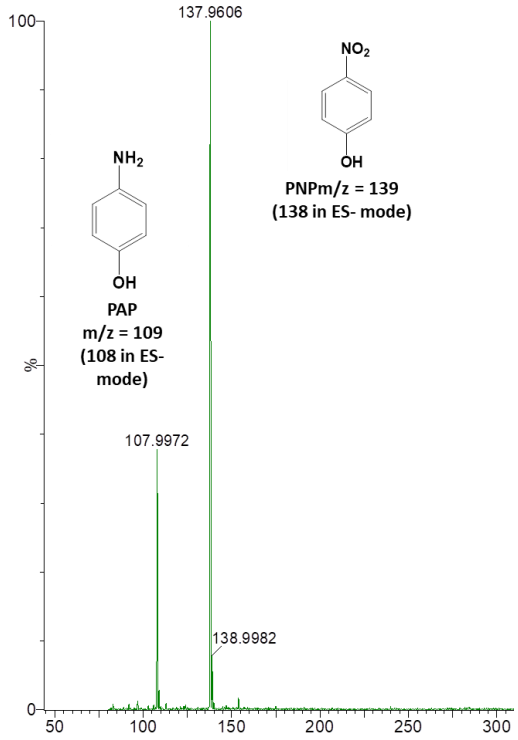

Figure 37 MS analysis (ES-) of reaction product. Reaction condition: C_{PNP}^0=0.5 mmol/L, C_{FA}^0=1.5 mmol/L, T=30°C, Q = 1mL/min, Conversion X=0.61(measured by off-line UV).

The evolution of PAP and PNP concentrations in the reactor effluent has also been observed by MS analysis. 1 mL-Samples of product are collected at 10-12 min, 23-25 min and 44-46 min after the beginning of the reaction sequence, and then analyzed by MS in ES+ and ES- mode. Figure 38 shows that the peak corresponding to PNP decreases while the peak corresponding to PAP increases simultaneously.

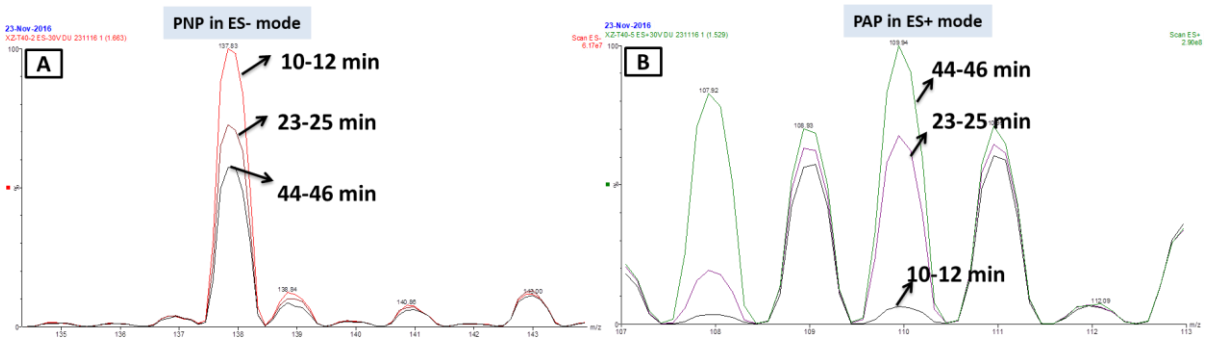

Figure 38 Change of PNP and PAP in the product of reaction analyzed by MS.

Reaction condition: C_{PNP}^0=0.5 mmol/L, C_{FA}^0=3 mmol/L, T=25°C, Q = 0.5mL/min

2.2.2 Comparison between batch and continuous conditions

The reaction has also been investigated in a batch reactor in order to get a better insight on the course of the reaction and on possible by-products. Two batch experiments at different initial concentrations are compared with flow experiments, under conditions where the conversion should be the same in both reactors, i.e. with the flow rate values equal to the batch reaction volume divided by the batch reaction time, and with the same local reaction conditions (catalyst amount, concentrations and temperature). Theoretical justifications are presented in chapter 3, section 3.1.2.

The batch set-up consists in a flask, magnetic stirrer and oil heating bath. The aqueous solution of PNP and FA is prepared, degassed and poured into the flask under stirring and heating, then the Pd@Al_2O_3 catalyst is added. The reaction product is analyzed by off-line UV-vis. and NMR. For NMR analysis, the solvent is D_2O.

The turnover frequency (TOF), defined as the turnover number (TON, the moles of substrate converted per the moles of catalyst used) per unit time, quantifies the activity of catalyst and is often used to compare catalyst performances. They are calculated as:

$$TOF_{batch} = V_{batch} \cdot C^0_{PNP} \cdot X_{batch} / (t_{batch} \cdot n_{Pd}),$$

$$TOF_{flow} = Q_{MR} \cdot C^0_{PNP} \cdot X_{MR} / n_{Pd}$$

t_{batch}: time of reaction in batch reactor
V_{batch}: total volume of the reactant
$Q_{MR:}$ flow rate in microreactor
n_{Pd} : moles of palladium in the reactor
C^0_{PNP} : initial concentration of PNP, at time 0 in batch or in the feed of microreactor
X : conversion in batch at time t_{batch} or at the outlet of microreactor

The conditions of the reaction in microreactor and batch reactor are listed in the following table:

Table 4 Comparison of reaction in microreactor and batch reactor (n_{Pd} = 0.3 mmol, T=30°C)

	V_{batch} (mL)	t_{batch} (min)	Q (mL/min)	C^0_{PNP} mmol/L	C^0_{FA} mmol/L	X	TOF (h^{-1})
Batch	20	20	/	10	30	**0.92**	**1.84**
Microreactor	/	/	1			**0.96**	**1.92**
Batch	20	20	/	0.5	1.5	**0.49**	**0.049**
Microreactor	/	/	1			**0.72**	**0.072**

This comparison indicates a slightly better activity of the catalyst in flow reactor, but without precision because of the shape of the spectra. Actually, Figure 39 shows that the products of

reaction differ in batch and flow reactor: at low concentration (Figure 39 (A)), the absorption band around 225 nm is very low in batch, while at high concentration (Figure 39 (B)), a new band at 400 nm appears on the batch spectrum.

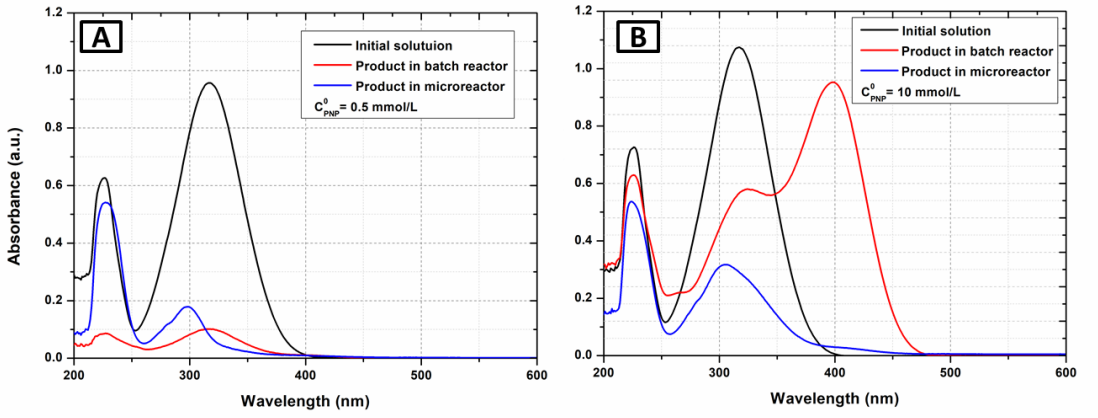

Figure 39 Comparison of UV spectrum of product in batch reactor and in microreactor under different reaction conditions. (A) $C_{PNP}{}^0$=0.5 mmol/L (B) $C_{PNP}{}^0$=10 mmol/L

In order to find the source of the 400 nm-band, in a further experiment, a solution of *p*-aminophenol carbonate is prepared by injection of CO_2 in a PAP solution in D_2O, and then analyzed by NMR. For sole PAP solution in D_2O, there is only one peak at 6.68 ppm (Figure 40(A)). After being mixed with PNP, coupling constant of PAP is $J_{HH}{}^a$=16 Hz (i.e. (6.77ppm - 6.73ppm)*400MHz) as shown in Figure 40 (B). When the CO_2 is injected in the PAP solution, coupling constant of PAP is $J_{HH}{}^b$ = 48Hz (Figure 40 (C)). In the product of batch reactor, coupling constant of PAP is $J_{HH}{}^c$ = 32Hz, which is exactly the average of $J_{HH}{}^a$ and $J_{HH}{}^b$, indicating the PAP in the batch product is partially in a carbonated form. It is probably due to the accumulation in the flask of the CO_2 evolved by the reaction, while in microreactor, the continuous flow remove the product off the reactor and avoid the accumulation of CO_2.

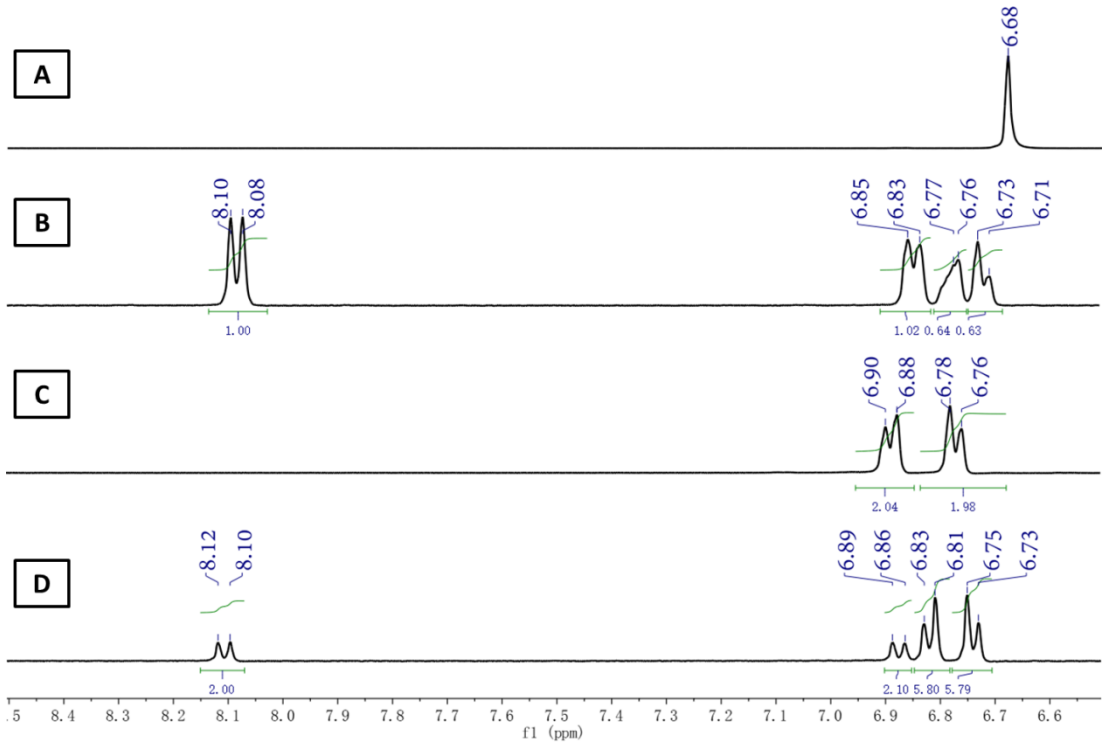

Figure 40 ^{1}H NMR spectra of (A) sole PAP solution (B) mixed solution of PAP and PNP (C) mixed solution of PAP and CO_2 and (D) reaction product in batch reactor with C_{PNP}^{0}=10 mmol/L (solvent D_2O δ=4.7(s,H))

2.2.3 Study of adsorption and desorption phenomena

In order to understand the difference between reaction products in batch and continuous flow reactor, check the effect of adsorption of PNP or PAP in the support on the decrease of UV spectrum, a series of adsorption-desorption tests have been carried out in batch conditions. In a typical adsorption experiment, a given amount of catalyst is contacted with a given volume of PNP or PAP aqueous solution of known concentration. The flask is stirred at temperature controlled with heating bath throughout the duration of the test. 1ml of sample is taken after a given contact time and analyzed by UV spectroscopy. For desorption test, the catalyst is filtered and then desorbed with a given amount of ethanol at 40℃ for 1 hour. The liquid is analyzed by UV and MS.

2.2.3.1 Adsorption of PNP

The adsorption isotherm is used to describe the equilibrium established between the concentration of component adsorbed and the concentration of the component in solution. In our tests, concentration in solution is measured by UV-vis., and adsorbed concentration is calculated by difference with initial solution:

$$q_e = \frac{(C^0 - C_e) \times V}{m_{cat}}$$

where

C_e : Solution concentration (mmol/L)
q_e : Adsorbed solute by adsorbent (mmol/g)
V : volume of solution

The adsorption isotherm of PNP is measured at 30℃ in 1 hour, with 0.05 g catalyst and 10 mL solution in each test, and initial concentration PNP varied from 1 to 25 mmol/L. At first, it was checked that concentration are stable after 1 hour, this indicates that equilibrium is established. More detailed experimental results are listed in Annex A-6 Table A2.

The plot of the results exhibits a linear part at low concentration and a slower augmentation of q_e with C_e at high concentration. This trend characterizes a Langmuir adsorption model:

$$q_e = \frac{Kc_e}{1 + K'c_e}$$

Figure 41 shows that experimental points are in reasonable agreement with the following correlation (calculated by OriginPro 8.5 software) :

$$q_{e,PNP} = 0.037 \times c_{e,PNP}/(1 + 0.04 \times c_{e,PNP})$$

Although the correlation is not very strong (R^2=0.887), the Langmuir model is acceptable to represent PNP adsorption onto Pd@Al_2O_3 catalyst.

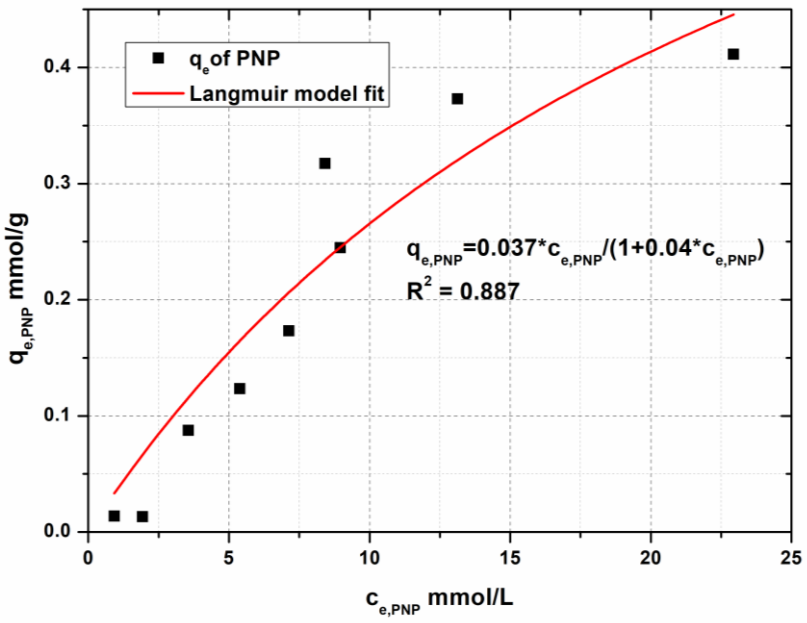

Figure 41 Experimental points and Langmuir model fitting of adsorption equilibria of PNP onto Pd@Al_2O_3 catalyst at 30°C.

2.2.3.2 Adsorption and desorption of PAP

The adsorption experiments of PAP are measured in the same way as for PNP. Detailed experimental results are listed in Annex A-6 Table A3.

The measurements are really dispersed (Figure 42). In spite of the bad experimental precision, it should be noted that in the same concentration range, the PAP adsorption seems to be 10 times higher than PNP adsorption.

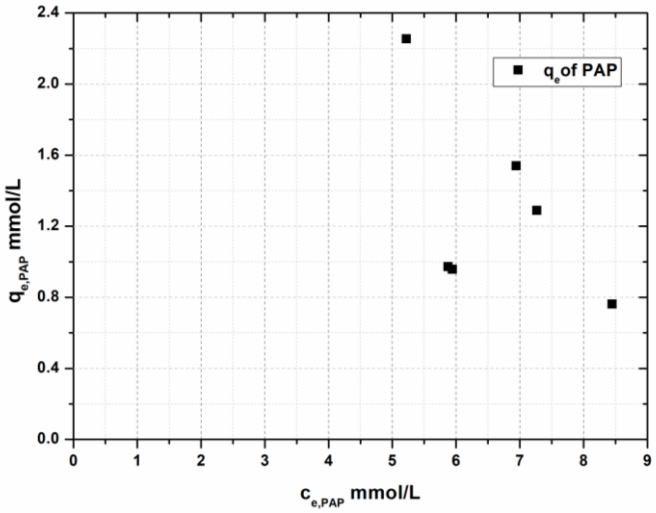

Figure 42 Adsorption equilibria of PAP onto $Pd@Al_2O_3$ catalyst at 30°C, contact time 1h.

With the goal to improve the precision measurements, evolution of adsorption equilibria was measured for a period of 19h and a very significant decreased in the concentration of PAP in the liquid above the catalyst was observed in Figure 43. Two hypotheses might be considered to explain the disappearance of PAP: a reaction of PAP leading to form a solid substance or a precipitation of PAP due to the low solubility. The product after 19h corresponds to an unknown product, which was explored in the following desorption test.

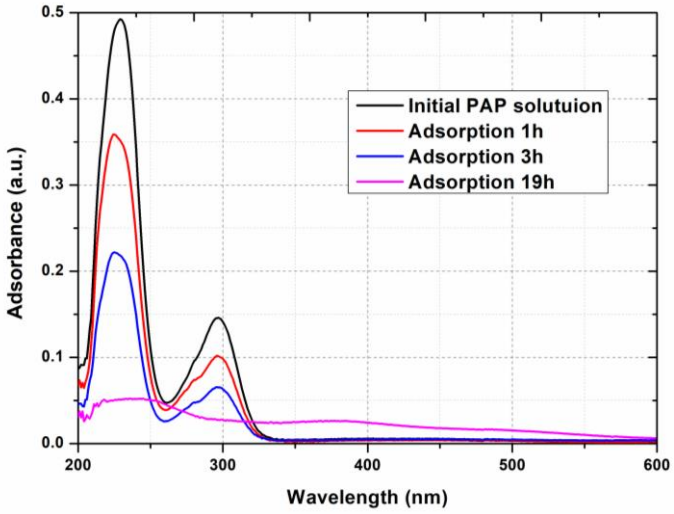

Figure 43 Adsorption of PAP for a longer period (19h)

The UV-vis. analysis of the desorption solution is shown in Figure 44, in comparison with initial solutions. Clearly, adsorption has transformed PAP in another product.

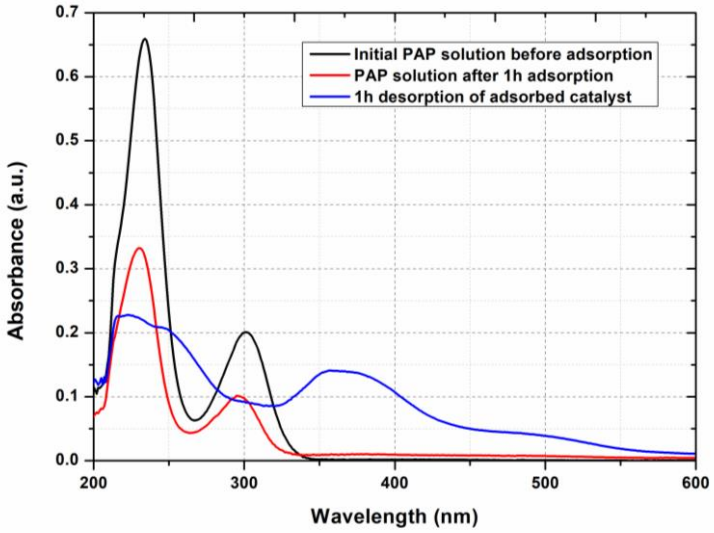

Figure 44 Example of desorption of PAP by UV-vis. analysis (adsorption condition: molar ratio Pd/PAP=0.1, V=1.51ml, C_{PAP}^{0}=10 mmol/L, adsorbed fraction 0.31, desorption with 1.51 mL ethanol)

To obtain further information on this unknown product, the desorption solution of PAP was analyzed by MS in ES+ mode in Figure 45. There are two main peaks at 100 m/z and 322 m/z. The product at 100 m/z perhaps corresponds to cyclohexylamine (**20**), the reduction product of PAP. The product at 322 m/z is supposed to be **21**, which can be obtained from the oxidation of PAP [84]. There is no PAP (110 m/z in ES+ mode) desorbed.

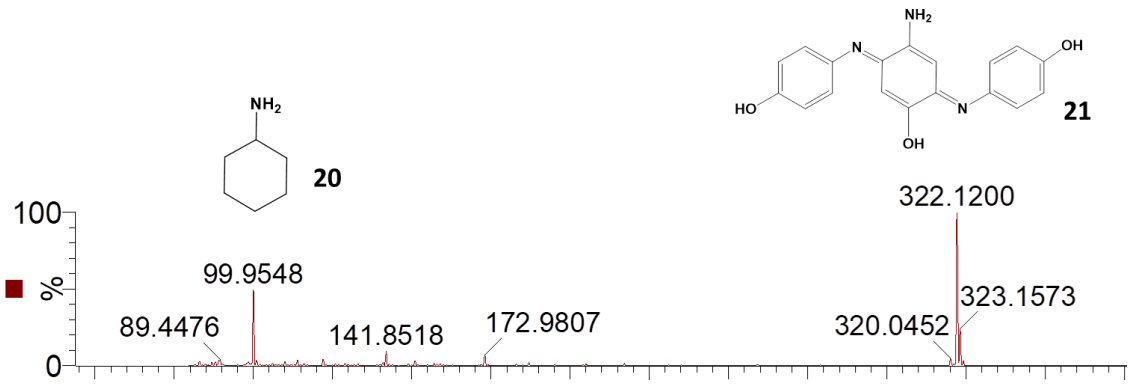

Figure 45 Mass Spectrometry of the supernatant of desorption solution of PAP (ES+ mode)

[84] Hauch Fenger, T.; Bjerre, J.; Bols, M., *Chembiochem* **2009,** *10* (15), 2494-503.

The main conclusion of this part is that off-line UV spectroscopy is not a convenient method to know the composition of a reaction mixture. Hence, in the following part, most of the reported results are measured by HPLC. Other experimental observations may be pointed out:

- The influence of CO_2 on PAP UV-vis spectrum.
- The difference of reaction course in batch and flow catalytic reactor, despite of the predictions of ideal models of reactors.

Along all these experiments, it was also observed that fresh catalyst has specific properties and it should be "aged" by some reaction cycles to give reproducible results.

2.3 Effect of reaction parameters on conversion

2.3.1 Preliminary results

The experimental conditions are varied in the range indicated in Table 5, in order to establish the reaction rate expression. Before this, some preliminary check-in were made.

Table 5 Range of experimental conditions for flow reaction with commercial $Pd@Al_2O_3$ catalyst

Symbol	Parameter	Unit	Dimension
Q	Flow rate	mL/min	0.1– 4
T	Temperature	°C	30 – 60
$\mathbf{C_{PNP}^{\circ}}$	Initial concentration of *p*-nitrophenol	mmol/L	0.1– 10
$\mathbf{C_{FA}^{\circ}}$	Initial concentration of formic acid	mmol/L	(1.5~6) × C_{PNP}°

a- As the reaction produces 3 mol of CO_2 per mol of PNP reacted, CO_2 bubbles were expected in first experiments, but never observed. Actually, the solubility of CO_2 under 1 bar is 38.4 mmol/L at 20℃ and 28.6 mmol/L at 30℃.[85] On the other hand, the maximum concentration expected in our experimental range is 30 mmol/L in case of total conversion of 10 mmol/L of PNP. This indicates that CO_2 evolved by the reaction remains dissolved in the reaction mixture.

b- As reaction onto the catalyst sites involves mass transfer from bulk liquid to the surface of the catalyst particle and then diffusion inside the porous structure up to the catalytic sites, the mass transfer criteria should be evaluated in order to know if reactant transport slow down the reaction process. Determination of rate-controlling step is particularly important in case of kinetics determination. Mass transfer criteria are calculated in Annex A-7.

[85] Don, W. G.; Robert, H. P., *Perry's Chemical Engineers' Handbook, SEVENTH Edition*, McGraw Hill: 2008; pp 2-125.

Mears external mass transfer criterion is in the 10^{-8} – 10^{-9} range, indicating that mass transfer from bulk to particle surface in much more faster than chemical reaction. For internal mass transfer, the Weisz-Prater criterion is in the 10^{-7} – 10^{-9} range, signifying that the influence of internal pore diffusion is also negligible.

c- As reported by Maschmeyer[86], stainless steel could catalyze hydrogenation reactions with formic acid. In order to investigate the effect of the stainless steel wall on the model reaction, sand has been filled into the tube to replace the catalyst. A series of tests with different reaction conditions have been carried out as summarized in Table 6.

Table 6 Effect of tube wall

C_{PNP}°, mmol/L	C_{FA}°, mmol/L	T, °C	Q, mL/mn	X
0,5	1,5	**30**	1	**0,019**
10	30			**0,012**
		50		**0,088**
		70		**0,064**
			0,5	**0,119**

In a very intense reaction condition (high initial concentration, high temperature and low flow rate), the conversion is about 12%. However, our experimental range never reaches so strong reaction conditions, therefore the effect of stainless steel wall can be ignored.

In summary, the bulk diffusion and the internal pore diffusion can be neglected; the inner wall of tube has no effect on the catalytic reaction; the CO_2 produced are all dissolved therefore no bubbles can be produced.

2.3.2 Influence of temperature and flow rate on the PNP conversion

Influence of temperature and flow rate on the conversion was studied. The results are summarized in the following Figure 46. The repeatability has been verified.

[86] Fábos, V.; Yuen Alexander, K. L.; Masters Anthony, F.; Maschmeyer, T., *Chemistry – An Asian Journal* **2012,** *7* (11), 2629-2637.

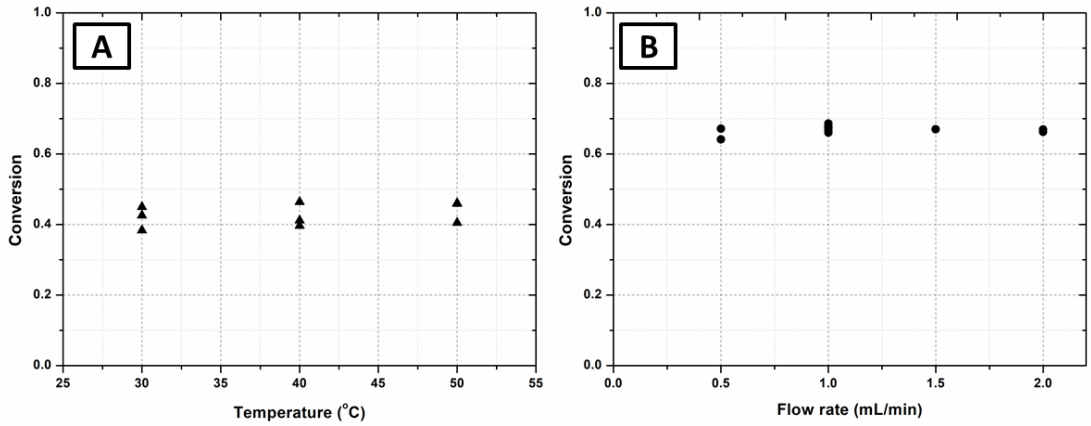

Figure 46 Effect of temperature and flow rate on the conversion.
(A) Effect of temperature (condition: C_{PNP}^0=0.4 mmol/L, C_{FA}^0=1.2 mmol/L, Q=0.5 mL/min)
(B) Effect of flow rate (condition: C_{PNP}^0=0.6 mmol/L, C_{FA}^0=1.8 mmol/L, T=40°C)

It indicates that the temperature and flow rate do not have effect on the conversion of PNP in packed-bed microreactor.

2.3.3 Influence of the concentrations of reactants

The effect of initial concentration of PNP and FA has been investigated with all three protocols, that give the same pattern, i.e. a strong effect of initial concentration on the conversion, as shown in Figure 47.

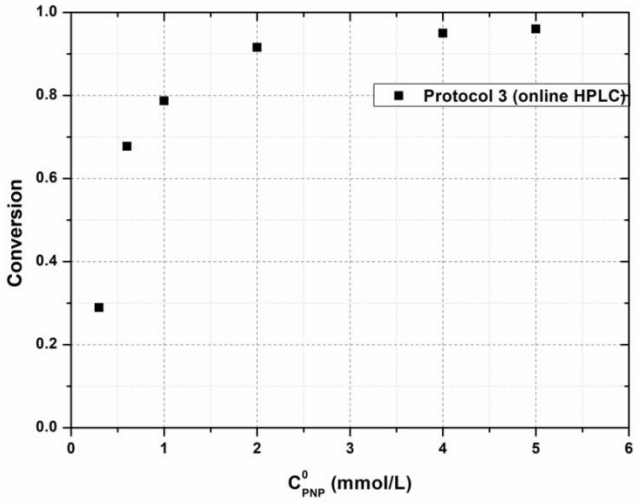

Figure 47 Effect of initial concentration on the conversion. Condition: protocol 3: C_{PNP}^0=0.3-5 mmol/L, C_{FA}^0/C_{PNP}^0=3, T=40°C, Q=1mL/min)

The strong dependence of PNP conversion on C_{PNP}^0 indicates a reaction order higher than 1. The kinetic study of the reaction is discussed in part 3.1.2.

The quantitative analysis of PAP has been realized by on-line HPLC. Thus the material balance of the reaction is calculated. The diviation between the quantity of initial reactant and final

products is calculated by (C_{PNP}^{f} + C_{PAP}^{f} - C_{PNP}^{0})/C_{PNP}^{0}, where C_{PNP}^{0} is the concentration in the reactor feed and C_{PNP}^{f} and C_{PAP}^{f} are the concentrations of PNP and PAP at the exit. The average deviation on the material balance is -4.0 %, it can be considered to be in the experimental error range.

2.4 Dynamic studies

As explained in the first part of this chapter, as soon as we observed the dependence of measurements on the history of the catalyst leading to a lack of reproducibility of experiments, we implement a protocol involving alternation of reaction sequences and catalyst washing sequences. This protocol induces a transient behavior of the catalyst during the first period of the reaction sequences.

2.4.1 Experimental observations

2.4.1.1 Concentration profiles

On-line analysis, either with UV-vis. PDA (protocol 2) or with HPLC (protocol 3) allows to observe the variations of composition of the reaction mixture flowing out of the reactor. The appearance and disappearance of a component, we call it intermediate I250, have been clearly detected as shown in Figure 48 (A).

Different experiments were performed with protocol 2 (PDA on-line analysis), in order to relate the amount of I250 to experimental conditions. This amount is roughly estimated from the surface area of the 250 nm UV-band. It is observed that the amount of I250 flowing out of the reactor is the same when the initial concentration of PNP or the flow rates are varied (figures and data in Annex A-8). This could indicate that this amount is related to the catalyst surface area, unchanged during tests.

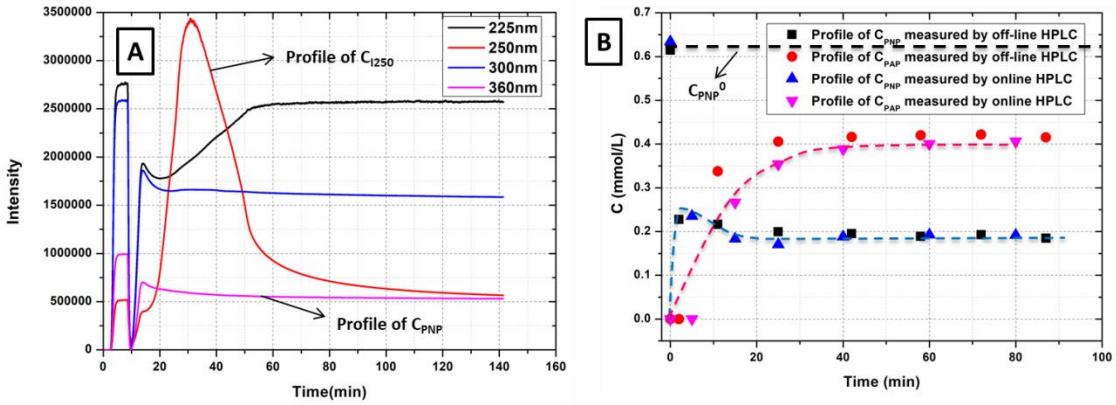

Figure 48 Concentration profile detected by

(A) Protocol 2 with on-line PDA UV-vis. (condition of example: C_{PNP}^{0}= 0.4 mmol/L, C_{FA}^{0} = 1.2 mmol/L, T = 40°C, Q = 0.5 mL/min)

(B) Protocol 3 with off-line and on-line HPLC analysis (condition of example: C_{PNP}^{0}= 0.6 mmol/L, C_{FA}^{0} = 1.8 mmol/L, T = 40°C, Q = 1 mL/min)

Both off-line and on-line HPLC analysis confirms the profiles of PNP and PAP concentrations: as we can see from Figure 48 (B), at the outlet of reactor, the concentration of PNP exhibits a shoulder at the beginning and then decreased continuously and finally stabilized; meanwhile the concentration of PAP increased and reaches the stationary value after a long time, as compared to residence time.

Actually, the period of unsteady-state behavior of a flow-reactor is normally in the range of the residence time, i.e. the time interval necessary to fill in the reactor with reactants mixture. In homogeneous reactor, it is simply the fluid volume divided by the flow rate. In our microreactor, this time is about 20 s at a 1 mL/min flow rate. With heterogeneous catalyst, a certain amount of reacting mixture is stored by adsorption onto the catalyst surface (support and sites). From adsorption experiments, the time on feed necessary to saturate the catalyst with PNP is roughly estimated about 15-20 min at 1 mL/min flow rate[87].

Several attempts were made to observe I250. With on-line HPLC analysis, we can also observe the presence of I250, but not with off-line HPLC. Figure 49 shows the series of chromatograms measured directly at the exit of the reactor: the first peak (purple) corresponding to PAP increases, while the last peak (blue) of PNP decreases. Moreover, at the time corresponding to maximum of 250 nm-UV band attributed to I250, a HPLC peak (red) appears between PAP and PNP peaks, then disappeared quickly. This peak is attributed to the intermediate I250.

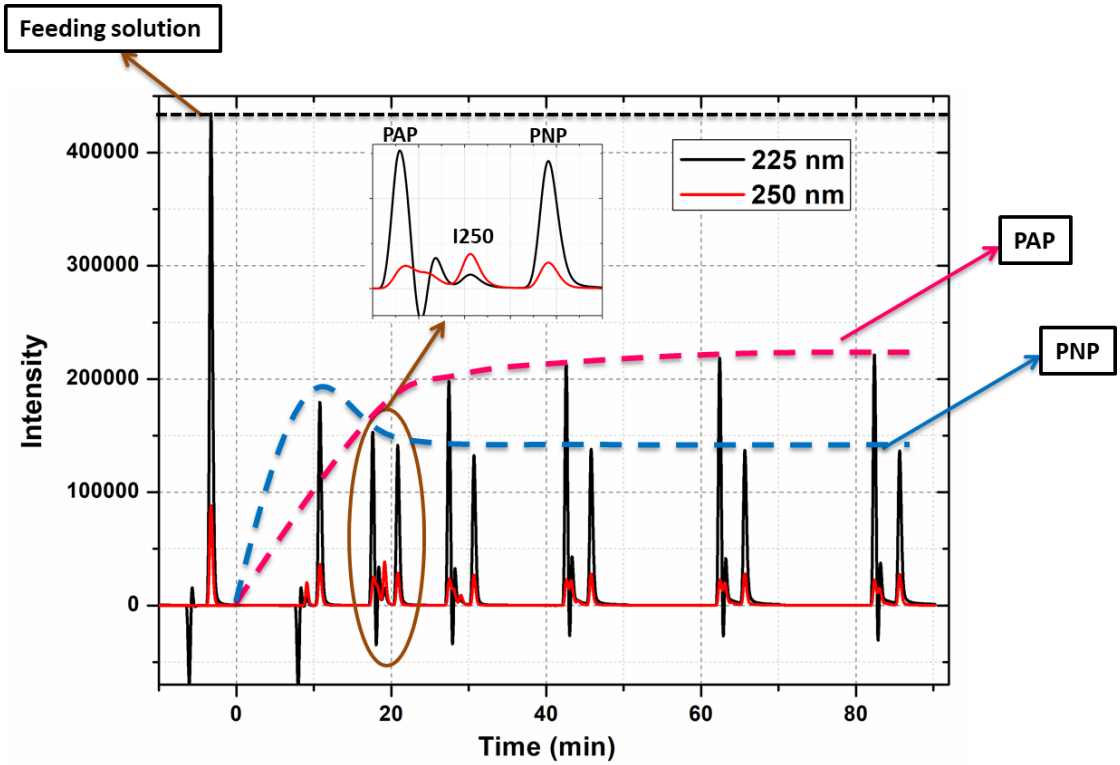

Figure 49 Investigation with on-line HPLC analysis before integration of peak (condition of example: C_{PNP}^0= 0.6 mmol/L, C_{FA}^0 = 1.8 mmol/L, T = 40°C, Q = 1 mL/min)

[87] Method of calculation: at saturation of the catalyst surface, adsorbed concentration q is in equilibrium with feed concentration. The amount of PNP adsorbed ($q \cdot m_{cat}$) is brought by the feed flow ($Q \cdot C_{PNP}^{\circ} \cdot \Delta t$).

This peak was not detected with traditional off-line HPLC which involves a step of collection of product, i.e. a delay between reaction and analysis. This could indicate that the intermediate I250 is quite unstable in air or under light, which means it could be easily oxidized or photo-decomposed.

2.4.1.2 Effect of formic acid on intermediate amount

It was noted that neither C_{PNP}^0 nor Q have an effect on the amount of I250 flowing out of the reactor. When the initial concentration of FA is varied, with on-line PDA UV analysis, the variation of I250 profile is observed as shown in Figure 50.

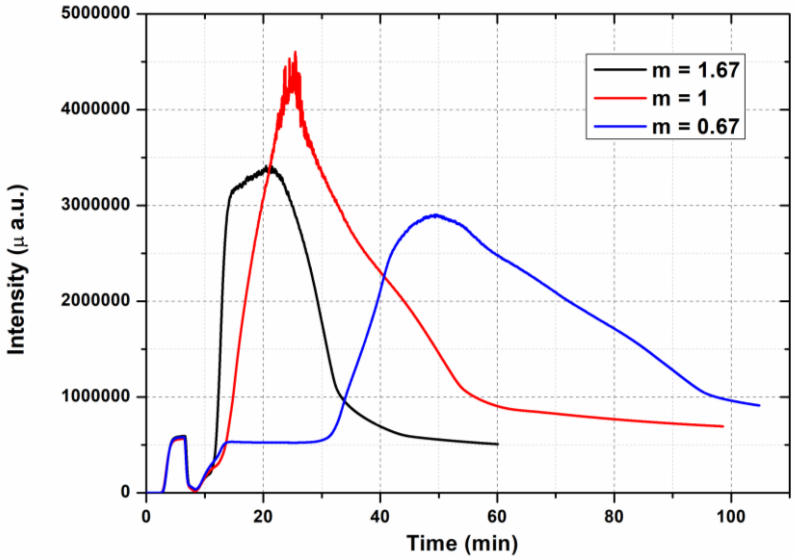

Figure 50 Effect of m = $C_{FA}^0/3\ C_{PNP}^0$ on the I250 profile (C_{PNP}^0 = 0.5 mmol/L, T=25°C, Q=0.5 mL/min)

When initial FA concentration decreases, the I250 outlet is delayed and spread during a longer time, while the quantity of I250 increases as indicated by the surface area under the I250 profile (62.2 when m=2.67, 104.2 when m=1, 138.8 when m=0.67). The volume of FA pumped before the appearance of I250 is approximately constant. It might demonstrate that the I250 desorbed as soon as enough FA has been introduced, which means it exists a faster route that could utilize the catalytic site. It is also observed that the concentration of I250 is approximately correlated to $1/C_{FA}^0$ (detailed listed in Annex A-9).

Based on these observations, we could conclude that there two reaction routes exist: one could be the direct route discussed in 1.2.1; the other one could be promoted by the deficit of FA, in which I250 is produced and transformed to PAP.

2.4.2 Attempts for the identification of intermediate product

2.4.2.1 Test of possible intermediate according to plausible mechanism

According to the plausible mechanism discussed in 1.2.1 in Figure 25, the possible intermediates are *p*-nitrosophenol (PNS), *p*-hydroxylaminophenol (PHx), 4,4'-Azoxydiphenol (PAXD), 4,4'-Azo diphenol (PAD) 4,4'-hydrazobisphenol (PHB) or *p*-Benzoquinone imine (PBQI). On considering the possible photosensitivity or instability of I250, we studied PNS, PHx , PAD and PBQI in this part.

PNS is a commercial product. PAD is successfully synthetized by modifying a method described in literature [88] (detailed synthesis information in Annex A-10). PHx is not commercial and there is not any synthesis method published, so that we modified the protocol of synthesis of hydroxylaminobenzene from nitrobenzene [89]. But we failed to synthetize PHx : the final product is the PAP according to the ^{1}H NMR analysis. Similar to PHx, PBQI is not commercial either and cannot be synthesized steadily[90].

As a first element of comparison, the UV-spectra of PNS and PAD, shown on Figure 51, do not exhibit a hug adsorption band around 250 nm.

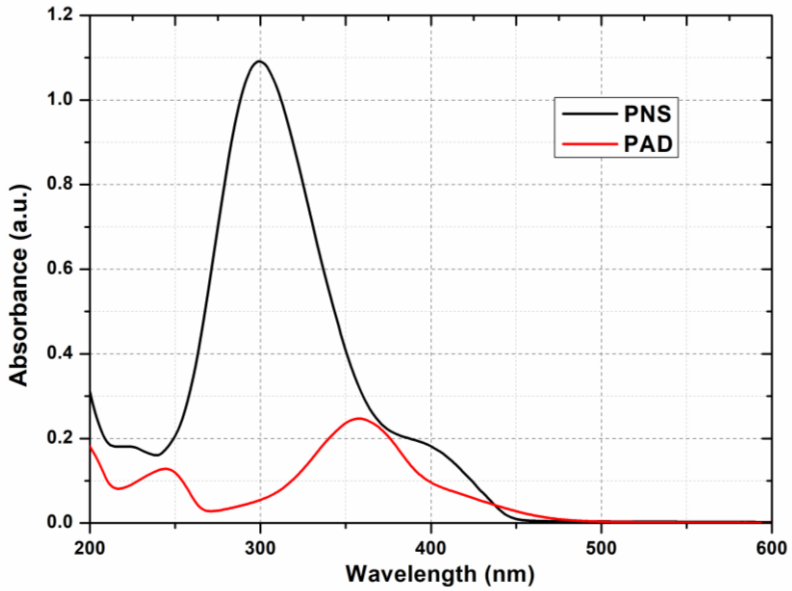

Figure 51 UV-vis. spectrum of PNS and PAD

In order to identify intermediates, analysis by NMR and MS of samples taken at the outlet of the reactor at regular time intervals are compared to analysis of PNS and PAD. The conditions of comparison are the following. An experiment with protocol 2 is performed, in order to monitor the PDA profiles, the experimental condition is: C_{PNP}^{0}=0.5 mmol/L, C_{FA}^{0}=3mmol/L, Q=0.5mL/min,

[88] Xiao, R.; Zhou, L.; Dong, Z.; Gao, Y.; Liu, J., *Chinese Journal of Chemistry* **2014,** *32* (1), 37-43.
[89] (a) Krüger, S.; Meier, C., *European Journal of Organic Chemistry* **2013,** *2013* (6), 1158-1169. (b) Meier, C.; Böge, N.; Krüger, S.; Schröder, M., *Synthesis* **2007,** *2007* (24), 3907-3914.
[90] Lerner, L., *Journal of Physical Chemistry A* **2011,** *115* (35), 9901-9910.

T=25°C. After the reaction begins, the samples are collected each 10-12 minutes (Figure 52) and analyzed by MS in order to acquire the variation of the constitution of the product. The time of collection is 2 minutes. Another similar experiment is carried out with D_2O solvent, so that the samples can be analyzed by ^1H NMR. As we can see in Figure 52, the curve of I250 reaches its maximum in the sample taken at 25 minutes, which is then compared with PNS and PAD.

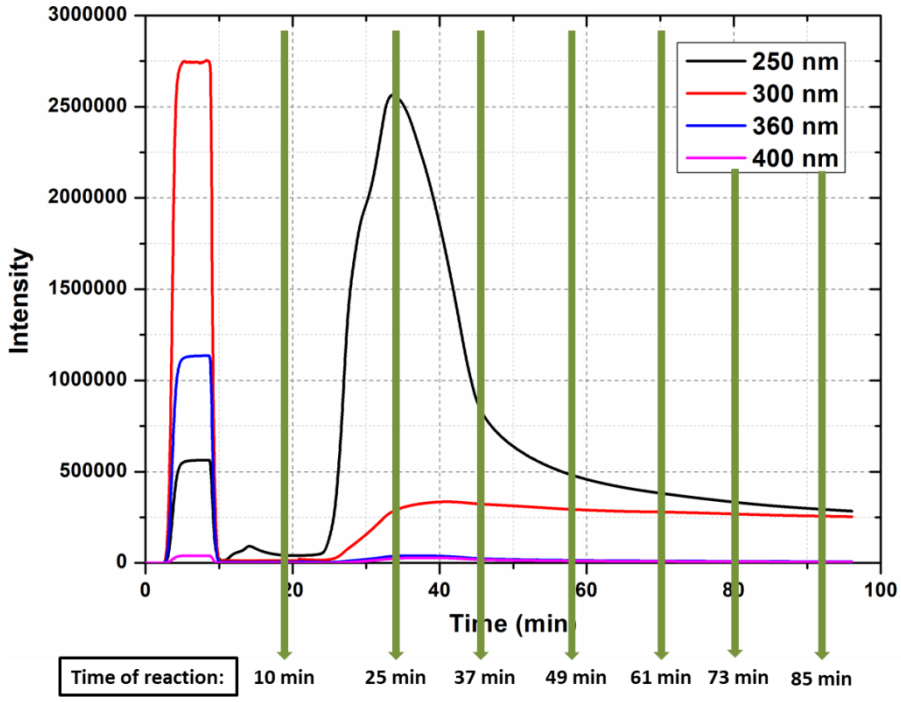

Figure 52 Samples collected at different reaction time then analyzed by MS and ^1H NMR

(a) Results of MS analysis

The MS analysis was performed in both ES- and ES+ mode. It is worth noting that when there are several components in a mixture, ionization of one species may be inhibited for the benefit of another one, more easily ionizable. Hence, the result is not quantitative but only indicative of the mixture composition. So we look for peaks whose intensity is the highest in the sample taken at 23-25 min, in which the concentration of I250 should be the maximum. As the precision is not good, both ES- and ES+ modes are presented on the same figure, with normed values because ES+ spectra are more intense.

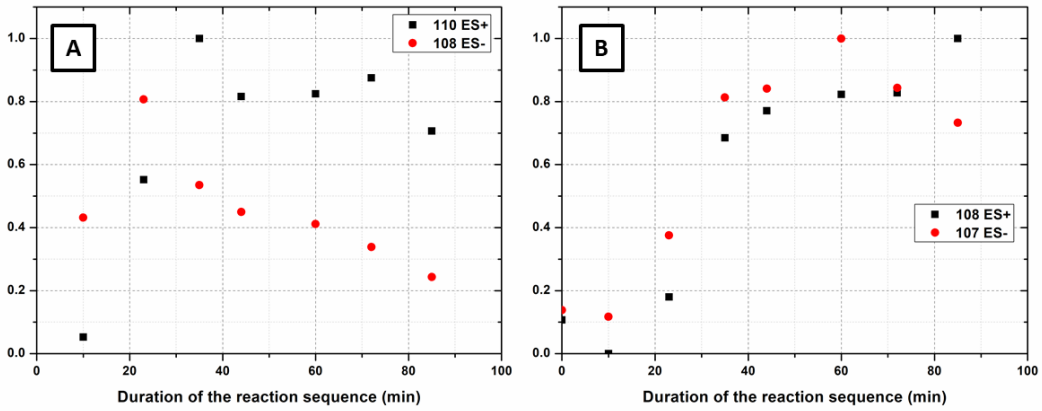

Figure 53 Relative intensity of MS peak of samples taken at the outlet of the reactor at different time. (A) Peaks corresponding to PAP (m/z= 108 in ES- mode, m/z= 110 in ES+ mode). (B) Peaks whose intensity changes in time (m/z= 107 in ES- mode, m/z= 108 in ES+ mode).

Only the peak at m/z=108 in ES- mode is maximum in the sample containing I250, it corresponds to PAP, or to an adduct of PAP (Figure 53 (A)). Besides this one, only 2 peaks increase significantly in time: m/z=108 in ES+ mode (molar mass 107 g/mol, same as PBQI), and m/z= 107 in ES- mode (molar mass 108 g/mol). Their variation is correlated with PAP variation. No peak corresponding to ionization of PNS (123 g/mol) or PAD (214 g/mol) has been detected.

(b) Results of NMR analysis

The reaction product with maximum I250 concentration, sampled at 25 minutes, is analyzed by ^{1}H NMR and compared with PNS and PAD. As shown on Figure 54, in the sample of reaction containing I250, PNP, FA and PAP are well identified, and there are several small peaks with δ between 6.89 and 7.22 which could corresponds to I250. The repeatability of these peaks is verified by repeating the same experiment. However, the ^{1}H NMR spectra of PNS and PAD do not match with these peaks detected.

Hence, UV-spectra as well as NMR indicate that I250 is neither PAD nor PNS.

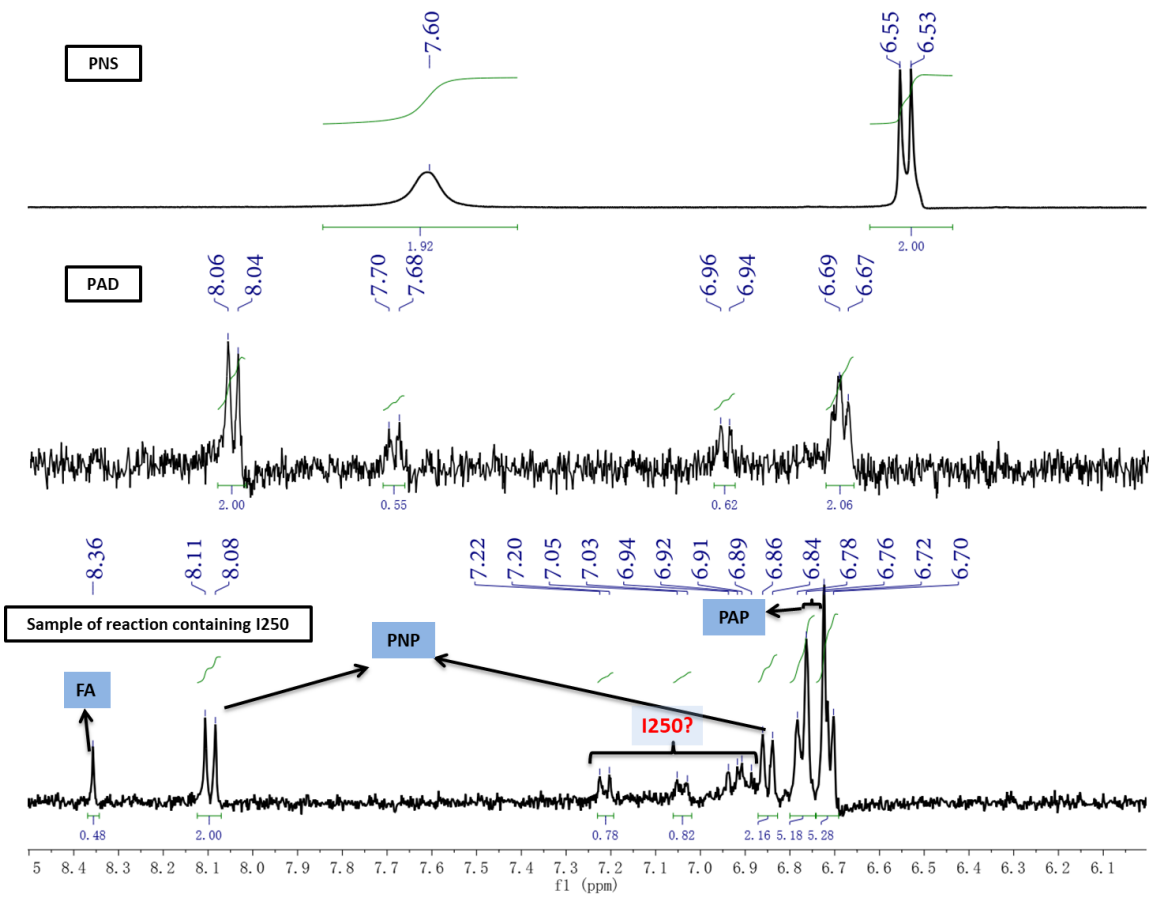

Figure 54 Comparison of ^{1}H NMR of PNS, PAD with the sample containing I250.

2.4.2.2 Evaluation of stability of intermediate

Several observations question the I250 stability : the peak corresponding to I250 is visible with on-line HPLC, but not with off-line HPLC ; with RMN as well as with MS, the signal that could be attributed to I250 is very weak. To evaluate the stability of I250, a special experiment was made with on-line PDA. The normal reaction is started according to protocol 2, and when I250 reaches its maximum, the pump is stopped and reaction mixture containing I250 still remains in the UV cell. We continue to store the variation of I250 in the UV cell till to the stabilization.

The instability of I250 is clearly demonstrated by Figure 55: after the stop of flow, the curve of 250 nm decreases rapidly, and the half-life time is just about 2 minutes. It explains that only traces of I250 are detected by methods involving a delay between reaction and analysis.

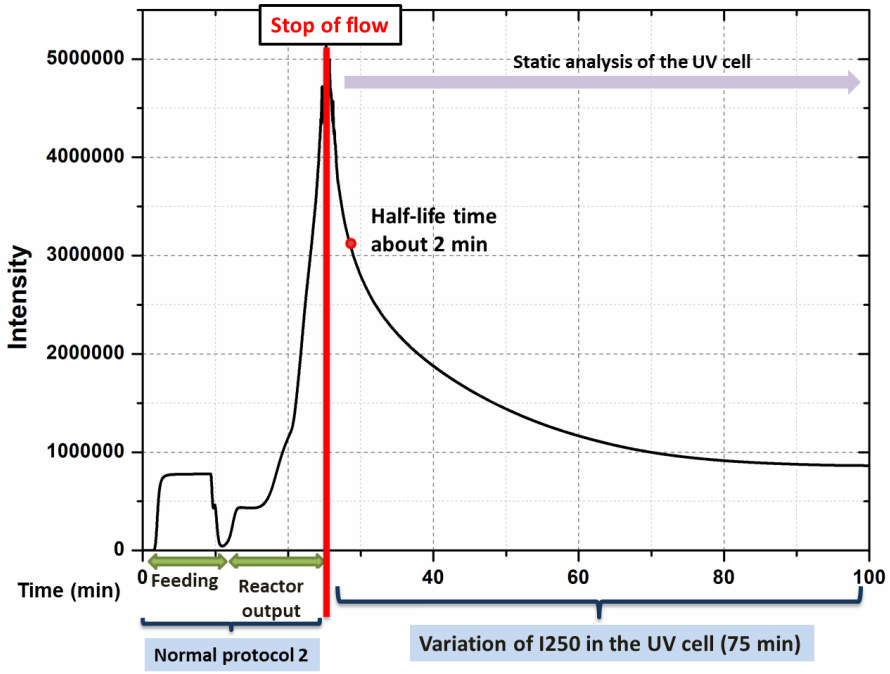

Figure 55 Evaluation of stability of I250 in the reaction media without catalyst measure by UV-vis. PDA at 250 nm (condition: C_{PNP}^0 = 0.6 mmol/L, C_{FA}^0 = 1.8 mmol/L, T = 40°C, Q = 1 mL/min)

The UV spectrum of final product of the stability test was compared with that of the final product of a normal reaction under the same condition in Figure 56. The product of decomposition of I250 has the same UV profile as the usual product of the reaction (i.e. PAP), which means I250 can be transformed in to PAP without catalyst.

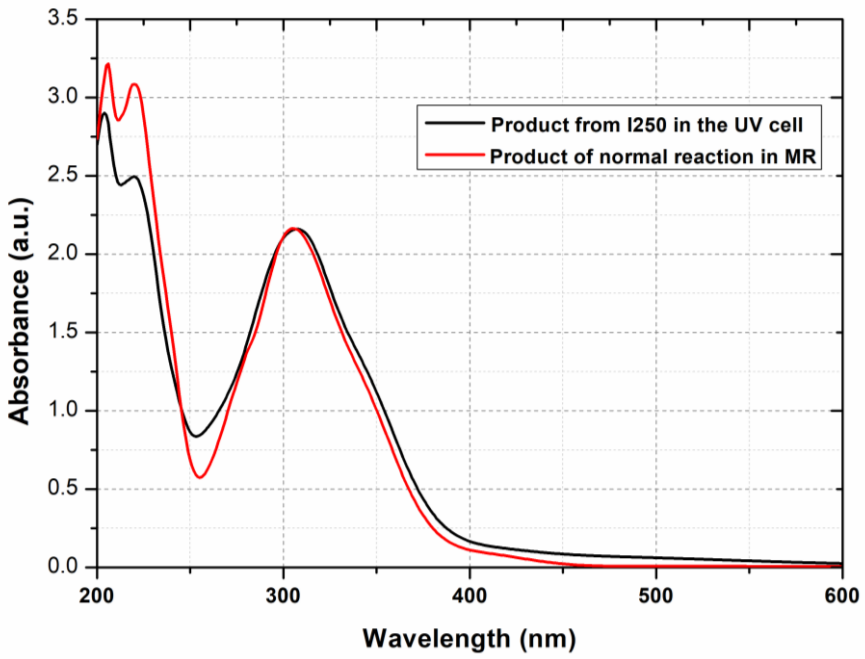

Figure 56 Comparison of final product from the stability test of I250 in the UV cell and THE usual product of the reaction in the same condition (condition: C_{PNP}^0 = 0.6 mmol/L, C_{FA}^0 = 1.8 mmol/L, T = 40°C, Q = 1 mL/min)

2.5 Conclusion

In this part, three protocols differing by the analysis methods are presented : with off-line UV analysis, the set-up is quite simple and the conversion of PNP can be calculated, but the quantitative analysis of PAP cannot be carried out; with on-line UV analysis, the variation of composition of the reaction mixture can be easily detected, for example the appearance and diminution of intermediate I250, but the quantitative analysis of PAP is still a problem; with on-line HPLC analysis, the quantitative analysis of both PNP and PAP can be realized, so that we can get the time-concentration profile of these components. Compared with traditional HPLC analysis, this protocol eliminates the step of collection of products, and can allow the detection of quite unstable intermediates such as I250.

The main reaction product, PAP, is confirmed by NMR and MS. The comparison between batch reactor and microreactor demonstrate that the microreactor limits the adsorption phenomena and formation of byproduct by successive reaction, because of its continuous-flow mode.

The effect of temperature and flow rate is not demonstrated in our study, but the strong effect of initial concentration of reactants has been found, which could indicate a second-order reaction kinetic.

Several possible intermediates PNP, PAD and PHx according to plausible mechanism have been investigated, but neither PNP nor PAD does not match with the nature of I250 according to the UV, MS and NMR analysis, and PHx and PBQI are not commercial and could not be synthetized. The I250 is quite unstable, but it could be transformed to the PAP without catalyst. Hence, we suppose that I250 is PBQI, by the following reasons:
a) PBQI is not stable and can generate PAP quickly.[91] Based on the mechanism proposed by Hart [82] and Bols [84], the reaction mechanism proposed in Figure 25 could be modified as follows:

[91] Conant, J. B.; Pratt, M. F., *Journal of the American Chemical Society* **1926,** *48* (12), 3178-3192.

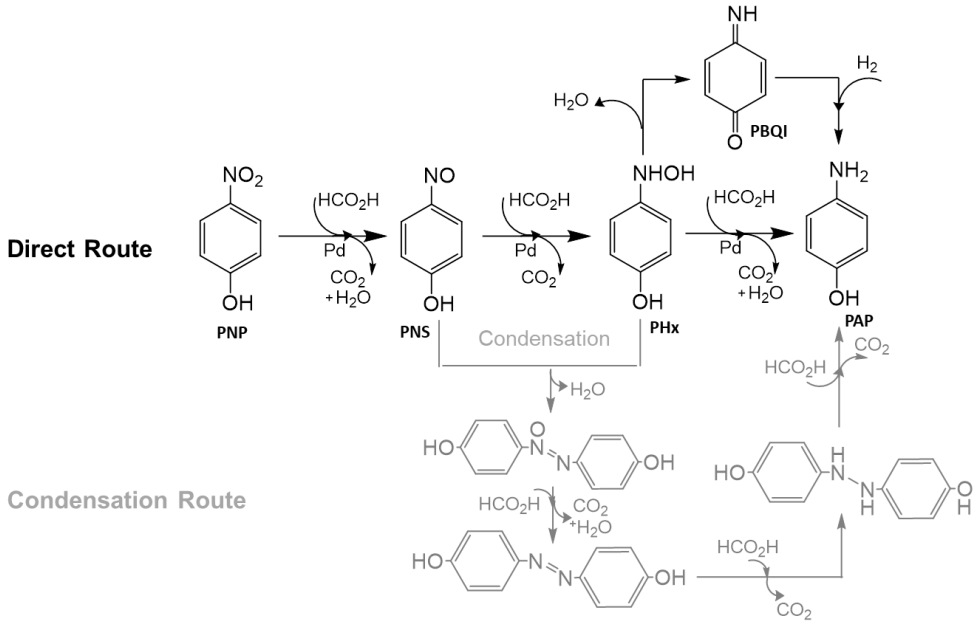

Figure 57 Modified mechanism of hydrogenation of *p*-nitrophenol in formic acid with Pd (black: proposed mechanism; grey: academic mechanism [77(b)])

It might exist two reaction routes to product PAP. In the upper route, the PHx could transform to PBQI with the dehydration, and then PBQI could be reduced to PAP with the hydrogen from the decomposed FA in the solution. This route could be favored with deficit of FA. The lower route is the direct route, where PHx could be directly reduced to PAP. This hypothesis of mechanism is also supported by the experimental observations in section 2.4.1.2.

b) The mass of PBQI is 107 m/z, which has been detected in the MS analysis in ES+ mode

c) The product **21** observed in adsorption and desorption test of PAP could be a final product of oxidation of PBQI [84]. It indicates that PBQI might exist during the reaction process.

d) In the former researches discussed, Parida[60(b)] and Saleh[75] have proposed the mechanism including PBQI as the intermediate. Saleh has observed a change of color during the reduction of PNP by hydrazine and attributed green color to PBQI. However, we have also observed the change of color of the product: the yellow color of PNP aqueous solution became colorless after the addition of FA; during the reaction, when the peak of I250 was intense, the color of product changed to blue purple; after the stable state of reaction arrived, the color was brownness (attributed to PAP). As we know that the green color can obtained by mixing yellow and blue, therefore the green color observed by Saleh could be the yellow color of PNP mixed by the color of PBQI, i.e. I250 (blue color in our investigations).

Further investigations are needed to confirm these hypotheses.

Chapter 3 - Modelisation of the reaction in packed-bed microreactor with heterogeneous catalyst

The reactor with solid catalyst can be classified as a fixed bed catalytic reactor. Models of such reactors range from the very simple one to some very sophisticated, depending on the type of convective heat and mass transfer, and on the objective of the modeling. We are interested in two objectives: (i) to find a model that mimics the dynamic behavior experimentally observed, in order to understand what happens onto the catalyst; (ii) to establish a kinetic model of the reaction under stationary conditions. For both objectives, the influence of flow pattern on the PNP conversion is much lower than that of reaction kinetics. Hence, the basic one-dimensional model, i.e. the ideal plug flow model, is adopted.

3.1 Ideal models of reactors and methods of calculation

3.1.1 Steady-state plug flow model

The ideal plug-flow model assumes that all the fluid elements move with a uniform velocity on a cross-section, so concentration and temperature gradients only occur in the axial direction. As the temperature of the catalytic reactor is controlled, constant temperature within the reactor is assumed. Volumetric flow rate Q is also considered as constant because of liquid incompressibility.

The reaction that takes place on the catalyst can be simplified as:

$$PNP + 3\ FA \text{ ----> } PAP + 3\ CO_2 + 2\ H_2O$$

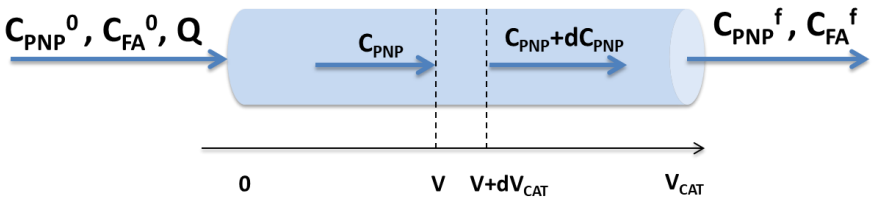

Figure 58 Schematic presentation of plug flow reactor

The steady-state continuity equation is written as the mass balance over a differential volume element of catalyst dV_{CAT} for **PNP** reactant:

Amount of **PNP** introduced per unit time	=	Amount of **PNP** leaving per unit time	+	Amount of **PNP** consumed per unit time

$$Q\ C_{PNP} = Q(C_{PNP} + dC_{PNP}) + r \cdot dV_{CAT}$$

$$<==> \qquad -Q \cdot \frac{dC_{PNP}}{dV_{CAT}} = r$$

$$<==> \qquad \frac{V_{CAT}}{Q} = \int_{C^\circ}^{Cf} \frac{-dC_{PNP}}{r} \qquad (4)$$

Boundary conditions:

Reactor entrance: V=0, $C_{PNP}=C_{PNP}^{0}$, $C_J=0$ for J ≠PNP

Reactor exit: V=V_{CAT}, $C_{PNP}=C_{PNP}^{f}$

with the notations illustrated in Figure 58:

C_i, molar concentration of component i in the liquid phase within the reactor, C_i° the feeding concentration

Q, volumetric flow rate

V, volume of catalyst between entrance of reactor and point under consideration, V_{CAT} the total volume of catalyst

r, rate of reaction of **PNP** per unit of catalyst volume

As the reaction rate r only depends on concentrations, the differential equation **(4)** can be solved by analytical or numerical integration of dC_{PNP}/r, depending on the form of the kinetic law. The steady-state relation **(4)** is used for kinetic analysis of the reaction (see 3.3).

3.1.2 Ideal batch reactor model

As we have compared experiments in flow reactor and in batch reactor, it is necessary to present a model of batch reactor. The simplest model, i.e. ideal batch reactor model is chosen. It is supposed to be perfectly mixed, so at any instant the composition throughout the reactor is uniform. The reactants are initially charged into a flask, are well mixed, and are left to react for a certain period. Hence, composition changes with time. The material balance for **PNP** reactant about the whole reaction mixture is:

Amount of **PNP** accumulated within the reactor per unit time	+	Amount of **PNP** consumed within the reactor per unit time	=	0

$$V_{LIQ}\frac{dC_{PNP}}{dt} + r \cdot V_{CAT} = 0 \qquad (5)$$

with:

V_{LIQ}, volume of the reaction mixture in batch reactor

X, conversion of **PNP**, calculated as $X = 1- C_{PNP}/C_{PNP}^\circ$

The time t necessary to obtain a conversion X is:

$$t = \frac{V_{LIQ}}{V_{CAT}}\int_0^X \frac{-dC_{PNP}}{r}$$

Whereas in a catalytic flow reactor the same conversion is reached after a “contact time”:

$$\tau = \frac{V_{CAT}}{Q} = \int_0^X \frac{-dC_{PNP}}{r}$$

Hence, at the same initial concentration and same temperature, the dependence of the reaction rate r on the concentration is the same in both reactors. If the same amount of catalyst is involved, the condition to get the same conversion is simply $Q_{FLOW} = V_{LIQ}/t_{BATCH}$.

3.1.3 Unsteady-state catalytic plug flow model

Changes in operating conditions result in step perturbation at the entrance of the reactor: at first, the catalyst is under pure water; then, at time 0, the reactant mixture is fed at constant flow rate and composition the mixture reacts in the reactor according to the time evolved since its entrance. As a result, at least during a time equal to the residence time, both composition of fluid and composition on the catalyst surface vary all along the reactor. Hence, the unsteady-state mass balance over a differential volume element of reactor containing a volume of catalyst dV_{CAT} and a volume of fluid $\varepsilon/(1-\varepsilon)\ dV_{CAT}$, during an elementary time interval dt, results in a partial differential equation. For example for **PNP**:

Amount of **PNP** introduced per unit time	=	Amount of **PNP** leaving per unit time	+	Amount of **PNP** consumed per unit time	+	Amount of **PNP** accumulated in dV per dt

$$Q\,C_{PNP} = Q(C_{PNP} + dC_{PNP}) + r \cdot dV_{CAT} + \left[\frac{\varepsilon}{1-\varepsilon}\frac{dC_{PNP}}{dt} + \frac{dq_{PNP}}{dt}\right] dV_{CAT}$$

$$<==> \qquad -Q \cdot \frac{dC_{PNP}}{dV_{CAT}} = r + \frac{\varepsilon}{1-\varepsilon}\frac{dC_{PNP}}{dt} + \frac{dq_{PNP}}{dt} \qquad (6)$$

with:

q_{PNP}, molar concentration of PNP adsorbed on the catalyst surface

ε, void fraction in the catalyst bed = $V_{LIQ}/(V_{LIQ}+V_{CAT})$

Boundary conditions:

t=0, $C_{PNP}=q_{PNP}=0$ within the reactor

t>0, $C_{PNP}= C_{PNP}^{0}$ at the reactor entrance (V=0)

3.1.4 Resolution method of the unsteady-state catalytic plug flow model

Except for a first order simple reaction and linear adsorption equilibrium, the resolution of the partial differential equation (PDE) **(6)** involves numerical calculation method. The finite difference method was selected because it gives the possibility to easily change the kinetic and the adsorption model.

The method is illustrated in Figure 59.

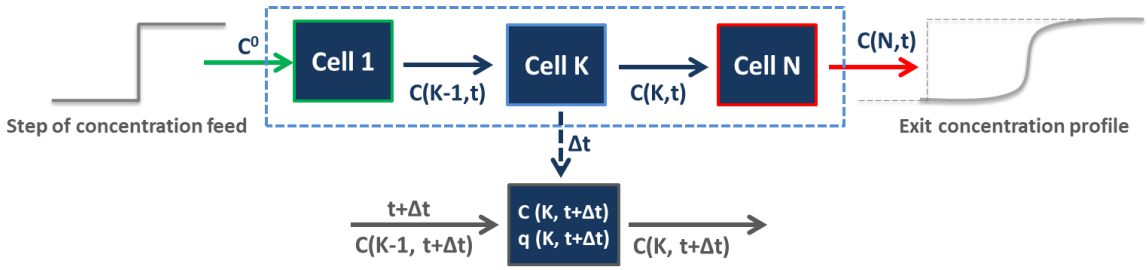

Figure 59 Schematic representation of finite difference method

The reactor volume is replaced by N cells; each one contains a catalyst volume $\Delta V_{CAT}=V_{CAT}/N$, and uniform concentrations in the fluid and on the catalyst surface. Derivatives are calculated according to a first order series expansion: $dC/dt \approx [C(j,t+\Delta t)- C(j,t)]/\Delta t$ and $dC/dV_{CAT} \approx [C(j-1,t)-C(j,t)]/\Delta V_{CAT}$. Compositions at time $t+\Delta t$ are easily calculated from composition at time t, as initial conditions are known. A Matlab program was created for the calculation of concentration profiles at the reactor exit.

As the evolution of concentration observed in the experimental reactor is quite slow in comparison with the fluid residence time, the number of cells has a little influence on the shape of the response curve. The results calculated with 1 cell or 16 cells differ in only a few percent. On the contrary the number of time intervals should be high (typically 100-200) to obtain a smooth response curve.

3.2 Simulation of reactor under transient conditions

In this section, we try to reproduce the concentration profiles observed when the flow reactor experiment starts with new operating conditions. For the record, catalyst bed is washed with water between each test; and after the beginning of the test, a peak of unknown compound (I250), appears in the reactor effluent during a quite long time before the achievement of steady-state conditions, as shown below.

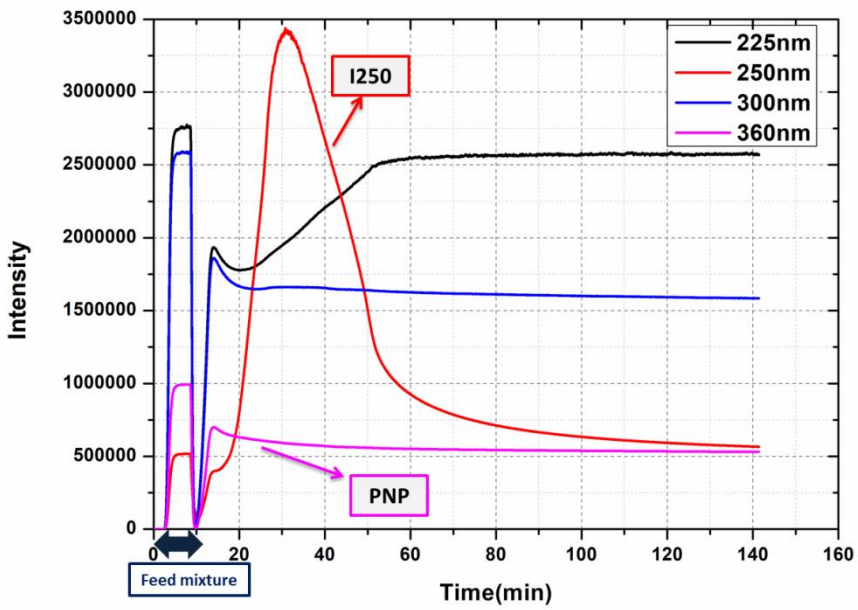

Figure 60 Intensity profile of 4 wavelengths by UV PDA.
I250 is at 250nm and **PNP** is around 360 nm.

3.2.1 Reaction model with successive reactions

3.2.1.1 Model hypothesis and resolution method

As a first model to account for the observations, a simple reaction with one intermediate species **I** is considered:

PNP --- > I --- > PAP

This model gives a simplified picture of the mechanism of the reaction presented in Chapter 1, as long as the rate of decomposition of one intermediate is slower than the others.

It is also supposed that all the reactions take place on the catalyst surface and that Langmuir hypothesis apply [92]:

- Uniformly energetic adsorption sites
- Monolayer coverage
- No interaction between adsorbed molecules

In addition,

- The adsorption phenomenon is supposed much faster than chemical reactions, so liquid and adsorbed phases are at equilibrium,
- First order reaction rates are considered

The elementary steps of reaction corresponding to these hypotheses are:

(1) Fast adsorption equilibrium of **PNP**, with the equilibrium constant $K_{PNP} = q_{PNP}/(s \cdot C_{PNP})$

$$PNP + s = PNP^{ads}$$

(2) Formation of intermediate **I**, with a first order reaction rate $r_1 = k_1 \, q_{PNP}$

[92] Hofmann, H., *Chemie Ingenieur Technik* **1991,** *63* (2), 103-103.

$$PNP^{ads} \rightarrow I^{ads}$$

(3) Fast adsorption equilibrium of **I**, with the equilibrium constant $K_I = q_I/(s \cdot C_I)$

$$I+s=I^{ads}$$

(4) Formation of **PAP**, with a first order reaction rate $r_2 = k_2\, q_I$

$$I^{ads} \rightarrow PAP$$

with:

PNP^{ads}, I^{ads}, PNP or I species adsorbed on a catalytic site, q_{PNP} and q_I, the corresponding adsorbed concentrations

s, the concentration of free catalyst sites

q_T, the total concentration of catalyst sites

r_i, the rate of reaction i (i=1,2) expressed on the catalyst volume basis.

The Langmuir-Hinshelwood model gives the total concentration of sites: $q_T = s+q_{PNP}+q_I$; Because of the adsorption equilibria, it is possible to express adsorbed concentrations as function of fluid concentration, as well as their time-derivatives :

$$q_J = \frac{K_J \cdot q_T \cdot C_J}{1 + K_{PNP}C_{PNP} + K_I C_I} \qquad J = PNP, I$$

$$\frac{dq_{PNP}}{dt} = \frac{\partial q_{PNP}}{\partial C_{PNP}}\frac{dC_{PNP}}{dt} + \frac{\partial q_{PNP}}{\partial C_I}\frac{dC_I}{dt}$$

$$= K_{PNP}q_T \frac{(1 + K_I C_I)\frac{dC_{PNP}}{dt} - K_I C_{PNP}\frac{dC_I}{dt}}{(1 + K_{PNP}C_{PNP} + K_I C_I)^2} \qquad (7)$$

The same expression holds for **I**, by inversion of **PNP** and **I** subscripts.

The mass balances equations **(6)** are expressed for components **PNP**, **I** and **PAP**, with the rates of consumption:

$r_{PNP} = r_1$

$r_I = - r_1+r_2$

$r_{PAP} = - r_2$

The mass balance equations constitute a system of 2 coupled linear equations, whose variables are the time-derivatives of fluid concentrations dC_{PNP}/dt and dC_I/dt. So, these derivatives are computed for each cell. Then, the concentrations at time $t+\Delta t$ are calculated as $C_J(t)+ dC_J/dt \cdot \Delta t$. It should be noted that the **PAP** mass balance is independent because **PAP** was supposed to immediately desorb.

3.2.1.2 Results of simulation

In order to reduce the number of parameters to handle, dimensionless groups of parameters are used. Time is divided by fluid residence time, and concentrations and adsorption equilibrium constants are divided by initial **PNP** concentration ($c_j = C_j/C_{PNP}^0$ and $K'_j = K_j\, C_{PNP}^0$). An adsorbed phase Damkholer number is introduced to express the reaction rates constants. A capacity ratio θ between liquid and catalyst phase is defined. It could be noted that the "traditional" Damkholer number, i.e. the product of the rate constant by the residence time, is simply $a \cdot Da_j$.

$\theta = t \cdot Q(1-\varepsilon)/(\varepsilon V_{CAT})$

$Da_j = k_j q_T V_{CAT}/(Q \cdot C_{PNP}^{0})$

$a = \varepsilon C_{PNP}^{0}/((1-\varepsilon) q_T)$

Typical concentration profile of this model is illustrated on Figure 61: all concentrations increase and reach a constant value (steady state) after a time depending on the parameters values, and longer for **PAP** than for **I**. Two points could be highlighted: (i) the **PNP** concentration increases just because the reactor is full of water at time 0; (ii) the residence time is calculated as the time necessary to treat the fluid volume, i.e. εV/Q and does not take into account the storage capacity of the catalyst (support and Pd).

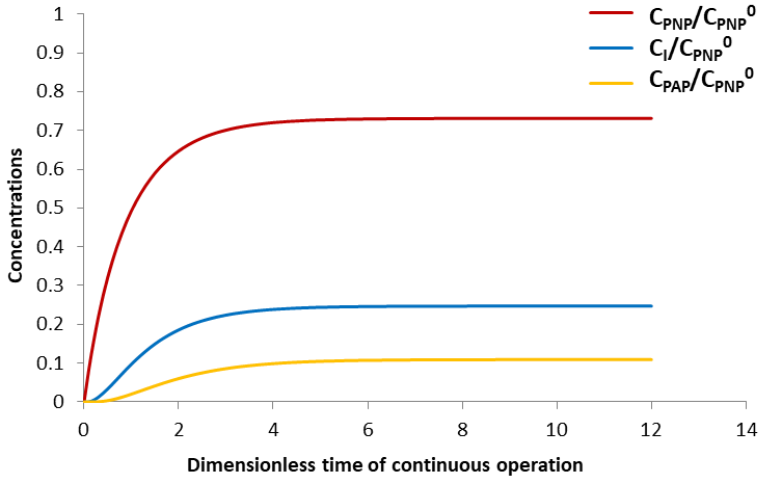

Figure 61 Dimensionless concentration profiles at the exit of reactor for model of reaction with one intermediate species. Values of parameters: Da_1=1, Da_2=0.06, a=5, $K_{PNP}C_{PNP}°$=1, K_I/K_{PNP}=4

The influence of the parameters was studied, and it was observed that an increase in the first reaction rate (Da_1), in **PNP** adsorption (K_{PNP}') or in fluid relative capacity (a), or a decrease in I adsorption (K_I'), are favorable to the extent of the reaction (decrease of **PNP** and increase of **PAP**), while an increase in the 2nd reaction rate (Da_2) has a low effect on **PNP**, and leads to a decrease of I for the benefit of **PAP**.

The parameters were largely varied and it was never observed a maximum on the **I** concentration profile. This result might seem surprising because it is well-known that in a batch reactor, successive reaction will lead to a maximum of intermediate concentration. Actually, during the course of the reaction, the rate of formation of the intermediate decreases while its rate of decomposition increases. In a steady-state flow reactor, this maximum also exists but it depends on the residence time. In conclusion, this simple model predicts that, under unsteady-state conditions, the compositions evolve regularly toward steady-state values, the intermediate just produces a delay before the product exit. Such model is not able to mimic the observations.

3.2.2 Reaction model with change in the catalyst surface

3.2.2.1 Model hypothesis and resolution method

In order to reproduce the appearance and then the disappearance of an intermediate, it is necessary to imagine a change in the mechanism of reaction. Hence, as the catalyst covered at first with water, and then with the reaction mixture, it is supposed that the properties of surface change, let's say from state s to state σ and that the intermediate is formed only on s and is not involved in **PAP** formation when **PAP** is formed on surface. The change in surface properties could be due to the decomposition of FA on the catalyst surface as proposed in section 1.2.1.2 Figure 26 or H-adsorption on Pd or Al_2O_3 support.

The simplest steps of reaction corresponding to these hypotheses are:

(1) Adsorption of **FA** and **PNP** on initial surface s, transformation to σ surface with adsorbed intermediate **I**, with reaction rate $r_3 = k_3\ s\ C_{PNP}$

$$FA + PNP + s \rightarrow I^{ads}$$

(2) Fast adsorption equilibrium of **I**, with equilibrium constant $K_I = q_I/(\sigma \cdot C_I)$

$$I^{ads} = I + \sigma$$

(3) Fast adsorption equilibrium of **PNP** on σ surface, with the equilibrium constant $K_{PNP} = q_{PNP}/(\sigma \cdot C_{PNP})$

$$PNP + \sigma = PNP^{ads}$$

(4) Formation of product **PAP**, with a first order reaction rate $r_1 = k_1\ q_{PNP}$

$$PNP^{ads} \rightarrow PAP^{ads}$$

(5) Fast desorption equilibrium of **PAP** on σ surface, with the equilibrium constant $K_{PAP} = q_{PAP}/(\sigma \cdot C_{PAP})$

$$PAP^{ads} = PAP + \sigma$$

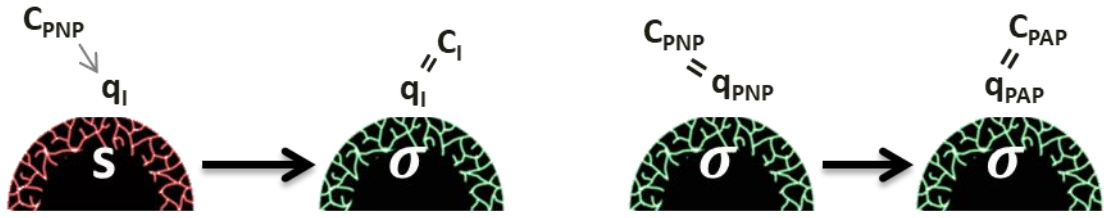

Figure 62 Schematic representation of the reaction model with properties surface change

In this model, the important point is that **I** adsorption occupies s sites and **I** desorption releases σ sites. For example, it is possible to dissociate the surface transformation s -> σ, with a rate r' = k's, from the reaction of **I** formation, or to involve other intermediates in the reaction from **PNP** to **PAP**. In a first attempt to mimic the result, the minimum number of steps are considered and only first order reactions are supposed.

As in the previous case, adsorption equilibrium is supposed and Langmuir-Hinshelwood model is used. The unsteady state mass balance equations are considered for each component with the following production reaction rates:

(1) Reactant **PNP** : $r_{PNP} = -r_1 - r_3$

(2) Product **PAP** : $r_{PAP} = r_1$

(3) Intermediate **I** : $r_I = r_3$

Additional relations concerning the catalyst surface are :

(4) Sites s : $-ds/dt = r_3$

(5) Catalyst surface : $\sigma + s + q_I + q_{PNP} + q_{PAP} = q_T = \text{const.}$

Initial conditions :

At t=0, $s = q_T$ and $C_J=0$ for J= PNP, PAP, I

At t>0, V = 0: $C_{PNP} = C_{PNP}^0$ and $C_J = 0$ for $J \neq$ PNP

The same dimensionless parameters and the same resolution method are used as for the previous model: analytical derivation of adsorption concentrations (Eq. **7**), calculation of derivative values at time t by resolution of the system of mass-balance equations, and calculation of concentration values at time t+ Δt from first order series expansion.

3.2.2.2 Results of simulation

Concentration profiles are drawn over a time from the beginning of the experiment equal to 20 times of residence time, and with different values of parameters. The typical shape of the concentration profiles is shown in Figure 63. For every data set, the intermediate profile exhibits a peak and the **PNP** profiles a shoulder more or less pronounced.

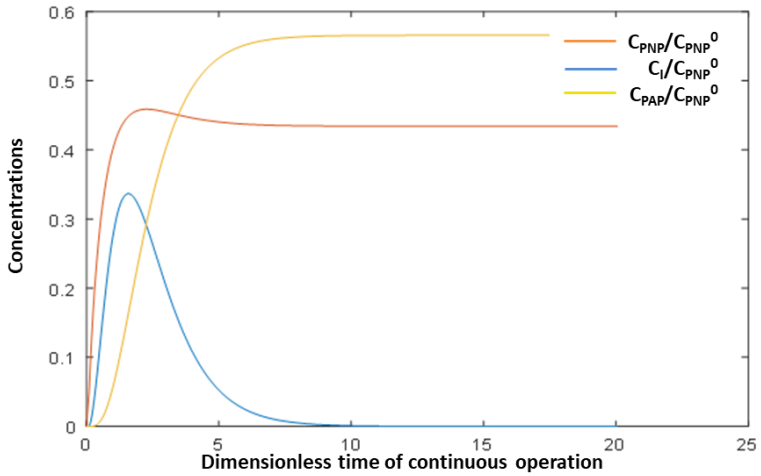

Figure 63 Concentration profiles at the exit of reactor for model of reaction with surface change. Values of parameters: $Da_1=1$, $Da_2=2$, a=1, $K_{PNP}C_{PNP}^0=3$, $K_I/K_{PNP}=0$

At this point, the model with change in the catalyst surface properties is satisfactory because it represents roughly the pattern of experimental results. To go further, it should be necessary to adjust the model parameters values with experiments. The effect of variation of parameters on the maximum value of intermediate concentration, on **PNP** conversion and on the magnitude of the **PNP** shoulder expressed as $C_{PNP,MAX}/C_{PNP,f}$ are studied in this objective.

- The main influence of the phases ratio a appears on the intermediate concentration, which increases while the catalyst capacity increases.
- An increase in the **PNP** adsorption equilibrium constant leads to an increase in the **PNP** storage on the surface, and a clear decrease in the intermediate concentration.
- An increase in the rate constant of **PAP** formation increases the **PNP** conversion and slightly decreases the intermediate concentration.

In conclusion, in order to simulate the concentrations profiles of **PNP**, **PAP** and intermediate **I** observed when the reactor is under transient conditions, two models have been investigated. With the hypothesis of the change of catalyst surface, the model established can well mimic the dynamic behavior observed in experiments. This successful simulation could also support the mechanism we proposed in Figure 26 that the first step of reaction is the decomposition of FA on the catalyst surface, which could lead the change of catalyst surface.

3. 3 Kinetic model of reaction under stationary conditions

The kinetics of the reaction is established with experimental results obtained with on-line HPLC analysis (protocol 3), at the end of a reaction sequence of 60-100 min, i.e. at steady-state. The data set is composed of 55 points, all of them measured at 40°C, most of them at a stoechiometric ratio $C_{FA}^0/C_{PNP}^0=3$, with a 1 mL/min flow rate. The range of variation of parameters is the following : C_{PNP}^0 = 0.3 - 5 mmol/L, C_{FA}^0 = 0.9 - 10 mmol/L, corresponding to m = 0.45 - 1.4, Q = 0.5 - 2 mL/min. The repetition of the same “base point” at C_{PNP}^0=0.6 mmol/L allows to check the stability of the catalyst over a 8 months period : the standard deviation of 15 measurements is about 12%, indicating a poor reproducibility as well as a slow deactivation (Figure 64). The table of measurement is presented in Annex A-11 .

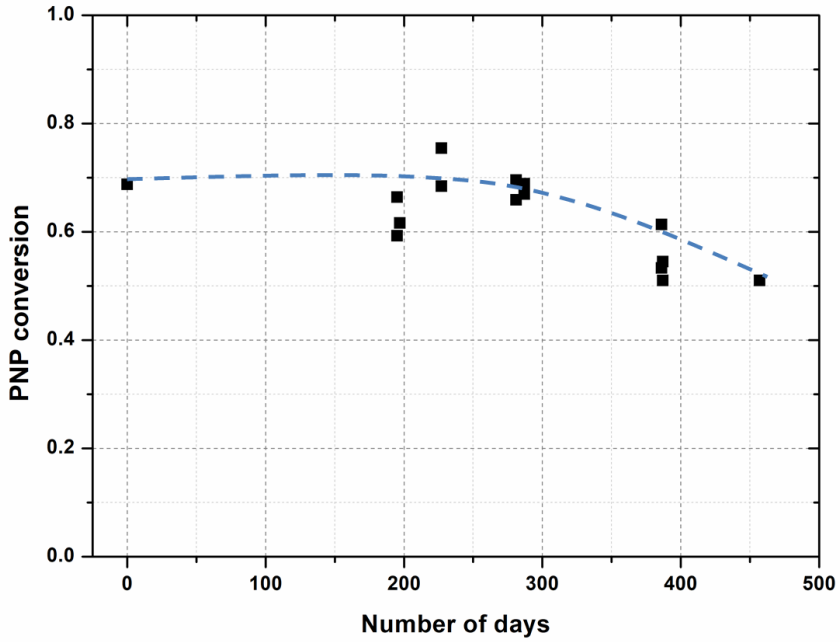

Figure 64 Catalyst evolution between the first measurement (january 2017) and last one (april 2018) with a slow desactivation (blue dashed line). Base point conditions : C_{PNP}^0 = 0.6 mmol/L, C_{FA}^0 = 1.8 mmol/L, Q = 1 mL/min, T=40°C.

The quality of the measurements is evaluated by comparison of initial **PNP** concentration measured by weighing and calculation from HPLC calibration curves, and by the material balance, i.e. the deviation between initial **PNP** concentration and final **PNP** plus **PAP** concentrations. The mean value of the deviation on material balance is 4.0%, and the deviation between the methods of evaluation of initial concentration is 3.0%.

3.3.1 Second order kinetics

As the strong dependence of **PNP** conversion on initial concentration was observed, a second-order kinetics was tested at first. Its main advantage is that it involves only one adjustable parameter, the rate constant k, unlike the models that take into account adsorption of reactant on the catalyst such as Langmuir-Hinshelwood model. The reaction rate r is expressed for an element of catalyst volume:

$$r = kC_{PNP}C_{FA}$$

In order to integrate the **PNP** material balance expression for an ideal plug-flow model (4), both concentrations have to be expressed as functions of **PNP** conversion:

$$\frac{V_{CAT}}{Q} = \int_{C^\circ}^{Cf} \frac{-dC_{PNP}}{r} \qquad (4)$$

With $C_{PNP} = C_{PNP}^0 (1-X)$, $C_{FA} = C_{FA}^0 - 3\, C_{PNP}^0 X = 3\, C_{PNP}^0 (m-X)$ with $m = C_{FA}^0/(3\cdot C_{PNP}^0)$, from **(4)** we can obtain:

$$Da = \frac{3\,k\,V_{CAT}C_{PNP}^0}{Q} = \int_0^X \frac{dX}{(1-X)(m-X)}$$

The result of integration differs according to the value of the reactant ratio m. It can be noted that we never get the exact equality m=1. So, the result of integration is:

$$Da = \frac{3\,k\,V_{CAT}C^0_{PNP}}{Q} = \frac{1}{m-1}\,Ln\left(\frac{1-\frac{X}{m}}{1-X}\right) \qquad (8)$$

The relation **(8)** indicates that the plot of 1/(m-1) Ln[(1-X/m) /(1-X)] versus C_{PNP}^0/Q, when C_{PNP}^0, Q and m are varied, should be a straight line passing by the origin, whose slope is $3k\cdot V_{CAT}$. With the whole set of points, we obtain $3k\cdot V_{CAT} \approx 2.9$ $L^2/(mol\cdot min)$, i.e. the rate constant $k \approx 3020.8$ $L/(mol\cdot min)$, as $V_{CAT} \approx V_{MR}/2 = 0.32$ mL in the microreactor.

The pertinence of the model is evaluated from the comparison of the **PNP** conversion calculated with the rate constant and the experimental conversion, as shown in Figure 65.

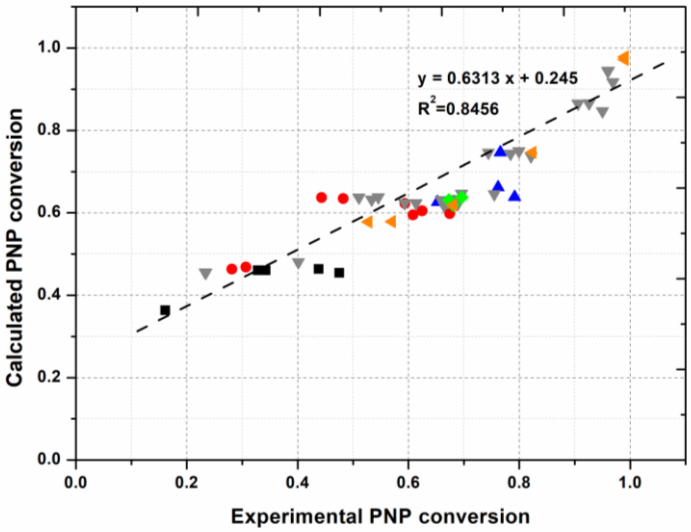

Figure 65 Comparison of the PNP conversion experimental versus calculated with the second order kinetics, with the rate constant k ≈ 3020.8 L/(mol·min). Color code: FA deficit (black m≈0.45, red m≈0.65), FA stoichiometry (blue Q=0.5 mL/min, grey Q=1mL/min, green Q=2 mL/min), FA excess (orange m≈1.4)

The correlation of the results, as shown in Figure 65 is not perfect, but the wide dispersion of data has to be considered. Nevertheless, the mean deviation between second order model and experiments is not acceptable (about 35%): the model fails at low conversion, where the model predicts higher reaction rate than observed.

Although the wide dispersion of data, the plot of the mean reaction molar flow rate over the catalyst bed, calculated as $Q\cdot C_{PNP}^0\cdot X$, as a function of the mean **PNP** concentration $(C_{PNP}^0 + C_{PNP}^f)/2$ clearly shows that the reaction rate is lower when there is a deficit in **FA** (Figure 66).

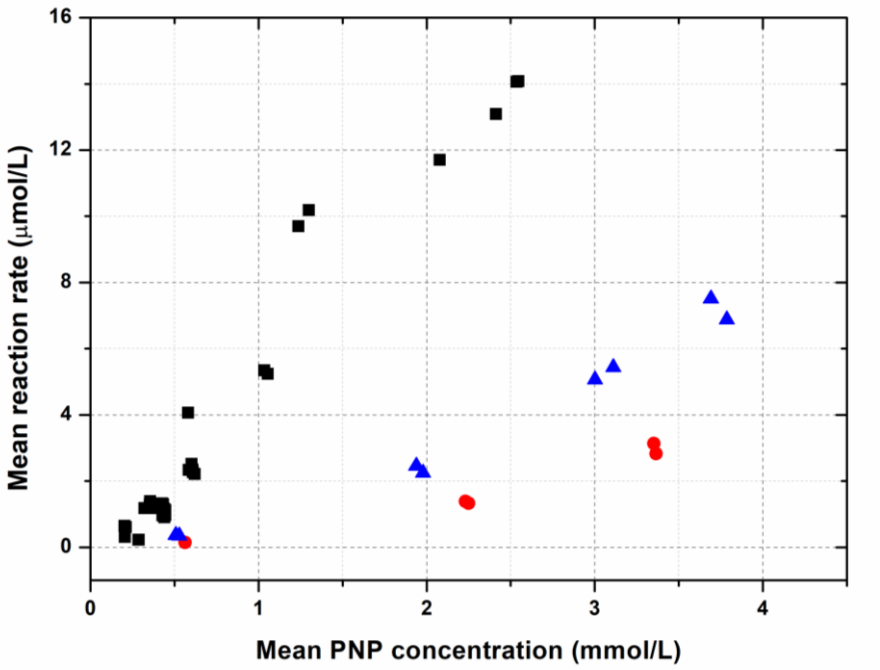

Figure 66 Plot of the mean reaction rate versus the mean **PNP** concentration. **FA** deficit (Red m≈0.45, blue m≈0.65), black all other points.

Hence, a second order model, with respect to **FA** is tested:

$$r = k\, C_{FA}^{\,2}$$

With the same parameters as previously, the reaction rate is $r = 9\, k\, C^{0}_{PNP}{}^{2}\, (m\text{-}X)^2$

And integration of the PNP mass balance equation becomes:

$$\mathrm{Da} = \frac{9\, k\, V_{CAT} C^{0}_{PNP}}{Q} = \int_0^X \frac{dX}{(m-X)^2} = \frac{X}{m(m-X)} \qquad (\mathbf{9})$$

The plot of X/(m-X) as a function of $m\, C_{PNP}{}^{0}/Q$ should be a straight line when m, $C_{PNP}{}^{0}$ and Q are varied. The rate constant thus obtained is $9k \cdot V_{CAT} \approx 7.5\ L^2/(mol \cdot min)$, i.e., $k \approx 2604\ L/(mol \cdot min)$. The comparison between experimental and calculated values is slightly better than with the previous model, with a mean error of 16%, but the trend is still the same (higher calculated reaction rate at low conversion).

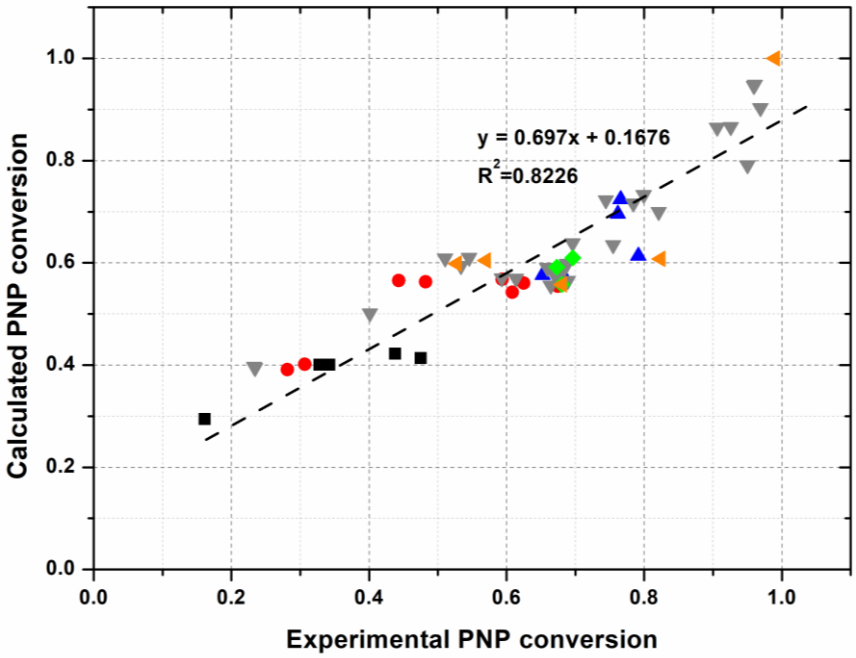

Figure 67 Comparison of the **PNP** conversion experimental versus calculated with the 2nd order kinetics relative to FA, with the rate constant k ≈ 2604 L/(mol·min). Color code: FA deficit (black m≈0.45, red m≈0.65), FA stoichiometry (blue Q=0.5 mL/min, grey Q=1mL/min,5 green Q=2 mL/min), FA excess (orange m≈1.4)

3.3.2 Comparison with possible mechanism of reaction

Despite the poor precision of experimental results, we tried to exploit the reaction mechanism presented in Chapter 1 (Figure 25), which involves two concurrent paths to form **PAP**. The reaction steps are:

(1) PNP + FA -> PNS + CO_2 + H_2O PNS = *p*-nitrosophenol : HO-φ-N=O

(2) PNS + FA -> PHx + CO_2 PHx = *p*-hydroxylaminophenol : HO-φ-NHOH

(3) PHx + FA -> PAP + CO_2 + H_2O

In case of FA deficit, the following steps could be favored:

(4) 2 PHx + FA -> PHB + CO_2 + 2 H_2O

PHB = 4,4'-hydrazobisphenol (PHB) : HO-φ-NH-NH-φ-OH

(5) PHB + FA -> 2 PAP + CO_2

It should be noted that only **PNP** and **PAP** are analyzed, so it is not possible to make a difference between two reaction paths having the same partial orders of reaction. Moreover, in case of successive steps, it is the slowest one that regulates the reaction rate. Hence, the model tested is as simple as possible : only steps (1) and (4) are considered, with different forms of kinetics law, and they are supposed to be much slower than the others. The reactions rates tested are:

(1) $r_1 = k_1 C_{PNP}. C_{FA}$

(4) $r_4 = k_4 C_{FA}^2$

Integration of these reaction rates in **PNP** material balance leads to a non-linear equation involving both rate constant as adjustable parameters. The values of these parameters that minimize the deviation between experimental and calculated **PNP** conversion are calculated by a Matlab program. We obtain a flat minimum, i.e. a zone where the residue $\sum(X_{calc}-X_{exp})^2$ varies a few, with $k_1 \approx$ 729.2-1038.4 L/(mol·min) and $k_4 \approx$ 69.4-121.5 L/(mol·min). The adjustment is slightly better than with only one reaction, but the general trend with poor representation of low conversion results, remains the same despite the use of two adjustable parameters.

3.4 Conclusion

In this chapter, firstly, in the simulation of reactor under transient conditions, the model has been established with the hypothesis of the change of catalyst surface, which can well feature the dynamic behavior experimentally observed: the intermediate profile exhibits a maximum, the **PNP** profiles a shoulder more or less pronounced and **PAP** increases and stabilizes after a longer time than **PNP**.

Secondly, the kinetic models of reaction under stationary conditions have been investigated. The second order kinetics has been explored as $r = K\, c_{PNP}\, C_{FA}$ and $r = k\, C_{FA}^2$. Both of them could basically reflect the experimental **PNP** conversion. But large deviation is observed in the low PNP conversion range, i.e. when reactant concentrations are low.

Chapter 4 - Preparation and characterization of monolithic microreactor

In this part, a microreactor with silica-based monolith incorporated palladium nanoparticles will be prepared in a brand-new method and characterized. Before that, the general research status about the monolithic catalysts will be firstly introduced, emphasizing the preparation method of monolithic catalysts. Then series of silica-based monoliths have been prepared in cylinder PP-PE polymer tubes (syringe), for optimizing the preparation conditions of the stable, well-formed, hierarchically porous and functionalized silica monoliths. With the optimized preparation conditions, the hybrid monolith is prepared in a stainless-steel tube pre-coated with glass successfully. Afterwards, by means of continuous flow, palladium nanoparticles have been immobilized with success in the tube containing monolith and confirmed by a series of characterization methods.

4.1 Monolithic catalyst

4.1.1 Generality properties of monolithic materials

According to the definition by IUPAC, a monolith is "a shaped, fabricated, intractable article with a homogeneous microstructure that does not exhibit any structural components distinguishable by optical microscopy". The most monolith families applied in catalysis under continuous flow for fine chemical production have a polymer, or inorganic matrices skeleton (such as silica, zeolites) exhibiting mesopores or/and macropores (typically inferior to 10μm).[54(a), 93] It exists also other monoliths made of ceramic or metal foils, but they present the very large flow-through pore or channels (>50μm) and their applications in the field of fine chemical synthesis is rare.

Upon most cases, monoliths are synthesized in one-step process, and exhibit a large pore volume (1-2 mL/g), which imparts these materials an excellent catalytic efficiency due to the large amount of active surface available,[54(a), 94] and therefore pose an attractive alternative to traditional catalyst powders or pellets.[95]

In recent years, the research on complex and hierarchically organized monolithic materials has been greatly improved and is still evolving rapidly. Various preparation techniques have been reported [96] for the hierarchically organized porous materials. This type of monolithic materials has a multi-level porous architecture, and offers unique properties with combination of pore sizes: micro- and mesopores offer the large interfacial areas and pore volumes; in the mesoporous dimension, either well-structured pores (e.g. 2D-hexagonal) or disorganized arrangements are

[93] Ricciardi, R.; Huskens, J.; Verboom, W., *ChemSusChem* **2015,** *8* (16), 2586-605.
[94] Kiwi-Minsker, L.; Wolfrath, O.; Renken, A., *Chemical Engineering Science* **2002,** *57* (22), 4947-4953.
[95] Govender, S.; Friedrich, H., *Catalysts* **2017,** *7* (2), 62-90.
[96] (a) Lopez-Orozco, S.; Inayat, A.; Schwab, A.; Selvam, T.; Schwieger, W., *Advanced Materials* **2011,** *23* (22-23), 2602-2615. (b) Triantafillidis, C.; Elsaesser, M. S.; Husing, N., *Chemical Society Reviews* **2013,** *42* (9), 3833-3846. (c) Feinle, A.; Elsaesser, M. S.; Husing, N., *Chemical Society Reviews* **2016,** *45* (12), 3377-3399.

possible (Figure 68); while macropores promote the mass transport to the active sites and decrease transport limitations within the materials.

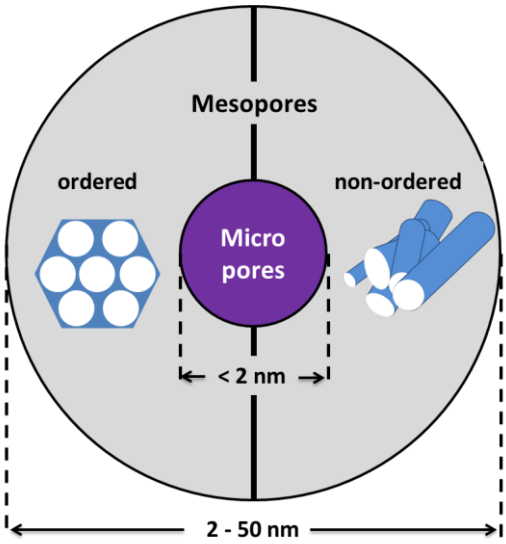

Figure 68 Concept of hierarchy in a porous material: micropores in purple circle and mesopores in grey circle. For the mesoporous regime, either well-organized pores with monomodal character as hexagonal organization or non-ordered arrangements are possible. Figure is modified from Husing [96(c)]

4.1.2 Preparation of monolithic catalyst

There are mainly three types of monolithic catalysts used for application in catalysis for fine chemical production in continuous processes, whose skeleton consist of organic polymer, silica or zeolite materials. As the researches of zeolite monolithic catalyst are quite limited, here we mainly present the organic polymer monolithic catalyst and silica-based monolithic catalyst.

4.1.2.1 Organic polymer based monolithic catalyst

Polymers can be easily modified with a wide variety of functionalities; in consequence they are outstanding substrates for catalytic functions and allow a wide range of possible applications. Kirschning[54(b)] and Galarneau[54(a)] have discussed their preparation and applications. Three main methods for the preparation of polymer monolithic catalyst have emerged.

The first approach is developed by the group of Fréchet, based on the "molding" process.[97] The general procedure is shown in Figure 69: the mixture of monomers and porogenic solvent was transported into a stainless-steel column tube acting as a mold, and then the column was sealed and heated for the polymerization, following by the washing process. Thus, the macroporous organic polymer monoliths with large flow-through macropores (0.7-2 μm) and a connected

[97] (a) Peters, E. C.; Svec, F.; Fréchet, J. M. J., *Advanced Materials* **1999,** *11* (14), 1169-1181. (b) Svec, F.; Fréchet, J. M. J., *Analytical Chemistry* **1992,** *64* (7), 820-822.

network of mesopore (10 nm) were obtained. Different monoliths, such as polyacrylamide, polystyrene etc. have been made.

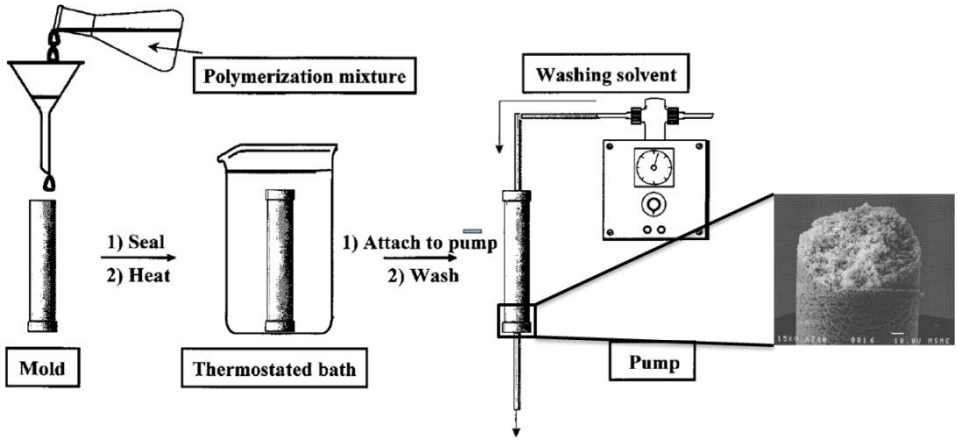

Figure 69 Scheme of the method of Fréchet for the preparation of macroporous polymer monoliths [97(a)]

Thereafter, based on this method, the group of Steven[98] has loaded Pd^0 nanoparticles into the monolith by pumping sodium tetrachloropalladate (K_2PdCl_4) and sodium borohydride ($NaBH_4$) for Pd reduction, and then performed series of Heck reactions (cross-coupling between aryl halides and alkenes) in continuous flow mode. The reactor was a 6.6 mm (ID) × 70 mm glass column filled with monolithic catalyst, but the quantity of Pd loaded was not mentioned. They obtained Heck products in high purity with good yields (> 80%), and shorter reaction times (2h) than in corresponding batch equivalent (16-20h).[99]

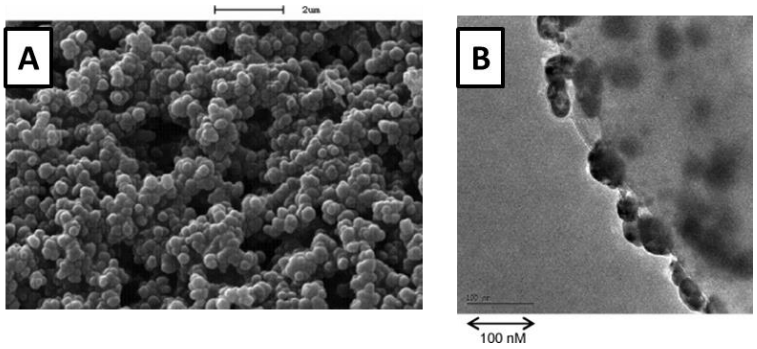

Figure 70 (A) SEM picture of the macroporous polymer before immobilization of Pd^0; (B) TEM image of immobilization of Pd^0 on monolith [98]

[98] Nikbin, N.; Ladlow, M.; Ley, S. V., *Organic Process Research & Development* **2007,** *11* (3), 458-462.
[99] Wang, L.; Zhou, L., *Synthesis* **2006,** *2006* (16), 2653-2658.

Despite of the improvement of production brought by Fréchet-type macroporous polymer monoliths, the defect of these materials is that the swelling of the skeleton, leading to variations of the pressure drop and residence time, can largely impact on their applications.

A second strategy has been introduced by Kirschning[100] to overcome this limitation. The polymer/glass monolith was prepared by synthesizing the polymers inside the porosity of a glass rod with macropores between 50-300 μm. This polymer/glass monolith, with macropores of 1-2 μm, can maintain the same versatility for functionalization as classical polymers; moreover, the rigid macroporous matrix can well limit the swelling of skeleton.

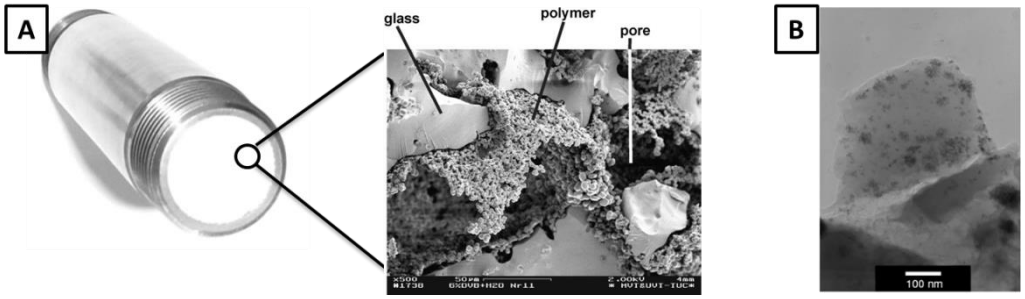

Figure 71 Structure of the polymer/glass monolith: (A) left: the picture of monolith inserted into a stainless-steel tube, right: SEM image of porous glass support structure with polymer [54(b),101] (B) TEM images of Pd(0) nanoparticles immobilized on the monolith [102]

On the basis of the polymer/glass monoliths, the same group has incorporated the Pd^0 nanoparticles into the materials by circulating the aqueous solution sodium tetrachloropalladate (Na_2Cl_4Pd) and then $NaBH_4$ for Pd reduction[102]. Thus, the catalytic monolith with a palladium content of 0.03 wt % has been prepared in a 5.3 (ID) × 110 mm stainless-steel column, and the Suzuki-Miyaura coupling reactions have been performed, with the yields up to 99%.

The third preparation method is based on the high internal phase emulsions (HIPE), which is defined as an emulsion containing more than 74% of internal phase and external phase[103]. After the pioneer work of Bartl[104] and Lissant[105], the polymer HIPE (polyHIPE) has drawn widespread attention in monolithic catalyst. The typical preparation strategy of polyHIPE is presented in Figure 72. PolyHIPE is characterized by the presence of open-cell structure, pore sizes of which are normally in the millimeter-scale, but the majority of polyHIPE have pores that are tens of

[100] Kirschning, A.; Altwicker, C.; Dräger, G.; Harders, J.; Hoffmann, N.; Hoffmann, U.; Schönfeld, H.; Solodenko, W.; Kunz, U., *Angewandte Chemie International Edition* **2001,** *40* (21), 3995-3998.
[101] Solodenko, W.; Kunz, U.; Jas, G.; Kirschning, A., *Bioorganic & Medicinal Chemistry Letters* **2002,** *12* (14), 1833-1835.
[102] Mennecke, K.; Kirschning, A., *Beilstein Journal Organic Chemistry* **2009,** *5*, 21-26.
[103] (a) Zhang, Y.; Pan, J.; Chen, Y.; Shi, W.; Yan, Y.; Yu, L., *Chemical Engineering Journal* **2016,** *283*, 956-970. (b) Yi, F.; Xu, F.; Gao, Y.; Li, H.; Chen, D., *RSC Advances* **2015,** *5* (50), 40227-40235.
[104] Bartl Von, H.; Von Bonin, W., *Die Makromolekulare Chemie* **1962,** *57* (1), 74-95.
[105] Lissant, K. J.; Mayhan, K. G., *Journal of Colloid and Interface Science* **1973,** *42* (1), 201-208.

micrometers in diameter[106], with a low density from around 0.1 to as low as 0.0126 g/cm^3 and a porosity up to 0.94.[107]

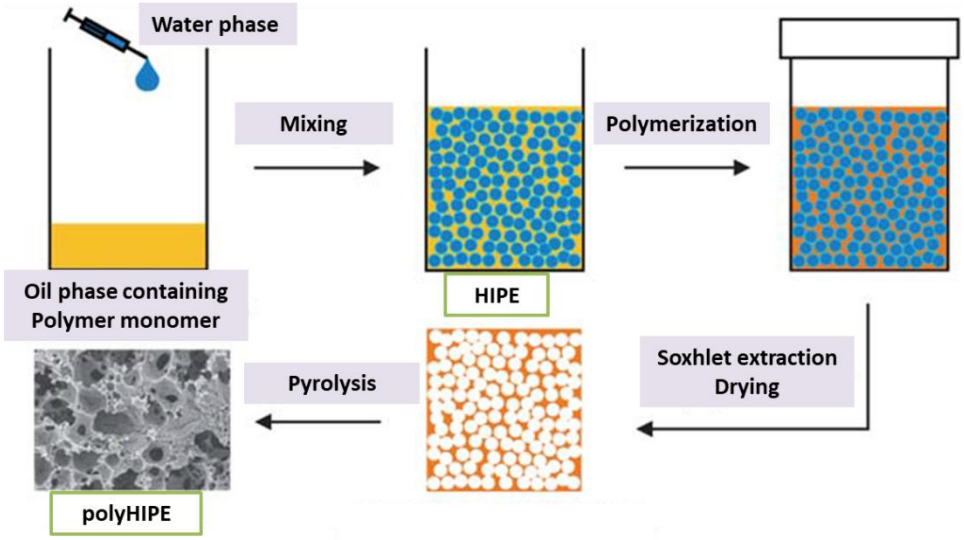

Figure 72 Schematic synthesis strategy of polyHIPE (modified from Kaskel[107(c)])

Afterwards the polyHIPE has been functionalized with various organic groups and immobilized palladium nanoparticles on its surface by batch method with reduction of K_2PdCl_4 or $Pd(OCH_2CH_3)_2$.[108] With the functionalization of primary amine group (-NH_2), the Pd loading could reach 8 wt %, and exhibits good catalytic performance in a Suzuki-Miyaura coupling reaction.

Thanks to the polymer-based monoliths, the first time a functionalized monolith can exhibit key advantages when used as a catalytic microreactor. However, the challenges still remain for these materials, particularly from the viewpoint of engineering: most of polymers are sensitive to mechanical forces and may show a limited thermal and chemical stability, and their properties may vary by shrinking or swelling.[54(a)]

4.1.2.2 Silica monoliths

The silica monoliths with either micro, meso, or macropores have been well known for several years. However, there are only two main types of silica hierarchically organized monolithic materials have been reported for catalytic reactions.

---

[106] Gong, X.; Wen, W.; Sheng, P., *Langmuir* **2009,** *25* (12), 7072-7077.

[107] (a) Richez, A.; Deleuze, H.; Vedrenne, P.; Collier, R., *Journal of Applied Polymer Science* **2005,** *96* (6), 2053-2063. (b) He, H.; Li, W.; Lamson, M.; Zhong, M.; Konkolewicz, D.; Hui, C. M.; Yaccato, K.; Rappold, T.; Sugar, G.; David, N. E.; Damodaran, K.; Natesakhawat, S.; Nulwala, H.; Matyjaszewski, K., *Polymer* **2014,** *55* (1), 385-394. (c) Frind, R.; Oschatz, M.; Kaskel, S., *Journal of Materials Chemistry* **2011,** *21* (32), 11936-11940.

[108] Desforges, A.; Backov, R.; Deleuze, H.; Mondain-Monval, O., *Advanced Functional Materials* **2005,** *15* (10), 1689-1695.

One family was firstly synthesized by the group of Imhof[109] by using an oil-in-water emulsion (for example, dodecane in water stabilized by quaternary ammonium surfactant) as a template. Then, it has been well developed for catalytic reactions by the group of Backov[110], by using emulsions stabilized by silica particles and sol-gel process in acidic condition (Figure 73(A)). The emulsifiers (surfactants), which allow the formation of polar and apolar regions, were mainly used to form the well-ordered nanostructure. These native silica porous monoliths are named Si(HIPE) for "silica high internal phase emulsion". They feature poly-dispersed macropores from 0.5 to 5 µm[110(b)], and mainly microporous and mesopores (Figure 73(B)), with about 700-800 m^2/g of surface area and 70-92% porosity, and a density as low as 0.08 g/cm^3.

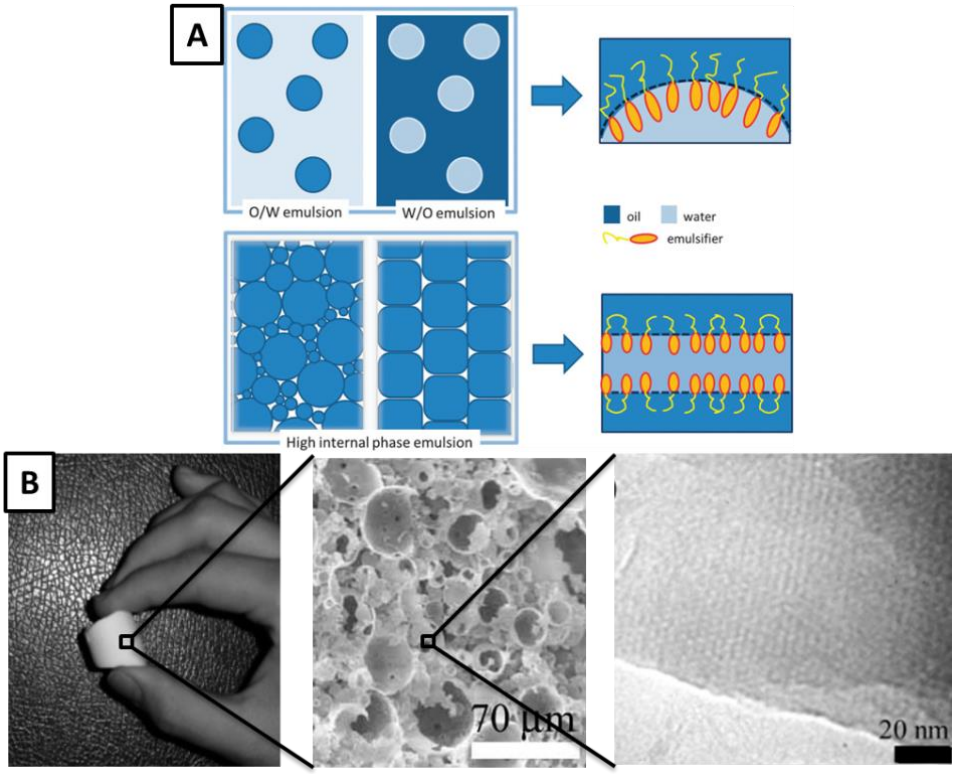

Figure 73 Preparation of Si(HIPE) by Backov: (A): Schematic of emulsions and high internal phase emulsions (HIPE). top: Normal oil-in-water (O/W) and the reverse (W/O) emulsion, bottom: high-internal-phase emulsion [95]; (B): SEM image of hierarchical well-organized monolith Si(HIPE)[110(b)(e)]

The general mechanism of sol-gel process in acidic condition is presented in Figure 74. There are two main steps. The hydrolysis step of the alkoxide of silicon in acidic condition is intended to initiate the formation of hydroxyls groups around Si for the following condensation step. The

[109] Imhof, A.; Pine David, J., *Advanced Materials* **1999,** *10* (9), 697-700.

[110] (a) Carn, F.; Colin, A.; Backov, R., *MRS Proceedings* **2011,** *847*, EE9.5. (b) Carn, F.; Colin, A.; Achard, M.-F.; Deleuze, H.; Sellier, E.; Birot, M.; Backov, R., *Journal of Materials Chemistry* **2004,** *14* (9), 1370-1376. (c) Ungureanu, S.; Deleuze, H.; Sanchez, C.; Popa, M. I.; Backov, R., *Chemistry of Materials* **2008,** *20* (20), 6494-6500. (d) Carn, F.; Colin, A.; Achard, M. F.; Deleuze, H.; Saadi, Z.; Backov, R., *Advanced Materials* **2004,** *16* (2), 140-144. (e) Ungureanu, S.; Birot, M.; Laurent, G.; Deleuze, H.; Babot, O.; Julián-López, B.; Achard, M.-F.; Popa, M. I.; Sanchez, C.; Backov, R., *Chemistry of Materials* **2007,** *19* (23), 5786-5796. (f) Ungureanu, S.; Deleuze, H.; Babot, O.; Achard, M. F.; Sanchez, C.; Popa, M. I.; Backov, R., *Applied Catalysis A: General* **2010,** *390* (1-2), 51-58. (g) Roucher, A.; Bentaleb, A.; Laurichesse, E.; Dourges, M.-A.; Emo, M.; Schmitt, V.; Blin, J.-L.; Backov, R., *Chemistry of Materials* **2018,** *30* (3), 864-873.

condensation step allows the growth of the chains by formation of siloxane bridges (Si-O-Si), and there are two possible reactions during this step: alkoxylation reaction between an alkoxide of silicon and another partially hydrolyzed alkoxide; oxolation reaction between two partially hydrolyzed alkoxides.

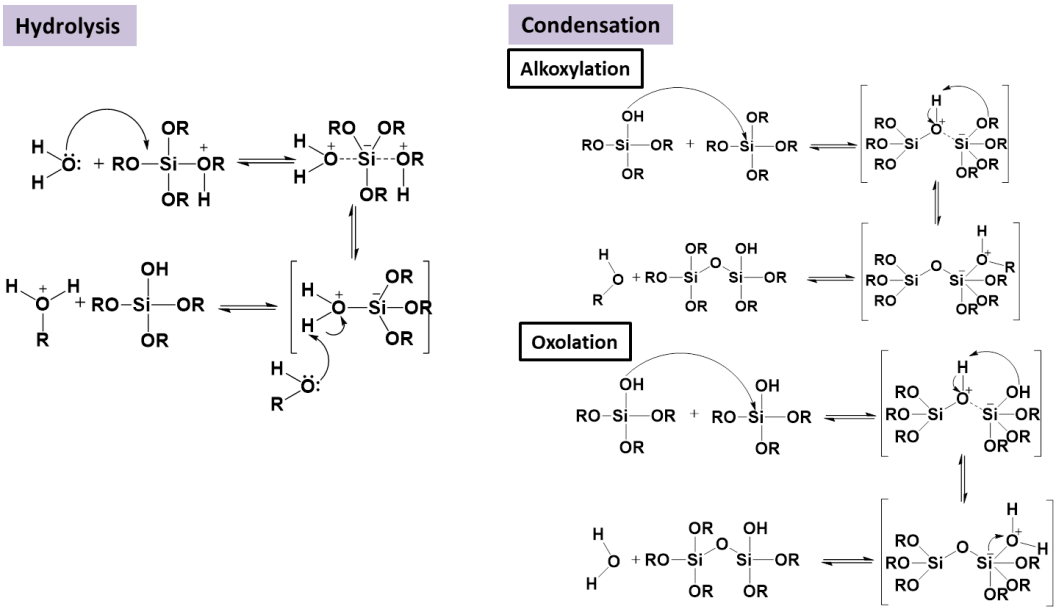

Figure 74 Mechanism of silica-based sol-gel process in acidic condition

In order to benefit the hybrid organic-inorganic chemistry versatility, the functionalization of native Si(HIPE) monoliths have been investigated subsequently with organically derived silane such as 3-(2,4-dinitrophenylamino)-propyltriethoxysilane (DPTS), (3-Mercaptopropyl)-trimethoxysilane (MPTS), (3-aminopropyl)-triethoxysilane (APTS) etc. to prepare hybrid organic-inorganic porous silica-based monoliths.[110(e)(f)] Two methods of functionalization have been carried out: direct synthesize by mixing the organosilane, tetraethylorthosilane (TEOS) and the emulsifier tetradecyltrimethylammonium bromide (TTAB) at the beginning of sol-gel process (co-condensation), or by grafting the organo-functional groups by immersing the prepared Si(HIPE) in the organosilane solution under vacuum.

It should be noted that, as shown in Figure 75, the mesoporosity of mercapto-Si(HIPE) (functionalized by MPTS), was characteristic of randomly dispersed pores, while that of the dinitro-Si(HIPE) (functionalized by DPTS) exhibits a hexagonal organization. Backov explained this difference by the aromatic structure of DPTS inducing an orderly arrangement, that would not be offered by the mercapto derivative. [110(e)]

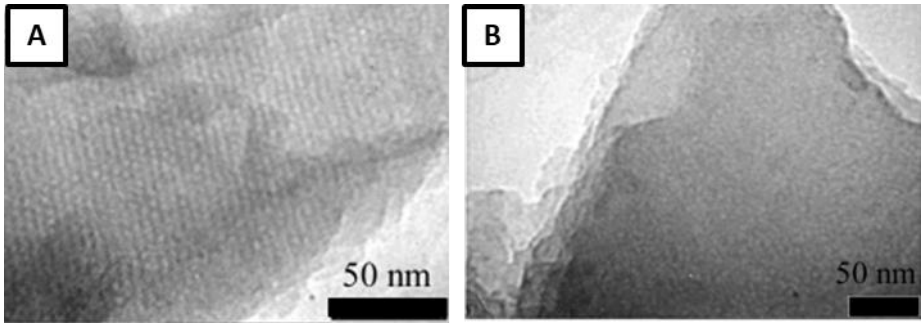

Figure 75 TEM pictures of the functionalized monoliths [110(e)]
(A) dinitro-Si(HIPE) (B) mercapto-Si(HIPE)

Then the Pd^0 nanoparticles are incorporated by immersing the functionalized support in a palladium acetate ($Pd(OAc)_2$) solution and then reduced by $NaBH_4$. In order to compare these monolithic catalysts, the Mizoroki-Heck coupling reaction has been carried out in a batch reactor.[110(c)] The Pd loadings are similar (3.9-4.1 wt%) for all monoliths, but the monolithic catalyst functionalized by MPTS and prepared by co-condensation method (mercapto-Si(HIPE)) have the best turnover and cycling performances, as compared in Table 7. The high TOF of MPTS indicates that the co-condensation method is more effective for functionalization than the grafting method; moreover, the silica monolith modified with a mercapto group provides a fairly good scavenging power toward Pd nanoparticles.

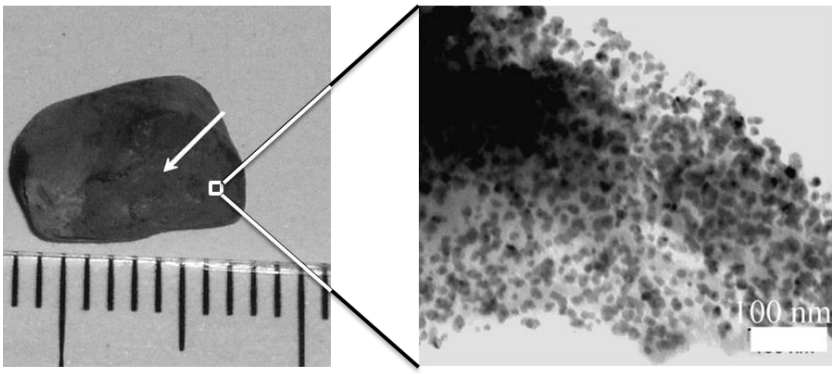

Figure 76 TEM images of Pd(0) nanoparticles immobilized on the grafted Si(HIPE): Left: Typical monolith after the Pd nanoparticles immobilization by grafting method (the white arrow indicates the monolith inner part);Right: Pd nanoparticles observed through TEM [110(c)]

Table 7 Comparison of different functionalized Si(HIPE) monoliths incorporated with Pd^0 in the Mizoroki-Heck coupling reaction

Names of samples	**Pd@mercapto-Si(HIPE)**	**Pd@g-mercapto-Si(HIPE)**	**Pd@g-amino-Si(HIPE)**
Functionalization organosilane	MPTS	MPTS	APTS

Functionalization method	Co-condensation	Grafting	Grafting
Porosity of monolith (%)	93	92	88
Bulk density of monolith (g/cm^3)	0.09	0.10	0.14
TON	2783	1409	1300
TOF (h-^{1})	103	78	62

A second family of silica monoliths was developed by the group of Galarneau[111], featuring a well-defined hierarchical porosity (macropores 2-10 µm and mesopores 7-20 nm) with high surface areas up to 600 m^2/g, on the basis of the monoliths first synthesized by Nakanishi[112] in 1997 for chromatographic applications. A typical synthesis involves an alkoxysilane and a polyethylene oxide (PEO) with water as porogenic solvent. A particular phase separation named spinodal decomposition occurred between the silica rich phase and PEO rich phase, which produced a homogeneous bi-continuous network of PEO/water and silica. Then this material was treated by alkaline, giving rise to the mesoporosity within the structures[111(e)]. It is worth noting that the well-ordered mesopores cannot be obtained by this method, unless the preparation based on the skeleton of MCM-41 (Mobil Composition of Matter No.41), a well-known mesoporous material.[111(e)]

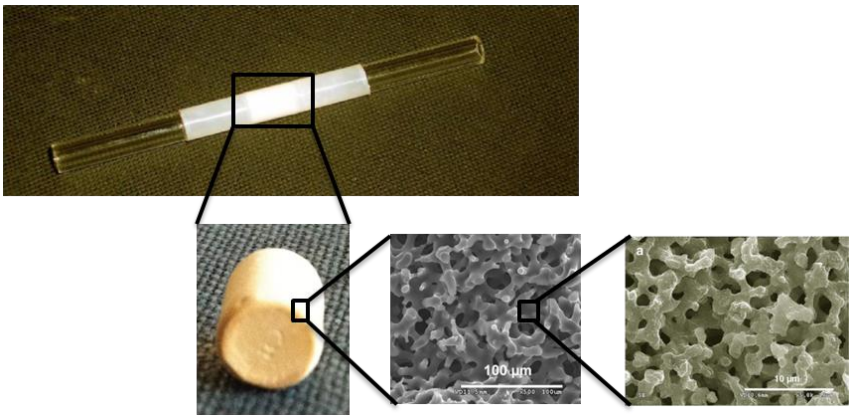

Figure 77 Photo of cladded monolith and SEM images of silica-based monolith prepared by the phase separation method [111(a)(e)]

The resulting monoliths were cladded by heat-shrinkable polytetrafluoroethylene (PTFE) and ended by two glass tubes, which allow the connection to the pump for further continuous-flow

[111] (a) Sachse, A.; Galarneau, A.; Fajula, F.; Di Renzo, F.; Creux, P.; Coq, B., *Microporous and Mesoporous Materials* **2011,** *140* (1-3), 58-68. (b) Sachse, A.; Linares, N.; Barbaro, P.; Fajula, F.; Galarneau, A., *Dalton Transactions* **2013,** *42* (5), 1378-1384. (c) Galarneau, A.; Sachse, A.; Said, B.; Pelisson, C.-H.; Boscaro, P.; Brun, N.; Courtheoux, L.; Olivi-Tran, N.; Coasne, B.; Fajula, F., *Comptes Rendus Chimie* **2016,** *19* (1-2), 231-247. (d) Le Bideau, J.; Miah, M. Y.; Vioux, A.; Fajula, F.; Galarneau, A., *Journal of Materials Chemistry* **2010,** *20* (5), 964-971. (e) Babin, J.; Iapichella, J.; Lefèvre, B.; Biolley, C.; Bellat, J. P.; Fajula, F.; Galarneau, A., *New Journal of Chemistry* **2007,** *31* (11), 1907-1917. (f) Linares, N.; Hartmann, S.; Galarneau, A.; Barbaro, P., *ACS Catalysis* **2012,** *2* (10), 2194-2198.

[112] Nakanishi, K., *Journal of Porous Materials* **1997,** *4* (2), 67-112.

processes.[111(a)(c)] An aqueous solution of palladium nitrate ($Pd(NO_3)_2$) was pumped through the cladded monolith, that was then washed and reduced by the H_2 flow, generating the catalytic monolith with 6 mm diameter, 1 cm length, 4.6 wt % Pd. The catalytic partial hydrogenation reaction of 3-hexyn-1-ol demonstrated an excellent yield (80%) and productivity (0.8 mol/g_{Pd}/h) compared to a commercial Pd@SiO_2 grain catalyst (32%yield, 0.3 mol/g_{Pd}/h productivity).[113]

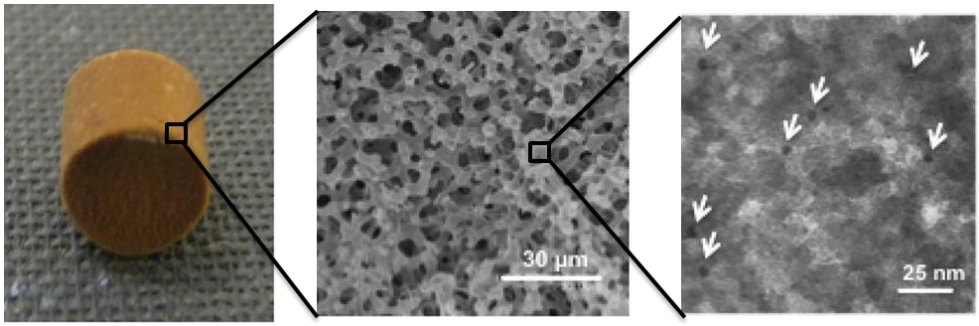

Figure 78 Left: Photo of monolith incorporated Pd^0; Middle: SEM image of monolith incorporated Pd^0; Right: TEM image with the arrows indicating the Pd nanoparticles in the skeleton of silica monolith[113]

Other bimodal meso and macro porous silica monoliths combined with SBA-15 (Stanta Barbara Amorphous-15) have been reported recently,[114] they bear a monolithic character and open macro-porosity while offering a highly ordered mesoporous network, but their applications in catalytic microreactors are rare.

In conclusion, each of these types owns its unique properties and limitations. With respect to polymer monoliths, key advantages like mechanical and thermal stability are offered by silica monoliths, which are also more resistant to a wider range of solvents. The obstacle of the development of silica monolith is the lack of reliable route between academic laboratories to industrial application, for example, the seamless cladding of the silica monolithic rods into microreactor. Up to now, preparation of silica catalytic monoliths in microreactors is mainly by the batch-continuous process: for example, the silica monolith is firstly prepared and functionalized in batch process, and then cladded by PTFE and ended with glass tube to be immobilized Pd nanoparticle in continuous process. However, this type monolithic microreactor is not enough attractive to the industry, because the PTFE materials do not allow the same range of operating conditions (in terms of resistance to pressure and solvents) as stainless-steel tube, hence they cannot meet the demand of industrial application. Hence, the following research on the preparation method of silica-based monolithic microreactor with Pd nanoparticle is quite unique and more convenient for the industrial purposes.

[113] Liguori, F.; Barbaro, P.; Said, B.; Galarneau, A.; Santo Vladimiro, D.; Passaglia, E.; Feis, A., *ChemCatChem* **2017,** *9* (16), 3245-3258.
[114] Postnova, I. V.; Chen, L.-J.; Shchipunov, Y. A., *Colloid Journal* **2013,** *75* (2), 231-233.

4.2 Experimental section

4.2.1 Preparation of functionalized monolithic catalyst

The procedure of preparation was based on the method of Backov [110(b)], and the proportion of reagent was varied to optimize the condition of preparation, in order to synthesize the mechanically stable hybrid monolithic catalyst in a PP-PE polymer tube (syringe) and in a stainless-steel tube, without shrinkage phenomenon. The chemicals utilized in this section are all commercial products.

4.2.1.1 Direct synthesis of functionalized monolith in polymer tube

The Native Silica Monoliths (NSM), Aminopropyl Silica Monoliths (ASM) and Mercaptopropyl Silica Monoliths (MSM) were prepared in similar procedure. The functionalization of NSM was carried out by co-condensation method, and it should be mentioned that the direct synthesis of ASM by co-condensation method has not been reported yet.

(1) The aqueous solution of TTAB was prepared in the mortar in a given concentration, followed the adding of concentrated HCl (37%).
(2) This step depends on the substrate: for NSM synthesis, a given amount of TEOS was added dropwise in the former mixture along with the vigorous agitation by pestle for approximately 5 minutes in order to perform TEOS hydrolysis. For ASM and MSM, TEOS was pre-mixed with (3-aminopropyl)-triethoxysilane (APTS) or with (3-mercaptopropyl)-trimethoxysilane (MPTS) before addition to TTAB solution.
(3) The emulsion was formed by adding of dodecane drop by drop on maintaining the vigorous agitation continually for about 7 minutes.
(4) The final step was the transfer of the emulsion into a plastic syringe, and then the syringe is sealed and left for 10 days for aging.
(5) The resulting materials were then washed dropwise with THF/Acetone (1:1) for 5 days and then with ethanol for two days in Soxhlet.

4.2.1.2 Growing of Pd nanoparticles within functionalized monolith in batch mode

On the basis of the researches of Backov[110(c)(f)], the catalytic performance of mercapto functionalized monolith is better than that of amino functionalized monolith. It was also demonstrated that addition of triphenylphosphine (PPh_3) during the impregnation step in the grafted hybrid monolith in a molar ratio 4:1 relative to palladium offer better catalytic performances. Thus in the following monolith preparation and characterization, the MSM is mainly investigated, and addition of PPh_3 is tested.

Hence, the Pd nanoparticles are impregnated by three ways:
(a) Direct immobilization of Pd nanoparticles in MSM with $Pd(0)(PPh_3)_4$.
(b) Immobilization of Pd nanoparticles in MSM by reducing $Pd(II)(OAc)_2$ with addition of PPh_3

(c) Immobilization of Pd nanoparticles in MSM by reducing $Pd(II)(OAc)_2$ without addition of PPh_3

The preparation procedures are similar:

(1) MSM (0.1 g) was added in a flask under argon atmosphere.

(2) (a) $Pd(PPh_3)_4$ (0.15 mmol) was then added,
or, (b) 3 mL of $Pd(OAc)_2$ (0.15 mmol) solution containing PPh_3 (0.6 mmol) was added,
or, (c) 3 mL of $Pd(OAc)_2$ (0.15 mmol) solution was added

(3) 3 ml of dry THF was added into the flask. The solution was left in dark under stirring for 2 days.

(4) A fresh solution $NaBH_4$ (1.5 mmol) prepared in THF/H_2O (v/v, 3mL) was degassed by argon bubbling for 30 minutes then quickly added into the previous solution.

(5) After the sufficient reduction within 1 hour, the resulting matrix was then washed in ethanol for 2 days then dried in air at room temperature.

4.2.1.3 Direct synthesis of functionalized monolith in stainless-steel tube

As the preparation of functionalized monolith immobilized by Pd nanoparticles has been explored successfully, the Pd@monolith has been synthesized in the stainless-steel tube with the optimized preparation condition (detailed in Annex A-12).

The emulsion was transposed into a special stainless-steel tube (internal diameter D_{MM}=4 mm, length L_{MM}=100 mm, GLT®(Glass Lined Tubing), TRAJAN), which has a layer of glass coated on the interior surface of tube. Then both ends of the tube were sealed up with the pre-sheared polytetrafluoroethylene (PTFE) sheets and Swagelok plugs, then left to age for 10 days at room temperature.

The tube containing the resulting material was connected with the micro flow pump and washed by pumping THF/acetone (v/v) for 3 hours with the flow rate 0.1 mL/min under 40℃, then washed with ethanol for 2 hours. The color of the effluent on the outlet of the tube changed from pale yellow to colorless at the beginning of washing process. Each hour, the outflow was collected, evaporated and analyzed by ^1H NMR for following and insuring the effectiveness of washing. This hybrid monolith is labeled **MSM-T**.

4.2.1.4 Continuous growing of Pd nanoparticles within functionalized monolith in stainless-steel tube

The continuous flow has been applied for the washing and *in-situ* growing of Pd nanoparticles, to prepare the microreactor with silica-based monolithic catalyst.

A solution of palladium acetate (20 mmol/L) in water was pumped through the tube containing monolith at 0.15 mL/min for 1 hour. The color of the outflow changed from colorless to brown.

And then the distilled water was pumped for 20 minutes at 0.15 mL/min in order to wash the redundant palladium acetate. Then the same procedure was repeated: after palladium acetate was pumped for another 1 hour at the same flow rate, the tube was washed by water for 20 minutes again. A fresh solution of $NaBH_4$ in water/2-propanol (1:59) (2-propanol was used to reduce the bubble formed by $NaBH_4$ in water, dissolved oxygen was removed from water by ultrasonic degassing for 30 min) was prepared and then pumped through the tube at 1 mL/min for 4 hours. Finally, the tube was conditioned by washing with water at 1 mL/min for 2 hours, and ethanol at 1 mL/min for 2 hours. The functionalized monolithic catalyst was labeled **Pd@MSM-T**.

Two tubes have been prepared in exactly the same conditions: one was sampled and dried for analysis and the other one was used as a monolithic microreactor for catalytic reactions. In order to prevent the shrinkage phenomena of MSM, the monolith in the tube for catalytic reaction was maintained wet in water.

The general preparation strategy of functionalized monolithic catalyst in stainless-steel tube is illustrated in Figure 79.

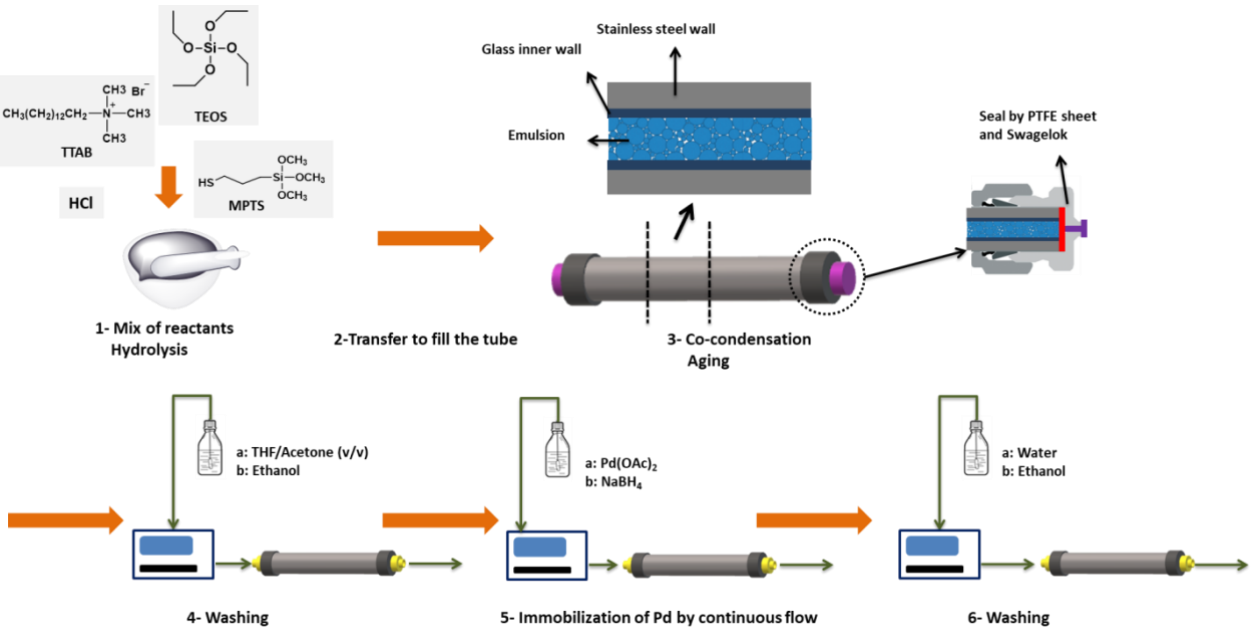

Figure 79 Schematic presentation of the preparation strategy of functionalized monolithic catalyst in stainless-steel tube

4.2.2 Characterization method

Several methods were utilized to characterize the monoliths.

a- Degree of condensation and types of silicate species

The functionalization of monolith can be measured qualitatively by Cross Polarization Magic Angle Spinning (CP-MAS) NMR analysis[115]. ^{29}Si and ^{13}C CP-MAS NMR spectra were obtained by solid-state NMR spectroscopy on a Bruker Avance-400 MHz NMR spectrometer operating at ^{29}Si resonance frequency of 79.5MHz. About 80mg of samples were placed in zirconium dioxide rotors of 4-mm outer diameter and spun at a Magic Angle Spinning rate of 10 kHz in a commercial Bruker Double Channel probe. ^{29}Si CPMAS experiments was performed with Cross Polarization (CP) technique using a ramped 1H-pulse starting at 100% power and decreasing until 50% during the contact time (5 ms) in order to circumvent Hartmann-Hahn mismatches. To improve the resolution, a dipolar decoupling GT8 pulse sequence was applied during the acquisition time.

To obtain a good signal-to-noise ratio, between 1K and 10K scans were accumulated using a delay of 2.5s. The ^{29}Si chemical shifts were referenced to tetramethylsilane.

^{29}Si CP-MAS NMR appears as a straightforward tool to detect the local chemical environment around the Si atoms, so that it allows to identify different siloxane species. The assignments of ^{29}Si NMR signals to the silicate species [110(e)] that could be formed during monolith synthesis are illustrated in Figure 80.

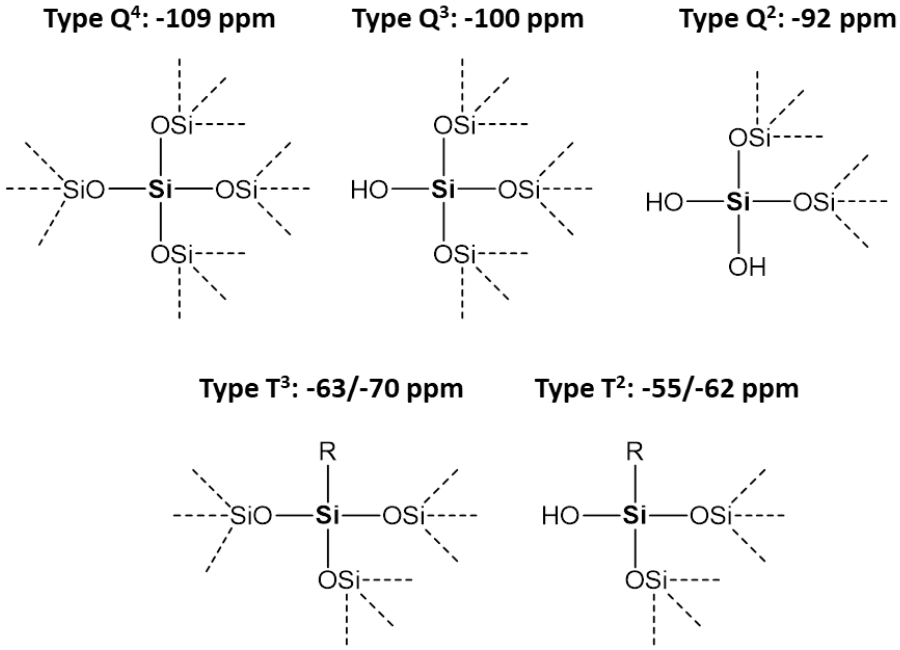

Figure 80 ^{29}Si NMR assignments (center Si)

[115] (a) Oviatt, H. W.; Shea, K. J.; Small, J. H., *Chemistry of Materials* **1993,** *5* (7), 943-950. (b) Cerveau, G.; J. P. Corriu, R.; Fischmeister-Lepeytre, C., *Journal of Materials Chemistry* **1999,** *9* (5), 1149-1154.

Moreover, deconvolution of the ^{29}Si resonances and integration of the areas allowed an estimation of the degree of condensation in the network; they are calculated by MestReNova V9.0 software. Figure 81 gives an example of deconvolution on a ^{29}Si CP-MAS spectrum. Hence, the condensation degree of T type (%C.D.T) and Q type (% C.D.Q) the materials could be evaluated by applying the formula:

$$\%\mathrm{C.D.T} = \frac{2 \times \%\mathrm{T}^2 + 3 \times \%\mathrm{T}^3}{3} \qquad (\mathbf{10-1})$$

$$\%\mathrm{C.D.Q} = \frac{2 \times \%\mathrm{Q}^2 + 3 \times \%\mathrm{Q}^3 + 4 \times \%\mathrm{Q}^4}{4} \qquad (\mathbf{10-2})$$

where $\%T^n$ and $\%Q^n$ (n=2,3 or 4) are the ratio of integration of each peak to the sum of integration of T and Q peaks, respectively. The higher C.D. of T and Q indicates a more complete condensation; it must be high enough to insure a good mechanical resistance.

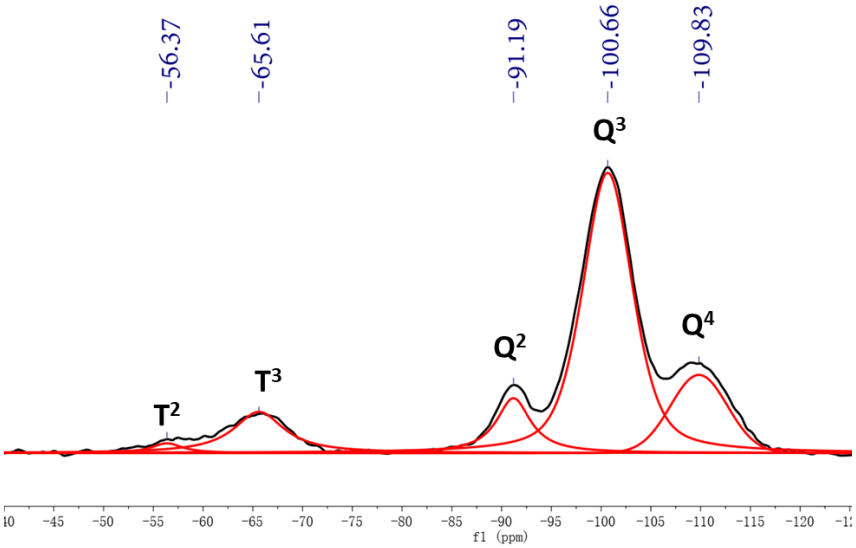

Figure 81 Example of ^{29}Si CP-MAS spectrum and deconvolution method.
Black: Experimental spectrum; Red: simulated spectrum with deconvolution of each peak

b- Internal structure and surface topography

Transmission electron microscope (TEM) was used to capture the internal structure of monoliths prepared, and normally requires an ultrathin specimen (less than 100 nm thick) on a grid. Thus, before the TEM analysis, an epoxy resin was prepared according to a protocol described in Annex A-13 , and then samples of monoliths finely grinded are incorporated into the resin, and cut in extremely thin slices (60-90 nm) with the ultramicrotomy (LBK BROMMA 8800 Ultrotome® III) equipped by a diamond knife (DiATOME Ultra Diamond Knife, Electron Microscopy Science). TEM was performed using a FEI Tecnaï G2 operating at 80 kV - 200 kV equipped with CCD TVIPS (1k*1k) camera.

Scanning electron microscopy (SEM) was used to observe the sample's surface topography, which was performed with Zeiss Gemini SEM 500 operating at 20 KV.

c- Elemental analysis

Energy-dispersive X-ray spectroscopy (EDS) was coupled with SEM, to perform the elemental analysis of samples. For EDS analysis, the specimens were grinded vigorously in the mortar and then carbon-coated before examination. At least 3 points of detection for each sample have been analyzed with EDS and the elemental composition of each material was the average of measurements of these points. The carbon was not taken into account because the samples were carbon-coated and fixed on the observation base by a conducting resin, a material rich in carbon.

d- Surface area

Surface areas and pore characteristics were obtained through nitrogen isotherm adsorption-desorption experiments using an ASAP 2020 Micromeritics automatic adsorption analyzers at 77 K. The Brunauer–Emmett–Teller (BET) theory was used to take into account the multilayer adsorption characteristic of the physical adsorption of gas molecules on a solid surface[116]. The resulting BET equation is

$$\frac{p}{V_a(p_0 - p)} = \frac{c-1}{V_m c}\frac{p}{p_0} + \frac{1}{V_m c}$$

where p and p_0 are the equilibrium and the saturation pressure of adsorbates at the temperature of adsorption, V_a (cm^3/g) is the adsorbed gas quantity per unit of solid and and V_m (cm^3/g) are the monolayer adsorbed gas quantity per unit of solid. c is the BET constant. Detailed calculation of V_m and c is presented in Annex A-14 . The specific surface areas of solids S_s are calculated as:

$$S_s = \frac{V_m N_A s_c}{V_g}$$

where N_A is the Avogadro's number, s_c is the adsorption cross section of the adsorbing species, V_g is the molar volume of the adsorbate gas. Nitrogen is the commonly employed gaseous adsorbate used for surface probing by BET methods.

The different forms of the hysteresis loop in adsorption-desorption isotherms have been schematized and classified by the IUPAC (Figure 82).

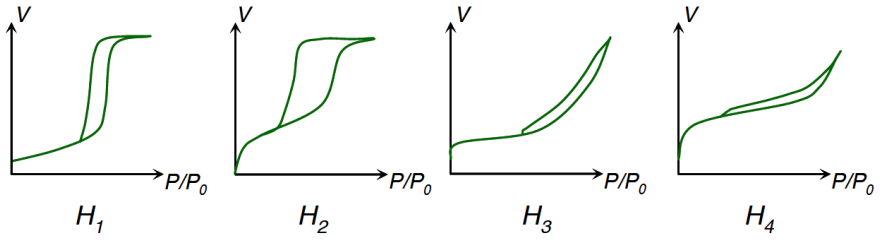

Figure 82 Classification of different hysteresis loops according to IUPAC[117]

The hysteresis loop H_1 and H_2 are observed in the mesoporous adsorbents. H_1 presents the narrow distribution of mesopores, and H_2 presents the mesopores in intercommunication. The

[116] Barrett, E. P.; Joyner, L. G.; Halenda, P. P., *Journal of the American Chemical Society* **1951,** *73* (1), 373-380.
[117] Françoise, R.; Jean, R.; Isabelle, B.; Philip, L.; Renaud, D., *Techniques de l'ingénieur Surfaces et structures fonctionnelles* **2017,** (ref. article : p1050).

hysteresis loop H_3 is normally observed if the adsorbent forms aggregates, and it is not characteristic of mesoporosity. The hysteresis loop H_4 indicates that the adsorbent bears essentially a microporous structure associated with some residual mesoporosity.

4.3 Characterization and discussion

4.3.1 Optimization of preparation conditions of NSM, ASM and MSM in polymer tube

In this part, the aim of optimization of the preparation conditions is to synthesize the mechanically stable monolith in tube without shrinkage. Hence, NSM, ASM and MSM were synthesized in PP-PE polymer tube (syringe), which allows rough estimation of the shrinkage ratio. The CP-MAS NMR analysis was used to characterize the condensation degree and the effectiveness of functionalization.

4.3.1.1 Optimization of preparation conditions of NSM

Our first concern was to elaborate mechanically stable aerogel after drying in preformed tube, so the first aim of the preparation of NSM was just to confirm the convenient condition for preparation of monoliths in the PP-PE polymer tube (syringe). Thus, several conditions of preparation are tested, the criteria are the shrinkage ratio, that might be as low as possible and the degree of condensation and the degree of functionalization, both expected high.

As discussed in publication [110(b)], in the preparation of Si(HIPE) by sol-gel process, the volume ratio of aqueous phase and oil phase could affect the properties of emulsion, and the quantity of TTAB and TEOS could have effect on hydrolysis and condensation steps. Hence, three coefficients have been considered when varying the preparation conditions:
R_1 is the total aqueous phase volume/dodecane volume
R_2 is the mass of TTAB/mass of total aqueous phase
R_3 is the mass of TEOS/mass of total aqueous phase
X_{SR} is the shrinkage ratio, corresponding to the ratio of decreased volume aerogel monolith to the volume of initial emulsion. The volume of shrunken monolith is estimated from the scale on the polymer tube by visual inspection, so estimation of X_{SR} is not precise.

The detailed preparation conditions were listed in Annex A-15 Table A9 and the variation of preparation parameters of NSM were summarized in Table 8, marked by the grey color. The preparation condition of **NSM-B** was the same as in publication of Backov [110(b)].

Table 8 Variation of preparation conditions of NSM and resulting shrinkage ratio and Q%

	NSM-1	NSM-2	NSM-3	NSM-4	NSM-5	NSM-6	NSM-7	NSM-B
R_1	**0,30**	**0,60**	0,47	0,47	0,47	0,47	0,47	0,36
R_2	0,24	0,24	**0,15**	**0,35**	0,24	0,24	0,24	0,32

R_3	0,22	0,22	0,22	0,22	**0,10**	**0,30**	0,22	0,28
X_{SR}	90%	20%	50%	-10%	40%	25%	10%	20%
%C.D.Q	75.1	74.8	73.2	-	75.1	74.1	74.0	74.3

The NSM have been successfully prepared, which demonstrated the feasibility of our concern. The ^{29}Si CP-MAS NMR spectra of NSM are summarized Figure 83 and the condensation degree %C.D.Q has been calculated as presented in section 4.2.2 (Table of values in Annex A-16 Table A12). The significant Q^3 type Si peak has been detected in all NSM samples, and weak Q^2 and Q^4 peaks have been found in some samples.

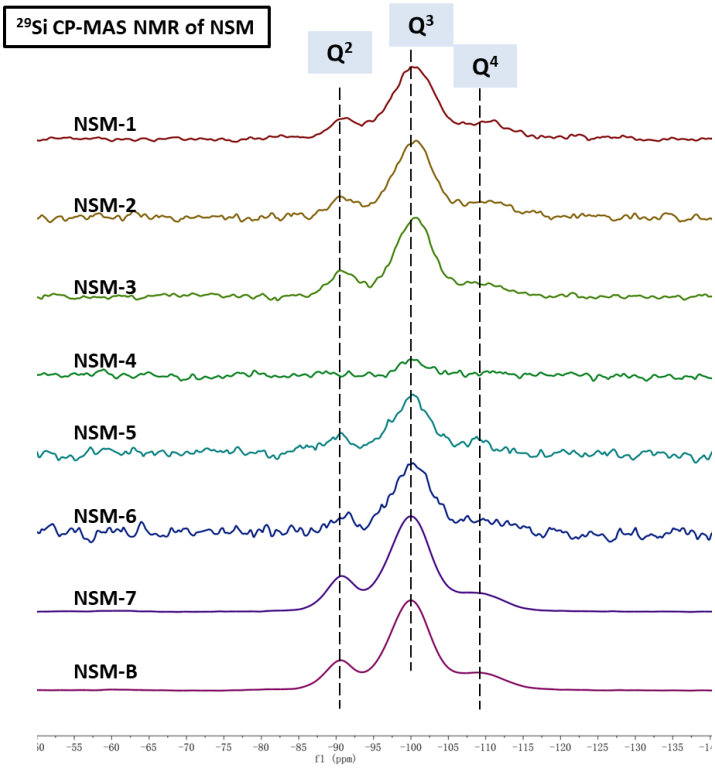

Figure 83 Stack plot of ^{29}Si CP-MAS NMR spectra for NSM in different preparation conditions

The 90% X_{SR} of **NSM-1**, in which R_1 was the lowest, corresponds a prodigious shrinkage as shown in Figure 84 (A), compared with **NSM-2** in Figure 84 (B). This is in accordance with the conclusion of Backov[110(b)]: as the condensation step started at the oil-water interface, the increase in oil (dodecane) fraction would destabilize the oil-water interface, going against the silica condensation and thus leading to the shrinkage of monoliths.

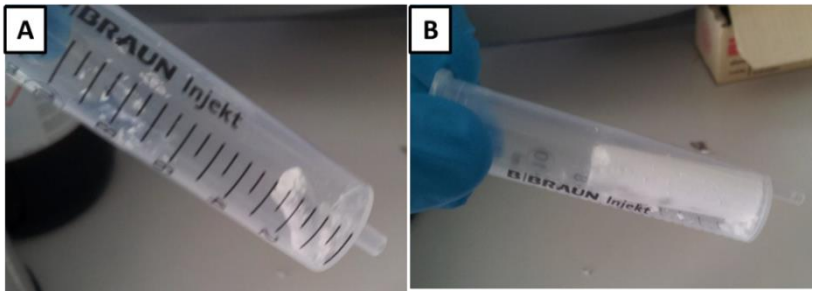

Figure 84 Example of shrinkage phenomena of monoliths
(A) NSM-1 with 90% shrinkage; (B) NSM-2 with 20% shrinkage

In the sample **NSM-4** with the highest amount of emulsifier R_2 = 0.35, the X_{SR} was -10%, indicating that the final volume of monolith was larger than the volume of starting emulsion. Poor condensation is indicated by the only slight Q^3 peak in ^{29}Si CP-MAS NMR analysis. The high quantity of emulsifier TTAB might destabilize emulsion, thus reducing hydrolysis and/or condensation step, so, it still exists some –Si-OH groups that did not bond to each other, leading to the augmentation of volume and the decrease of mechanical stability.

Comparison of X_{SR} of **NSM-3, NSM-4** and **NSM-7**, shows that higher or lower TTAB quantities were both not favorable conditions in the preparations of NSM. The effect of quantity of TEOS was not obvious on the preparation of NSM in the range of $0.1 < R_3 < 0.3$, by comparing **NSM-5**, **NSM-6** and **NSM-7**. All the NSM samples had similar degrees of condensation %C.D.Q lying in the range about 73%-75%, as expected.
^{13}C spectrum of NSM was just used to demonstrate the effectiveness of washing process. The peaks of TTAB have been detected in some samples of NSM (results in Annex A-17), corresponding the residual TTAB in the monolith after washing.

To sum up, the preparation conditions of **NSM-2, NSM-6, NSM-7** and **NSM-B** are all favorable, considering their small shrinkage ratio and good condensation degree. By summarizing the above investigations on the effect of preparation conditions, it could be roughly concluded that with $R_1 > 0.36$, $0.15 < R_2 < 0.35$ and $0.1 < R_3 < 0.3$, the NSM could be prepared steadily with little shrinkage phenomena.

4.3.1.2 Optimization of preparation conditions of ASM

In fact, the direct synthesis of ASM by co-condensation method has not been reported yet. Hence, the major aim of the synthesis of ASM in this thesis was mainly to verify the feasibility of the co-condensation method on the preparation of ASM and to compare with MSM.

To explore this synthesis method, preparation conditions have been largely tuned, which was different from the synthesis of NSM. The detailed preparation conditions were listed in Annex A-15 Table A10 and the variation of preparation conditions of ASM were summarized in Table 9, marked by the grey color. R_4 represents the n(TEOS)/n(organosilane) (APTS in this synthesis).

Table 9 Variation of preparation conditions of ASM and resulting shrinkage ratio and C.D.

	ASM-1	ASM-2	ASM-3	ASM-4	ASM-5	ASM-6	ASM-7	ASM-8	ASM-9
R_1	**6.46**	**0.41**	**0.82**	0.64	0.64	0.64	0.64	0.64	0.64
R_2	0,18	0,18	0,18	**0,10**	**0,28**	0,15	0,18	0,18	0,18
R_3	0,23	0,23	0,23	0,23	0,23	**0,30**	0,23	0,23	0,22
R_4	21.5	19	19	19	19	19	**10**	**15**	**19**
X_{SR}	10%	80%	40%	60%	-60%	20%	20%	70%	60%
%C.D.T	100.0%	98.0%	96.4%	95.8%	95.8%	92.3%	94.7%	95.5%	98.2%
%C.D.Q	80.1%	77.4%	78.4%	78.5%	77.4%	78.9%	80.4%	79.5%	78.4%

The shrinkage phenomena of **ASM-2** was associated the low R_1 during the preparation. The similar phenomenon was also observed in **NSM-1**, which gave the evidence of our previous explanation: the increase of quantity of dodecane in the starting emulsions could lead the shrinkage of monoliths. The effect of augmentation of R_1 in **ASM-1** was not obvious on the shrinkage.

The high emulsifier ratio R_2 led the high volume of **ASM-5**, and the low R_2 could give rise to the shrinkage phenomena (**ASM-4**). These results perfectly matched with the NSM syntheses.

Similar to NSM preparation, effect of TEOS (R_3) was not obvious to be observed. As for the effect of R_4, it was difficult to draw a general conclusion in current synthesis of ASM. However, the object is to functionalize the NSM, so with the high R_4 of **ASM-7**, perhaps we could obtain more functionalized monolith, which will be verified in the following CP-MAS NMR analysis.

The ^{29}Si CP-MAS NMR spectra for ASM are illustrated in Figure 85. With the deconvolution of spectra, the area proportion of T and condensation degree of ASM samples are listed in Table 9 (table of detailed values in Annex A-16 Table A13). The presence of T type proves the successful functionalization of monolith. T^3, Q^2, Q^3 and Q^4 existed in all samples, and T^2 was not as obvious as other peaks.

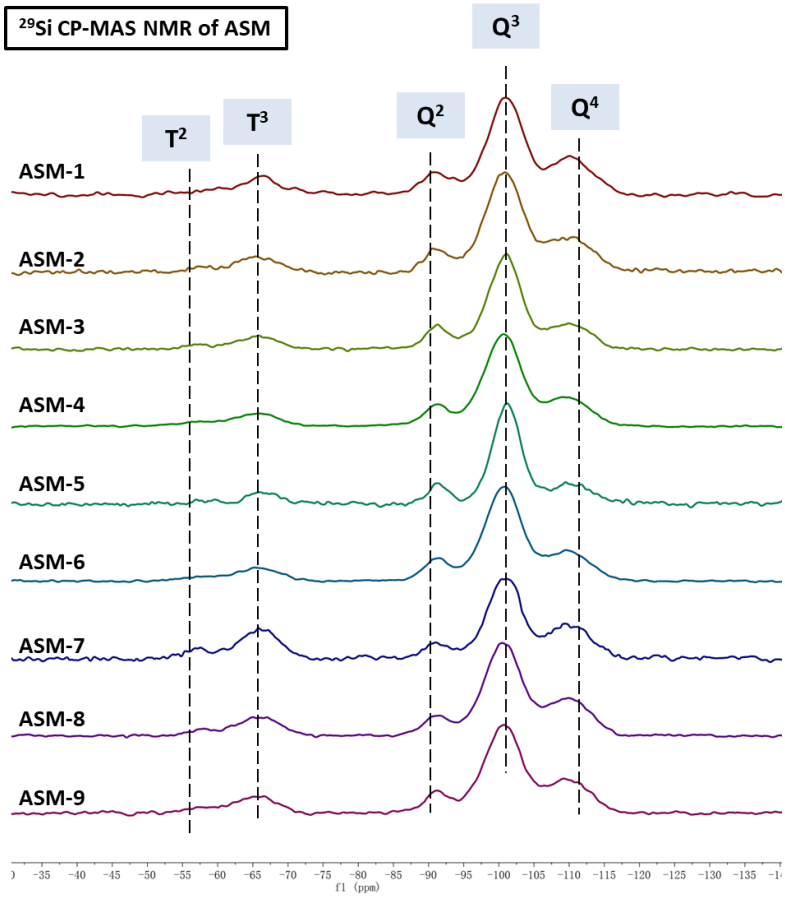

Figure 85 Stack plot of ^{29}Si CP-MAS NMR spectra for ASM in different preparation conditions

The condensation degree T varies in the range of 92.3% - 100% and %C.D.Q varies in the range of 77.4% - 80.4%, higher than that of NSM, which demonstrates the effectiveness of co-condensation method to synthesize ASM. It is worth noting that with high value of R_4, **ASM-7** exhibits the high proportion of T type, compared to other samples. It indicates that the high quantity of APTS in the emulsion is beneficial to functionalize the monolith, and also favorable to the condensation process.

^{13}C CP-MAS NMR spectra of ASM are stacked in Figure 86. There are mainly 5 significant peaks. It should be noted that the peaks at 3, 15 and 36 ppm (black dashed line) change together in all the spectra. Considering the chemical shift of R**C**H_2NH_2 is 30-65 ppm and R_2**C**H_2 is 16-25 ppm[118], the monolith peaks at 3, 15 and 36 ppm perfectly match with group R–**C**H_2**C**H_2**C**H_2NH_2. This demonstrates directly that with the co-condensation method, the NSM can be successfully functionalized by amino group. The red dashed line mark other two peaks, which could be attributed to –**C**H_2**C**H_3 group in monolith, due to the probable incomplete hydrolysis of TEOS or APTS.

[118] Lindeman, L. P.; Adama, J. Q., *Analytical Chemistry* **1971,** *43* (10), 1245-1252.

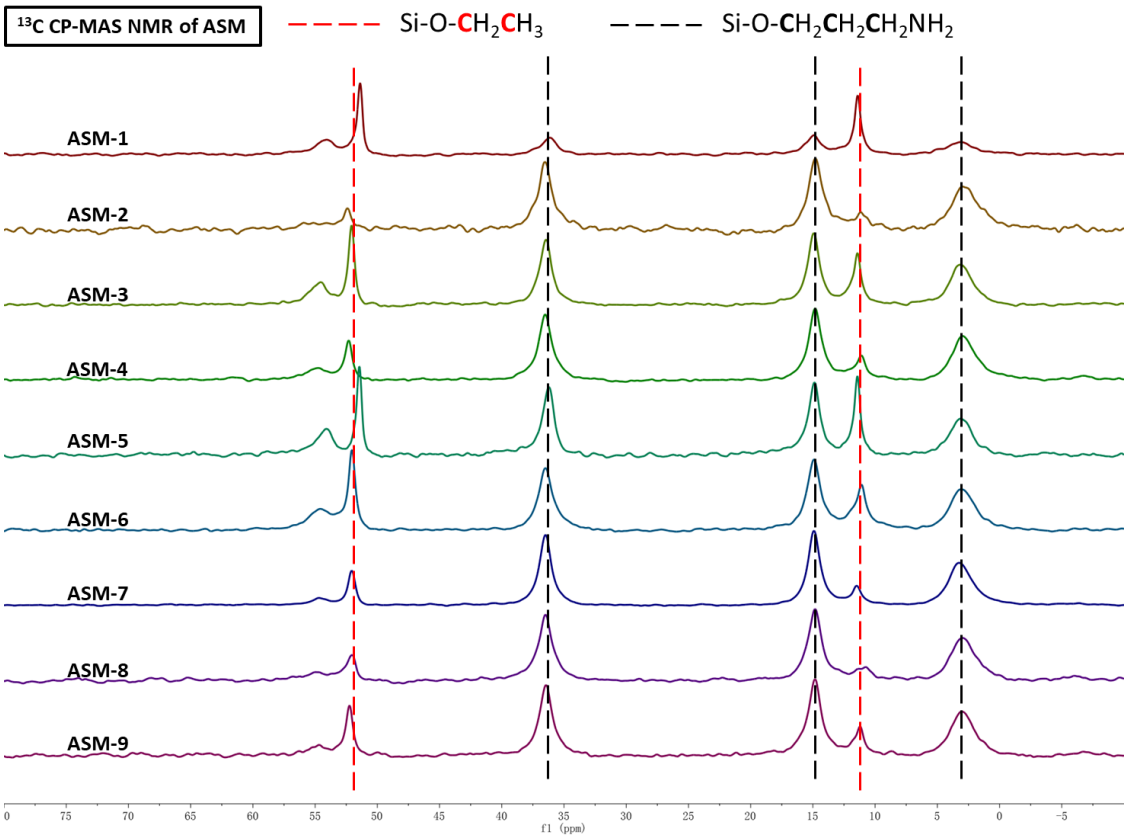

Figure 86 Stack plot of ^{13}C CP-MAS NMR spectra for ASM in different preparation conditions

The peak TTAB (30.4 and 67 ppm) cannot be found, this confirms the monoliths were all well washed. In **ASM-1**, the proportion of amino group can be hardly found, but the $-CH_2CH_3$ group is significant, indicating the week functionalization with $-NH_2$ group and strong condensation with $-CH_2CH_3$. Considering the high R_1 value of **ASM-1**, we can conclude that the too little quantity of oil phase in the emulsion is not favorable to the co-condensation functionalization, because it could prevent the formation of stable oil-water interface during the condensation.

By combining the results of shrinkage ratio and NMR analyses, we can see that the best range for preparation of NSM was also applicative in the preparation of ASM. And we can define more precise condition range for ASM synthesis: $0.41 < R_1 < 6.46$, $0.15 < R_2 < 0.28$, and $0.1 < R_3 < 0.3$.

4.3.1.3 Optimization of preparation conditions of MSM

The preparation conditions of MSM were basically based on the favorable range for monolith synthesis concluded in NSM investigations, with slight change of R_1 and R_2 in the safe range, and vast variation of R_4 to explore the convenient proportion of MPTS in the co-condensation process.

The detailed preparation conditions were listed in Annex A-15 Table A11 and the variation of preparation conditions of MSM were summarized in Table 10, marked by the grey color. R_4 represents the n(TEOS)/n(organosilane) (MPTS in this synthesis). The **MSM-B** was the preparation condition of Backov [110(b)].

Table 10 Variation of preparation conditions of MSM and resulting monolith characteristics

	MSM-1	MSM-2	MSM-3	MSM-4	MSM-5	MSM-6	MSM-7	MSM-B
R_1	**0.40**	**0.55**	0.47	0.47	0.47	0.47	0.47	0.36
R_2	0.24	0.24	**0.19**	0.24	0.24	0.24	0.24	0.31
R_3	0.21	0.21	0.21	0.22	0.22	0.22	0.21	0.28
R_4	9	9	9	**2.3**	**4**	**19**	9	9
X_{SR}	15%	30%	10%	80%	50%	20%	10%	10%
%C.D.T	93.0%	96.1%	89.9%	92.8%	90.4%	94.3%	92.1%	93.2%
%C.D.Q	77.4%	76.1%	77.2%	79.3%	80.8%	76.6%	78.4%	77.1%

The X_{SR} augmented with the increase of $1/R_4$, which indicated the excessive of MPTS could not promote the co-condensation process, because too much organo- groups which could not react in the condensation, might destabilize the emulsion. Hence, the R_4=9 was the favorable condition for the MSM synthesis by co-condensation method.

The ^{29}Si CP-MAS NMR spectra of MSM in Figure 87 exhibit the presence of T^2, T^3, Q^2, Q^3 and Q^4 peak, and T^2 type was not always obvious.

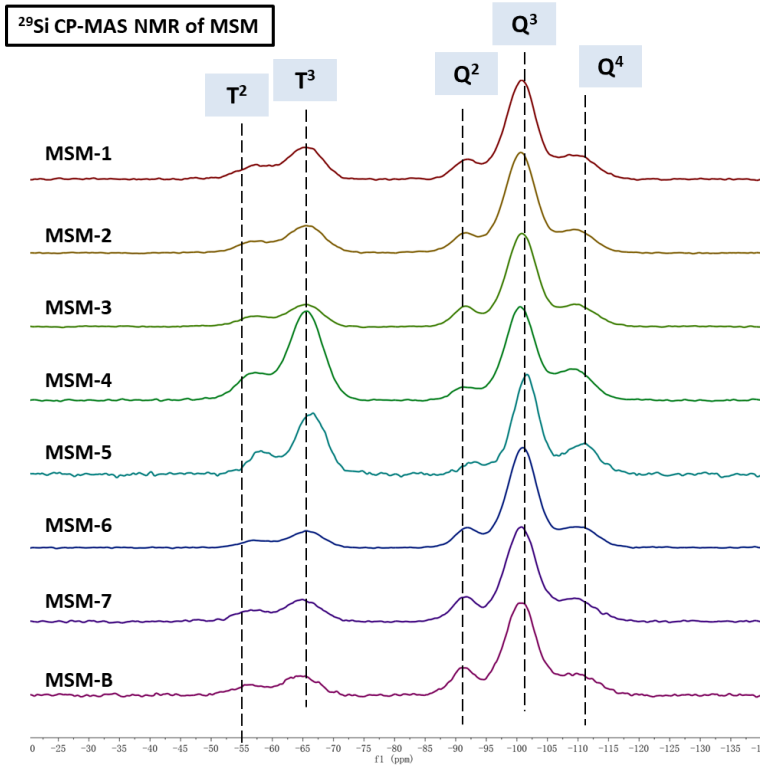

Figure 87 Stack plot of ^{29}Si CP-MAS NMR spectra for MSM in different preparation conditions

With the deconvolution of spectra, the condensation degree of MSM samples are listed in Table 10 (table of detailed values in Annex A-16 Table A14). With overall consideration, the preparation conditions of **MSM-1**, **MSM-7** and **MSM-B** are all favorable for the synthesis of MSM in tube.

In the ^{13}C CP-MAS NMR spectra for MSM illustrated in Figure 88, the peak of around 27 ppm in the ^{13}C NMR spectra demonstrates directly the existence of -SH group in the MSM prepared[118]. The other peaks around 30 ppm could be attributed to the surfactant.

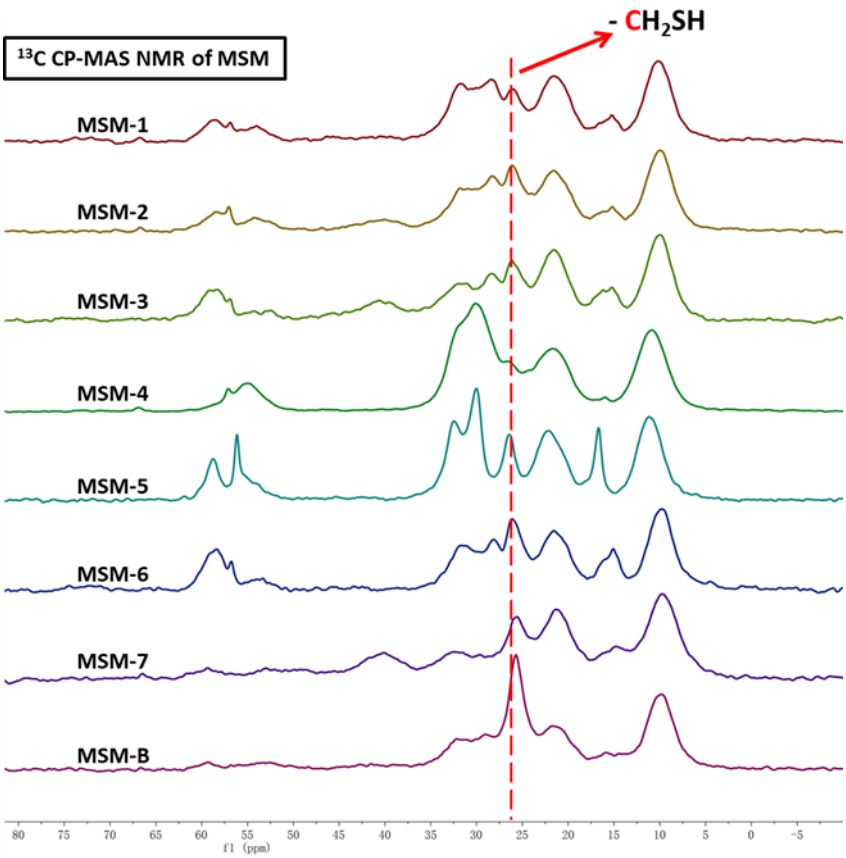

Figure 88 Stack plot of ^{13}C CP-MAS NMR spectra for MSM in different preparation conditions

In conclusion, in this part, by co-condensation method, the optimizations of preparation conditions for NSM, ASM and MSM have been explored in the polymer tube (syringe). The shrinkage ratio and CP-MAS NMR analyses have been carried out to characterize the shrinkage phenomena, condensation degree and the functionalization results. The effects of preparation parameters such as ratio of aqueous phase (R_1), TTAB quantities (R_2), TEOS quantities (R_3) and MPTS or APTS quantities (R_4) in reactants have been investigated, and a favorable preparation condition range is proposed: $R_1 > 0.3$, $0.15 < R_2 < 0.35$ and $0.1 < R_3 < 0.3$. As for ASM and MSM, this range is $0.41 < R_1 < 6.46$, $0.15 < R_2 < 0.28$, and $0.1 < R_3 < 0.3$. The functionalized monoliths with low shrinkage ratio and good condensation degree such as **ASM-7, MSM-1**, **MSM-7** and **MSM-B** have been prepared with success.

According to the work of Backov[110(c)(f)], mercapto group provides good stabilizing power toward Pd nanoparticles, therefore the catalytic performance of mercapto functionalized monolith should be better than that of amino functionalized monolith. Hence, in the following catalytic

monolith preparation and characterization, the MSM was mainly investigated, due to lack of time to test all samples.

4.3.2 Characterization of the hierarchy of pores

Here the macroporosity and mesoporosity of monoliths prepared in polymer tube are characterized by SEM and TEM, and the microporosity and specific surface of monoliths are characterized by BET analysis through N_2 adsorption-desorption isotherm. The functionalized monolith used for characterization is **MSM-7**, owing to its low shrinkage ratio, successful functionalization and good condensation degree.

4.3.2.1 SEM and TEM analysis

For the characterization of macroporosity of MSM, SEM analysis of **MSM-7** (Figure 89 (A) and (B)) was investigated and compared with the **NSM-6** before functionalization (Figure 89 (C) and (D)). The typical interconnected macroporous textures of high internal phase emulsion have been observed in both MSM and NSM, which indicates that the functionalization of mercapto group does not destroy the intrinsic structure of NSM, even if the spherical structure of foam in MSM is smoother, probably due to its organic functionalization. The polydisperse opened cells are connected with the "external junction" pointed by the white arrows. The "cell windows" are the holes in the cells marked by the black arrows in the image Figure 89 (A) and (C), and there are also holes between different cells. All these holes are in the micrometer range, about 2μm–10μm, revealing the macro-porosity of the NSM and MSM prepared.

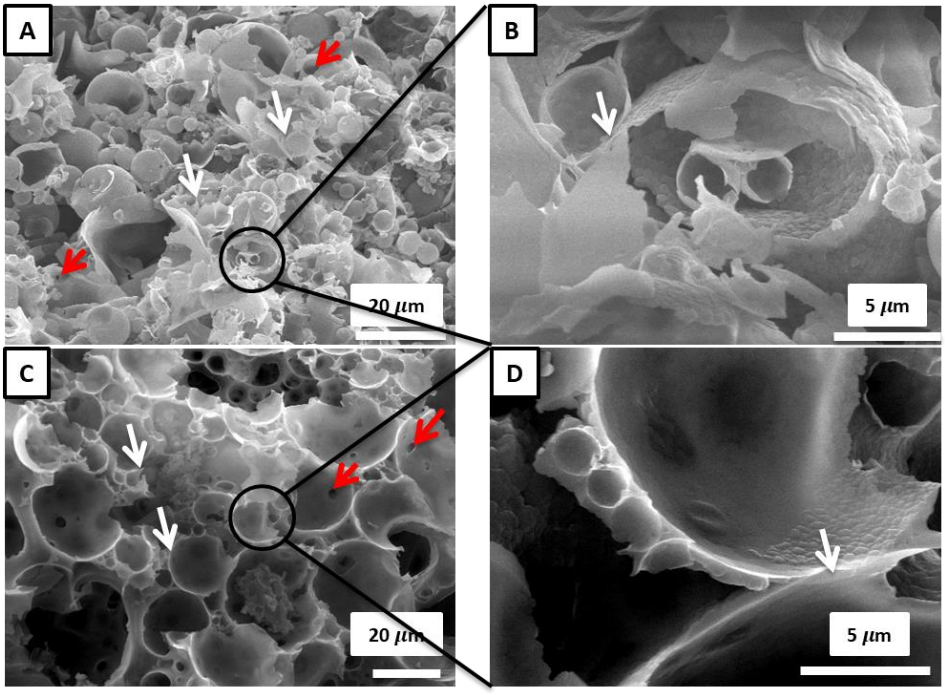

Figure 89 SEM images of (A)(B)MSM-7 and (C)(D) NSM-6. The white arrows show the example of the "external junction" between cells and the black arrows show the typical cell windows

The TEM analysis was investigated to observe the mesoporosity of MSM prepared. Because Backov[110(e)] did not observe the organization in the prepared mercapto-fonctionalized monolith as we discussed in the part 4.1.2.2, we will compare the TEM of **MSM-7** and **MSM-B** (prepared with the conditions of Backov), to confirm the difference of MSM prepared.

As shown in Figure 90 (A)-(C), the typical 2D-hexagonal organization has been observed in the **MSM-7**, with the interval about 5 nm, therefore the mesoporosity of **MSM-7** can be verified. With regard to **MSM-B** (Figure 90 (D)-(F)), there are only randomly dispersed pores, and the hexagonal organization cannot be observed, just as the published results. Backov explained that this difference of organization was because the mercapto derivative did not offer high organization. However, based on our investigations, with a favorable preparation condition of MSM such as that of **MSM-7**, the typical 2D-hexagonal organization could be clearly observed.

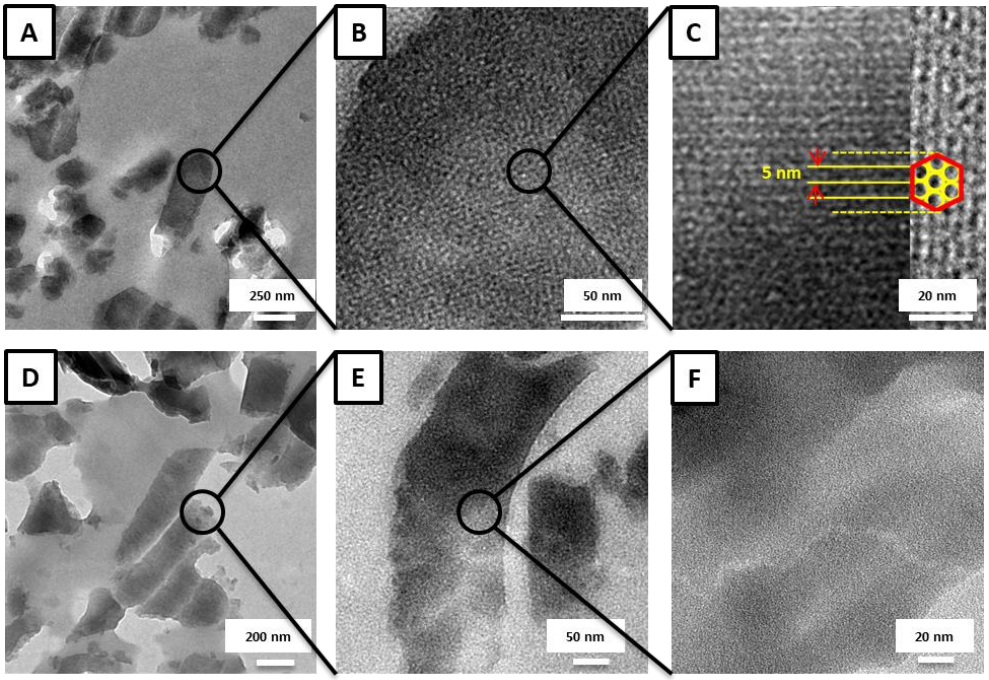

Figure 90 TEM images of (A)-(C): MSM-7 and (D)-(F): MSM-B

4.3.2.2 N_2 Adsorption-desorption isotherm

For the further confirmation of the meso- and the micro- porosity of **MSM-1**, and for the measurement of specific surface, the N_2 adsorption-desorption isotherm analysis has been investigated. As shown in Figure 91 (A), a weak hysteresis loop can be observed between the adsorption and desorption curves, which matches with hysteresis loop H_4 as discussed in 4.2.2, and indicates microporosity with fewer numbers of mesopores[110(c)]. The hysteresis loop of MSM investigated by Backov (Figure 91 (B)) marches with hysteresis loop H_2, indicating the existence of only the mesoporosity not microporosity.

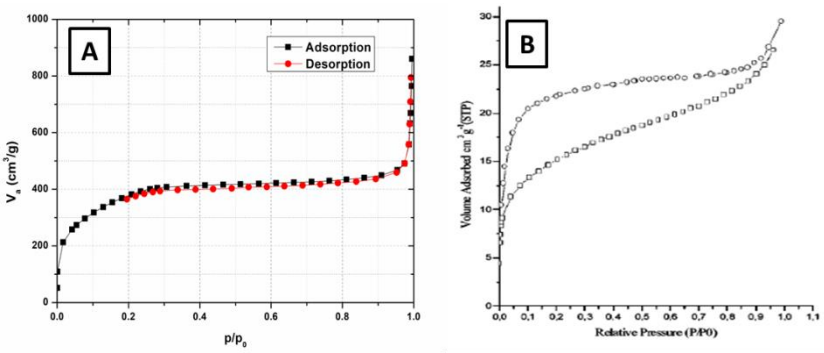

Figure 91 N_2 Adsorption-desorption isotherm analysis of (A) MSM-1 and (B) MSM-B (from Backov [110(e)])

With the BET analysis, the specific surface area of **MSM-1** is 1260 m^2/g. Compared with other monoliths in publications summarized in Table 11, our prepared MSM has an impressive surface area, perhaps thanks to its well-ordered 2D-hexagonal organization.

Table 11 Specific surface area of monoliths in recent publications

Reference	Monolith	Surface area (m^2/g)	Published year
This work	MSM-1	**1260**	-
Backov [110(d)]	SiO_2 foam	**1450**	2004
Backov [110(b)]	SiO_2	**830**	2004
Backov [110(g)]	SBA-SiO_2	**760**	2018
Backov [119]	Imidazole-SiO_2	**462**	2013
Backov [110(e)]	Methyl-SiO_2	**450**	2007
Backov [110(e)]	Pyrrol-SiO_2	**392**	2007
Backov [110(e)]	Mercapto-SiO_2	**53**	2007
Bakker [120]	Polymer	**482**	2015
Barbaro [113]	$ArSO_3$-SiO_2	**322**	2017
Barbaro [111(f)]	TiO_2	**148**	2012
Debecker [121]	Al-SiO_2	**900**	2013
Galarneau [111(d)]	BMIM-TFSI-SiO_2[a]	**761**	2010
Galarneau [111(a)]	SiO_2	**750**	2011
Galarneau [111(e)]	MCM-41-SiO_2	**500**	2007
Kaskel [107](c)	SiC-polymer	**167**	2011
Mrowiec-Białon [122]	SiO_2	**575**	2017
Zhou [123]	C_{16}MIM-SiO_2[b]	**1340**	2003

a: BMIM-TFSI: 1-butyl-3-methylimidazolium bis(trifluoromethylsulfonylimide

[119] Brun, N.; Hesemann, P.; Laurent, G.; Sanchez, C.; Birot, M.; Deleuze, H.; Backov, R., *New Journal of Chemistry* **2013,** *37* (1), 157-168.
[120] Kotbagi, T. V.; Hakat, Y.; Bakker, M. G., *MRS Communications* **2015,** *5* (1), 51-56.
[121] Debecker, D. P.; Boissiere, C.; Laurent, G.; Huet, S.; Eliaers, P.; Sanchez, C.; Backov, R., *Chemical Communications* **2015,** *51* (74), 14018-14021.
[122] Ciemięga, A.; Maresz, K.; Malinowski, J.; Mrowiec-Białoń, J., *Catalysts* **2017,** *7* (9), 255-264.
[123] Zhou, Y.; Antonietti, M., *Advanced Materials* **2003,** *15* (17), 1452-1455.

b: C_{16}MIM 1-hexadecyl-3-methyl-imidazolium

4.3.3 Characterization of Pd growing in batch mode within functionalized monolith

In the following catalytic monolith characterizations, hybrid monolith MSM-7 was chosen to carry out the immobilization of Pd nanoparticles because it was well functionalized, bearing the hierarchy macro-, meso- and micro- porosity, with typical hexagonal organization in mesoscale, and it has the high specific surface. The monolith MSM-B was also loaded with Pd nanoparticles for the comparison. As described in section 4.2.1.2, the Pd nanoparticles were impregnated by three ways:

(a) Direct immobilization of Pd nanoparticles in **MSM-7** with $Pd(0)(PPh_3)_4$, labeled **Pd@MSM-7-D.**

(b) Immobilization of Pd nanoparticles in **MSM-7** or **MSM-B** by reducing $Pd(II)(OAc)_2$ with addition of PPh_3, labeled **Pd@ MSM-7-P** or **Pd@ MSM-B-P**, respectively.

(c) Immobilization of Pd nanoparticles in **MSM-7** or **MSM-B** by reducing $Pd(II)(OAc)_2$ without addition of PPh_3, labeled **Pd@ MSM-7-NP** or **Pd@ MSM-B-NP**, respectively.

The main target of the immobilization synthesis is to incorporate the Pd nanoparticles into the monolith structure, with good dispersion. With the TEM analysis, the dispersion situation of Pd nanoparticles could be observed easily.

The Figure 92 demonstrates that, by direct immobilization of Pd nanoparticles in monolith MSM with $Pd(0)(PPh_3)_4$, the Pd nanoparticles with diameter about 3 -10 nm have been deposed inside the interior of grains, but the clustering phenomena is observed. Due to the poor dispersity, this method is not favorable for the immobilization of Pd nanoparticles.

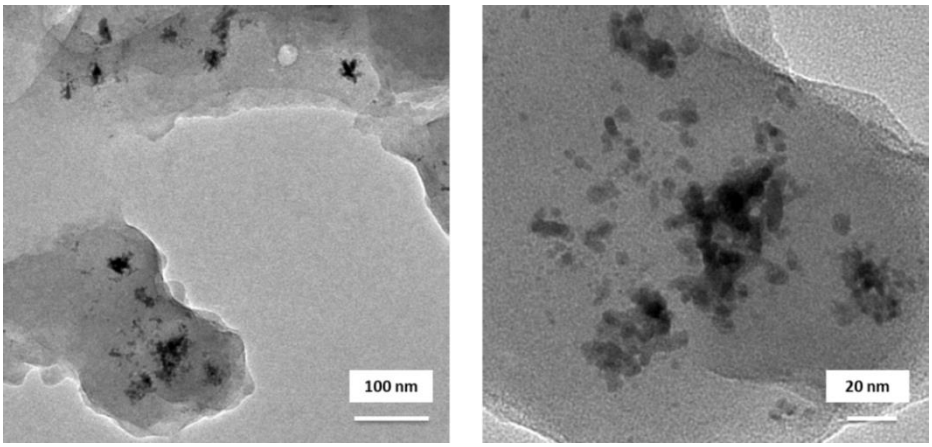

Figure 92 TEM images of Pd@MSM-7-D

Figure 93 shows the effect of addition of PPh_3 on **MSM-B** : in both samples, Pd are impregnated into the monolith, but the dispersion of Pd nanoparticles is better without PPh_3 (Figure 93 (C) and (D)).

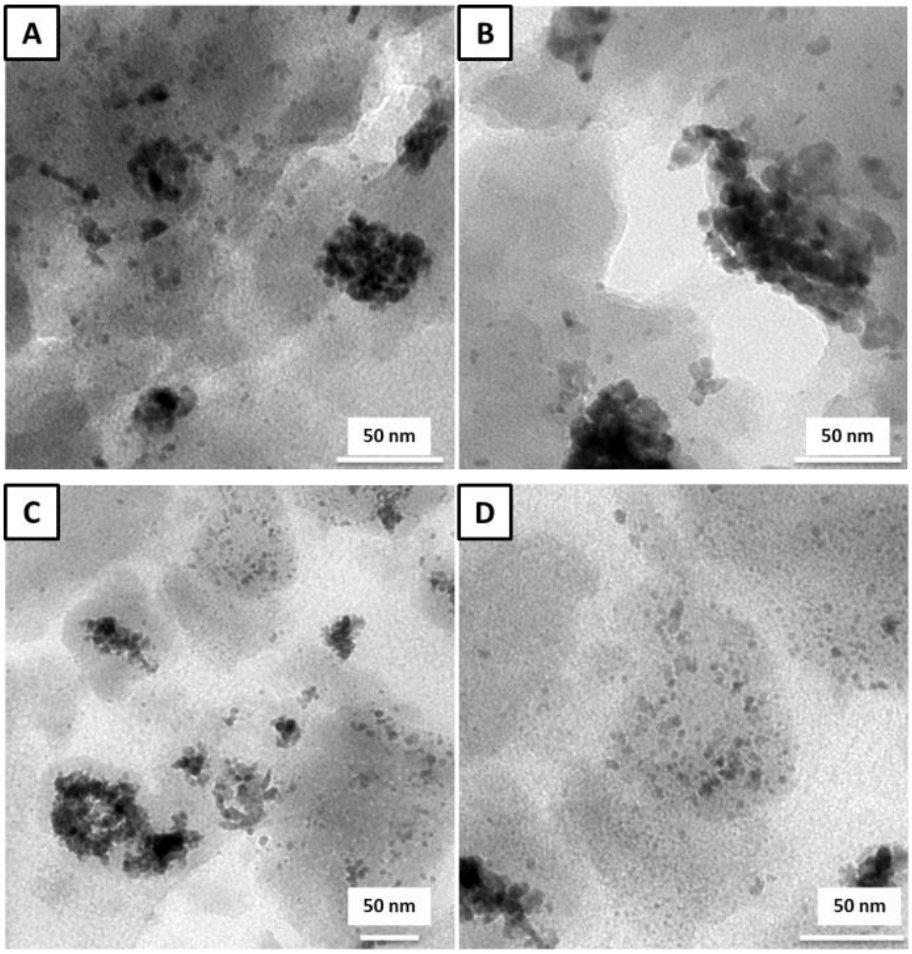

Figure 93 TEM images of (A) (B)Pd@MSM-B-P and (C) (D)Pd@MSM-B-NP. Effect of PPh_3

For the parallel comparison of the effect of PPh_3 with samples based on **MSM-7**, the TEM images are illustrated in Figure 94: with addition of PPh_3, the Pd nanoparticles are only impregnated at the rim of grains prepared, as pointed by the white arrows in Figure 94 (A) and (B); while without PPh_3, the Pd nanoparticles with the diameter about 4-10 nm are well entered and dispersed in the grain.

Comparison of **MSM-B** and **MSM-7**, impregnated without PPh_3, shows that with the well-ordered 2D-hexagonal organization, the Pd nanoparticles are better dispersed in the **Pd@MSM-7-NP** (Figure 94 (C) and (D)), while in **Pd@MSM-B-NP** (Figure 93 (C) and (D)), the Pd nanoparticles aggregate. It indicates that the organization of monolith is favorable for the immobilization of Pd nanoparticles, because palladium precursors can diffuse within the 2D-hexagonal organization more easily. It is worth noting that the 2D hexagonal organization is not observed in all the monoliths modified by Pd nanoparticles.

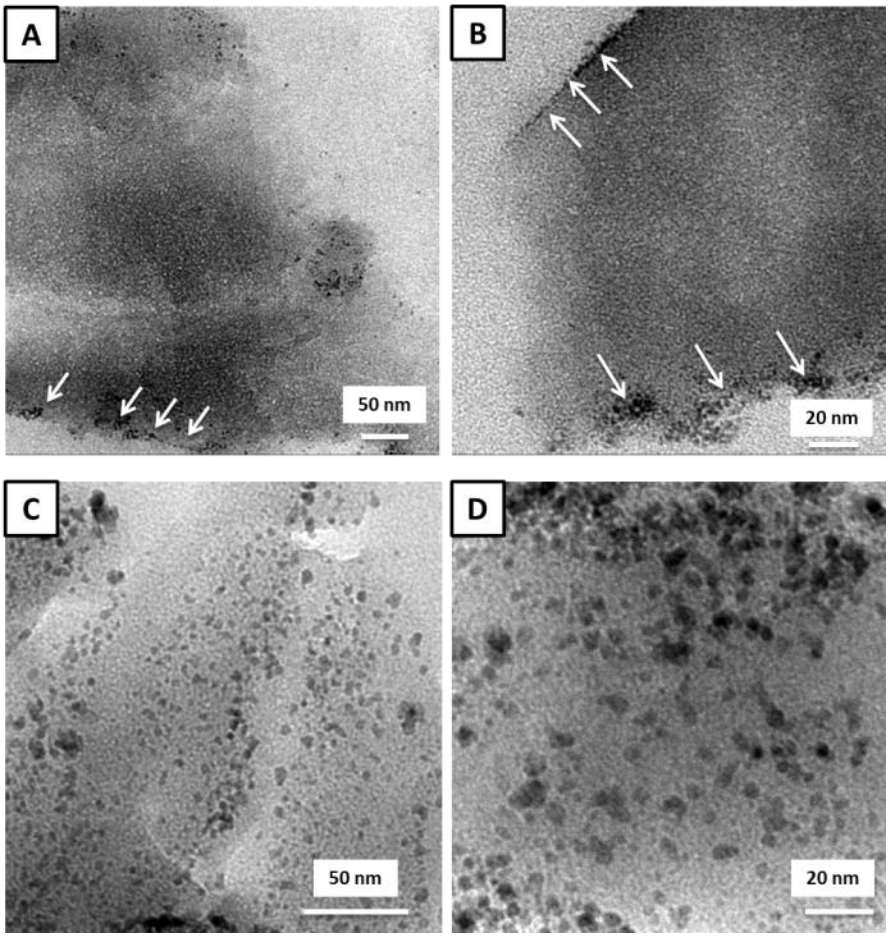

Figure 94 TEM images of (A) (B)Pd@MSM-7-P and (C) (D)Pd@MSM-7-NP. The white arrows pointed out the Pd nanoparticles on the boundary of monoliths

In conclusion, by reducing $Pd(II)(OAc)_2$ without addition of PPh_3 in **MSM-7**, Pd nanoparticles are well dispersed and incorporated in the grains, this is an ideal preparation method. Therefore, in the following investigation of monolithic catalyst in the stainless-steel tube, the same method is adopted.

4.3.4 Characterization of functionalized monolith prepared in the stainless-steel tube

As the preparation of MSM immobilized by Pd nanoparticles has been explored successfully, the hybrid monolith has been synthesized in the stainless-steel tube, it is labeled **MSM-T**. The preparation parameters of reactants are those of **MSM-7**. The difference is that the condensation step of **MSM-T** is performed in stainless-steel tube and its washing step and impregnation of Pd step are conducted with continuous flow.

The prepared **MSM-T** was analyzed by CP-MAS NMR firstly to characterize the result of co-condensation in the tube. The ^{29}Si NMR of **MSM-T** (Figure 95 (A)) indicated the similar results to **MSM-7**. T^3 and T^2 proved the successful functionalization, which was confirmed by the peak of

C-SH group in ^{13}C NMR (Figure 95 (B)). The peak around 60 ppm and 15 ppm reveals the presence of SiO-CH_2CH_3 group in resulting monolith.

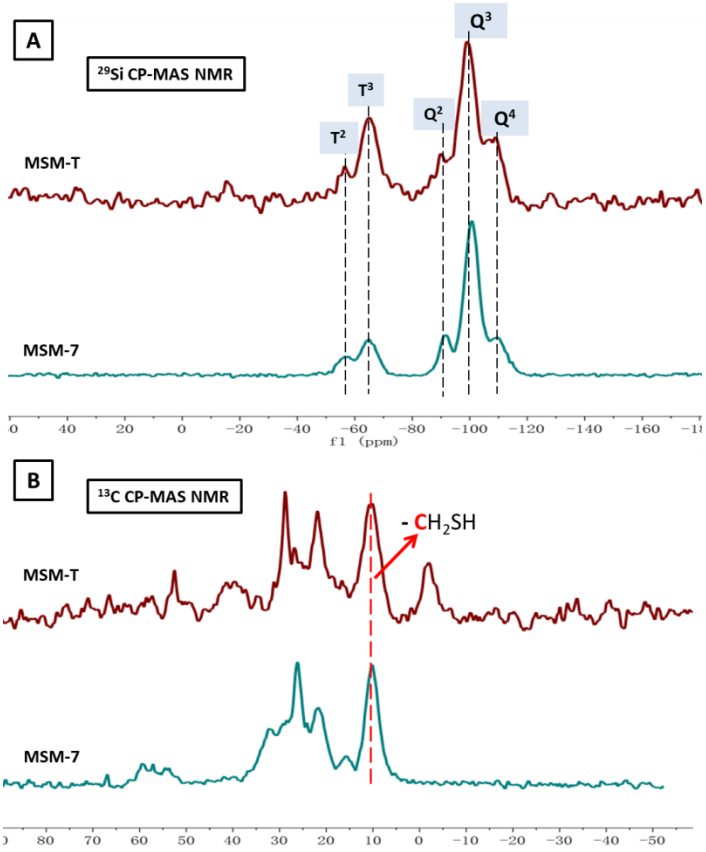

Figure 95 CP-MAS NMR analysis of MSM-T and comparison with MSM-7: (A) ^{29}Si CP-MAS NMR of MSM-T and MSM-7 (B) ^{13}C CP-MAS NMR of MSM-T and MSM-7

The condensation degree and proportion of each type peak of **MSM-T** is summarized in Table 12 with the comparison of **MSM-7** (detailed values in Annex A-16 Table A15). The higher %C.D.T indicates the functionalization of **MSM-T** is more effective compared with **MSM-7**.

Table 12 Comparison of condensation degree of MSM-T and MSM-7

	MSM-T	**MSM-7**
%C.D.T	93.9%	92.1%
%C.D.Q	78.5%	78.4%

The scheme of co-condensation steps in the tube is presented in Figure 96. When the prepared emulsion was transferred into the tube, we assume that the glass wall was activated by the acidic solution, therefore the co-condensation was conducted between the hydroxylated silica wall, the hydrolyzed MPTS and TEOS.

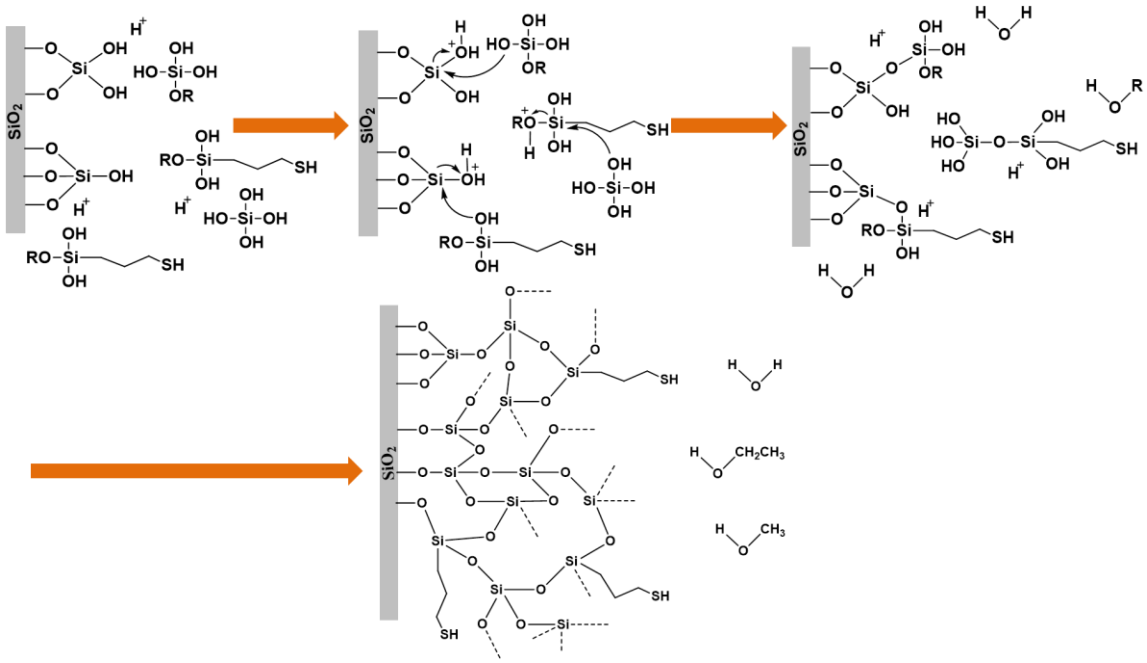

Figure 96 Co-condensation step of sol-gel process in the stainless-steel tube pre-coated with glass

4.3.5 Characterization of Pd growing by continuous flow within functionalized monolith

Under continuous flow, Pd nanoparticles have been impregnated in the **MSM-T** in the stainless-steel tube. The resulting catalyst named **Pd@MSM-T** has been analyzed by TEM as shown in Figure 97 and compared with the **MSM-T**.

The **MSM-T** (Figure 97 (A) and (B)) exhibits the same well-ordered 2D-hexagonal structuration as **MSM-7**, with the interval of meso-organization about 5 nm. It indicates that the co-condensation conducted well in the stainless-steel tube. The Pd nanoparticles have been successfully incorporated into the monolith as demonstrated in Figure 97 (C) and (D). Although the dispersion was not as ideal as the **Pd@MSM-7** because in some areas the Pd nanoparticles have aggregated, none the less, the Pd nanoparticles are reasonably dispersed in the monolith.

The aggregation phenomenon of Pd nanoparticles might be explained by the Oswald ripening, which describes the phenomenon of coarsening - the large particles grow at the expense of small particles[124]. This phenomenon has been observed in the growth of Pd nanoparticles[125]. In our case, the continuous flow might promote the Oswald ripening, because once some Pd nanoparticles have been immobilized in the monolith, the following small Pd nanoparticles in the continuous flow could continue to aggregate on the former larger Pd fixed.

---

[124] Ratke, L.; Voorhees, P. W., *Growth and Coarsening: Ostwald Ripening in Material Processing*, Eds. Springer Berlin Heidelberg: 2002; pp 117-126.

[125] (a) Gholami, R.; Alyani, M.; Smith, K., *Catalysts* **2015,** *5* (2), 561-594. (b) Kang, S. B.; Lim, J. B.; Jo, D.; Nam, I. S.; Cho, B. K.; Hong, S. B.; Kim, C. H.; Oh, S. H., *Chemical Engineering Journal* **2017,** *316*, 631-644.

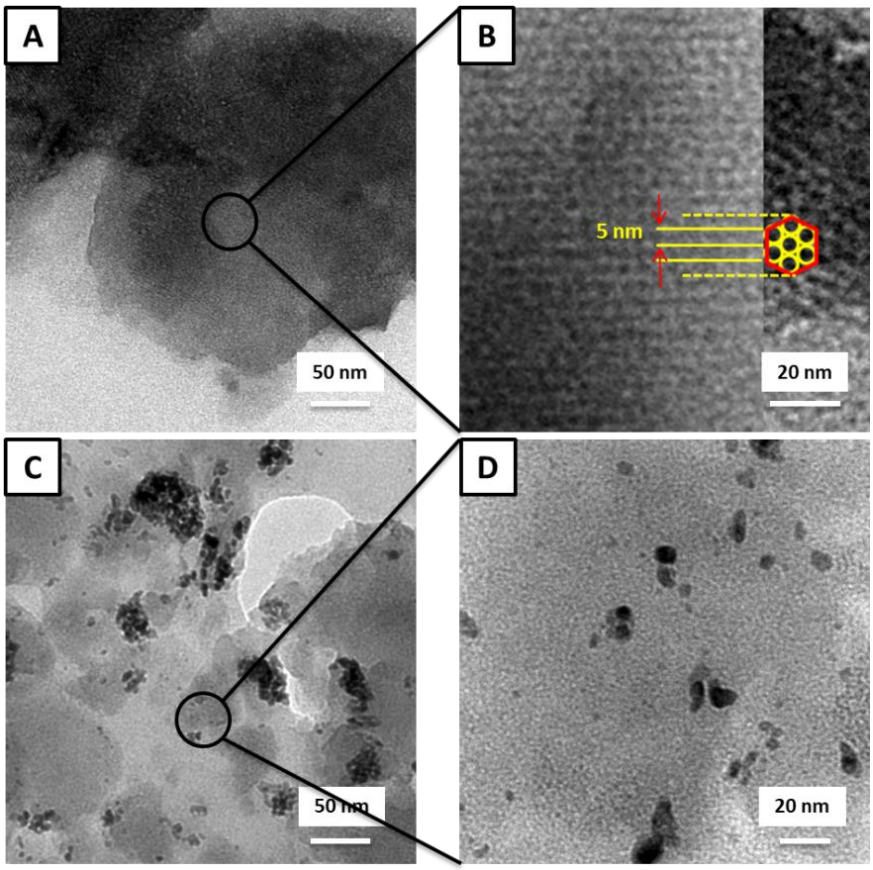

Figure 97 TEM images of (A)(B)MSM-T before impregnation and (C)(D)Pd@MSM-T after impregnation of Pd nanoparticles

The following EDS analysis has been investigated for **MSM-T** and **Pd@MSM-T**, and **MSM-7** for comparison. The detected sulfur (S) proved again the successful functionalization of monolith as demonstrated by CP-MAS NMR. The unstable ratio of S/Si might indicate the non-uninform distribution of -SH group in the monolith.

The atomic ratios of O on Si measured by EDS in three samples are all a little higher than 2: O/Si for **MSM-7** is about 2.12 and for **MSM-T** is 2.3. With the deconvolution calculations of NMR analyses of **MSM-7** and **MSM-T**, the estimated O/Si ratio for **MSM-7** is 2.24 and for **MSM-T** is 2.18 (detailed calculation in Annex A-18 Table A16). Thus, the high O/Si ratio is entirely reasonable.

Table 13 EDS analysis of MSM-7, MSM-T and Pd@MSM-T

Sample name	**MSM-7**	**MSM-T**	**Pd@MSM-T**
Elements	**Atomic%**	**Atomic%**	**Atomic%**
O	65.5	68.7	68.3
Si	30.9	29.6	23.2
S	3.6	1.7	3.8
Pd	–	–	4.7

The Pd incorporated in **MSM-T** by continuous flow method was up to 19.6% in weight, much higher than the commercial catalyst **Pd@Al_2O_3** (5.3 wt %, confirmed by EDS analysis) we used in the packed-bed microreactor. The characteristics of **Pd@MSM-T** are summarized Table 14 and compared with different monolithic catalysts in publications in recent years. It is obvious that **Pd@MSM-T** has a quite high porosity and Pd loading, proving that the MSM prepared and the continuous immobilization method in our work are extraordinary effective.

Table 14 Monolithic catalysts with Pd on different supports published in recent years

Monolithic catalyst support	Immobilization method [a]	V_{tube} (ml) [b]	Density (g/cm^3)	Porosity	Content Pd (wt %)	Specific Surface (m^2/g)
MSM-T	continuous	**1.256**	**0.0179**	**0.987**[c]	**19.6**	**1260**
Al_2O_3 (powder)	batch	-	3.97	-	5.3	110
ASM-gB[d] [110(c)]	batch	-	0.14	0.92	3.9	300
MSM-gB[e] [110(c)]	batch	-	0.10	0.88	4.1	400
MSM-B[f] [110(c)]	batch	-	0.09	0.93	3.9	53
SiO_2-Pyrrol [110(f)]	batch	-	0.07	0.962	3.9	392
SiO_2-$ArSO_3$ [113]	continuous	0.283	-	-	4.6	322
SiO_2-PMHS[g] [126]	continuous	1.256			0.9	220
SiO_2-[Bmim]BF_4[h] [119]	batch		0.16	0.89	0.99	187
Polymer [127]	batch	-	-	-	0.3	305
Polymer [120]	batch	-	-	-	5	482
CGO[i] [128]	batch	-	-	-	4.73	-
TiO_2 [111(f)]	continuous	0.377	-	-	0.24	148

a: Immobilization of Pd are either in the flask (batch) or in continuous flow (continuous)

b: V_{tube} is the volume of continuous flow reactor

c: Porosity of MSM-T is estimated approximately by density(MSM-T)/skeletal density, the skeletal density for MSM is 1.36 g/cm^3 [110(e)]

d: ASM-gB is silica monolith functionalized by amino group by grafting method

e: MSM-gB is silica monolith functionalized by mercapto group by grafting method

f: MSM-B is silica monolith functionalized by mercapto group by co-condensation method

g: PHMS: Polymethylhydrosiloxane

h: [Bmim]BF_4 : 1-Butyl-3-methylimidazolium tetrafluoroborate

i: CGO: Carbon based graphene oxide

4.4 Conclusion

In the light of the state of the art of monolithic catalyst, the silica-based monoliths exhibit distinct advantages; nevertheless, the lack of effective means for synthesizing porous silica-based

[126] Pelisson, C. H.; Nakanishi, T.; Zhu, Y.; Morisato, K.; Kamei, T.; Maeno, A.; Kaji, H.; Muroyama, S.; Tafu, M.; Kanamori, K.; Shimada, T.; Nakanishi, K., *ACS Applied Materials & Interfaces* **2017,** *9* (1), 406-412.

[127] Jumde, R. P.; Marelli, M.; Scotti, N.; Mandoli, A.; Psaro, R.; Evangelisti, C., *Journal of Molecular Catalysis A: Chemical* **2016,** *414*, 55-61.

[128] Nakhate, A. V.; Yadav, G. D., *ChemistrySelect* **2016,** *1* (13), 3954-3965.

monolithic catalyst in the industrial grade continuous flow reactor makes it only applied in lab scale application.

In order to make a breakthrough over this, the optimized preparation condition range for native silica monolith and functionalized monolith has been investigated. Then the mechanically stable mercapto-functionalized silica monolith has been prepared with success in polymer tube and characterized, demonstrating it possesses the flow-through macropores, typical hexagonal organization of mesopores and micropores, high specific surface and scarcely any shrinkage.

Same monolith then was synthesized by co-condensation method in a stainless-steel tube with the inner wall pre-coated by glass. Afterwards, palladium nanoparticles have been immobilized within the monolith in this tube by a continuous flow method. The high content of Pd in the monolithic catalyst highlights the effectiveness of the continuous *in-situ* incorporation of Pd nanoparticles. The practicability of prepared microreactor with monolithic catalyst will be verified by the following catalytic test.

Chapter 5 - Study of *p*-nitrophenol hydrogenation as model reaction in the monolithic microreactor and comparison with packed-bed microreactor

In this chapter, the monolithic catalyst **Pd@MSM-T** in the microreactor prepared in the chapter 4 is tested on the transfer hydrogenation of *p*-nitrophenol (PNP) with formic acid (FA), and then its properties are compared with that of the commercial catalyst in packed-bed microreactor. A first experimental section presents the influence of reaction parameters such as temperature, flow rate and initial concentration of reactants, then a kinetic model of the reaction under stationary conditions is established and the dynamic study of the reaction is presented. Last but not least, the performances of monolithic catalyst and commercial catalyst (Pd@alumina powder) are compared, including the catalyst performance, the dynamic and kinetic study and the pressure drop.

5.1 Experimental section

5.1.1 Experimental conditions

The same transfer hydrogenation of PNP by FA is chosen to compare the performance of the new Pd@silica based monolith catalyst with commercial Pd@alumina powder presented in Chapters 2 and 3. The characteristics of microreactor are listed in Table 15.

Table 15 Characteristics of the monolithic microreactor

Symbol	Parameter	Unit	Dimension
D_{ML}	Internal diameter of monolithic microreactor	mm	4
L_{ML}	Length of monolithic microreactor	mm	100
V_{ML}	Volume of tube of monolithic microreactor	mL	1.256
$m_{cat,ML}$	Catalyst mass	mg	22.5
$m_{pd,ML}$	Palladium mass	mg	4.4

5.1.2 Experimental set-up and protocol

The on-line HPLC analysis (protocol 3 described in the section 2.1.4), which allows the quantitative analysis of both PNP and PAP directly at the outlet of the microreactor, is adopted. The experimental set-up is similar to the set-up in Figure 34 of Chapter 2; the only difference is that the monolithic microreactor replaces the packed-bed microreactor. Some experiments with on-line PDA analysis (protocol 2) are performed in order to observe the dynamic behavior of the new catalyst.

The full protocol is the same as presented in the section 2.1.4.2, including the analysis of the feed reactor mixture, a reaction sequence of 60-200 min with periodic analysis of the reactor effluent, and the washing process with water at 40℃ after each reaction.

5.1.3 Experimental condition range

The experimental conditions vary in the range summarized in Table 16, in order to establish the reaction rate expression. 45 points have been measured, around a base point defined by concentrations C_{PNP}^{0} = 0.6 mmol/L and C_{FA}^{0} = 1.8 mmol/L (i.e. in a stoichiometric ratio), 1 mL/min flow rate and at 40°C. All experiments are at least doubled. The same calibration equation as discussed in 2.1.4.3 is used to analyze the quantity of PAP and PNP.

Table 16 Range of experimental conditions for flow reaction with monolithic catalyst

Symbol	Parameter	Unit	Dimension
Q	Flow rate	mL/min	0.2 – 1
T	Temperature	°C	40 – 80
$C_{PNP}°$	Initial concentration of *p*-nitrophenol	mmol/L	0.6 – 4.5
$C_{FA}°$	Initial concentration of formic acid	mmol/L	(1.5 – 6) × $C_{PNP}°$

5.2 Effect of reaction parameters on conversion under stationary conditions

5.2.1 Evaluation of catalyst stability

The establishment of steady-state was checked during dynamic study (see 5.4). The evolution of monolithic catalyst in the microreactor is verified by repeating the reaction under the same “base” condition over about 50 days period. The results on Figure 98 show an evident dispersion, with a standard deviation of the PNP conversion X about 18.3% (C_{PNP}^{0}=0.6 mmol/L) and 9% (C_{PNP}^{0}=1 mmol/L). The conversion of the final point (53 days after the first point) is 0.46, still superior to the average value of X (0.38). It indicates that, in spite of the poor reproducibility, the activity of the new monolithic catalyst is stable with time.

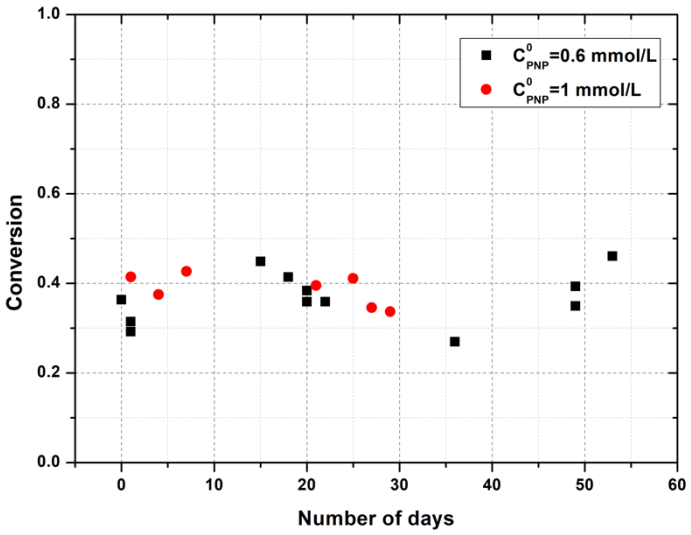

Figure 98 Catalyst evolution over 53 days period. C_{PNP}^0= 0.6 or 1 mmol/L, C_{FA}^0/C_{PNP}^0=3, Q = 1 mL/min, T=40°C

5.2.2 Influence of temperature and flow rate on the PNP conversion

The effect of temperature and the flow rate on the conversion of PNP were studied and the results are summarized in Figure 99. Graph (A) shows that the temperature does not have any effect on the conversion of PNP in monolithic microreactor. A significant effect of flow rate is observed clearly on Graph (B). As expected, the conversion increased with the decrease of flow rate, i.e. with increasing residence time.

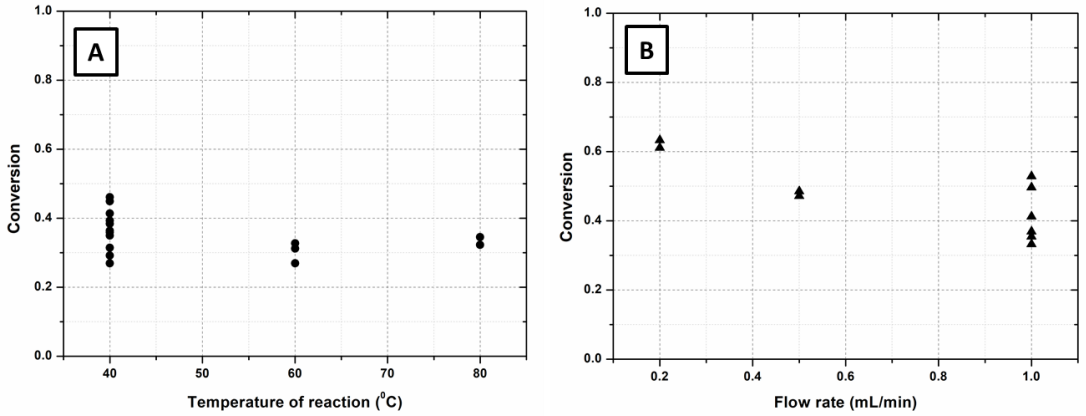

Figure 99 Effect of (A) reaction temperature and (B) flow rate on the PNP conversion. (Condition: A : C_{PNP}^0 =0.6 mmol/L, C_{FA}^0=1.8 mmol/L , Q = 1mL/min ; B : C_{PNP}^0 =2 mmol/L, C_{FA}^0= 6 mmol/L ,T=40°C)

5.2.3 Influence of concentrations of reactants on the PNP conversion

The influence of initial concentration of PNP and FA on conversion of PNP has been investigated. As shown in Figure 100 (A), despite of the dispersion of the results, the conversion of PNP always varies in the range of 0.3-0.5, regardless of the large variation of C_{PNP}^{0} from 0.5 mmol/L to 4.5 mmol/L. This indicates the conversion of PNP is independent of the initial concentration of PNP. In Figure 100 (B), the conversion of PNP increases along with the augmentation of C_{FA}^{0}, exhibiting roughly a linear relation. It could indicate a first order reaction with respect to FA.

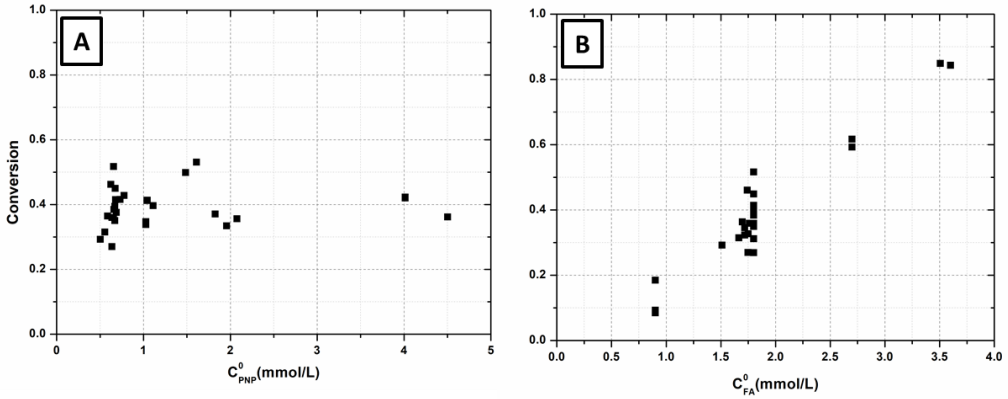

Figure 100 Effect of initial concentration of (A) PNP and (B) FA on the PNP conversion. (Reaction conditions : A : C_{FA}^{0}/C_{PNP}^{0}=3, T=40°C, Q = 1mL/min ; B : C_{PNP}^{0} =0.6 mmol/L, T=40°C, Q = 1mL/min)

5.3 Kinetic analysis of the reaction in the monolithic reactor

The kinetics model of the reaction in monolithic microreactor is based on the experimental results of on-line HPLC analysis at the end of a reaction sequence of 60-200 min (steady-state). The data set is composed of 45 points:

- Temperature = 40°C, except 3 points at 60°C and 2 at 80°C;
- Flow rate 1 mL/min except 2 points at 0.2 mL/min and 2 at 0.5 mL/min
- Concentrations C_{PNP}^{0} = 0.6 mmol/L and C_{FA}^{0} = 1.8 mmol/L (i.e. stoichiometric ratio, m = $C_{FA}^{0}/3\,C_{PNP}^{0}$ =1) at base point, C_{PNP}^{0} varied between 0.6 and 4 mmol/L, and m varied between 0.5 and 2.

For reminding, the steady-state plug flow reactor model is used to represent the operation in the monolith reactor. The PNP material balance on an elementary slice of reactor containing a volume of catalyst dV_{CAT} is :

$$Q\,C_{PNP} = Q(C_{PNP} + dC_{PNP}) + r \cdot dV_{CAT}$$

$$<==> \qquad -Q \cdot \frac{dC_{PNP}}{dV_{CAT}} = r$$

$$<==> \qquad \frac{V_{CAT}}{Q} = \int_{C^\circ}^{Cf} \frac{-dC_{PNP}}{r} \qquad (4)$$

with the r, the volumetric reaction rate expressed per catalyst volume unit.

The first order reaction rate, relative to FA concentration is: $r = k\,C_{FA}$ **(11)**

FA concentration depends on PNP conversion X :

$$C_{FA} = 3\,C^0_{PNP}\,(m - X)$$

with the stoichiometric ratio m= $C_{FA}^0/3C_{PNP}^0$.

$$\frac{V_{CAT}}{C^0_{PNP}\cdot Q} = \int_0^X \frac{dX}{r} = \int \frac{dX}{3kC^0_{PNP}\,(m - X)}$$

$$Da = \frac{3\,k\,V_{CAT}}{Q} = \int \frac{dX}{(m - X)} = -Ln\left(1 - \frac{X}{m}\right) \qquad \textbf{(12)}$$

$$<==> \qquad X_{CALC} = m\left(1 - \exp\left(\frac{3\,k\,V_{CAT}}{Q}\right)\right) \qquad \textbf{(13)}$$

Because of the strong dispersion of data, the mean values of measurements made in the same experimental conditions are considered for the first kinetics trials, they compose a reduced data set (Annex A-19). The rate constant $3kV_{CAT}$ is calculated onto reduced data using Eq.(**12**), we obtain 0.486 mL/min. As the porosity of monolithic materials is about 0.987 (estimated in chapter 4), so k ≈ 9.94 min^{-1}, with $V_{CAT} \approx V_{ML}$*(1-0.987) = 0.0163 mL. The conversions calculated with this value and Eq.(**13**) are compared with experimental ones for all data in Figure 101.

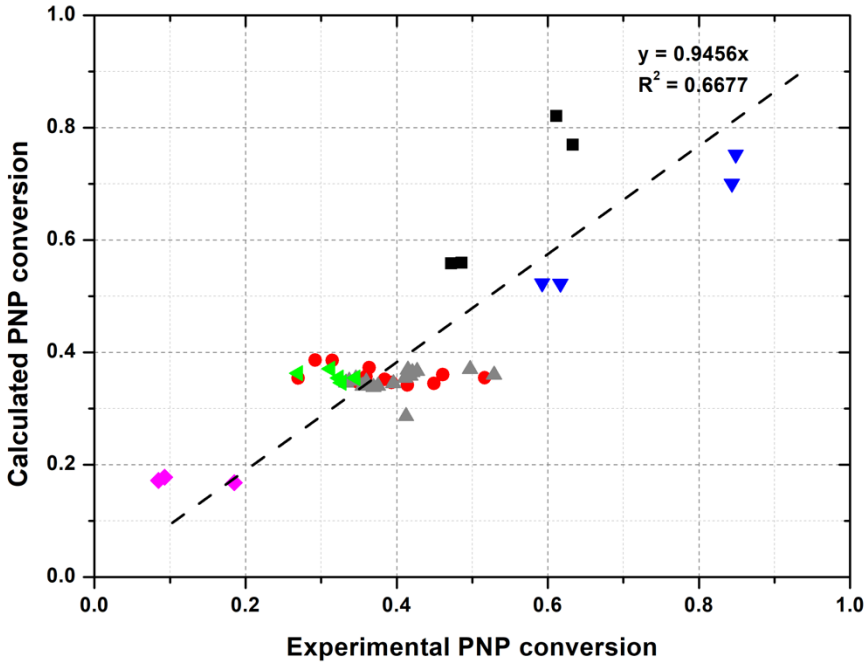

Figure 101 Comparison of calculated X and experimental X. (X calculated with first order reaction rate with respect to FA with k= 9.94 min^{-1}. Q=1mL/min except black points; T=40°C except green points. Red: base points; Grey m≈1. Bleu FA excess (m>1); Purple FA deficit (m<1))

Considering the large dispersion of data, the model $r=kC_{FA}$ gives a good representation of variation of PNP conversion. When all parameters remain constant except the FA concentration,

the influence of FA concentration (or stoichiometric ratio) is very clear on reduced data as shown in Figure 102.

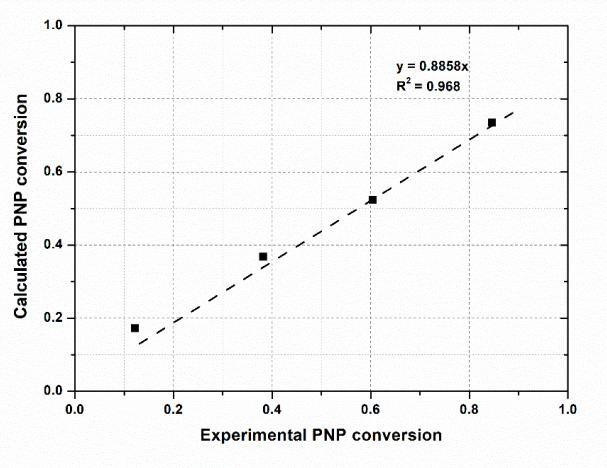

Figure 102 Comparison of calculated X with mean values of experimental X. C_{FA} varies from 0.9 to 3.5 mmol/L; $C_{PNP}{}^{0}$= 0.6 mmol/L, Q=1 mL/min, T=40°C.

As all experimental conditions except temperature are the same on red and green points, their comparison on Figure 101 confirms the absence of temperature influence noted in 5.2.2. This could indicate that adsorption phenomenon is rate determining. Actually, when the reaction rate is proportional to the quantity of adsorbed molecules, at low surface coverage, the kinetic expression reduces to $r = k \cdot K \cdot C$[129]. Thus, the experimentally observed rate constant k_{EXP} equals k·K, where k is the reaction rate constant for the surface reaction and K the adsorption equilibrium constant. K decreases with increased temperature by the factor $e^{\lambda/RT}$. As $k = Ae^{-E/RT}$, therefore, the apparent activation energy E_{app}= E-λ, is lower than the true activation energy of the surface reaction E.

It could be noted that X_{EXP} is slightly higher than predicted by the model when the reaction rate is high, i.e. at high FA concentration. This deviation cannot be attributed to the saturation of the surface, that would lead to an opposite trend, as indicated by a Langmuir Hinshelwood model.

5.4 Dynamic studies

The sequence washing-reaction results in a step perturbation at the entrance of the reactor: at first, the catalyst is under pure water. Then, the reactant mixture is fed at constant flow rate and composition: the mixture reacts in the reactor according to the time evolved since its entrance.

Both on-line PDA UV and on-line HPLC were used to observe and quantify the variation of the composition of reaction mixture flowing out of the reactor. The profiles of concentration are shown on Figure 103 and Figure 104. On both figures, the concentration of PNP exhibits a slight shoulder at the beginning of the sequence and then stabilizes rapidly. Meanwhile, the

[129] Satterfield, C. N., *Heterogeneous catalysis in industrial practice. SECOND EDITION*. McGraw Hill :1991.

concentration of PAP increases and reaches the stationary value after a little longer time than PNP, as shown by on-line HPLC analysis (Figure 103). Unlike with the commercial catalyst, it is noteworthy that the intermediate I250 or other intermediate have not been detected neither at 250 nm nor at other wavelengths, as illustrated by red line at 250 nm in Figure 104(A) and by 3D-PDA UV in Figure 104(B).

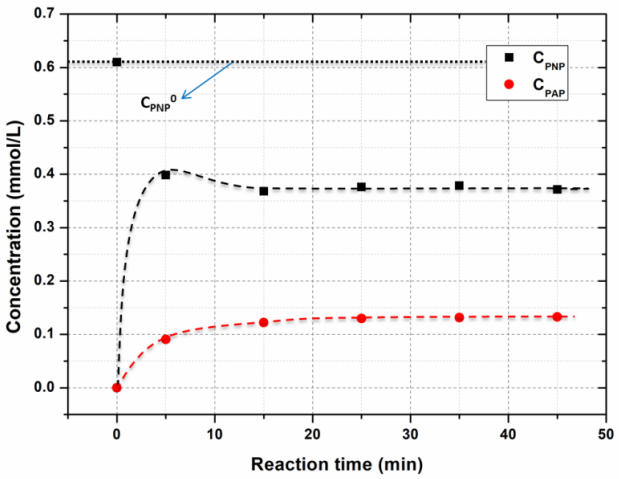

Figure 103 Concentration profile of PNP and PAP at outlet of reactor detected by on-line HPLC (Reaction condition: C_{PNP}^0 =0.6 mmol/L, C_{FA}^0 =1.8 mmol/L,T=40°C, Q = 1mL/min)

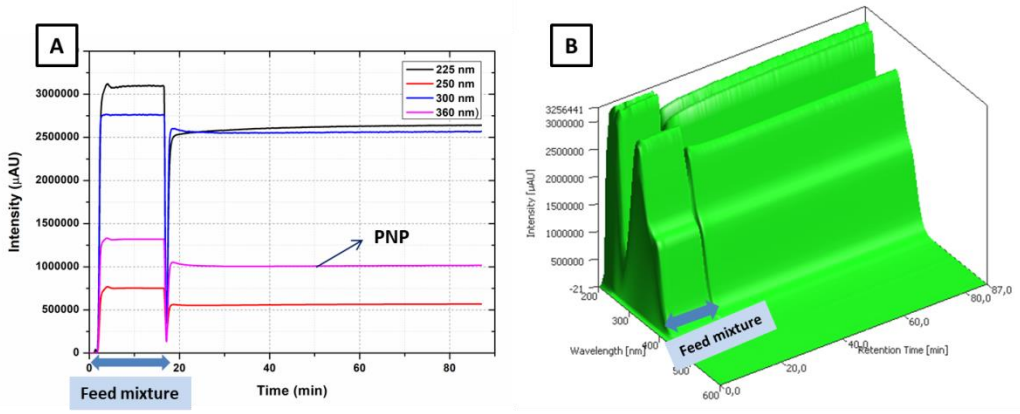

Figure 104 On-line PDA UV analysis of the reaction sequence (A) variation of 4 wavelength (225, 250, 300, 360 nm) (B) 3D spectrum (Time-Wavelength-Intensity) (Reaction condition: C_{PNP}^0 =0.6 mmol/L, C_{FA}^0 =0.9 mmol/L, T=40°C, Q = 1mL/min)

The deviation between PAP formed and PNP consumed was calculated for each experiments, at the end of the reaction sequence, i.e. at steady state. The average of the absolute value of deviation is 7%, while the average deviation is less than 1 %, indicating random deviations. So, it can be concluded that, at steady-state, PAP is the only product of PNP hydrogenation, at least within the limits of analytical precision.

However, on-line HPLC analysis has allowed the detection of I250 during the washing sequence with water (red line in Figure 105). This indicates that I250 is indeed formed during the reaction as an intermediate, but in monolithic microreactor, it is adsorbed on the catalyst support and probably a part is quickly converted into the final product, therefore it does not flow out of the reactor during the reaction sequence. The purple and blue dashed lines correspond to the decrease of PAP and PNP, respectively. The first HPLC chromatogram is that of the mixture after 10 min washing. PNP concentration is reduced by a factor 7 and PAP concentration by 20. Hence, the washing sequence is quite effective for PNP and PAP. However, concentration of I250 decreases very slowly, indicating a difficult desorption of I250. Figure 103 shows that there is no catalyst deactivation during a reaction sequence, therefore I250 could be adsorbed on silica support rather on Pd nanoparticles.

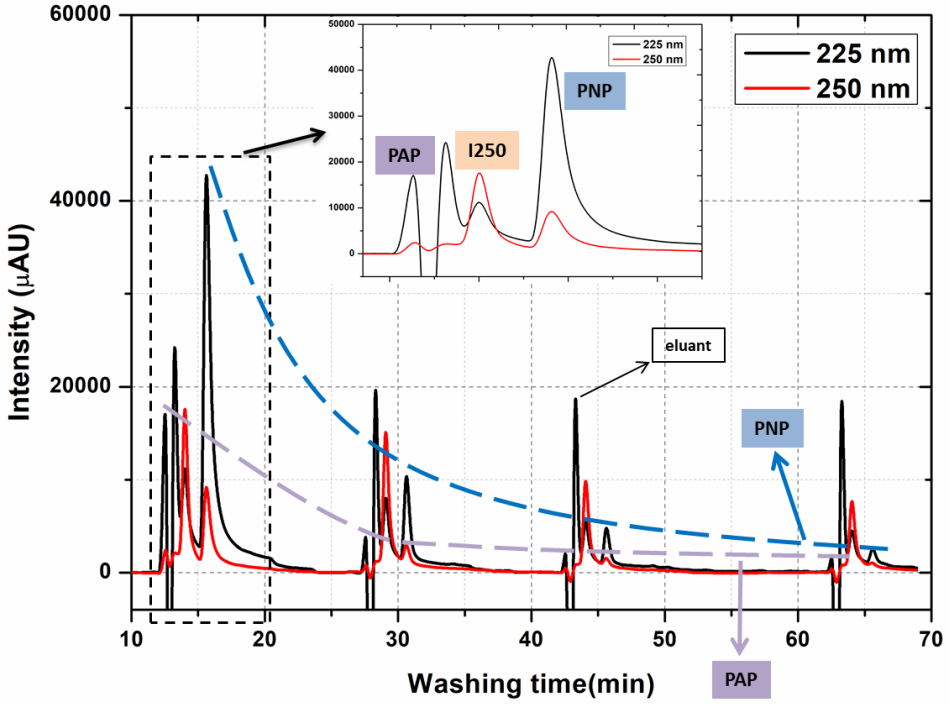

Figure 105 On-line HPLC analysis of the washing process of the reactor (purple dashed line: PAP, blue dashed line: PNP. Washing condition: 40°C with water for 1h)

5.5 Comparison of packed-bed and monolith microreactors

The main subject of comparison of commercial Pd@alumina powder catalyst and new Pd@silica monolithic catalyst concerns their activity towards transfer hydrogenation of PNP reaction. The catalyst performances are firstly compared by calculating the turnover frequency. A subsidiary comparison concerns the pressure drop and permeability of the catalyst, which is an important criterion for industrial applications. The differences in dynamic studies and kinetic models are discussed afterwards.

5.5.1 Catalyst performance in transfer hydrogenation reaction

TOF (turnover frequency), defined as the TON (the turnover number, the moles of substrate converted per the moles of catalyst used) per unit time, is used to compare the catalyst performance of the commercial catalyst in packed-bed microreactor (**Pd@Al_2O_3**) with the catalytic monolith **Pd@MSM-T** in the monolithic microreactor. In flow reactor, TOF is calculated as:

$$TOF_{flow} = Q_{MR} \cdot C_{PNP}^{0} \cdot X / n_{Pd}$$

with

$Q_{MR:}$ flow rate in microreactor

n_{Pd} : moles of palladium in the reactor

C_{PNP}^{0} : initial concentration of PNP in the feed of microreactor

X : conversion of PNP at the outlet of microreactor

The comparison of TOF is listed in Table 17. The n_{Pd} of **Pd@Al_2O_3** is 0.301 mmol and the n_{Pd} of **Pd@MSM-T** is 0.042 mmol. The conversion of PNP is the average value of all measurements in the same condition.

Table 17 TOF of commercial catalyst and monolithic catalyst (Q = 1 mL/min, T = 40°C)

C_{PNP}^{0}	C_{FA}^{0}	$X_{packed\text{-}bed}$	$X_{monolith}$	$TOF_{packed\text{-}bed}$	$TOF_{monolith}$	$\frac{TOF_{monolith}}{TOF_{packed-bed}}$
mmol/L	mmol/L			h^{-1}	h^{-1}	
0.6	1.8	0.625	0.382	0.075	0.327	4.360
0.6	0.9	0.161	0.122	0.019	0.104	5.474
0.6	3.6	1	0.846	0.120	0.725	6.042
1	3	0.787	0.384	0.157	0.549	3.497
2	6	0.916	0.408	0.366	1.167	3.189
4	9	0.959	0.398	0.765	2.274	2.973

The TOF of monolithic catalyst **Pd@MSM-T** is about 3 - 6 times larger than that of commercial catalyst **Pd@Al_2O_3**, that demonstrates the excellent activity of **Pd@MSM-T.** When initial concentration of PNP increases, the ratio of $TOF_{monolith}/TOF_{pack\text{-}bed}$ decreases, as expected from the difference in reaction order.

The highlighted catalytic performance of monolithic catalyst probably owes to the following reason: as shown in Figure 106(A), the monolith skeleton is heavily loaded by Pd nanoparticles (19.6 wt%), and the large surface area of monolith (1260 m^2/g) give large accessible surface between reactants and Pd, while in the commercial **Pd@Al_2O_3** powder catalyst, the poor loading of Pd (5.3 wt%) and the small surface area (110 m^2/g) could limit the sufficient contact between reactants and Pd.

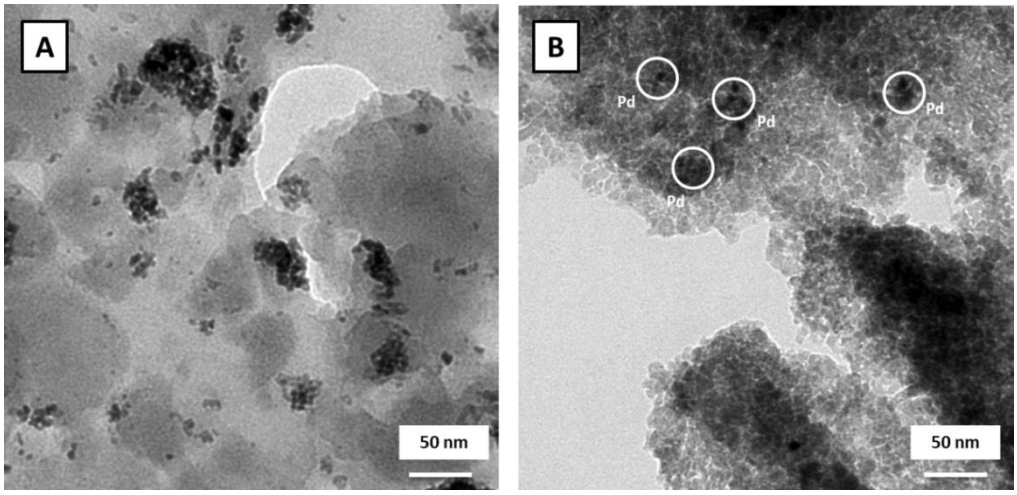

Figure 106 TEM images of (A) monolithic catalyst Pd@MSM-T and (B) commercial Pd@Al_2O_3 powder catalyst (Pd pointed by white circle)

5.5.2 Pressure drop and permeability

Mechanical stability and hydraulic permeability of the packed-bed and monolithic microreactor are determined by analyzing the pressure drop - flow rate relationship, which characterizes the resistance to hydraulic flow and provides additional information in assessing process economics. For comparison, pressure drop at 1 mL/min is 25 bar for packed-bed microreactor, and 5 bar for monolithic microraector.

According to Darcy's law, the pressure drop over the reactor length ($\Delta p/L$) is related to the permeability as follows [130]:

$$\frac{\Delta p}{L} = \frac{\eta}{K_D}\frac{Q}{A_c} \qquad (\mathbf{14})$$

where

η is the viscosity of liquid (water in our study, with dynamic viscosity 0.89 mPa·s at 25℃)

K_D is the Darcy permeability

Q is the volumetric flow rate

A_c is the cross-sectional area of tube ($A_{c,PB}$ = 0.157 cm^2 for packed-bed microreactor and $A_{c,ML}$ = 0.126 cm^2 for monolithic microreactor)

Hence, the pressure drop over the reactor length ($\Delta p/L$) is in a linear relation with the volumetric flow rate (Q), with slope of $\eta/(K_D \cdot A_c)$.

The pressure drop is measured by KELLER digital Manometer LEO 2. The measurement is repeated three times for each flow rate of each reactor and the average value is utilized. The pressure drop (Δp) divided by tube length (L_{PB} = 4 cm for packed-bed microreactor and L_{ML} = 10 cm for monolithic microreactor) is summarized in Figure 107 with the variation of flow rate (Q).

[130] Hlushkou, D.; Tallarek, U., *Journal of Chromatography A* **2006,** *1126* (1), 70-85.

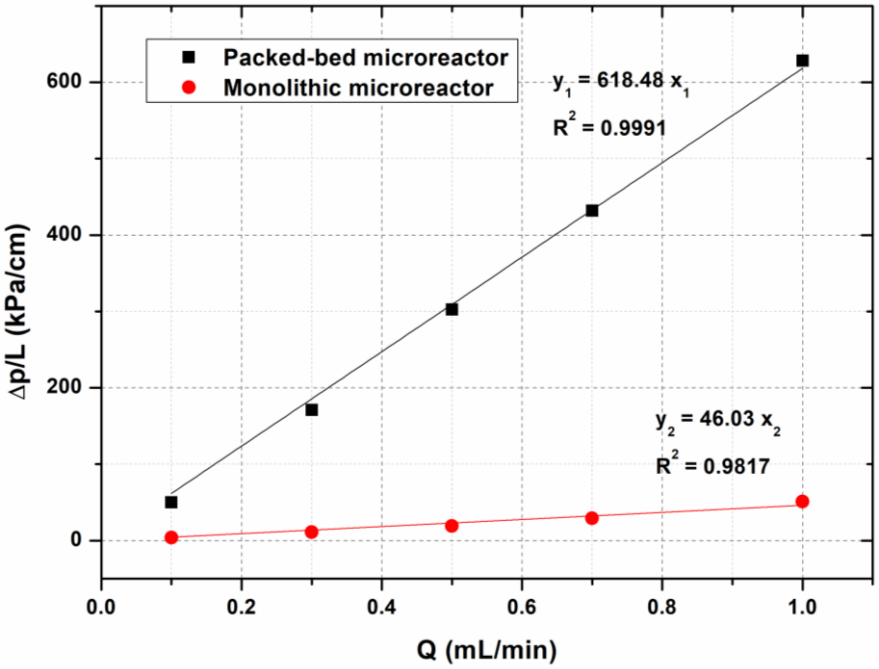

Figure 107 Pressure drop-flow rate in packed-bed and monolithic microreactors

With equation **(14)**, the permeability of packed-bed microreactor is $K_{D,PB}$ = 1.53×10^{-14} m^2, and that of monolithic microreactor is $K_{D,ML}$ = 2.57×10^{-13} m^2, about 17 times higher. The high permeability of monolithic catalyst matches well with its highly porous nature, which can enhance the through-flows of fluid in macropores.

The typical linear relationship between Δp/L and flow rate indicates the mechanically stable bed morphology of monolithic catalyst, resistant to time and use [131]. It is also obvious that the pressure drop over the reactor length of monolithic microreactor is about 10 times smaller than that of packed-bed microreactor. It reveals that the monolithic microreactor have an advantage over pack-bed microreactor from an economic perspective, especially in industrial application.

5.5.3 Difference in dynamic behavior and kinetic model

a- The main difference of dynamic behavior concerns the formation of intermediate I250. With commercial catalyst **Pd@Al$_2$O$_3$**, I250 exits massively from the reactor a few minutes after the beginning of the reaction sequence. Conjunction of observation indicates that hydrogenation of PNP involves two distinct reaction paths, the main classic one and another one with I250 as intermediate in PAP formation, slower and favored when there is not enough FA (Figure 57). With monolith, exit of I250 is not observed during reaction sequence, but it appears in washing sequence.

b- Another difference concerns the reaction rate models. In the kinetic model established, the reaction with commercial catalyst is in second order (either r = k$C_{PNP}C_{FA}$ or r = k C_{FA}^2), while

[131] Kohns, R.; Haas, C. P.; Höltzel, A.; Splith, C.; Enke, D.; Tallarek, U., *Reaction Chemistry & Engineering* **2018,** *3* (3), 353-364.

the reaction with monolithic catalyst is first order with respect to C_{FA} ($r = kC_{FA}$). Both involve the influence of FA, and the step of FA dissociation should be rate determining. As effect of temperature is absent in both commercial and monolithic catalysts, it indicates the reaction rate depends on concentration of FA adsorbed on the catalyst as discussed in section 5.3.

c- Concentration profile at the beginning of reaction sequence is very sharp with monolithic microreactor, and much smoother with packed-bed microreactor. This indicates a very narrow residence time distribution (RTD) in monolith. This probably can be attributed to the high porosity combined to a very regular structure, like a foam, of monolith. Actually, the large specific surface of monolith **MSM** (1260 m^2/g) compared to **Pd@Al_2O_3** powder (110 m^2/g), allows efficient contact between flowing fluid (in the macropores) and stagnant fluid (in the mesopores and micropores), which intensifies mass transport from and to the active surface sites in the mesopores and micropores[131].

Finally, in monolith, the narrow RTD and the easy access to Pd sites seems to favor selectively the main reaction path.

5.6 Conclusion

In this chapter, monolithic microreactor is firstly tested by the model reaction, with on-line UV PDA and on-line HPLC analysis. The reaction parameters on conversion under stationary conditions have been investigated: the reaction temperature and initial concentration of PNP have no effect on conversion; the effects of flow rate and the initial concentration of FA have been found. The first order reaction rate with respect to FA has been established successfully, it gives a good representation of variation of PNP conversion with experimental conditions. The absence of temperature effect reveals that the reaction rate depends on concentration of FA adsorbed on the catalyst.

In dynamic studies, the intermediate I250 is not observed with the monolith supported catalyst, confirmed by on-line PDA UV analysis, but it is detected during the washing process. It demonstrates that the I250 is formed on the catalyst support. It can be either transformed to PAP quickly or stay adsorbed.

Last but not least, the comparison of packed-bed and monolith microreactors has been investigated. The catalyst performances are first compared by calculating the turnover frequency, and the outstanding activity of monolithic catalyst has been demonstrated. The comparison of pressure drop demonstrates the mechanical stability of monolithic microreactor and its industrial potential. The comparison of dynamic study and kinetic model highlights the large specific surface of monolith and the specific texture of the hierarchical porosity.

General conclusion and outlook

The main purpose of this thesis was to explore the preparation of microreactors with monolithic catalyst, and to compare its performance to a packed-bed microreactor by a convenient model reaction. Thus, the transfer hydrogenation of *p*-nitrophenol (PNP) by formic acid (FA) catalyzed by palladium has been chosen as the model reaction.

First of all, concerning the analysis of this reaction, among the three developed protocols, the on-line analysis exhibits instinct advantages. In our investigations, despite the off-line UV analysis is easy to access and can analysis the conversion of PNP, the quantitative analysis of the main product, *p*-aminophenol (PAP) cannot be carried out, whereas it is possible in transfer hydrogenation with $NaBH_4$. With on-line UV analysis, the variation of composition of the reaction mixture can be easily detected. We were also able to detect the appearance and diminution of an unstable intermediate I250, which has never been done. With on-line HPLC analysis, the quantitative analysis of both PNP and PAP can be realized, therefore we can get the time-concentration profile of these components. The simultaneous quantification of PNP and PAP indicates that, within the experimental error range, PAP is the only product of reaction at steady-state. Compared with traditional HPLC analysis, this protocol eliminates the step of collection of products, and can allow the detection of quite unstable intermediates I250.

Secondly, conjunction of experimental observations and numerical simulation of the reactor under transient conditions give some insight about the reaction mechanism. Briefly, pertinent observations concern :

- The differences between batch and continuous flow modes : flow reaction seems to limit adsorption phenomena and formation of by-product by successive reaction.
- The numerical simulation of the microreactor, showing that only a change in the catalyst surface can produce the transient formation of a reaction product.
- Experimental observations about I250, notably analytical investigations and effect of reaction parameters, lead to the conclusion of 2 simultaneous reaction paths. The path involving I250 would be favored by acid deficit.

The successful hypothesis of the change of catalyst surface can well support the proposed reaction mechanism: the first step of reaction is the decomposition of FA on the surface of Pd catalyst, which could lead to the change of catalyst surface. Finally, from these observations, we suppose that I250 could be *p*-Benzoquinone imine (PBQI).

Thirdly, a breakthrough has been made in the preparation of mechanically stable hybrid inorganic-organic silica monolith, notably the mercapto-functionalized silica monolith in the stainless-steel tube with the inner wall pre-coated by glass. With our methodologie, for the first time, we optimized and characterized the preparation condition range of monolith in stainless-steel tube (4mm diameters). The prepared mercapto-functionalized silica monolith possesses the flow-through macropores, typical hexagonal organization of mesopores and micropores, high specific surface and scarcely any shrinkage. Afterwards, a high content of

palladium nanoparticles (4.4 mg/22.5mg) have been immobilized within the monolith in this tube by a continuous flow method.

After the comparison of packed-bed and monolith microreactors, some points have to be highlighted:

a- The outstanding activity of monolithic catalyst in the transfer hydrogenation of PNP with FA reaction has been demonstrated with a TOF of monolithic catalyst Pd@MSM-T about 3 - 6 times larger than that of commercial catalyst $Pd@Al_2O_3$, demonstrating the large accessible surface of Pd catalyst in monolithic catalyst. The chemical stability is proved by a campaign of reaction during several weeks;

b- The mechanical stability of monolithic catalyst in microreactor is proved by a much lower pressure drop of monolithic microreactor than packed-bed microreactor. This is very important for an industrial application;

c- The differences of dynamic study and kinetic model reveal the differences of catalyst properties: the large specific surface and specific texture of the hierarchical porosity of monolithic catalyst favor a narrow residence time distribution (RTD) in monolithic microractor.

The outlook of this project mainly consists of two aspects:

The hybrid inorganic-organic monolithic catalyst in the stainless-steel tube offers a new tool for that can be largely expanded in different applications.

The proof of concept with mercapto-functionalized silica monolith opens methods for the immobilization of other organic functions such as metal nanoparticles ligands (for example amine which to be fully studied), chiral or achiral ligands and chiral selectors.

The prepared microreactor with monolithic catalyst offers particular industrial interests, because of its low pressure drop, good mechanical stability, high specific surface and excellent catalytic performance. With the same preparation method, the scale-up and numbering-up methods can be taken into consideration, to increase the throughput for pilot scale and industrial scale production.

Annex

A-1 Calibration of UV-Visible analysis of PNP (protocol 1)

As shown in Figure A1, the response factor is quite constant in the wavelength range 325-349nm, the standard deviation is 6%.

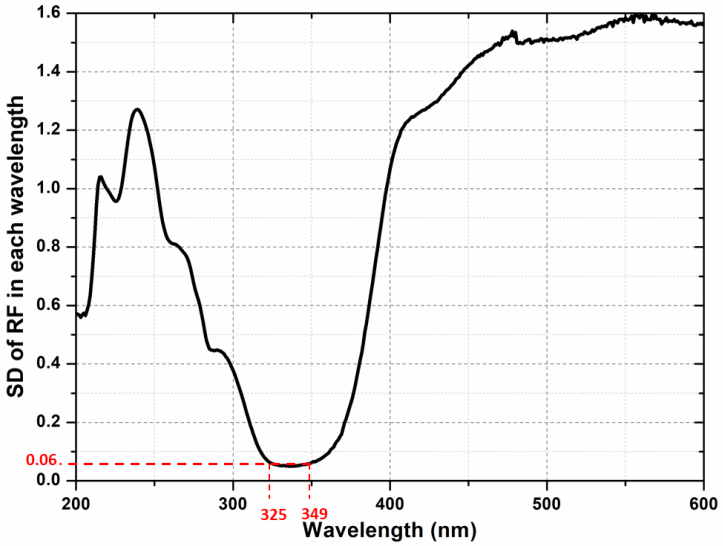

Figure A1 Standard deviation (SD) of response factor (RF) in each wavelength with the results of off-line UV-vis. of different calibration solutions

A-2 Calibration of on-line UV PDA analysis of PNP (protocol 2)

The concentrations of calibration solutions are listed in Table A1.

Table A1 Calibration conditions for on-line UV PDA

Assumed C_{PNP}° mmol/L	C_{FA}^{0}/C_{PNP}^{0}	Assumed conversion	Composition of calibration solution		
			C_{PNP} mmol/L	C_{FA} mmol/L	C_{PAP} mmol/L
0.1	3	0.9	**0.01**	**0.03**	**0.09**
0.1	2.1	0.1	**0.09**	**0.18**	**0.01**
0.1	4.5	0.1	**0.09**	**0.42**	**0.01**
0.3	3	0.5	**0.15**	**0.45**	**0.15**
0.5	3	0.9	**0.05**	**0.15**	**0.45**
0.5	4.5	0.9	**0.05**	**0.9**	**0.45**
0.5	2.1	0.5	**0.25**	**0.3**	**0.25**
0.5	2.1	0.1	**0.45**	**0.9**	**0.05**
0.5	4.5	0.1	**0.45**	**2.1**	**0.05**

The calculations on the response factor and regression are shown in Figure A2 and Figure A3, respectively. The final range for the calculation of PNP conversion with online UV PDA is 357-367 nm.

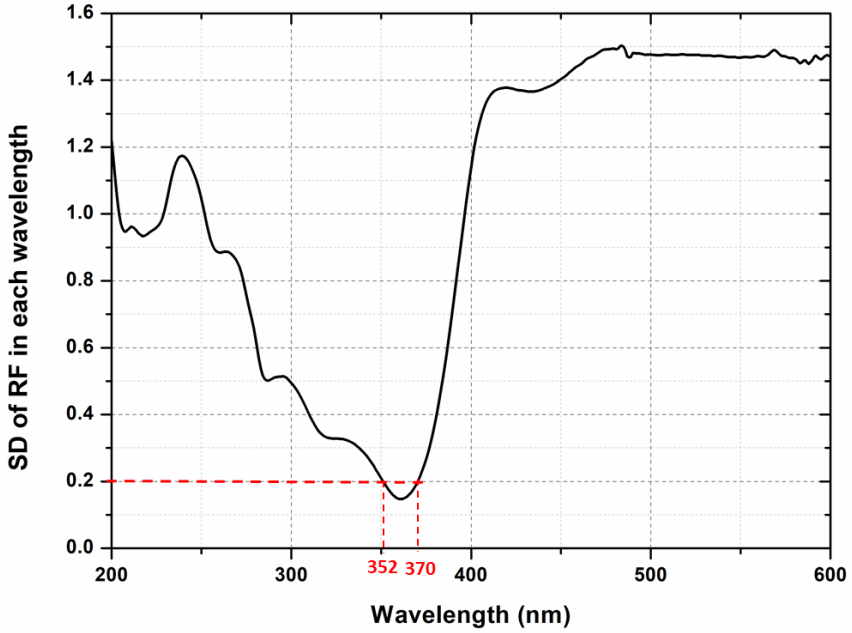

Figure A2 Standard deviation (SD) of response factor (RF) in each wavelength with the results of on-line UV-vis. of different calibration solutions

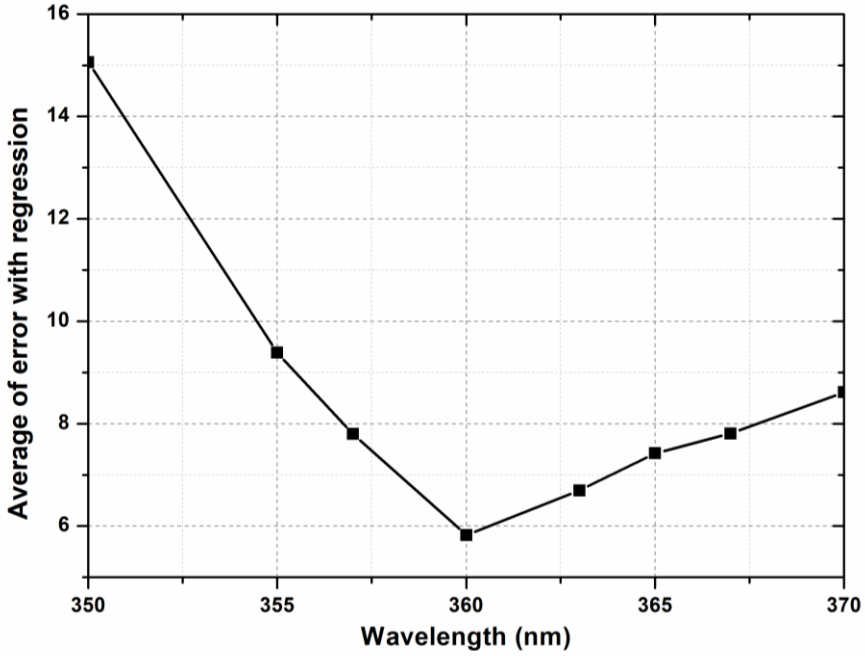

Figure A3 Average of error with regression method of different wavelength with on-line UV-vis.

A-3 Calibration of off-line HPLC analysis

In order to ensure the feasibility of HPLC method in quantitive analysis of PNP and PAP, several calibration solutions with different concentrations of PNP and PAP in the range of concentrations below 0.4 mmol/L have been prepared for that. The plots of PNP or PAP concentration as a function of the surface area of chromatographic peak S exhibit excellent linear correlation as shown in Figure A4.

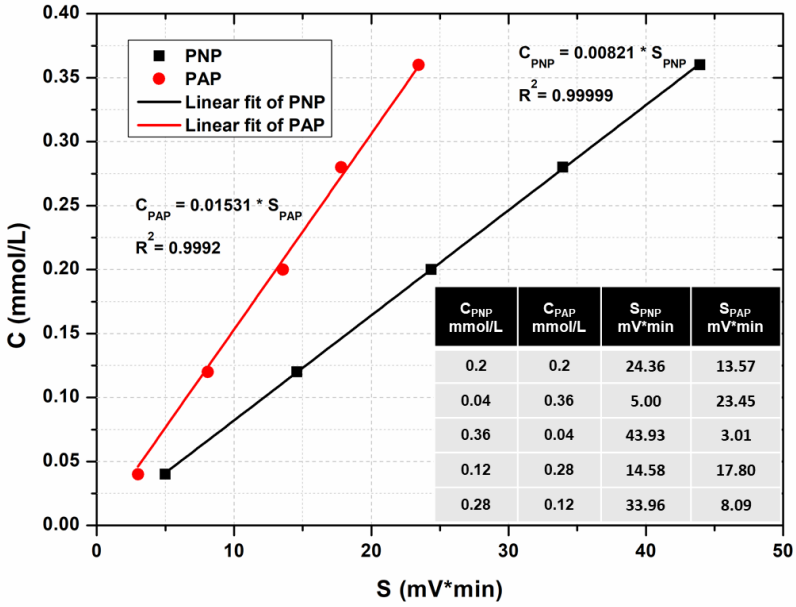

C_{PNP} mmol/L	C_{PAP} mmol/L	S_{PNP} mV*min	S_{PAP} mV*min
0.2	0.2	24.36	13.57
0.04	0.36	5.00	23.45
0.36	0.04	43.93	3.01
0.12	0.28	14.58	17.80
0.28	0.12	33.96	8.09

Figure A4 Calibration of PNP and PAP with off-line HPLC: concentration of different calibration solutions and linear fit of concentration of PNP and PAP as a function of S (integration of peak)

A-4 Effect of pH values on PAP chromatogram

The effect of pH values on the PAP chromatogram has been observed. In order to improve the precision of measurements, the effect of pH, varied either with hydrochloric acid (HCl) or FA has been investigated and summarized in the following tables.

PAP with FA solutions		
C_{FA} mmol/L	pH	S_{PAP}
6	3.07	10026265
6	3.07	10078025
3	3.3	10147242
3	3.3	9999195
3	3.3	9977280
1	4.52	11227483
1	4.52	10978924

1	4.52	10849226
1	4.52	10875100
0	6.49	12404700
0	6.49	12274379
0	6.49	11999127
0	6.49	12260721

PAP with HCl solutions	
pH	S_{PAP}
1.8	9972638
3.9	11027872
5.6	11696891

Relation of e^{-pH} and C_{FA}

pH	**C_{FA} mmol/L**	e^{-pH}
3.07	6	0.0008511
3.3	3	0.0005012
4.52	1	3.02E-05
6.49	0	3.236E-07

A-5 NMR analysis details

^{1}H NMR spectra are recorded on a Bruker Avance DPX-400 spectrometer.
^{1}H NMR information is given in the following format: multiplicity (s, singlet; d, doublet), coupling constant(s) (*J*) in Hertz (Hz), number of protons.

PNP ^{1}H NMR (400 MHz, D_2O):
δ=8.12 (d, J_{HH}=12Hz, 2H), 6.88 (d, J_{HH}=8Hz, 2H);

PAP ^{1}H NMR (400 MHz, D_2O, mixed with PNP and FA):
δ=6.88 (d, J_{HH}=8Hz, 2H), 6.77 (d, J_{HH}=8Hz, 2H);

FA ^{1}H NMR (400 MHz, D_2O):
δ=8.37(s,H); solvent D_2O δ=4.7(s,H);

PNS ^{1}H NMR (400 MHz, D_2O):
δ=7.60 (s, 2H), 6.55 (d, J_{HH}=8Hz, 2H);

PAD ^{1}H NMR (400 MHz, D_2O):
δ=8.06 (d, J_{HH}=8Hz, 2H), 7.70 (d, J_{HH}=8Hz, 2H), 6.96 (d, J_{HH}=8Hz, 2H), 6.69 (d, J_{HH}=8Hz, 2H);

A-6 Adsorption isotherm results of PNP and PAP

The results of adsorption investigations of PNP and PAP are summarized in Table A2 and Table A3.

Table A2 The adsorption isotherm of PNP

Molar ratio Pd/PNP	$X_{ads,PNP}$	V/mL	C_{PNP}^0 mmol/L	m_{cat}/g	$c_{e,PNP}$ mmol/L	$q_{e,PNP}$ mmol/g
0.0940	0.082	10	25	0.05	22.94345	0.41131
0.1566	0.124	10	15	0.05	13.13499	0.373003
0.2349	0.159	10	10	0.05	8.41371	0.317258
0.2936	0.108	10	8	0.05	7.133543	0.173291
0.3915	0.109	10	6	0.05	5.382284	0.123543
0.5873	0.110	10	4	0.05	3.561901	0.08762
1.1746	0.03	10	2	0.05	1.934446	0.013111
2.3492	0.068	10	1	0.05	0.931608	0.013678
0.1992	0.104	10	10	0.0424	8.9621	0.24479

Table A3 The adsorption isotherm of PAP

Molar ratio Pd/PAP	$X_{ads,PAP}$	V/mL	C_{PAP}^0 mmol/L	m_{cat}/g	$c_{e,PAP}$ mmol/L	$q_{e,PAP}$ mmol/g
0.1000	0.3059	1.51	10	0.003	6.941	1.539697
0.1000	0.1553	6.08	10	0.0124	8.447	0.761471
0.1000	0.2733	10	10	0.0212	7.267	1.289151
0.1000	0.4781	10	10	0.0212	5.219	2.255189
0.2000	0.4058	10	10	0.0424	5.942	0.957075
0.2000	0.4126	10	10	0.0424	5.874	0.973113

A-7 Mass transfer criteria

The external mass transfer can be analyzed by the mass transfer coefficient k_D (m/s), and the internal mass transfer can be analyzed by the effective diffusion coefficient D_{eff} (m^2/s).

External mass transfer

To obtain the mass transfer coefficient, the Reynolds number Re, the diffusion coefficient D_m(m^2/s), the Schmidt number Sc and the Sherwood number Sh must be calculated as follows.

The Reynolds number Re:

$$\mathrm{Re} = \mathrm{u}\mathrm{d}_{\mathrm{cat}}\rho/\mu$$

where

u (m/s) the superficial flow velocity of the fluid,
d_{cat}(m) the catalyst average diameter,
ρ (g/m^3) the density of the fluid
μ (Pa.s) the viscosity of the fluid

D_m is the mutual diffusion coefficient of solute A at very low concentrations in solvent B. It exist many correlations to estimate the diffusion coefficient. A widely used correlation called Wilke-Chang[132] estimation method is adopted here:

$$\mathrm{D_m} = \frac{7.4 \times 10^{-8} (\emptyset \mathrm{M_B})^{1/2} \mathrm{T}}{\mu \mathrm{V_A^{0.6}}}$$

where
M_B (g/mol) the molecular weight of solvent B, here is 18 g/mol,
Ø the association factor of solvent, for water Ø=2.6,
T (°C) the temperature,
μ (Pa.s)the viscosity of solvent
V_A(ml/mol) the molar volume of solute A at its normal boiling temperature, for PNP, V_A = 151 mL/mol

The Schmidt number Sc:

$$\mathrm{Sc} = \mu / (\rho \cdot \mathrm{D_m})$$

The Sherwood number Sh can be estimated by a large number of correlations. We utilize the most widely used correlation here:

$$\mathrm{Sh} = 2 + 0.6\ \mathrm{Re}^{1/2} Sc^{1/3}$$

From Sh, the mass transfer coefficient k_D can be estimate:

$$\mathrm{k}_D = Sh \cdot D_m / D_{cat}$$

For investigating the external mass diffusion, Mears proposed a criterion, Mears' criterion f_E , the ratio of the rate of reaction to the external diffusion rate. If this criterion is less than 0.05, it means that the external diffusion resistance is low and can be neglected.

$$\mathrm{f_E} = \frac{\mathrm{r_{exp}}}{\mathrm{r_{diffusion}}} = \frac{\mathrm{Q} \cdot \mathrm{X/V}}{\mathrm{k_D} \cdot \mathrm{S_{cat}/V_{cat}}}$$

where S_{cat} the external surface of catalyst and V_{cat} the volume of catalyst.

The related calculation results are listed in the following table:

Table A4 Parameters of external mass transfer

Entry	Re	D_m(m^2/s)	Sc	Sh	k_D(m/s)	f_E
1	0.03717	7.81126E-10	1280.20	3.26	3.63E-05	8.11E-09
2	0.03717	7.56182E-10	1322.43	3.27	3.53E-05	8.23E-09
3	0.03717	7.81126E-10	1280.20	3.26	3.63E-05	8.09E-09
4	0.03717	8.0607E-10	1240.59	3.24	3.73E-05	7.86E-09
5	0.03717	8.31014E-10	1203.35	3.23	3.84E-05	7.67E-09
6	0.07434	7.56182E-10	1322.43	3.80	4.10E-05	1.42E-08

[132] Cox, K. R.; Chapman, W. G., *Journal of the American Chemical Society* **2001,** *123* (27), 6745-6745.

7	0.14869	7.56182E-10	1322.43	4.54	4.90E-05	2.37E-08
8	0.18586	7.56182E-10	1322.43	4.84	5.23E-05	2.78E-08
9	0.29737	7.56182E-10	1322.43	5.59	6.04E-05	3.83E-08
10	0.07434	7.56182E-10	1322.43	3.80	4.10E-05	1.37E-08
11	0.07434	7.81126E-10	1280.20	3.78	4.21E-05	1.33E-08
12	0.07434	7.56182E-10	1322.43	3.80	4.10E-05	8.78E-10
13	0.07434	7.81126E-10	1280.20	3.78	4.21E-05	8.60E-10
14	0.03717	7.56182E-10	1322.43	3.27	3.53E-05	6.55E-10
15	0.05947	7.56182E-10	1322.43	3.61	3.90E-05	4.65E-10
16	0.07434	7.56182E-10	1322.43	3.80	4.10E-05	5.21E-10
17	0.03717	7.56182E-10	1322.43	3.27	3.53E-05	6.21E-09
18	0.05947	7.56182E-10	1322.43	3.61	3.90E-05	9.00E-09
19	0.07434	7.56182E-10	1322.43	3.80	4.10E-05	1.07E-08
20	0.07434	7.56182E-10	1322.43	3.80	4.10E-05	4.23E-09
21	0.07434	8.0607E-10	1240.59	3.76	4.33E-05	3.86E-09

In fact in all the experiments, the Mears' criterion f_E << 0.05. Therefore, the bulk diffusion can be neglected.

Internal mass transfer

The effective diffusion coefficient D_{eff} is calculated by diffusion coefficient D_m, the porosity ε and the tortuosity τ :

$$D_E = D_m \cdot \varepsilon/\tau$$

The porosity ε can be calculated by the correlation proposed by Tsotsas and Schlünder[133] which were adapted from the empirical formula of Dixon[134].

$$\varepsilon = 0.37 + \frac{0.05}{N} + \frac{0.5344}{N^2}$$

$$N = \frac{D}{D_{cat}}$$

We can get the porosity ε = 0.371

The tortuosity τ can be calculated by the correlation reported by Puncochar and Drahoš[135]:

$$\tau = \frac{1}{\sqrt{\varepsilon}}$$

so τ = 1.64

[133] Tsotsas, E.; Schlünder, E. U., *Wärme - und Stoffübertragung* **1990,** *25* (4), 245-256.
[134] Dixon Anthony, G., *Canadian Journal of Chemical Engineering* **1988,** *66* (5), 705-708.
[135] Punčochář, M.; Drahoš, J., *Chemical Engineering Science* **1993,** *48* (11), 2173-2175.

For investigation of internal mass diffusion effect inside the catalyst pellet, the Weisz-Prater criterion Θ_w is used to determine whether internal mass transfer is limiting the reaction.

$$\Theta_w = \frac{QX/V}{(S_{cat}/V_{cat})^2 D_E}$$

If Θ_w <0.1, the internal pore diffusion can be negligible.

From Table A5, the Weisz-Prater criterion is much smaller than 0.1, signifying that internal pore diffusion is also negligible.

Table A5 Parameters of internal mass transfer

Entry	D_{eff}(m^2/s)	Θ_w
1	1.76E-10	3.90E-08
2	1.71E-10	3.97E-08
3	1.76E-10	3.89E-08
4	1.82E-10	3.76E-08
5	1.88E-10	3.66E-08
6	1.71E-10	7.93E-08
7	1.71E-10	1.59E-07
8	1.71E-10	1.98E-07
9	1.71E-10	3.16E-07
10	1.71E-10	7.68E-08
11	1.76E-10	7.44E-08
12	1.71E-10	4.92E-09
13	1.76E-10	4.79E-09
14	1.71E-10	3.16E-09
15	1.71E-10	2.47E-09
16	1.71E-10	2.92E-09
17	1.71E-10	2.99E-08
18	1.71E-10	4.79E-08
19	1.71E-10	6.01E-08
20	1.71E-10	2.37E-08
21	1.82E-10	2.14E-08

A-8 Estimation of the quantity of I250 in different experimental conditions

Different experiments were performed with protocol 2 (PDA on-line analysis), in order to relate the amount of I250 to experimental conditions. This amount is roughly estimated from the surface area of the 250 nm UV-band. Figure A5 shows the variation of I250 on time under different conditions.

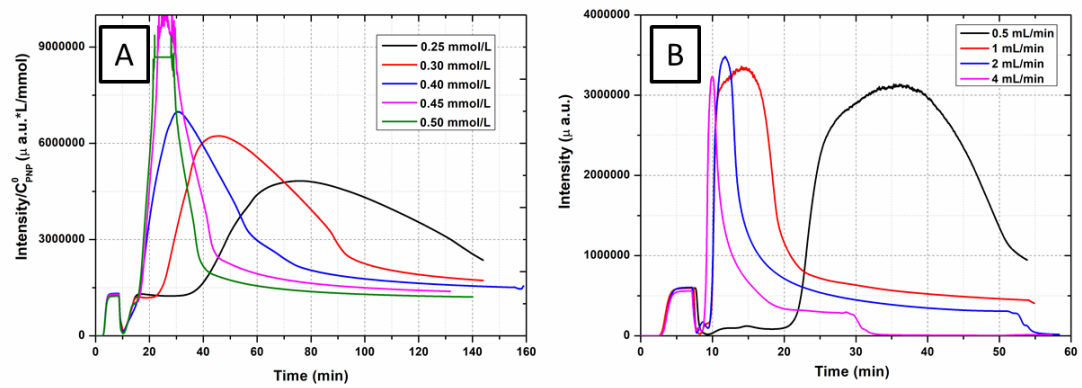

Figure A5 (A) Variation of I250 on time with different initial concentrations C_{PNP}^0. Y-axis is the intensity/ C_{PNP}^0 for clearer comparison. Reaction condition: C_{FA}^0/C_{PNP}^0 = 3, Q=0.5 mL/min, T=25 °C (B) Variation of I250 on time with different flow rates Q. Reaction condition: C_{PNP}^0=0.5 mmol/L, C_{FA}^0/C_{PNP}^0 = 6 , T=25 °C

The quantity of I250 Q_{I250} (a.u.*mL) is estimated by S_{I250}*Q, where S_{I250} the surface under the curve (Indensity/Time) and Q the flow rate:

Table A6 Quantity of I250 with variation of C_{NP}^0 and Q

With variation of C_{NP}^0					
C_{NP}^0 mmol/l	0.5	0.45	0.4	0.3	0.25
Q_{I250} a.u.*mL	27.99	30.07	33.00	34.19	33.87
With variation of Q					
Q mL/min	0.5	1	2	4	
Q_{I250} a.u.*mL	33.98	27.15	30.61	35.94	

A-9 Effect of FA on the intermediate I250

In Table A7 it is clear to see the quantity of I250 (S_{I250}) increases with m, and the quantity of I250 is correlated to $1/C_{FA}^0$. FA pumped is calculated by C_{FA}^0*Q*t^0, where t^0 is the reaction time before the appearance of FA.

Table A7 Effect of concentration of FA on the intermediate

m	t^0, min	FA pumped	S_{I250}	S_{I250}*m
0.67	35	**17.7**	138.8	**93.0**
1	18	**13.5**	104.2	**104.2**
1.67	10	**12.5**	62.2	**103.9**

A-10 Synthesis of 4,4'-Azodiphenol (PAD)

A mixture of KOH (23g, 0.38 mol), PNP (5.2g, 0.038 mol), and water (6,25mL) is heated to 120℃ and maintained for 1h, then the mixture is heated slowly to 200℃ and left to reactor for 12h. During the heating, the mixture changed into a brown viscous liquid along with the appearance of large numbers of bubbles. The products in the flask is then dissolved by adding water in maintaining the heating, and then acidified with 2 mol/L HCl 40ml. The dark red solution is extracted with ethyl acetate and dried with Na_2SO_4 overnight, and then the solvent was removed under reduced pressure. The residue is purified by silica gel column chromatography eluting with dichloromethane and then ethyl acetate. The tawny solid of 0.429g (10.55% yield) is obtained after the evaporation of solvent. ^{1}H NMR (400 MHz, DMSO): δ=7.71 (d, J_{HH} = 12 Hz, 4H), 6.90 (d, J_{HH} = 12 Hz, 4H).

A-11 Experimental steady-state results measured for kinetics determination

The results of experiments of steady-state with packed-bed microreactor are summarized in Table A8.

Table A8 Table of experimental steady-state results measured for kinetics determination

Entry	Q	T	C_{FA}^0	C_{PNP}^0	C_{PAP}^f	C_{PNP}^f	C_{FA}^f	X	m= C_{FA}^0/3 C_{PNP}^0
	ml/min	°C	mmol/L	mmol/L	mmol/L	mmol/L	mmol/L		
1	0.5	40	1.8	0.59	0.41	0.12	0.41	0.791	1.023
2	0.5	40	1.8	0.62	0.40	0.22	0.58	0.652	0.961
3	0.5	40	1.8	0.62	0.40	0.20	0.52	0.682	0.961
4	0.5	40	1.8	0.52	0.38	0.12	0.62	0.762	1.160
5	0.5	40	3	0.99	0.77	0.23	0.74	0.766	1.014
6	1	40	0.9	0.61	0.07	0.51	0.60	0.161	0.490
7	1	40	3.75	2.69	1.04	1.81	1.10	0.328	0.465
8	1	40	3.75	2.69	1.04	1.77	0.99	0.342	0.465
9	1	40	6	4.31	2.13	2.42	0.34	0.438	0.464
10	1	40	6	4.40	2.10	2.31	-0.27	0.475	0.455
11	1	40	1.2	0.60	0.22	0.41	0.65	0.306	0.669
12	1	40	1.2	0.61	0.20	0.44	0.68	0.281	0.652
13	1	40	5	2.55	1.59	1.32	1.30	0.482	0.653
14	1	40	5	2.54	1.63	1.41	1.62	0.443	0.656

15	1	40	8	4.47	2.76	1.75	-0.16	0.609	0.596
16	1	40	8	4.27	2.91	1.73	0.40	0.594	0.625
17	1	40	10	5.57	3.43	1.81	-1.27	0.675	0.598
18	1	40	10	5.51	3.62	2.07	-0.32	0.625	0.605
19	1	40	0.9	0.26	0.07	0.15	0.59	0.401	1.170
20	1	40	0.9	0.32	0.07	0.25	0.67	0.233	0.926
21	1	40	0.9	0.33	0.08	0.25	0.67	0.234	0.920
22	1	40	1.8	0.60	0.34	0.19	0.56	0.688	0.997
23	1	40	1.8	0.64	0.41	0.20	0.48	0.689	0.941
24	1	40	1.8	0.59	0.34	0.29	0.89	0.510	1.015
25	1	40	1.8	0.63	0.32	0.24	0.64	0.613	0.949
26	1	40	1.8	0.61	0.33	0.28	0.83	0.533	0.990
27	1	40	1.8	0.59	0.34	0.27	0.84	0.545	1.017
28	1	40	1.8	0.59	0.34	0.29	0.89	0.510	1.015
29	1	40	1.8	0.62	0.42	0.21	0.54	0.670	0.961
30	1	40	1.8	0.62	0.41	0.20	0.53	0.678	0.961
31	1	40	1.8	0.57	0.38	0.14	0.52	0.755	1.058
32	1	40	1.8	0.61	0.39	0.21	0.60	0.659	0.984
33	1	40	1.8	0.56	0.45	0.17	0.62	0.696	1.064
34	1	40	1.8	0.65	0.36	0.22	0.51	0.664	0.926
35	1	40	1.8	0.61	0.36	0.19	0.55	0.685	0.989
36	1	40	1.8	0.63	0.32	0.26	0.68	0.593	0.949
37	1	40	3	1.02	1.09	0.18	0.49	0.821	0.980
38	1	40	3	0.97	0.81	0.20	0.66	0.799	1.026
39	1	40	3	0.99	0.84	0.25	0.79	0.744	1.011
40	1	40	3	1.00	0.87	0.22	0.65	0.784	1.003
41	1	40	6	1.93	2.16	0.14	0.65	0.926	1.039
42	1	40	6	1.93	2.11	0.18	0.76	0.906	1.038
43	1	40	12	4.59	4.34	0.23	-1.09	0.950	0.871
44	1	40	12	4.03	4.63	0.13	0.30	0.969	0.993
45	1	40	15	4.88	5.81	0.19	0.93	0.961	1.025
46	1	40	15	4.89	6.11	0.20	0.92	0.959	1.022
47	1	40	1.2	0.28	0.14	0.12	0.72	0.570	1.411
48	1	40	1.2	0.29	0.14	0.14	0.75	0.527	1.397
49	1	40	10	2.57	4.15	0.00	2.28	0.990	1.295
50	1	40	10	2.45	3.76	0.00	2.66	0.990	1.362
51	1	40	3	0.99	0.78	0.17	0.56	0.824	1.013
52	1.5	40	1.8	0.65	0.42	0.21	0.48	0.681	0.930
53	2	40	1.8	0.65	0.41	0.21	0.48	0.681	0.930
54	2	40	1.8	0.59	0.39	0.18	0.57	0.696	1.017
55	2	40	1.8	0.61	0.39	0.20	0.57	0.673	0.986

A-12 Detailed direct synthesis of functionalized monolith in stainless-steel tube

A concentrated hydrochloric acid (37%, 0.36 mL) was rapidly added to aqueous solution of TTAB (0.336 g, 1 mmol) of 26% mass concentration in the mortar. Then, TEOS (0.27 g, 1.3 mmol) and MPTS (0.028 g, 0.143 mmol) were mixed uniformly, and added in the former solution drop by drop along with the vigorous agitation by pestle for approximately 5 minutes in order to perform TEOS hydrolysis. Then the emulsion was formed and dodecane (2.82 mL) was added drop by drop for 7 minutes along with the vigorous agitation continually.

A-13 Preparation of TEM analysis samples

Before the TEM analysis, the EMBed-812 epoxy resin (Electron Microscopy Science) was prepared freshly: the EMBed-812 (22.6 g), DDSA (16 g), NMA (9.8 g) DMP-30 (0.7 g) were mixed and stirred for 2 hours. All these reagents were from EMBed-812 EMBEDDING KIT. Then the mixture was transferred into the BEEM® embedding capsules (Electron Microscopy Science). Samples of monoliths were grinded vigorously in the mortar then added into the prepared resin mixture in the capsules, following the heating of 60℃ for 24 hours in the oven. The specimens for TEM then prepared.

A-14 Detail calculation of V_m and BET constant of BET analysis

The BET equation can be plotted as a straight line with p/V (p_0-p) on the y-axis and p/p_0 on the x-axis based on the experimental results. This linear relationship of BET plot can be only maintained in the range of $0.05 < p/p_0 < 0.35$. The slope and intercept of the line are used to calculate the monolayer adsorbed gas quantity V_m and BET constant c as follows:

$$V_m = \frac{1}{\text{slope} + \text{intercept}}$$

$$c = 1 + \frac{\text{slope}}{\text{intercept}}$$

A-15 Preparation conditions of monoliths in polymer tube

The preparations conditions of Native Silica Monoliths (NSM), Aminopropyl Silica Monoliths (ASM) and Mercaptopropyl Silica Monoliths (MSM) are varied as in the following tables.

Table A9 Preparation conditions of NSM

Sample name	NSM-1	NSM-2	NSM-3	NSM-4	NSM-5	NSM-6	NSM-7	NSM-B
m_{TEOS} (g)	1	1	1	1	0.46	1.39	1	1
V_{H_2O} (mL)	3.2	3.2	3.2	3.2	3.2	3.2	3.2	2.145
V_{HCl} (37%)(mL)	1.2	1.2	1.2	1.2	1.2	1.2	1.2	1.2
m_{TTAB} (g)	1.12	1.12	0.69	1.61	1.12	1.12	1.12	1.155
$V_{dodecane}$ (mL)	14.7	7.3	9.4	9.4	9.4	9.4	9.4	9.4

Table A10 Preparation conditions of ASM

	ASM-1	ASM-2	ASM-3	ASM-4	ASM-5	ASM-6	ASM-7	ASM-8	ASM-9
m_{TEOS}(g)	0,201	0,201	0,201	0,201	0,201	0,201	0,201	0,201	0,201
m (APTES) (g)	0,0102	0,011	0,011	0,011	0,011	0,011	0,021	0,015	0,011
V_{H2O} (mL)	0,639	0,642	0,642	0,642	0,642	0,418	0,674	0,652	0,696
V_{HCl}(37%)(mL)	0,24	0,24	0,24	0,24	0,24	0,24	0,24	0,24	0,24
m_{TTAB} (g)	0,1631	0,1639	0,1635	0,0968	0,2574	0,1068	0,172	0,1667	0,1776
$V_{dodecane}$ (mL)	0,136	9,4	9,4	9,4	1,88	0,892	1,88	1,88	1,88

Table A11 Preparation conditions of MSM

	MSM-1	MSM-2	MSM-3	MSM-4	MSM-5	MSM-6	MSM-7	MSM-B
m_{TEOS}(g)	0.18	0.18	0.18	0.1488	0.8335	0.9895	0.9	0.9
m (MPTES) (g)	0.019	0.019	0.019	0.059	0.196	0.049	0.094	0.094
V_{H2O} (mL)	0.64	0.64	0.64	0.64	3.2	3.2	3.2	2,145
V_{HCl}(37%)(mL)	0.24	0.24	0.24	0.24	1.2	1.2	1.2	1.2
m_{TTAB} (g)	0.224	0.224	0.176	0.224	1.12	1.12	1.12	1.12
$V_{dodecane}$ (mL)	2.2	1.6	1.88	1.88	9.4	9.4	9.4	9.4

A-16 Detailed information of calculation of condensation degree for NSN, AMS and MSM

The detailed information of area proportions of each type peak is summarized in the following tables for condensation degree calculation.

Table A12 Condensation degree of NSM samples and area proportions of each type peak

	NSM-1	NSM-2	NSM-3	NSM-4	NSM-5	NSM-6	NSM-7	NSM-B
$\%Q^2$	5.9%	8.5%	12.6%	-	6.5%	3.9%	16.3%	18.5%
$\%Q^3$	87.6%	83.7%	81.8%	-	86.7%	95.9%	71.3%	66.0%
$\%Q^4$	6.5%	7.8%	5.6%	-	6.8%	0.2%	12.4%	15.5%
%C.D.Q	75.1	74.8	73.2	-	75.1	74.1	74.0	74.3

Table A13 Condensation degree of ASM samples and area proportions of each type peak

	ASM-1	ASM-2	ASM-3	ASM-4	ASM-5	ASM-6	ASM-7	ASM-8	ASM-9
%T^2	0.0%	6.0%	10.8%	12.6%	12.5%	23.0%	16.0%	13.4%	5.4%
%T^3	100.0%	94.0%	89.2%	87.4%	87.5%	77.0%	84.0%	86.6%	94.6%
%Q^2	11.4%	5.4%	13.9%	10.7%	11.5%	11.8%	11.1%	6.8%	6.4%
%Q^3	56.7%	79.5%	58.7%	64.4%	67.3%	60.7%	56.4%	68.3%	73.6%
%Q^4	31.8%	15.1%	27.4%	24.9%	21.2%	27.5%	32.5%	24.9%	20.0%
%C.D.T	100.0%	98.0%	96.4%	95.8%	95.8%	92.3%	94.7%	95.5%	98.2%
%C.D.Q	80.1%	77.4%	78.4%	78.5%	77.4%	78.9%	80.4%	79.5%	78.4%

Table A14 Condensation degree of MSM samples and area proportions of each type peak

	MSM-1	MSM-2	MSM-3	MSM-4	MSM-5	MSM-6	MSM-7	MSM-B
%T^2	21.1%	11.7%	30.2%	21.5%	28.7%	17.1%	23.8%	20.5%
%T^3	78.9%	88.3%	69.8%	78.5%	71.3%	82.9%	76.2%	79.5%
%Q^2	12.9%	14.3%	11.6%	10.0%	3.9%	11.4%	14.8%	13.0%
%Q^3	64.6%	67.0%	68.0%	62.7%	69.0%	70.9%	57.0%	65.8%
%Q^4	22.6%	18.7%	20.3%	27.3%	27.1%	17.8%	28.3%	21.2%
%C.D.T	93.0%	96.1%	89.9%	92.8%	90.4%	94.3%	92.1%	93.2%
%C.D.Q	77.4%	76.1%	77.2%	79.3%	80.8%	76.6%	78.4%	77.1%

Table A15 Detailed information of condensation degree of MSM-T compared to MSM-7

	MSM-7	MSM-T
%T^2	23.8%	18.3%
%T^3	76.2%	81.7%
%Q^2	14.8%	9.3%
%Q^3	57.0%	67.5%
%Q^4	28.3%	23.2%
%C.D.T	92.1%	93.9%
%C.D.Q	78.4%	78.5%

A-17 ^{13}C CP-MAS NMR of NSM

The ^{13}C CP-MAS NMR of NSM is just used to confirm the effectiveness of washing process. The following figure indicates the presence of TTAB (main at 30.4 ppm) in the NSM, which was not totally washed out.

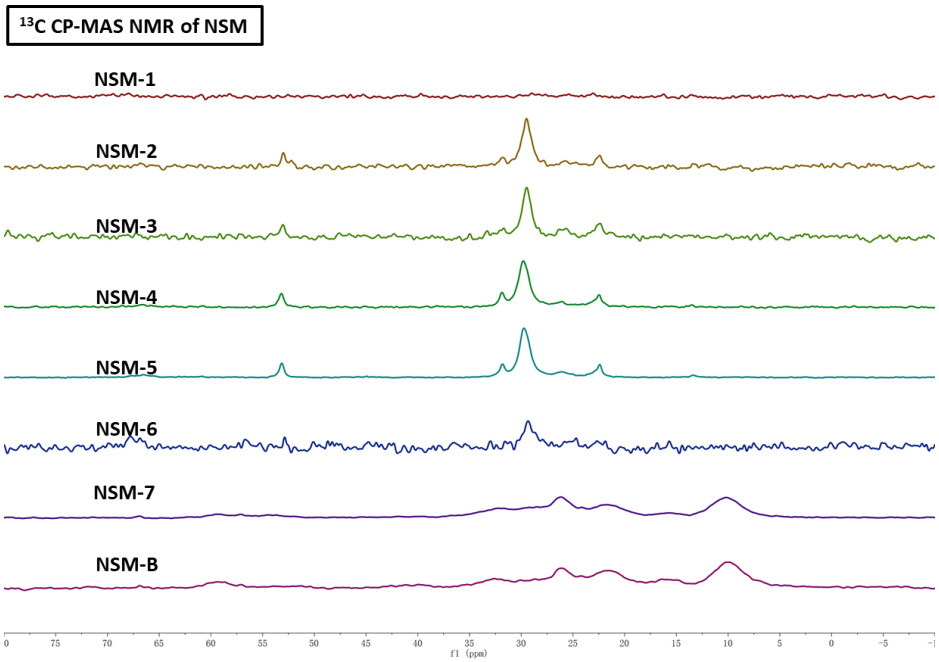

Figure A6 ^{13}C CP-MAS NMR of NSM

A-18 Calculation of O/Si ratio by CP-MAS NMR analysis

The O/Si ratio is calculated on the basis of deconvolution of CP-MAS NMR analysis.

Table A16 Calculation of O/Si ratio by CP-MAS NMR analysis

	O/Si	MSM-T	MSM-7	O/Si of MSM-T	O/Si of MSM-7
T^2	2	5.4%	5.8%	0.108	0.116
T^3	1.5	24.1%	18.5%	0.362	0.278
Q^2	3	6.6%	11.2%	0.198	0.336
Q^3	2.5	47.5%	43.2%	1.188	1.080
Q^4	2	16.4%	21.4%	0.328	0.428
Sum				**2.18**	**2.24**

A-19 Test of kinetics with mean values over the reactor

Because of the strong dispersion of data, the mean values of measurements made in the same experimental conditions are considered for the first kinetics trials (reduced data are listed below). This approach allows the direct plot between volumetric reaction rate and reactant concentrations.

Table A17 Reduced data set for the first kinetics trials

Entry	Q	T	C_{FA}^{0}	C_{PNP}^{0}	C_{PAP}^{f}	C_{PNP}^{f}	C_{FA}^{f}	X	m= $C_{FA}^{0}/3\ C_{PNP}^{0}$
1	**ml/min**	**°C**	**mmol/L**	**mmol/L**	**mmol/L**	**mmol/L**	**mmol/L**		
2	0,2	40	4,841	1,852	1,538	0,699	1,385	0,623	1,080
3	0,5	40	4,653	1,725	1,077	0,899	2,770	0,479	1,159
4	1	40	1,748	0,628	0,207	0,388	1,179	0,382	0,956
5	1	40	3,553	0,629	0,531	0,097	2,006	0,846	1,909
6	1	40	2,700	0,662	0,356	0,262	1,631	0,605	1,359
7	1	40	0,900	0,669	0,060	0,588	0,721	0,122	0,448
8	1	40	2,502	0,908	0,308	0,559	2,077	0,384	1,102
9	1	40	4,410	1,649	0,767	0,975	3,699	0,408	1,213
10	1	40	11,420	4,106	2,236	2,472	5,293	0,398	0,974
11	1	60	1,783	0,636	0,184	0,443	1,248	0,303	0,944
12	1	80	1,717	0,621	0,198	0,413	1,205	0,334	0,966

The material PNP balance over the reactor with a mean value of the reaction rate is:

Difference in molar flow rate between feed and exit = Molar flow rate reacted within the reactor

$$Q\left(C_{PNP}^{0} - C_{PNP}^{f}\right) = Q \cdot C_{PNP}^{0} \cdot X = r_m \cdot V_{CAT}$$

with

r_m the mean reaction rate

V_{CAT} the volume of catalyst

C_{PNP}^{f} and C_{PAP}^{f} the concentrations of PNP and PAP in the final product.

Mean value of concentration C^m is calculated as $(C^0+C^f)/2$. As the experimental variation of C_{PNP}^{0} is much wider than that of the conversion, we compare $r_m \cdot V_{CAT} / C_{PNP}^{0}$ (= $Q \cdot X$) to $C_{PNP}^{m} / C_{PNP}^{0}$ and to C_{FA}^{m} / C_{PNP}^{0}. The plots clearly show that the reaction rate is roughly first order with respect to FA, and not to PNP.

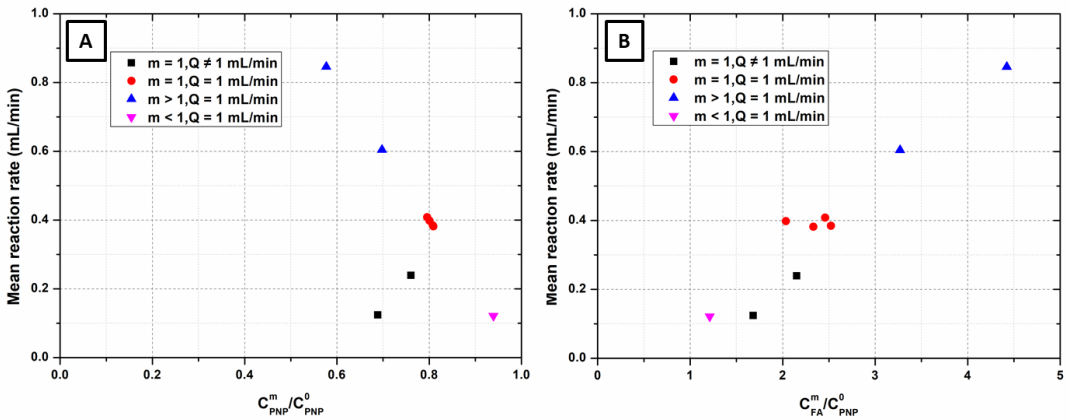

Figure A7 Comparison of mean reaction rate ($r_m \cdot V_{CAT}/C_{PNP}^{0}$) to mean dimensionless concentration of (A) PNP and (B) FA at T=40°C. Q=1mL/min except black points. Red m=1, Blue FA excess (m>1), Purple FA deficit (m<1)

Heterogeneous catalysis in microreactors: study of the performance of various supports

Abstract :

This study presents the preparation and the evaluation of performance of a new monolithic catalyst in microreactor. The transfer hydrogenation of *p*-nitrophenol by formic acid is chosen as the model reaction for the comparison of the monolith with a traditional packed-bed microreactor containing commercial catalyst.

This thesis includes an important experimental part. On the one hand, experimental set-up and protocols involving on-line analysis have been developed in order to study quantitatively the model reaction; On the other hand, the conditions of preparation of functionalized silica monolith in a stainless steel tube with the inner wall pre-coated by glass were optimized, and the palladium nanoparticles were immobilized by a continuous flow method. The monolith possesses the flow-through macropores, typical hexagonal organization of mesopores and micropores, and scarcely any shrinkage.

The comparison of the two types of catalysts mainly focuses on the activity of catalysts in the model reaction, their kinetic model and their dynamic behavior in the start-up phase of the flow microreactor. In the theoretical part, the modelisation of reactor has been investigated both under stationary conditions for kinetics determination and under transient conditions for the rationalization of experimental observations. Pd@silica monolith and commercial Pd@alumina powder have different behavior and gives different kinetic laws. A reaction model with change in the catalytic surface properties could explain the unusual profile of concentrations observed with commercial catalyst. The superior performance of monolithic catalyst is demonstrated, which also exhibits particular industrial interests.

Key words :

Microreactor, Heterogeneous catalyst, Transfer hydrogenation, Kinetics modelisation, Catalyst synthesis

Catalyse hétérogène en microréacteur : Etude de performance de differents catalyseurs

Résumé :

Cette étude présente la préparation et l'évaluation de l'activité d'un nouveau catalyseur monolithique en microréacteur. La réaction d'hydrogénation du *p*-nitrophénol par transfert d'hydrogène avec l'acide formique a été choisie comme réaction modèle pour comparer les performances du monolithe à celles d'un catalyseur commercial en lit fixe.

Cette thèse comporte une partie expérimentale importante. D'un côté, un montage expérimental et des protocoles d'analyse en ligne ont été mis au point pour faire une étude quantitative précise de la réaction modèle. De l'autre côté, les conditions de préparation d'un monolithe de silice fonctionnalisée dans le tube-réacteur en acier chemisé de verre ont été optimisées. Il a été chargé en nanoparticules de Pd par une méthode en écoulement. Le monolithe comporte un réseau de macropores pour l'écoulement et une organisation hexagonale typique de mésopores et micropores, et cela presque sans retrait au séchage.

L'activité des 2 types de catalyseurs dans la réaction modèle a été comparée par leur cinétique de réaction et leur comportement dynamique dans la phase de mise en régime du microréacteur. Une partie théorique présente la modélisation du microréacteur en régime stationnaire pour l'établissement des cinétiques et en régime transitoire pour rationaliser les observations expérimentales. Le monolithe Pd@silice et le catalyseur commercial Pd@alumine ont des comportements différents et obéissent à des lois cinétiques différentes. Un modèle réactionnel impliquant un changement de propriétés de la surface catalytique pourrait expliquer le profil de concentration inhabituel observé avec le catalyseur commercial. La comparaison démontre la supériorité du nouveau catalyseur monolithe, et lui ouvre de bonnes perspectives industrielles.

Mots clé :

Microréacteur, Catalyse hétérogène, Transfert d'hydrogène, Modélisation cinétique, Synthèse de catalyseur